Super-resolution Imaging with Metamaterials

by

Naomi Ariane Waterman

A thesis submitted to the University of Birmingham for the degree of

Doctor of Philosophy

Physical Sciences of Imaging in the Biomedical Sciences Doctoral Training Centre

School of Chemistry

College of Engineering and Physical Sciences

University of Birmingham

September 2017

Abstract

The key area of investigation of this research project was the application of metamaterials to super-resolution optical imaging. Specifically, an optical microscope was proposed to emulate a TIRF-SIM microscope, but using metamaterials to create a structured evanescent field. A metamaterial unit cell design of two 'H' shape nano-holes at ±45° to the normal in a gold film, with 50nm feature size was developed and simulated in CST Microwave Studio, able to produce structured evanescent illumination patterns. Although this original design proved unsuccessful, both in terms of fabrication and image reconstruction, an alternative design was developed.

Alongside this, in MATLAB an algorithm for SIM image reconstruction using the typical sinusoidal masks was created successfully. Then to accommodate atypical SIM masks, such as those produced by the metamaterials, new approaches to SIM image reconstruction were also developed. These approaches modelled the masks as the sum of sinusoids and as the product of sinusoids. These reconstruction approaches were unsuccessful when using the original metamaterial masks, but were successfully able to reconstruct image with improved resolution, compared to standard SIM, using the alternative metamaterial masks. Moreover, resolution enhancement was demonstrated using six masks instead of the nine or more typically used.

This thesis is dedicated to
Christopher Mathew King,
without whom it would not have
possible.

Acknowledgements

I would like to acknowledge: my supervisors Iain Styles, Shuang Zhang, and Steve Thomas for their help and support; Mark Lawrence for helping me learn how to use CST Microwave Studio; Guy Dawson for his help doing electron-beam lithography; Alex Robinson for his advice and support with nanofabrication; Mark Rosamond for his efforts with nanofabrication; Guixin Li for his advice on metamaterials and help in the lab; everyone at the PSIBS DTC for their help and support. Finally I gratefully acknowledge the funding from the EPSRC through a studentship from the PSIBS Centre for Doctoral Training (EP/ F50053X/1).

Table of Contents

List of Figures

Chapter 1: Introduction & Background

Chapter 2: Design & Simulation

Chapter 3: Image Reconstruction

Demonstrating standard SIM image reconstruction

Chapter 5: Alternative Metalens Design

*

List of Abbreviations

CST MWS – Computer Simulation Technology Microwave Studio

CVD – Cardiovascular disease

FTIR – Fourier Transform Infra-Red (spectroscopy)

SEM – Scanning Electron Microscopy

SIM – Structured Illumination Microscopy

TIRF – Total Internal Reflection Fluorescence

TIRF-SIM - Total Internal Reflection Fluorescence- Structured Illumination Microscopy

Chapter 1: Introduction & Background

1.1 Introduction

The aim of this PhD study was to investigate and implement the use of metamaterials in biomedical imaging. The primary aim was to build a Super-resolution Total Internal Reflection Fluorescence (TIRF) Microscope with structured illumination, utilising the unique electromagnetic (EM) properties of metamaterials[8-12] to construct a metamaterial lens (metalens) to enable sub-diffraction limit imaging with an evanescent EM field[13-28], and employ it in the study of cardiovascular disease. The improved resolution as compares to a TIRF system would allow detailed study of the surface proteins of platelets, including looking at actin filaments and microtubules, which are implicated in cardiovascular disease[29-31] . In addition, Structured Illumination Microscopy (SIM) image reconstruction algorithms were investigated and implemented, in order to reconstruct the images from the proposed microscope, and for use with other structured illumination systems[33-40].

Consequently, this PhD thesis incorporates elements of physics, specifically optical theory and metamaterials in particular, as the key design foundation; biomedical science, particularly biological imaging, as the driving force behind the project; and computer science and the investigation of image reconstruction algorithms, alongside critical simulation work that formed an essential component of this research. The key area of investigation of this research project was the application of metamaterials to super-resolution optical imaging. Specifically, an optical microscope was proposed to emulate a TIRF-SIM microscope, but using metamaterials to create a structured evanescent field.

1.2 Aims

The key aims of this PhD were as follows:

- Design, simulate and fabricate a metamaterial suitable for a novel TIRF-SIM microscopy system.
- Develop and test SIM reconstruction algorithms suitable for use with this system and other SIM-type systems.

1.3 Introduction to Background

In this section, background material and literature of relevance to this research project is reviewed. This includes the biological motivation and guidance for the project; the background of biomedical imaging and imaging in general; the relevant physical theory behind optical microscopy, metamaterials and optics; the current state of research in the fields of super-resolution microscopy, metamaterials as applied to optics, structured illumination microscopy, and surface-enhanced fluorescence and non-linear optics.

1.4 Biological Imaging

1.4.1 Introduction

The ultimate aim of this PhD is to apply the proposed metamaterial systems to biological imaging. In order to effectively study and understand biological systems, imaging is crucial. Indeed, biological research has been a prime factor in the development of the fields of microscopy and imaging, from the first images taken of bacteria by Antoni van Leeuwenhoek in the 17th century with a simple optical microscope[46,47], to the current ability to see individual molecules with electron microscopy[48], spectroscopic brain imaging with MRSI[49-51],

and the ability to do time resolved whole body imaging of embryos with the recently developed light-sheet microscopy system[52-56].

1.4.2 Cardiovascular Disease & Platelets

The biomedical field of particular interest to this PhD is to apply the proposed metamaterial systems, particularly the super-resolution TIRF-SIM microscope, to the study of cardiovascular disease (CVD). CVD is a broad term for a range of conditions and diseases that affect the cardiovascular system; these include: coronary heart disease, atherosclerosis, cerebrovascular disease, peripheral arterial disease, rheumatic heart disease, congenital heart disease, deep vein thrombosis and pulmonary embolism[57]. These conditions can lead to acute events including heart attacks and strokes[57,58] and globally more people die annually from CVD than from any other cause[57-59]. Indeed in 2008 an estimated 17.3 million people died from CVD worldwide, representing 30% of all global deaths, and by 2030 this is expected to rise to 23.3 million[59,60].

Consequently, the study of CVD is a major healthcare priority. In the biomedical sciences this involves research into not only treatment and prevention, but detection and imaging of the condition[57,58,61]. On the scale of organs and blood vessels, the most common imaging technologies used to study CVD are CT (Computed Tomography) and MRI (Magnetic Resonance Imaging)[61]. However, this PhD will aim to investigate CVD on the sub-cellular scale, looking at receptors and proteins, with specific interest in the role of platelets in CVD[60].

Platelets are the smallest cells in circulating blood and are traditionally known for their involvement in haemostasis – the process of stopping blood flow which is particularly

important in wound healing[21-23]. Platelets also have a key role in thrombosis, the formation of blood clots within blood vessels[29,30], which has obvious implications for CVD conditions such as Deep Vein Thrombosis[57]. The formation of a blood clot or thrombus is mediated by the expression of multiple membrane receptors, which besides being crucial to haemostasis and thrombosis are thought to promote inflammatory and immune responses[29-31]. Moreover recently platelet receptors such as GPIb/IX/V, P-selectin, P-selectin glycoprotein ligand 1, CD40 and the αIIbß3 integrin have been implicated in the progression of such inflammatory conditions as atherosclerosis, in tumour cell proliferation, metastasis, and tumour angiogenesis, and in the immune response to bacteria. Therefore it is these receptors and surface proteins and their link to CVD that this PhD is interested in[60].

1.4.3 Microscopy for Biology

Microscopy is widely used for biomedical imaging, in a variety of techniques adapted for different purposes. The many microscopy techniques that exist, have different advantages and disadvantages for biological imaging, each fulfilling certain criteria and being of use when imaging some types of sample or investigating different phenomena, but none achieving a 'perfect' imaging system[62,63].

The ideal biological imaging setup incorporates: high spatial resolution in x, y and z; good time resolution for monitoring active systems; suitability for use with labelling techniques including fluorescent dyes and proteins, and the ability for multiple fluorescent channels or imaging modes to be captured for the same sample area; live cell or tissue imaging capability, so the information gleaned is more biologically relevant; non-damaging to the biological sample, so non-ionising radiation; minimal sample preparation required, meaning

the sample used is in a state closer to in vivo; ease of use of the imaging equipment[23,37,41,43,62-71]. However, all current biological imaging systems have a trade-off between these factors. Different imaging systems are capable of achieving different ones of these factors, depending on what type of sample or what type of imaging they are aimed at. For example, electron microscopy achieves very high spatial resolution (50pm[66]), but requires high levels of sample preparation meaning live cell imaging is often impossible, and fluorescent labelling cannot be done[48,72-74]. Whereas, epi-fluorescence imaging systems allow for fluorescent labelling of multiple channels of interest, can do time-resolved live cell imaging, but is diffraction limited in its spatial resolution[75,76].

Therefore, when utilising or designing a biological imaging system, the biological question wanting to be answered dictates the choice of microscopy technique and prioritisation of the imaging factors.

1.4.4 Impact of Biological Constraints on Microscopy

Although the field of microscopy started primarily with imaging biological samples[46,47], using microscopy to image biological samples places constraints on the imaging and the imaging technique chosen[43,63]. These constraints depend greatly on the sample to be looked at, and what question is being investigated with the imaging. As the ultimate aim of this PhD is to apply metamaterials to biomedical imaging, this places constraints on the study. Potential constraints to be considered are:

- Damaging sample preparation – sample preparation is often a key stage in biological imaging, whether it be fluorescent labelling, fixing the sample, or more damaging sample preparation. Often these techniques are used to enable the imaging to elucidate more

information or improve the imaging, such as labelling specific structures of interest, however they can also damage the sample. If possible it can be desirable to image with minimal sample preparation, thus without affecting the structures of the biological sample. This is because, the less that is done to the sample, arguably the more biologically relevant the resultant images are[63,64,77-80]. This is as opposed to techniques such as SEM where extensive sample preparation, including coating the sample with a conductive metal, is required[72]. Such extensive methods of sample preparation can shift structures, artificially cross-link proteins as occurs when fixing cells changing the shape of biological structures, or simply damage biological structures so that they cannot be imaged[77,78]. In many cases damaging sample preparation is not restrictive, especially in light of potential gains to resolution as with electron microscopy or the need to label specific features. The proposed imaging systems require sample preparation on a par with epifluorescence imaging, thus are not overly damaging, which is what is desired from the imaging system[75,76].

- Live cell imaging – as with non-damaging sample preparation, live cell imaging can allow for even more biologically relevant imaging, as biological samples can be imaged as living organisms and their live behaviour can be observed[78]. This requires the imaging system to have environmental controls, for example temperature and pressure control, ability for 'wet' samples to be imaged, and potentially sterile conditions so that the sample remains alive[64,67,78,79]. Moreover, certain fluorescent labels or dyes cannot be used as they can be toxic[81]. This places constraints on the imaging system that have to be overcome if live cell imaging is desired, although it is not always required. The imaging system proposed by this PhD did not include live cell imaging as it is based upon TIRF-SIM

and brightfield microscopy, it would potentially be adaptable to a live cell imaging modality, similar to those used for more conventional fluorescence imaging[38,70,75,82,83].

- Resolution limitations. A major consideration with biological imaging is the resolution, either spatial or temporal, and generally it is very hard to achieve high spatial and temporal resolution simultaneously. In addition, it can also be challenging to achieve high spatial resolution both laterally and axially, which makes techniques capable of optical-sectioning, thus improving the axial resolution, very important in biological imaging[35,41,43,48,52,53,55,56,65,75,82-84]. Therefore there is generally a compromise to be made between spatial and temporal resolution, and between resolution and other imaging constraints.
- Optical limitations. A key constraint is the optical range of the incident light, when considering optical microscopy. As defined by the diffraction limit, which is discussed in greater detail in *Section 1.5.2*, the spatial resolution is constrained by the wavelength of light used for imaging, thus non-super resolution optical microscopy typically can only achieve resolutions of 200nm at best, which is larger for longer wavelengths[43,77,83,85]. This can be combatted by using shorter wavelengths of light, as is done in X-ray and electron microscopy, but this resolution improvement is countered by the constraints on sample preparation and potential damage to biological samples[48,66,72,73,86]. In addition, the choice of incident or excitation wavelength impacts on the choice of fluorescent labelling, as the excitation wavelength must correspond to that of the fluorophore[75,81]. In addition, when using metamaterials a balance has to be achieved between the operating frequency range of the metamaterials, and the best frequencies to use with biological

samples[13,26,87]. On a practical level, having a microscopy system that easily operates at the excitation frequencies of commonly used fluorophores can be very desirable.

1.4.5 Discussion

In conclusion, there are many challenges and constraints associated with imaging biological samples, which then impact upon the choice of imaging technique. However, a wide variety of imaging techniques have been developed to allow for better imaging of biological samples. These techniques allow many areas of biological research to be investigated, each with different aims and requirements, including the important research into cardiovascular disease.

1.5 Optical Microscopy

1.5.1 Introduction

Optical microscopy is a key tool in biomedical research, and has been since the first microscopes were developed in the 17th century, and can be broadly described as a technique for magnifying small samples via a system of visible light and lenses to produce images[46,47]. Optical microscopy, particularly fluorescence microscopy, is a primary method of imaging cells and their organelles[41,43,77,83,85]. Much progress has been made in developing different optical microscopy techniques, leading to techniques such as Confocal Microscopy and TIRF Microscopy, in order to meet the multivariate demands of biomedical imaging[33,35,38,43,77,83,85,88].

1.5.2 The Diffraction Limit

Despite being widely used, a key limitation of optical microscopy is its spatial resolution, which for non-super resolution techniques is controlled by the diffraction limit. When light

passes through an aperture such as a lens in an imaging system, it is diffracted. The behaviour of the diffracted light depends on whether it is in the near-field (Fresnel diffraction), near to the diffracting element, or the far-field (Fraunhofer diffraction), 'far' from the diffracting element, region. The transition distance between these two regions depends upon the wavelength of the diffracted light and the size of the diffracting element, but the near-field is generally considered to be <1-2 wavelengths from the diffracting element. In the near-field, high frequency waves which contain high resolution information about the diffracting element (imaging sample) exponentially decay evanescently. Whereas the far-field waves, which contain low resolution information about the diffracting element, propagate and these are what are observed in standard optical imaging systems. The near-field high resolution information is unrecoverable in the far-field, thus giving rise to the diffraction limit on imaging resolution. Consequently, optical microscopy always has inherently limited spatial resolution even with a perfect imaging system, due to the loss of the higher resolution information in the near-field[41,43,63,76,89].

In the far-field, which is the relevant component for most optical microscopy, the diffraction of the propagating wave produces a diffraction pattern of a bright circle surrounded by concentric circles which decrease in intensity, known as an Airy disk. The diameter of an Airy disk is defined by the wavelength of light used. When such Airy disks produced by features on an imaging sample get close, they overlap and eventually become indistinguishable or unresolvable, which is also defined as the diffraction limit[90,91].

The Abbe limit defines the Airy disk which characterises the point spread function (PSF) of an imaging system, which determines the lateral resolution[77]. This means that a limit is imposed

upon the resolution of the images obtained due to the nature of the light used for imaging[33,41,43,77,85,88]:

$$x = \frac{\lambda}{2 \cdot NA} \qquad [1.1]$$

$$NA = n \cdot sin(\alpha) \qquad [1.2]$$

Where: x – smallest distance over which two objects can be resolved, λ – wavelength of light, NA – numerical aperture, n – refractive index of the medium, α – half the angular aperture of the lens. Consequently most optical microscopy techniques can only reach lateral resolutions of ~200 - 250nm at best within optical wavelengths[43,77,85].

1.5.3 Diffraction Limited Optical Microscopy

There are many forms of optical microscopy currently in use, what they hold in common is the use of visible light for imaging, ~400 – 700nm in wavelength, although many optical microscopy techniques can extend this range into the infra-red or ultraviolet[41,43,63,76,77,82,86,92]. As previously discussed, optical microscopy techniques are limited in their spatial resolution by the Abbe limit; they are limited in their temporal resolution by the technological capabilities of the imaging system, i.e. image frame rate, scan time and computer storage capabilities. Development of the many optical imaging techniques from the original compound microscopes, made of simple hand-ground lenses in the late 16th and 17th centuries, has primarily been driven by the desire to improve resolution, spatially and temporally, and to discern different features in the sample[46,47,77].

In terms of biomedical imaging, a critical advance was the development of fluorescence imaging; whereby fluorescent agents, be they fluorescent dyes, fluorescent proteins or

fluorophores, are used to label sample features of interest and are excited at specific frequencies, and then emit light at different frequencies. It is this emission which is detected and forms the image[41,70,75,80,82,83]. This fluorescent labelling allows specific structures to be identified and thus their specific behaviour to be investigated. Consequently the development of fluorescent agents has been a key area of improvement for optical imaging[67,75,81,92]. The standard optical microscope in use today for biological research is widefield epi-fluorescence microscopy. This optical microscopy technique is used to image fluorescently labelled samples, by exciting them with widefield incident light at the excitation frequency of the chosen fluorophores, and then collecting their emitted fluorescence. This is a diffraction limited technique, but it is suitable for live cell imaging[75,79,83,93].

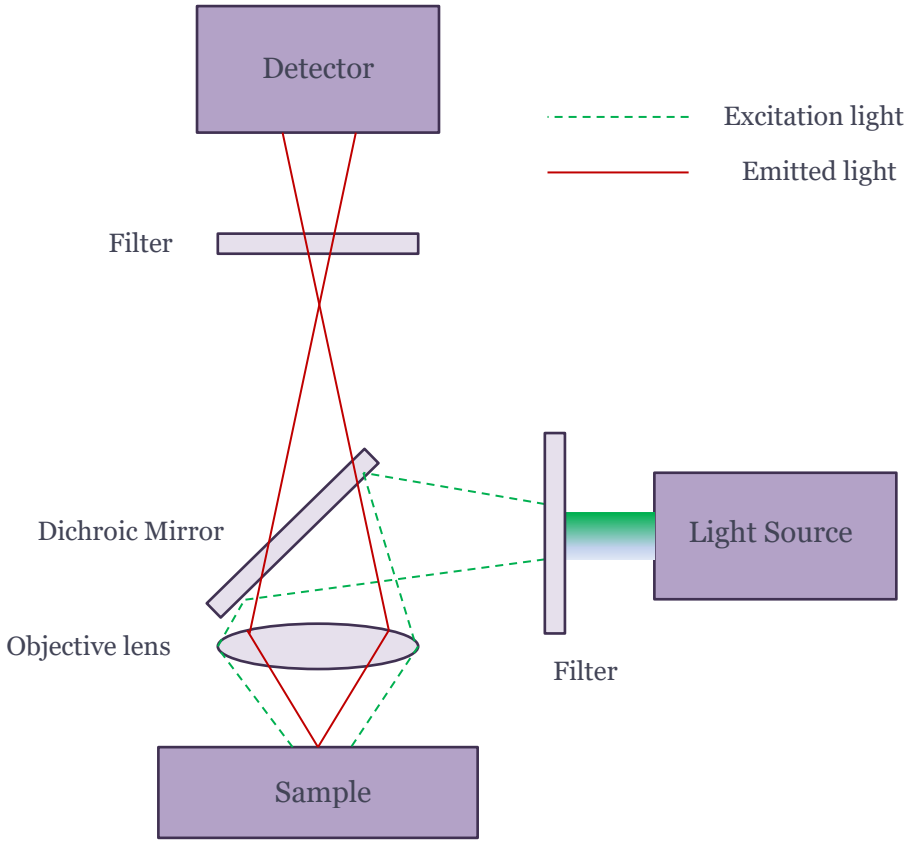

Figure 1.1: Diagram outlining a widefield epi-fluorescence microscope, including light paths and key components[42,43].

In addition, the confocal microscope is also widely used[63,82]. Its defining feature is the ability to exclude out of focus photons from a focal plane within a sample, using pinholes, and thus optically sectioning the sample[77,85]. This produces very clear, unblurred images, however it does affect the signal-to-noise ratio (SNR)[85]. If a stack of images from different optical sections or focal planes are taken then a 3D image of the sample can be constructed, which is very useful for biomedical applications[62,77,82].

From the standard epi-fluorescence microscopes, novel techniques including multi-photon fluorescence imaging have developed. Multi-photon fluorescence microscopy works by using multiple long-wavelength (typically near infra-red range) photons to excite fluorescence,

which then emits at a shorter wavelength. This improves the penetration depth, suppresses background signal, and reduces damage to the sample[43,94-97]. By contrast, TIRF (Total-Internal Reflection Fluorescence) microscopy, described further in *Section 1.5.6*, selectively excites only the surface region of a sample allowing for improved resolution imaging of the surface, but again suppresses background fluorescence improving the signal to noise ratio (SNR)[41,70,98,99].

Diffraction-limited Optical Microscopy Technique	**Typical Spatial resolution (lateral)**	**Comments**
Epi-fluorescence microscopy	Up to 200 – 300nm	Standard widefield fluorescence microscopy technique[42,75,93,100].
Confocal microscopy	Up to 180 – 250nm	Eliminates out of focus light for high SNR, scanning technique not widefield, 3D volume imaging[63,85,100,101].
Total Internal Reflection Fluorescence microscopy	200 – 300nm	Surface imaging technique, only surface fluorophores are excited, improved axial resolution[41,70,100].
Multi-photon microscopy	<1µm, up to 200nm	Low photo-damage and high penetration depth.[96,97,102]
Light Sheet microscopy	0.5 - 6µm	High temporal resolution, and large volume 3D imaging possible[52-56,103].

Figure 1.2: Table outlining key diffraction-limited optical microscopy techniques.

1.5.4 Going Beyond the Diffraction Limit – Super-resolution

As already mentioned, a primary aim in the field of imaging has been improving the spatial resolution of optical microscopy techniques, beyond the diffraction limit. Super-resolution techniques can achieve resolutions below this limit. Of particular interest to this thesis is structured illumination microscopy (SIM), which utilises additional light patterns and post processing to achieve super resolution. It is discussed in greater detail in *Section 1.6*. It is one of the many modern optical imaging techniques to extensively use computational post-processing to improve spatial resolution, achieving resolutions of 100nm or better, with generally no sample damage[33,36,39,100]. Stochastic methods also require computational post-processing, including STORM (Stochastic Optical Reconstruction Microscopy), which can achieve a lateral resolution of ~25nm, and PALM (Photoactivated Localisation Microscopy). These techniques utilise innovative 'blinking' fluorophores that are excited stochastically, as opposed to the norm of all fluorophores of that excitation frequency being excited together, allowing for single molecule localisation and much improved spatial resolution, however image acquisition is slow[43,69,88]. In addition, techniques such as STED (Stimulated Emission Depletion) microscopy, which uses the nonlinear response of the fluorophores to excitation, can also achieve lateral resolution at the molecular level, but these techniques carry the risk of damaging the sample with the high-powered lasers required[43,100]. Metamaterial-based approaches also aim to achieve these resolutions or better, but with rapid image acquisition and low sample damage[15,17,19,25-28].

All of the imaging techniques mentioned above are far-field techniques, so detection is in the far-field, and the super-resolution techniques that have been discussed are attempting to overcome the diffraction limit. However, the diffraction limit is only applicable to far-field

techniques and not near-field techniques[76,90,100,101,104]. Thus near-field imaging, such as Near-field Scanning Optical Microscopy (NSOM), is able to achieve super-resolution, of the order of 20nm lateral resolution, as the evanescent near-field contains information beyond the diffraction limit. However, in order to achieve this an imaging probe has to be within one wavelength of light from the sample, which can be challenging, and generally image acquisition is slow for large samples and only surface imaging is possible[43,104]. NSOM is also able to acquire spectroscopic information about the sample, which allows for even greater knowledge to be gained from imaging a sample[105,106].

In contrast, an exciting recent development in optical microscopy in terms of temporal resolution is light-sheet microscopy. Also known as selective plane illumination microscopy (SPIM), it is similar to confocal microscopy in that it can selectively illuminate planes within a sample; however instead of doing this with a spot of light, it uses a sheet of light. It most effective for use with highly transparent samples and it cannot achieve the same spatial resolutions of super-resolution optical techniques[64], it is diffraction limited, but it can be combined with super-resolution techniques such as SIM[56] or single-molecule localisation[64] to improve its spatial resolution. Furthermore, the key advantage of light-sheet is its high temporal resolution. Unlike point-scanning techniques like confocal, or the super-resolution techniques that involve a lot of image post-processing, it can achieve 10 – 1000 times faster than other 4D imaging techniques[107]. Indeed it has been used to image intact live samples, including neuronal firing in the intact brain of awake behaving mice, as well as freely moving transgenic Drosophila larvae[52].

1.5.5 Comparing Optical and Non-Optical Microscopy

Even super-resolution optical microscopy techniques have low spatial resolution compared to non-optical techniques such as electron microscopy, including Scanning Electron Microscopy (SEM) and Transmission Electron Microscopy (TEM), Atomic Force Microscopy (AFM), and X-ray Microscopy (XRM). For example, resolutions of <1nm[48], 50pm[66], <1nm[108,109] and 10nm[86] respectively have been achieved, allowing for molecular resolution. However these techniques also have their drawbacks, which often outweigh their high spatial resolution. In particular, these techniques are generally unsuitable for imaging live biological samples and fluorescent labelling is not possible, and they require extensive and damaging sample preparation, thus limiting the biological relevance of the images produced[39,52,63,66,72,73,75,99,100,103]. Moreover, one of the key advantages of optical microscopy as a field is its adaptability. There is an enormous variety of optical microscopy techniques available, each adapted to different areas of scientific investigation and suited for different imaging challenges, and they are also able to be combined to provide even greater information[39,55,76,79,82,94,110,111].

1.5.6 Total Internal Reflection Fluorescence (TIRF) Microscopy

TIRF microscopy itself is designed to improve image resolution, however it is not a super-resolution technique. Instead TIRF improves resolution by reducing background fluorescence and improving the signal-to-noise ratio[41,43,70]. In the case of a brightfield or epifluorescence microscope the incident light is perpendicular to the sample and illuminates the whole sample, which thus excites all fluorophores within the sample[43,77,83]. In in a TIRF microscope, the incident light is incident at an angle to the dielectric substrate of the sample (commonly

a glass slide). If this incident angle is larger the critical angle, θ_c, then frustrated Total Internal Reflection (TIR) will occur within the dielectric substrate[43].

$$\theta_c = sin^{-1}\left(\frac{n_1}{n_2}\right) \qquad [1.3]$$

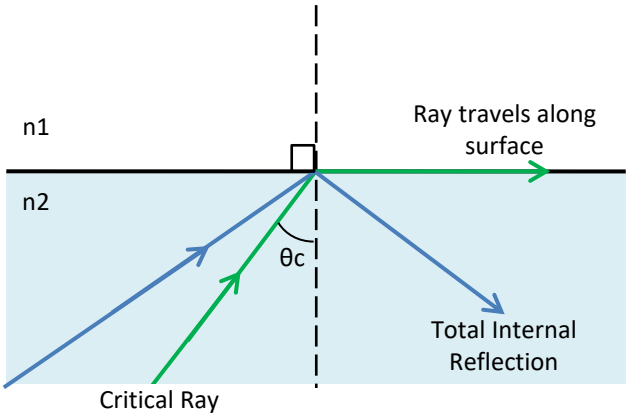

Figure 1.3: Schematic of Total Internal Reflection.

In TIR no light escapes and propagates, see figure 1.3; conversely in frustrated TIR some light will still reach the sample as an evanescent wave which propagates along the interface between the substrate and the sample. An evanescent wave is a near-field wave whose intensity decays exponentially without absorption away from its originating surface, making it strongly confined, and in TIRF microscopy it is this evanescent wave that excites the fluorophores in the sample, see figure 1.4, their emission is then collected by a CCD camera[41,43,77,83,94].

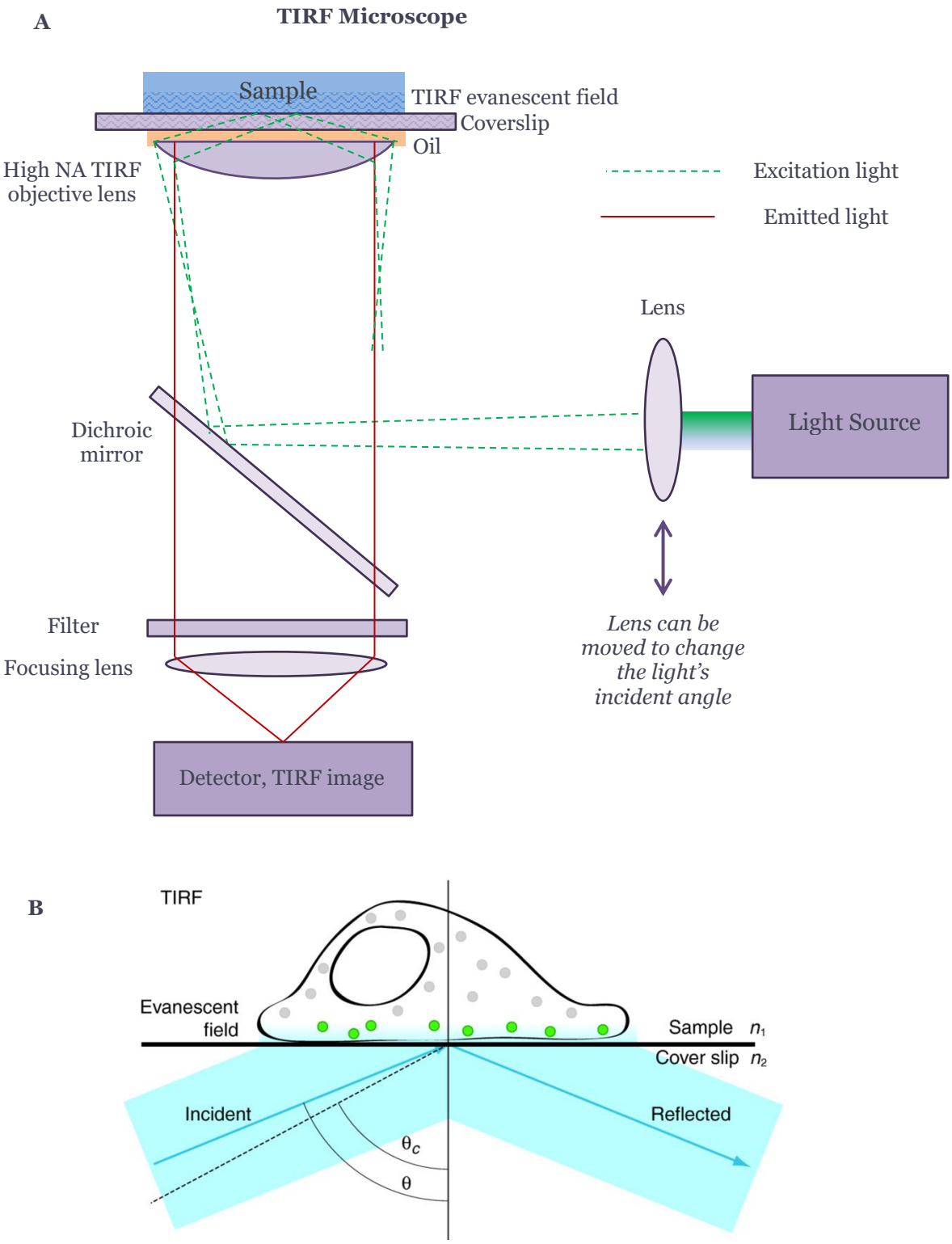

Figure 1.4: A - *Diagram outlining a TIRF microscope, including light paths and key components*[4]*; B - Schematic of TIRF microscopy, demonstrating the creation of the evanescent field via frustrated TIR, which excites the fluorophores (green) in a thin slice of the sample*[2,41].

As a result of the confined nature of the evanescent wave only a thin section of the sample is illuminated (~100-200nm thick), thus only fluorophores in this thin section are excited, reducing background fluorescence and improving image resolution to ~100nm[41,43,83]. Consequently TIRF microscopy can only be used for looking at the surface of a sample, which limits its potential uses, and achieving the correct illumination angle can be challenging. Conversely it is the principal technique for imaging the cell membrane, cytoplasmic filament structures of cells, the process of endocytosis, and the adsorption of liquids at interfaces[41,43]. Recently, TIRF microscopy has been used to dynamically image individual endocytic events at the apical membrane of thick ascending limb cells, specifically the NaCl reabsorption by Na-K-2Cl cotransporters in the membrane of kidney cells, which plays a crucial role in the maintenance of body salt and fluid homeostasis[99]. In addition it has been used to investigate the actin cytoskeleton, which is key to cell shape and movement, and its formation mechanics and patterning specifically the contribution made by the lower dimer in actin polymerisation of skeletal muscle actin[112].

It is hoped that the proposed microscope of this PhD will retain the positive aspects of TIRF microscopy, including its narrow excitation and ability to study surface phenomenon, whilst improving the resolution.

1.6 Structured Illumination Microscopy (SIM)

1.6.1 Introduction

Structured illumination (SI) is another technique employed in optical microscopy to enhance spatial resolution, but it does not always confer super-resolution[33,35,38,43,113], it can also be used to optically section a sample[33-35,38,113], akin to confocal microscopy[77,83,85,113]. It is easily applicable to pre-existing optical imaging systems, giving them greater functionality[98,114,115], and is generally not damaging or phototoxic[36,37,116].

1.6.2 Theory of SIM

This section describes the standard wide-field SIM methodology that is most commonly used and is available commercially[36,117], and it also forms the basis for the other SIM methods, some of which are described in detail in *Section 1.6.3*.

The sample is illuminated with spatially structured excitation light – a periodic pattern – this creates a low-frequency beating effect with the features of the sample. This encodes the higher frequency and thus higher resolution structural details, which would normally be excluded by the diffraction limit by being outside the pass-band of the system's Optical Transfer Function (OTF), in the low frequency signal via spatial frequency mixing. This makes normally inaccessible high-resolution information visible in the observed image in the form of Moiré fringes[33,43]. The structured light can be produced by a spatial light modulator[98], an optical grating[33] or by the interference of two or more coherent illumination beams[38]. A series of such images is taken, with the pattern at several different orientations and different phase shifts. This series of images allows higher frequency information to be captured, extending the area where the higher resolution information can be retained, allowing for

uniform improvement in spatial resolution across the whole 2-dimensional imaging plane as opposed to resolution improvement in only one direction, see figure 1.5. Moreover, in order to then separate these higher frequency spectra, the phase shifts are required, and the multiple images allow for the removal of the spatial pattern from the final image. These images are then processed to extract the higher resolution information and generate a reconstruction with the improved resolution[28-31,52], see figure 1.5.

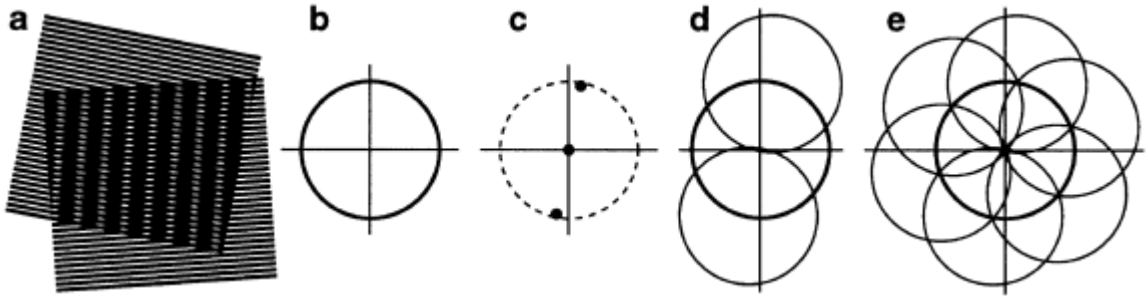

Figure 1.5: Image from Gustafsson (2000). Structured Illumination and resolution enhancement: a – two line patterns superpose, their product contains Moiré fringes (the vertical stripes); b – representation of the Airy disk of a conventional microscope, the circle represents its observable region; c – a sinusoidally striped illumination pattern has only three Fourier components, the possible positions of the two side components are limited by the same circle that defines the observable region (dashed); d - the moiré fringes represent information that has changed position in Fourier space, with the amount of movement corresponding to the three Fourier components of the illumination, these circles are centred on the positions seen in (c), the observable region will thus contain the normal and the moved information that originates in two offset regions; e – from a sequence of images with different orientation and phase of the pattern, it is possible to recover information from an area twice the size of the normally observable region, corresponding to twice the normal resolution[2,33].

The basic principles of SIM are shown in figure 1.5. Generally, if two patterns are superposed, Moiré fringes appear which are coarser than either of the original patterns; these fringes represent information from the patterns that has been shifted in Fourier space as a result of the superposition. In terms of imaging, the sample to be imaged and the structured illumination incident upon it act as the two patterns. As a result, the observed

image is the product of the two patterns including the sample, and will contain the Moiré fringes. These fringes are easily observable, compared to the fine detail of the sample that is not observable because of the diffraction limit, but contain information about this fine detail. Thus, in standard SIM, if the illumination pattern is known, this higher resolution information from the sample can be accessed, creating a super-resolution imaging technique[33,35,36].

The resolution of standard SIM is still partially diffraction limited, despite being able to achieve super-resolution beyond the diffraction limit. The resolution achievable by standard SIM is limited by the spatial frequency of the illumination pattern, which is produced with standard optics and thus is diffraction limited[118]. The higher the spatial frequency of the illumination pattern theoretically results in more higher-resolution information that can be retained in the far-field, and consequently the higher the spatial resolution achievable[40].

The addition of SI can allow features of 100nm or smaller to be imaged, if nonlinear processing techniques are used[35], in the sample to be successfully resolved, and it can be applied to fluorescence microscopy[33,43]. However as multiple images are required, image acquisition is often relatively slow[43,119].

1.6.3 Different SIM Methods

There are now a wide variety of SIM techniques in use[36,37,120]. The original description of SIM in 2000 by Gustaffson used sinusoidal stripe patterns of light, projected onto the sample via a line-patterned phase grating[33]. By creating pattern masks at different orientations and different phases, it is possible to retain near-field, higher resolution, data and access it in the far-field[33,35-37,121]. The original 2-dimensional implementation of SIM uses three orientations

and three phases, as described by Gustaffsson, so nine images in total are required[33]. This is still the essential premise of SIM, but it has been altered and expanded to give greater functionality[116,121]. Three-dimensional SIM has been realised, but if using the standard sinusoidal stripe patterns it requires typically fifteen images[40,121], but this gives much greater imaging potential.

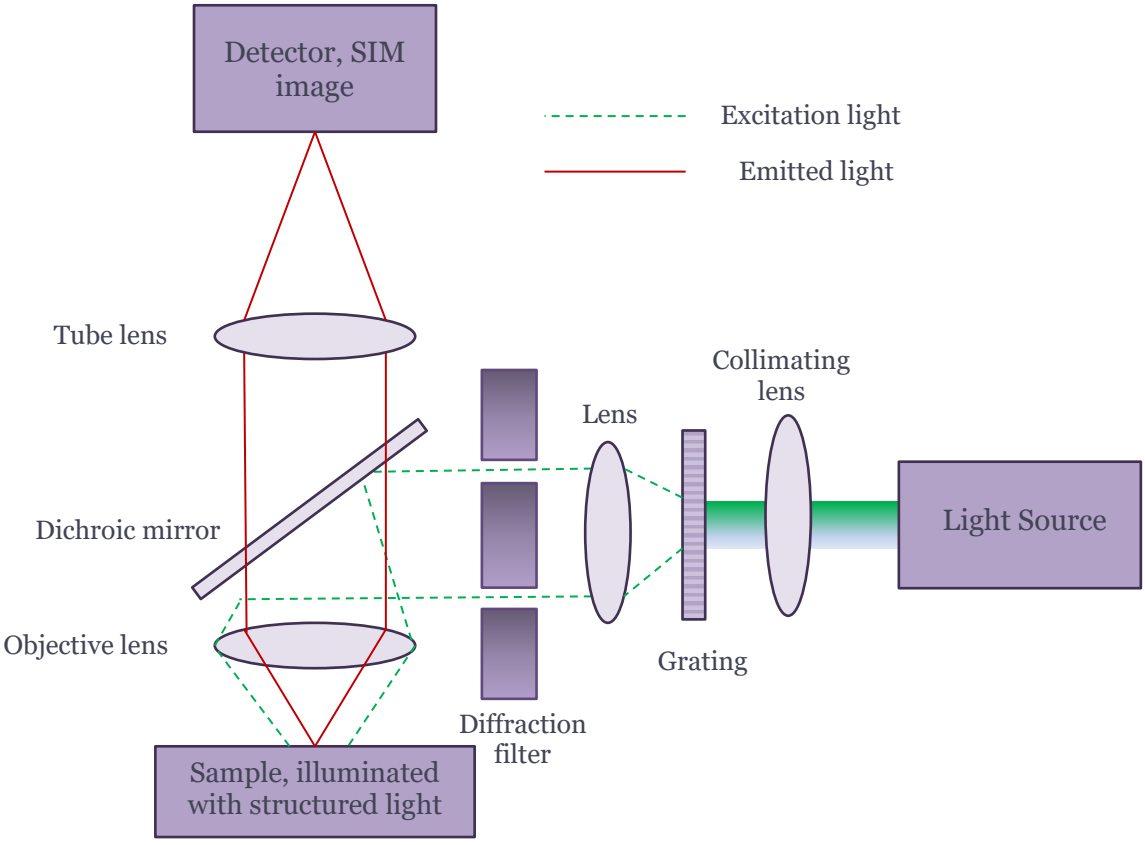

Figure 1.6: Schematic of a standard structured illumination microscope, for 2D fluorescence super-resolution imaging using sinusoidal patterns, including light path and key components[5-7].

Figure 1.6 above shows a typical setup for structured illumination microscopy, using sinusoidally structured patterns for super-resolution imaging. This setup remains very similar even for Blind SIM and Non-linear SIM, discussed further below, as the key change is replacing the grating with an element such as a spatial light modulator to produce the different structured illumination, and then different methods of post-processing[35,120,122-124].

1.6.3.1 Blind-SIM

As already described in *Section 1.6.2*, 'standard' SIM requires prior knowledge of the patterns used in order to achieve image reconstruction[33,36]. However, even if the patterns are well known, there are often artefacts in the imaging system that distort the patterns, which limits the effectiveness and resolution improvement of the SIM system[36,38,123]. Techniques have been developed to help retrieve the pattern parameters accurately, but low SNR and strong distortion of the patterns limit the success[120]. Therefore, advances have been made in developing reconstruction methods that do not require this prior knowledge[120,124]. The key method for achieving this is known as 'Blind-SIM'.

As suggested by its name, this SIM reconstruction method assumes no prior knowledge of the illumination patterns, but does assume homogeneous illumination of the sample across all of the illumination patterns. This is in direct contrast to standard SIM reconstruction, where prior knowledge of the structured illumination patterns is what allows for higher resolution information to be reconstructed, resulting in a super-resolution image. This requirement for prior knowledge, as well as instrumental constraints, is part of the reason that sinusoidal structured illumination is so common to SIM, as it easy to produce and characterise[33-37]. However, Blind-SIM has been demonstrated using a random speckle pattern of illumination, instead of the typical sinusoidal stripes, where prior knowledge of the pattern is inherently limited[120,123,124]. There have been several variations of the Blind-SIM method, primarily from the Sentenac research group at the CNRS at Institut Fresnel, but their shared approach is avoiding the problem of prior knowledge of the structured illumination[120,123-126].

In order to reconstruct an image in Blind-SIM, the image (typically fluorescence density) and the illumination patterns must be reconstructed simultaneously via an iterative method. Typically this is an iterative solution of a constrained least-squares problem based on a conjugate gradient method. Iterative solvers are ideal for solving large problems, such as image reconstruction, as they simplify the problem down to a set of linear equations. However, the parameters used for the solution can have a large impact on the final reconstruction and errors can dominate or convergence can be reached before the solution has been found[127,128]. Another limitation of this type of reconstruction technique is speed, which generally makes it suitable for situations where temporal resolution is important. As it is an iterative method, this makes it more computationally expensive and slower; however this is an area that is being improved with methods such as the joint reconstruction Blind-SIM, which simplifies the Blind-SIM reconstruction method by treating the reconstruction as a set of smaller sub-problems to solve[120].

1.6.3.2 Non-Linear SIM

Another key SIM method is Non-Linear SIM (NL-SIM). This method is theoretically not diffraction limited; standard SIM although a super-resolution technique, is diffraction limited in terms of producing the illumination patterns. NL-SIM generally utilises high intensity sinusoidal illumination patterns to illuminate fluorescent samples. By using this high intensity illumination, the fluorophores' optical transitions have the potential to become saturated, particularly in the bright regions of the illumination pattern. Consequently the degree of excitation saturation varies with respect to the illumination pattern, meaning that the pattern of emission from the fluorophores is no longer purely sinusoidal, instead the emission response is non-linear. This extends the emission into having higher harmonics

beyond the spatial frequency of the illumination excitation pattern, allowing for higher resolution information to be obtained beyond linear SIM techniques[37,40]. The main limitation of this technique is that shared by all high intensity illumination optical techniques, the problem of photobleaching and associated phototoxicity[3,35,100,122].

1.6.4 Uses of SIM

There are two key uses of SIM: optical sectioning and super-resolution imaging[34]. However it has also been used for surface profiling and phase imaging[39]. Optical sectioning and super-resolution have obvious advantages and applications in imaging, particular biomedical imaging, with the focus of this research project being on the super-resolution aspect.

Super-resolution SIM allows for imaging beyond the diffraction limit, resulting in higher spatial resolution than diffraction-limited imaging techniques. This leads to being able to obtain more detailed data from images, and has led to important scientific discoveries[39,40,116,120,121]. Since its inception, SIM for super-resolution imaging has remained at the forefront of biomedical research. As a super-resolution optical imaging technique it is ideal for live-cell imaging, and due to its optical sectional capability, it is also suited to 3D imaging. SIM has been used to image nuclear structures using multiple colours, and in 3D, allowing quantitative analysis of 3D nuclear structures and epigenetic modifications to be performed[129]. Moreover, it has been used to study in vivo sub-chromosomal chromatin organisation in mammalian cell nuclei with unprecedented detail[130], and has formed a key part of a method for imaging synaptic structures, achieving resolutions such that the functionality of these neuronal connections can be resolved[131].

The use of SIM also goes beyond mammalian cells, and it is now being used in the field of plant science. Recently, a form of time-lapse SIM was used to study living cortical microtubules of different plant cell types. This was done using a commercially available SIM platform, and shows that SIM can be widely applied to the imaging of plant cells[132]. This demonstrates that SIM is a powerful imaging tool in the field of biomedical imaging.

1.6.4.1 Combining SIM with Other Imaging Techniques

As already mentioned, SIM has great potential for being combined with other optical imaging techniques. The ability for an optical imaging system to do SIM can be generally be achieved simply by adding the framework for producing structured illumination onto the pre-existing system. SIM has been successfully combined with many techniques including: multi-photon imaging[114,115]; TIRF[98], which is discussed in more detail in *Section 1.6.5*; single-molecule localisation techniques such as PALM and STORM[110]; light sheet microscopy[121]; and Raman microscopy[111].

1.6.5 TIRF-SIM

TIRF-SIM is the application of structured illumination to total-internal reflectance fluorescence microscopy. TIRF is discussed in *Section 1.5.6*, and is an important imaging technique, particularly in biomedical imaging. TIRF-SIM combines TIRF and SIM to produce a super-resolution TIRF imaging technique. As with TIRF, TIRF-SIM uses evanescent light to illuminate a thin surface slice of a sample, instead of the whole sample volume. This eliminates out of focus light and improves the SNR, but does mean it is limited to imaging the surface of samples, making it very useful for imaging cell membranes[70,98].

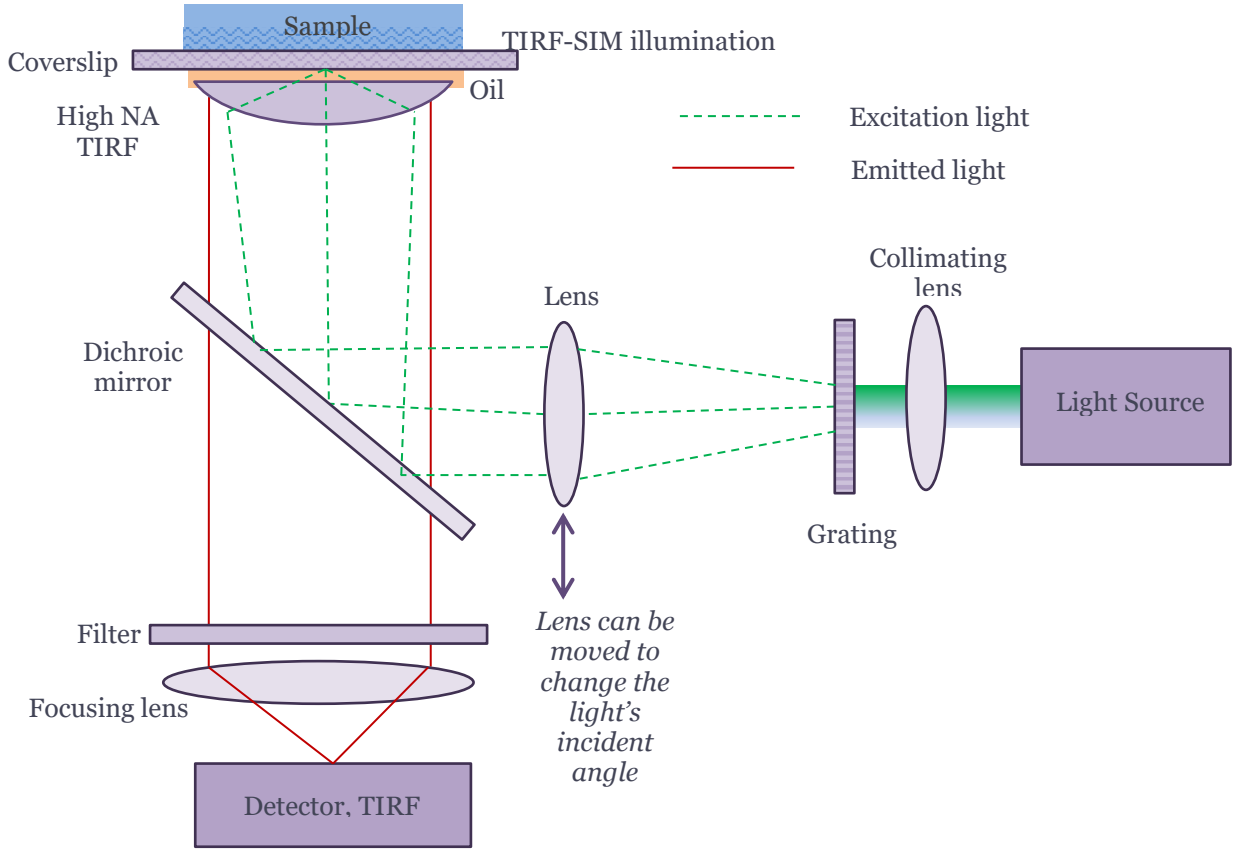

Figure 1.7: Schematic of TIRF-SIM, including key components and light paths[1,2].

As shown in figure 1.7, the setup for TIRF-SIM is very similar to that of standard TIRF microscopy, see figure 1.4, thus achieving the critical angle required for an evanescent field

to be created to illuminate the sample is still necessary. However, a component such as a grating has been added to create the structured illumination. This means that creating the illumination is more complex than for a brightfield microscope, and is something that the microscope proposed by this PhD aims to address, by using a brightfield-style light path whilst still creating a structured evanescent field.

In addition, as with SIM multiple images with different illumination patterns are required in order to produce a final super-resolution image, which can make imaging slower. However TIRF-SIM has achieved *in vivo* imaging with frame rates of up to 20Hz capturing images in two colours, and has achieved spatial resolutions of up to 100nm. The main limitation of TIRF-SIM, which results from the TIRF foundation to the technique, is the sensitivity of the system to becoming misaligned and thus not achieving the critical angle required for total internal reflection. This is combined with requiring precision polarisation of the illuminating laser light and synchronisation of the TIRF laser with the SIM illumination pattern, in order to produce optimal patterns with minimal aberrations, which will result in images free from artefacts and with higher resolution, but can be achieved[98].

Nevertheless, TIRF-SIM is a very useful imaging tool particularly for biomedical imaging. The TIRF element of TIRF-SIM means only a thin section of the surface is illuminated, improving axial resolution compared to epi-fluorescence microscopy, and improves the SNR by reducing the contribution of out-of-focus fluorescence to the image[41,43]. The addition of SIM to create TIRF-SIM then means super-resolution imaging is possible, with lateral resolutions of 100nm[98] compared to ~200 – 300nm for TIRF being achieved[41,43,99], without the need for specialised fluorophores as for single-molecule localisation techniques[2,88], or high laser

energies as for STED which can damage the sample[43,100]. TIRF-SIM has been used to image the yeast plasma membrane[133], designer artificial cellular components in *E. Coli* cells[134], and individual non-muscle myosin II bipolar filaments which are involved in many cellular processes, including embryo formation and cell migration[135].

1.6.6 Advantages and Limitations of SIM

Some of the advantages and limitations of SIM have already been discussed in *Section 1.6*. As with all imaging systems and modalities, there are advantages and limitations depending on what is desired from the images, and no imaging system is ideal for all imaging situations; whether that be due to resolution, spatial or temporal, sample preparation methods, potential damage to the sample, sample size or type, portability of the imaging system, labelling mechanisms, amongst many other considerations.

The various types of SIM imaging systems are advantageous. A key advantage compared to techniques such as epi-fluorescence microscopy is that SIM allows for super-resolution imaging. SIM is able to achieve spatial resolutions beyond the diffraction limit, generally achieving a 2× resolution improvement, therefore lateral spatial resolutions of 100nm[33,36] compared to 200 – 300nm of epi-fluorescence[5,33,42,43,93]. In addition, good temporal resolution can be also achieved, with imaging at up to 10Hz having been performed using SIM[98]. Generally, SIM is also it is technique that does not damage the samples as high-power illumination is not normally required, meaning fixed samples can be re-used, or samples can be imaged over longer periods of time[33,36,37,100,119]. This is not the case of non-linear SIM where high-intensity structured illumination is used[35,37,40]. Consequently, most SIM is suitable for live cell imaging, meaning more biologically relevant information can be

obtained[78,116,119,132]. In addition, SIM is compatible with most types of labelling, so can be used with the fluorophores used in epi-fluorescence microscopy, such as fluorescent dyes and fluorescent labelled proteins[35,38,75,100,123,125], but unlike techniques including STORM it is not dependent of special fluorophores or labelling techniques[2,43,88]. However, SIM can also be used without labelling or specialised sample preparation required, and as a widefield technique it can be used for large scale and 3-dimensional imaging[34,36,37,39]. Importantly, SIM can be used to enhance other imaging modalities, as it can be added into other imaging systems, including TIRF[98], STORM[2,110], Raman[111], and multiphoton imaging[114,115], indeed SIM can be seen as an addition to brightfield or epi-fluorescence microscopy.

However SIM, like all imaging techniques, has its limitations. The lateral spatial resolution of SIM, although a great improvement on diffraction-limited techniques, is still low compared to other techniques such as STORM which can achieve resolutions of up to 25nm compared to 100nm for SIM[33,43,69,88]. In addition, temporal resolution can be limited as image acquisition and reconstruction can be slow due to acquiring multiple images, although live cell imaging has been demonstrated with SIM[5,33,119]. Furthermore, the reconstruction process required to produce a super-resolution image in SIM can result in image artefacts, which affect the final image quality[34,36,38,113,123,124]. Nonetheless, SIM is still an important imaging tool in the field of biomedical imaging.

1.6.7 Discussion

Structured Illumination Microscopy is an important and useful imaging technique that has already proved its worth and has great potential for improvement. As already discussed, it is

adaptable, can achieve super-resolution beyond the diffraction limit, is non-damaging, and it is multi-modal[5,33,34,36,37,119,121,125,129].

However, SIM also has its limitations. Aspects such as temporal resolution and image artefacts produced during image reconstruction, are gradually being overcome, meaning SIM can achieve live cell imaging and high-quality super-resolution reconstructed images[34,77,116,119,121,125]. The main limitation of SIM, in spite of being a super-resolution optical microscopy technique, is its spatial resolution. Although SIM can achieve 2× spatial resolution (up to 100nm) compared to standard epi-fluorescence microscopy, its resolution improvement is still less than other super-resolution optical microscopy techniques[5,33,100]. This is because, even though SIM achieves resolutions beyond the diffraction limit, the structured illumination is still diffraction limited, meaning that the resolution improvement is constrained[118].

Non-linear SIM overcomes this achieving resolutions of up to 50nm[35,136], although techniques such as STORM achieve 25nm resolution[2,69,88,136], but it suffers from photo-damage to the sample, making it less ideal for some aspects of biomedical imaging[35,136]. Another potential approach is the use of metamaterials and plasmonics to produce the structured illumination, as they would not be diffraction limited[84,118]. This would also allow for simpler TIRF-SIM imaging, as a brightfield-type light path could be used instead of that used in TIRF microscopy.

Consequently, this research aims to build upon that which has already been achieved and is still emerging in the field of structured illumination imaging. In particular, this PhD will contribute by continuing forward with the use of plasmonics, by using metamaterials, and

applying them to a TIRF-SIM type imaging system, and then developing and expanding upon the reconstruction methodology that is crucial to SIM.

1.7 Metamaterials

1.7.1 Introduction

A metamaterial can be defined as "an arrangement of artificial structural elements, designed to achieve advantageous and unusual electromagnetic properties"[137]. Therefore instead of a traditional material whose properties derive primarily from its constituent atoms, a metamaterial derives extra, novel properties from its constituent structural elements or units[8,11,138-141]. There has been extensive research into their potential uses in a variety of fields, including optics and imaging, and the limits of their novel properties[11,12,15,142-149].

1.7.2 Physics of Metamaterials

A metamaterial, which although it is composed of atoms, it derives its unique properties from its artificial structural elements known as meta-atoms. These meta-atoms must be much smaller than the wavelength of electromagnetic light, and as a result these meta-atoms 'appear' atomic and thus dictate the material's properties, essentially overriding the inherent atomic-derived properties[12,14,32,44,150]. If correctly designed and fabricated, this means that a metamaterial can couple to both the electric and the magnetic field components, unlike standard materials which only effectively couple to the electric component, meaning that new properties are possible[11,12,26,32,44,141,143,150,151].

1.7.2.1 Meta-atoms

The structural elements of metamaterials, the meta-atoms, can be many different shapes, sizes and materials, and they can be arranged periodically or randomly, depending on the desired function of the metamaterial[152]. If these meta-atoms are disordered, so not arranged periodically, the electromagnetic field response to the metamaterial is generated across a broad spectral range; however, the meta-atoms are ordered periodically, then the electromagnetic response is at selected frequencies. The periodicity of the metamaterial's geometry plays a vital role in tuning the electromagnetic response of the metamaterial[151]. The quintessential metamaterial meta-atom is the split ring resonator (SRR). First demonstrated in 1981[150,153], SRRs are comprised of a double ring, with one nested inside the other, with either the inner or both rings split[150,153,154]. SRRs have been used to create magnetic resonances[13,153], for infra-red detection of single molecular monolayers[155], and for creating left-handed waveguides[156,157]. SRRs have led to many similar meta-atom resonator designs including the open-SRR which resembles a capital omega, but many other designs exist including simple pairs of short rods, nano-holes in a metal film which in an array create a fish-net structure, and even small particles both regularly and irregularly shaped[150].

1.7.2.2 Electrical Permittivity and Magnetic Permeability

The key physical properties of interest in creating a metamaterial are the material's electrical permittivity, ε, which describes a materials response to an electric field, and the magnetic permeability, μ, which describes a materials response to a magnetic field, and as a result the refractive index. Between them, these properties describe how a material interacts with an electromagnetic field, with metamaterials it is possible to create values of if ε and μ such that negative refractive index values and negative refraction are possible, discussed in detail in *Section 1.7.4*[45,151,158].

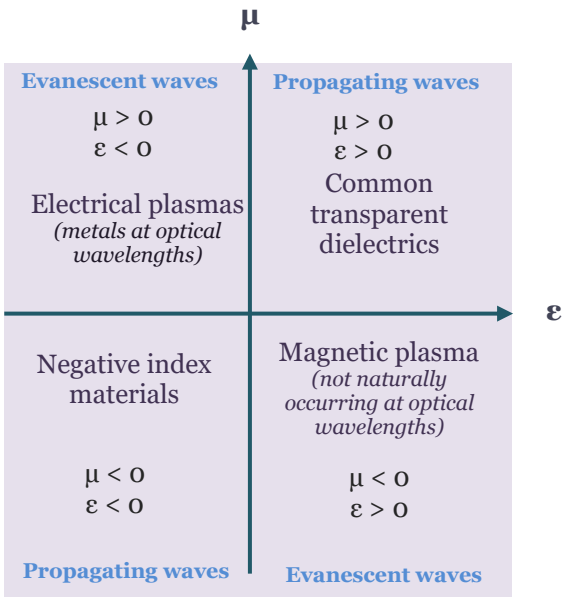

Figure 1.8: Schematic of the intersection of materials based upon their electrical permittivity, ε, and their magnetic permeability, μ[44,45].

The values of ε and μ have both real (ε', μ') and imaginary (ε", μ") components. The real components describe the optical response of the material, whereas the imaginary components describe the losses that limit the performance of optical devices. These losses, in the case of metals, arise largely from electronic transitions within the metal[152].

1.7.2.3 Materials

The designs and materials used to create metamaterials are wide-ranging, depending on the desired function. Many metamaterial designs involve layering metal and dielectric components to create a composite material, and generally most metamaterials have both metallic and dielectric constituents, this is in order to produce surface plasmon modes[150], see *Section 1.7.3*. Some of the most commonly used metals for metamaterial construction are gold and silver. This is because as metals they already have negative electrical permittivity values at optical wavelengths, which is important in the pursuit of negative refraction, see *Sections 1.7.2.2 & 1.7.4*, and thus are able to support surface plasmons, see *Section 1.7.3*. Furthermore, they also have small ohmic losses or high direct current conductivity, but at optical frequencies losses play a significant role in the function of these materials, meaning that alternatives are being investigated[152]. As a result of the potentially unique and tuneable properties of metamaterials, their response to electromagnetic fields is unique.

1.7.3 Uses and Types of Metamaterials

The origin of the first metamaterial is widely acknowledged to be the use metal-dielectric plates to create a refractive index of less than one by Winston E. Kock in 1946[159]. Although some earlier examples of metamaterial-like behaviour exist, including an early example of a potential meta-atom proposed by Jagadis C. Bose to create artificial chiral molecules[160]. Since the mid-twentieth century the field of metamaterials has continued to grow, with key landmarks being the proposal of creating a 'left-handed' material with negative values of ε and μ[161], a 'perfect lens' for super-resolution imaging[162], and a potential 'invisibility cloak'[163].

There is a great variety of metamaterials being used for a wide variety of purposes. As already discussed, the functionality of the metamaterial is determined by its overall design, the design of the meta-atoms and the materials used in its fabrication, consequently the range of applications of metamaterials is vast and they can be tailored to best fulfil the desired function. The focus of this thesis is the use of metamaterials in imaging, discussed in detail in *Sections 1.6.4 & 1.6.5*, and they have great potential in this field. In addition, metamaterials have achieved widespread interest in their potential for transformation optics, whereby metamaterials are used to distort or re-configure electromagnetic fields, particularly the area of cloaking[143]. Initial potential optical 'invisibility cloaks' have been demonstrated, where a metamaterial is used to steer light around an object by changing how it propagates, making it appear invisible[142,143,164-169]. However, the challenges of fabrication are still significant, especially at optical frequencies. Most examples of these cloaking devices have been bulky, making them detectable, and hard to scale up to hide macroscopic objects[167], or have only been operable in a limited frequency range[165]. Other areas of note utilising metamaterials are the fields of holography[145,170-172], biological and chemical sensing[173-176], and remote sensing[144,146,173,177].

There are even developments in the use of metamaterials that defy the definition given in *Section 1.6.1*. In that instead of using artificial structural elements to give novel electromagnetic properties, these metamaterials affect sound waves (acoustic metamaterials) and can have negative effective density and bulk modulus properties unlike standard materials, and analogous to the left-handed electromagnetic materials discussed in *Section 1.6.4*[178]. Acoustic metamaterials have been used to focus ultrasound waves[179], for sound attenuation at certain frequencies[180], and generally show great promise for new sonic

devices[149,179,180]. Furthermore, elastic metamaterials have been proposed, that can behave as either liquids or solids, and may enable new applications by allowing novel control of acoustic, elastic and seismic waves[147].

1.7.4 Negative Refractive Index

A key property of metamaterials of interest is their capability of having a negative refractive index, *n*[8,9,11,14,22,24,138-141,161,181-188]. Refractive index is determined by the material's electrical permittivity, ε, and the magnetic permeability, μ, according to the following equation:

$$n = \pm\sqrt{\varepsilon \cdot \mu} \qquad [1.4]$$

The refractive index is in turn related to the wave vector, k:

$$k = \frac{\omega}{c_0} \cdot n \qquad [1.5]$$

Where c_0 is the speed of light in a vacuum, and ω is the angular frequency[138,158].

If either ε < 0, or μ < 0, n and k are imaginary, and the material is opaque; if ε & μ > 0, n> 0 and the material is transparent[138,161]. However, as demonstrated by Victor Veselago in 1968[161] in his groundbreaking work[189], if ε & μ < 0, then we are forced by Maxwell's equations to choose the negative root of n, thus n < 0[138,139,161,186]. Subsequently the refracted light makes a negative angle with the normal, as opposed to a positive angle in a positive-index material[8,11,138,139,148,182,187], see figure 1.9.

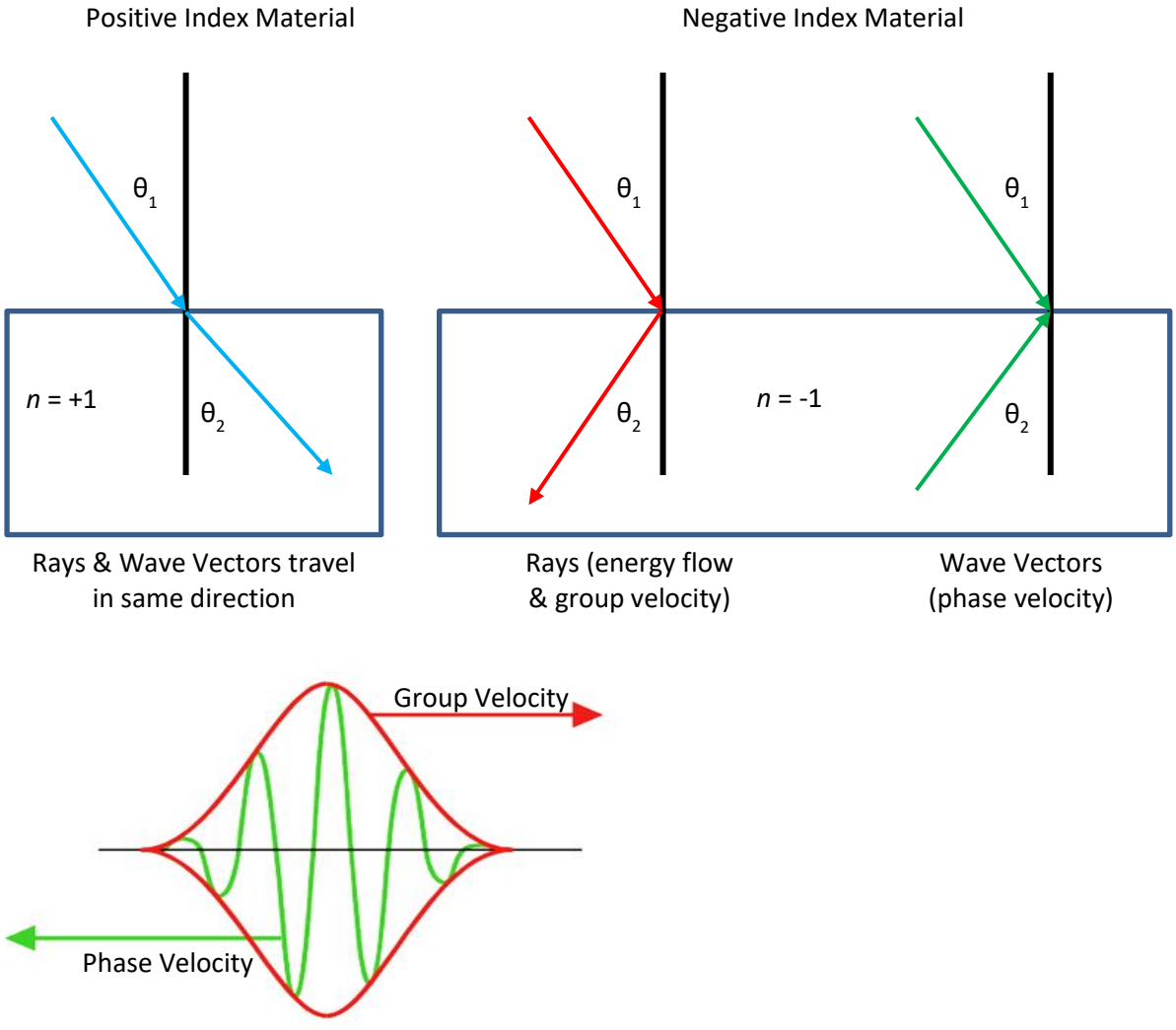

Figure 1.9: Schematics comparing negative & positive index materials and the effects on refraction, and the group and phase velocities of an EM wave in a negative index material[32].

Materials with negative refraction created by both ε & μ < 0 are sometimes called left handed materials (LHMs)[10,15,16,28,141,190] because the Poynting vector, which represents the directional rate of energy transfer density of an electromagnetic field, has the opposite sign and the energy flow and group velocity are opposite to the wave vector (phase velocity), the parallel component of the wave vector is always preserved in transmission[138,141,187,191,192]. Negative refraction can also be achieved with only one of ε, μ < 0, but these are not classed as true negative-index materials and are referred to as single-negative metamaterials[8,32,44], but must obey the following inequality:

$$n < 0, \text{if} \quad Re(\varepsilon)|\mu| + Re(\mu)|\varepsilon| < 0 \qquad [1.6]$$

Where *Re()* represents the real component of the variable[9,32,44].

The implications of having a negative refractive index, something that is not seen in nature[14,16,18,137,143,148,151], are potentially vast in terms of imaging. As described in S*ection 1.5.2****Error! Reference source not found.***, the spatial resolution of optical microscopy is fundamentally limited by the diffraction limit in the far-field, consequently the higher resolution near-field information is lost in standard optical microscopy as it cannot propagate into the far-field and be retained in the image, instead it decays rapidly[33,43,63,77,93,100,136]. However, this is the case for optical systems using lenses with a positive refractive index, whereas by using a negative refractive index lens it is theoretically possible for this high resolution near-field information to be conveyed into the far-field, resulting in a super-resolution imaging system, with potentially unlimited resolution[11,138,187,189].

In practice, to achieve the best resolution, a material with ε, μ, and $n = -1$ is required otherwise spatial resolution is drastically reduced[11,138,162,187]. It is inherently challenging to create a material that fulfils these properties, particularly at optical wavelengths, as the meta-atoms that form the properties of the material must be smaller than the wavelength of light with which they are being used, making fabrication challenging[12,14,18,32,44,150,151,193,194]. Moreover, at these shorter optical wavelengths that are desired for imaging, the metals which metamaterials are typically constructed from behave less like conductors which dampens the resonance effects that metamaterials depend upon[10,32,44,137,151,172,194-196]. Nevertheless, promising work has been done demonstrating the potential of these negative refractive index lens (known as superlenses and hyperlenses) based imaging systems[14,16-20,23,25,26,28,148].

1.7.5 Plasmonics

Plasmonics is an important part of explaining how metamaterials can achieve novel electromagnetic properties. When an electromagnetic wave propagates through a polarisable medium, which includes metals, this induces polarisation. Metals, due to their free conducting electrons, exhibit plasma-like behaviour, but are not plasmas, and thus are often used in plasmonics. This polarisation modifies the electromagnetic wave which is then coupled to the induced polarisation, the properties of which depend on both the incident electromagnetic wave and the medium[150].

This coupling of the electromagnetic wave to the polarised medium causes oscillations in the uncoupled electrons, known as a plasma wave classically, or if it is significant they become plasmons. Consequently, when there is significant change to the electromagnetic wave due

to the medium, this is then known as a plasmon polariton. These plasmon polaritons are then divided into bulk, where they propagate inside a homogeneous medium, or surface plasmon polaritons (SPPs) where they are confined to the surface of the material[150]. As metamaterials are not homogeneous materials and only the surface is of interest, only SPPS will be considered. The collective oscillation of the uncoupled electrons at the surface is known as surface plasmon resonance (SPR)[151].

Surface plasmons only occur at the interface between a metal and a dielectric, and the electromagnetic field of SPPS can be described by solving Maxwell's equations in each medium and the associated boundary conditions, using the Drude model to describe the materials.

$$\text{Drude model for a free-electron model, } \varepsilon_r = 1 - \frac{\omega_p^2}{\omega(\omega - i \cdot \gamma_p)} \qquad [1.7]$$

Where ε_r is the relative electrical permittivity, ω_p is the plasma frequency, ω is the frequency, and γ_p is a damping constant[150,151].

These fields decline away from the boundary evanescently, according to the SPP dispersion relationship:

$$k_x > \frac{\omega}{c}\sqrt{\varepsilon_{r_{dielectric}}} \qquad [1.8]$$

Where: k_x is the wavenumber along the surface, c is the speed of light, ω is the frequency, and $\varepsilon_{r\_dielectric}$ is the relative electrical permittivity of the dielectric[150,151].

If a thin metal film is layered between two dielectric layers, then both interfaces can support SPPs and a SPR. Furthermore, if the metal is sufficiently thin then the SPP modes at each

surface are coupled and can interact. Consequently, the SPP dispersion is split, meaning that the conditions for the existence of surface modes are eased. Subsequently, for the existence of SPP modes it is no longer required that the electrical permittivities of the metal and the dielectric have the same sign, and the frequency can approach the plasma frequency[150]. This means that it is much easier to create metamaterials with strong plasmonic properties.

SPPs can couple light strongly to the materials surface and thereby greatly enhance light-matter interactions. SPPs are non-radiative, they are bound and do not propagate away from the surface[150]. As a result, electromagnetic fields can be concentrated to a small area, a fraction of the wavelength[152]. This surface mode is capable of interacting with the evanescent part of a spectrum from a sub-wavelength object, leading to the potential of sub-diffraction limit imaging[150], see *Section 1.7.5*. Moreover, the surface plasmon resonance enhances the local electromagnetic field strengths by several orders of magnitude[151,152].

Plasmonic nanostructures, which often form the meta-atoms that compose a metamaterial, are optical couplers, so they allow for the interaction between electromagnetic fields and the material. Therefore, they act as optical nano-antennas and enhance the efficiency of the optical coupling. Moreover, the optical cross-section of the metamaterial, which describes the maximum amount of optical flux reflected or emitted, greatly increases as described below, resulting in field enhancement[151].

$$\text{Optical Cross-section magnitude:} a^2 \rightarrow \lambda^2 \qquad [1.9]$$

Where *a* is the structure (plasmonic nanostructure) size and λ is the wavelength of light[151].

Plasmonics and metamaterials are closely linked fields, as most metamaterials utilise surface plasmons and SPR in order to achieve their novel electromagnetic and optical properties not typically seen in nature. These metamaterials can be described as plasmonic metamaterials[146,150-152,174,195,197].

1.7.6 Metamaterials and Microscopy

Metamaterials have the potential to dramatically improve the field of microscopy, via their novel electromagnetic properties. As described in Section 1.7.4, metamaterials can be fabricated to have a negative-refractive index, creating a lens with great spatial resolution potential beyond the diffraction limit[14,138,141,162,181,184,186]. Typically, the metamaterial acts as a lens (metalens) in conjunction with the objective lens, with the aim of being able to implement a metalens within existing optical imaging systems making them more practical and simple to operate[14,15,20,21,25,26,28]. However, due to the nature of many metamaterials being fabricated from metal films or using metal nanorods and consequently being non-transparent to light in the standard sense, there are imaging challenges particularly if being utilised in a fluorescence microscopy setup. It is often necessary to collect emission via a separate transmission objective lens if using a metalens, not through the objective lens used for excitation or the incident lens which is the standard light path for most fluorescence microscopes[3,42,75,100]. Nonetheless, suitable pre-existing imaging systems for use with metalenses do exist, and others can be adapted. These metalenses are described as superlenses and hyperlenses, and their super-resolution potential is derived from being able to retain the higher resolution near-field information that is typically lost[14,15,17,19,23,25-27,187].

In an optical imaging system with a conventional lens, this near-field is lost due to its evanescent nature, it decays rapidly, and only the propagating field containing lower

resolution information is retained[43,71,104,105,138]. A superlens enhances this evanescent near-field via surface plasmon resonance created by the metamaterial so that although it still decays away from the lens, there is greater potential to capture it as well as the propagating field[17-19,27,32,187]. By contrast, a hyperlens converts the evanescent field into a separate propagating wave, such that both the propagating fields, one of which contains the higher-resolution information, can be captured to produce a super-resolution image[20,23,25,26,32]. Both of these systems are limited by being sensitive to losses and disorder, and particularly by being difficult to manufacture[18,23,26-28,187]. However, some implementations are showing great potential and have demonstrated spatial resolutions of sub-20nm[20,198,199].

In addition to being used to produce a 'perfect lens', metamaterials have been utilised for surface enhancement, in the cases of fluorescence[67,84] and surface-enhanced Raman spectroscopy (SERS)[151,197,200,201]. In both cases, a plasmonic metamaterial is used to enhance signal, and has evolved into the use of metamaterials for bio-sensing applications[173,175,176].

1.7.7 Plasmonics & SIM

The use of plasmonics with SIM has recently started to be investigated, and this thesis aims to expand and add to this existing research[40,84,118,202-205]. In plasmonic SIM, the plasmonic structure is used to produce the structured illumination instead of using a spatial light modulator or interfering beams of light[40,202,203]. The theory behind plasmonics, particularly metamaterials, is discussed in greater detail in *Section 1.7.5*, but fundamentally the electric field component of light can interact with the surface electrons in plasmonic materials, and drives these electrons into a collective oscillation or plasmon resonance, which can lead to enhanced electromagnetic fields at the surface of the material[12,32,45,146,150,151,203,206].

Consequently, by tailoring the plasmonic material, very fine stripe patterns can be produced compared with standard SIM patterns, increasing the spatial resolution potential[40]. The plasmon resonance is generally confined to the surface of the plasmonic material and the resulting electromagnetic field decays rapidly,[12,32,44,150,151] it is an evanescent field, akin to those in TIRF microscopy, providing localised excitation and suppressing background fluorescence[41,70,75]. As a result plasmonic SIM (PSIM) can be used in a setup very similar to TIRF microscopy to provide a powerful super-resolution TIRF-SIM type imaging technique[1,65,84]. However like TIRF microscopy, this technique still relies on a specific incident angle of the illumination light in order to operate. Another plasmonic SIM technique known as localised plasmon SIM (LPSIM) does not have this constraint. LPSIM utilises a nanostructure pattern to produce structured illumination, and unlike PSIM, it is the spatial period of these nanostructures that dictates the spatial frequency of the structured illumination. Whereas in PSIM, it is the frequency of the illumination light that dictates the spatial frequency of the structured illumination[40,118,202]. Both of these plasmonic SIM techniques are still in their infancy, having predominantly been investigated in simulation and with basic experimentation, but 75nm spatial resolution has been demonstrated[118]. This thesis aims to expand and build upon these types of plasmonic SIM, particularly LPSIM.

1.7.8 Discussion

Overall, metamaterials show great potential in many fields of research, due to their ability to create novel electromagnetic properties including negative refractive index[11,71,138,141,166,187,189,190]. They show great potential, particularly for imaging, both in terms of the search for a 'perfect' lens and through the application of plasmonics to fluorescence

and SIM[14,16,18,26,118,193,207]. However, the use and development of metamaterials is still limited, as fabrication and losses still restrict their uses and functionality[8,45,151,193-196,199,208].

Nonetheless, metamaterials are a promising and growing field, which should be ideal for enabling the creation of the TIRF-SIM inspired microscope that forms the focus of this PhD, due to their novel electromagnetic properties that can be tailored to different applications. This PhD was primarily concerned with plasmonic metamaterials and their application to microscopy. Of particular interest was the work that has already been done to create a metamaterial lens for super-resolution imaging and in applying plasmonics to SIM[14,26,118,202,204].

1.8 Discussion & Conclusions

This thesis seeks to build upon the large literature-base of research in many fields, from optical imaging, metamaterials, biological imaging and many others, and add to these important areas of research by taking an inter-disciplinary approach. In particular structured illumination microscopy, TIRF microscopy, and plasmonic metamaterials will be utilised in order to add to the field of biological imaging, and biological imaging will drive this research in the very physical and computational field of metamaterials.

Hence, this thesis is split into multiple chapters dealing with the different elements of this PhD research: Chapter 1 – Introduction & Background, covers the background research and theory for the entire PhD, combined with a literature review of current research in the fields relevant to this thesis; Chapter 2 – Design & Simulation, covers simulation work done to create a metamaterial design and simulate its structured evanescent field; Chapter 3 – Image Reconstruction, covers the development and implementation of SIM based image

reconstruction algorithms using metamaterial-based structured illumination; Chapter 4 – Fabricating & Characterising the Metalens, covers the fabrication methods used to create the metalens and to investigate its properties; Chapter 5 – Alternative Metalens Design, covers an alternative metamaterial design developed to address issues that arose with the original design, and image reconstruction using structured illumination produced in simulation by this alternative design; Chapter 6 – Conclusions & Evaluation, summarises the key findings and conclusions presented in this thesis, and proposes potential future work that could build upon this research project.

Chapter 2: Design & Simulation

2.1 Introduction

This Chapter describes the simulation work carried out during this research project and the resulting metamaterial designs. Simulations were performed to inform the metamaterial design of the metalens for the TIRF-SIM biomedical imaging system. The metalens design was required to produce a set of nine sinusoidally structured evanescent illumination patterns (three phases and three orientations), with as small a spatial wavelength as possible, to allow for greater resolution enhancement (ideally below 1μm thus making it considerably smaller than those produced by gratings[36]). This would allow for a standard SIM reconstruction algorithm to be used when reconstructing the images produced by the metalens-based imaging system. Moreover these simulations allowed for testing the design for robustness to manufacturing imprecisions. The results of these simulations – the resonant frequencies and the electromagnetic fields produced by the metamaterial – were then used for testing and validating the image reconstruction algorithms, see Chapter 3, required to produce a successful reconstruction of the structured illumination image, as well as for comparison to experimental results, see Chapter 4.

2.1.1 Aims

The aims of the simulation work were to:

- Design a suitable metamaterial unit cell for the TIRF-SIM imaging system, including choosing parameters for the unit cell design, such as size, shape and materials used.
- Test the design for robustness to manufacturing imprecisions, to see what effects if any imperfect manufacture has on the metamaterial properties.

- Simulate the final design with simulated samples to investigate the sensitivity of the metamaterial design's structured evanescent field to a sample – can a sample be detected.
- Provide a set of simulated SIM patterns for testing the image reconstruction algorithms.
- Provide a set of simulated SIM patterns for comparison to those produced experimentally by the fabricated metamaterial.

2.2 Overall Microscope Design

2.2.1 Introduction & Requirements

The microscope is designed to emulate the capabilities of TIRF-SIM imaging systems pioneered by E. Chung, D. Kim D, and P.T. So in 2006[65,98]. However, in terms of optical design, this microscope is more akin to a standard transmission brightfield or fluorescence microscope.

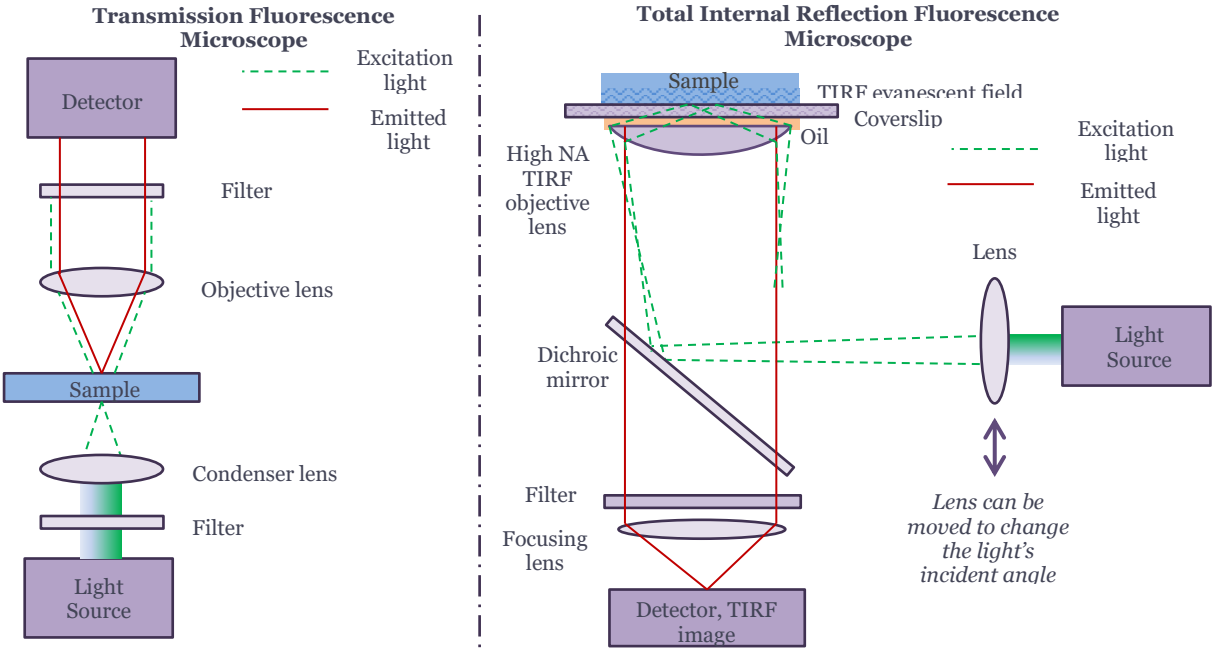

Figure 2.1: Diagram outlining a transmission fluorescence microscope and TIRF microscope, including light paths and key components[3,4].

This novel design combines the simplicity of a brightfield microscope's optical setup with the superior spatial resolution capability of the TIRF-SIM, made possible with the metamaterial lens. For this design to be successful, an evanescent field must be produced in order to achieve the TIRF-like selective illumination, this evanescent field must be structured to generate a spatially structured pattern with the properties necessary to achieve super-resolution imaging. The field will also be enhanced so that if being used with fluorophores, enhanced fluorescence can be achieved. However this incident evanescent field must not be so strong as to cause damage to biological samples, which can be controlled with a dielectric spacer of appropriate depth. Functionally, the incident evanescent field needs to be able to be altered in both phase and orientation in order to produce the multiple images required for SIM, although if not possible through electromagnetic affects, this can be achieved experimentally via physically rotating to achieve different orientations.

2.2.2 Metamaterial Design Constraints

The choice of metamaterial design places constraints upon the overall microscope design parameters. This is due to the electromagnetic response of the metamaterial affecting the optical requirements of the imaging system. The design was required to produce evanescent sinusoidally structured light, with the ability to change the phase and orientation of the structured light. At least three phases and three orientations, thus producing a set of nine structured illumination patterns, were desired, with a small spatial wavelength. In addition, the design had to be able to be fabricated using the facilities available. The intended use in biomedical imaging of the proposed imaging system also affected the choice of metamaterial design, in terms of choice of wavelengths and energies used for imaging. There

were many constraints associated with the design and fabrication of the metamaterial lens and the overall proposed imaging system:

- ***Fabrication feasibility.*** Ultimately, fabrication feasibility often dictates what can be achieved with metamaterials; whether this is due to feature size, accuracy of the design compared to the theoretical design, size of sample to be fabricated, or design complexity. All fabrication methods or instruments are limited in what they can achieve in terms of these factors. With this in mind, the metamaterial design must be possible to fabricate with the resources available to this research project.
- ***Metamaterial unit cell size and super-resolution.*** Generally the larger the metamaterial unit cell, the longer the wavelength of light it interacts with, and as a result fabrication limits can restrict the compatible wavelengths to the infra-red. The size of the metamaterial unit cell also dictates at what wavelength of light the imaging systems can be termed as being super-resolution, in order to be operating as a super-resolution system, the wavelength of light being used should be twice the size of the unit cell. In terms of LPSIM, the unit cell size dictates the spatial frequency of the structured light the metamaterial produces, and so can limit the super-resolution gains that having a finer pattern results in.
- ***Resonant frequency of the metamaterial.*** The resonant frequency peaks of the metamaterial are where it is possible for the incident light to couple to the surface plasmons, meaning the metamaterial will be operating at its peak, producing a strong well-structured evanescent field. Ideally the metamaterial will have a strong resonant frequency peak in the optical frequency range as this is ideal for imaging biological

samples, however even into the near-infra-red region, it is still possible to image biological samples and near-IR fluorophores do exist.

- ***Dielectric spacer.*** The electromagnetic fields at the surface of the metalens are generally very strong, so potentially pose a risk to biological samples. Moreover, this metalens was designed to produce a structured evanescent field, which is not fully structured at the surface of the metamaterial. Therefore a dielectric spacer is required to protect the sample and ensure the sample is illuminated by structured light. In addition, this spacer also protects the metamaterial from physical damage and provides a surface for the sample to be mounted, making the metalens potentially reusable and more robust.
- ***Transmission setup due to the metamaterial.*** Unlike most modern fluorescence microscopes where the detector is on the same side of the sample as the light source, meaning the emission is collected via the same lenses as the excitation is focussed, the metalens requires that the detector be the opposite side of the sample. This means that the proposed microscope is a transmission setup, and this is because of the opacity of metal film metamaterials and more generally, the novel properties of a metalens would alter the emission detected.

2.2.3 Design Schematic

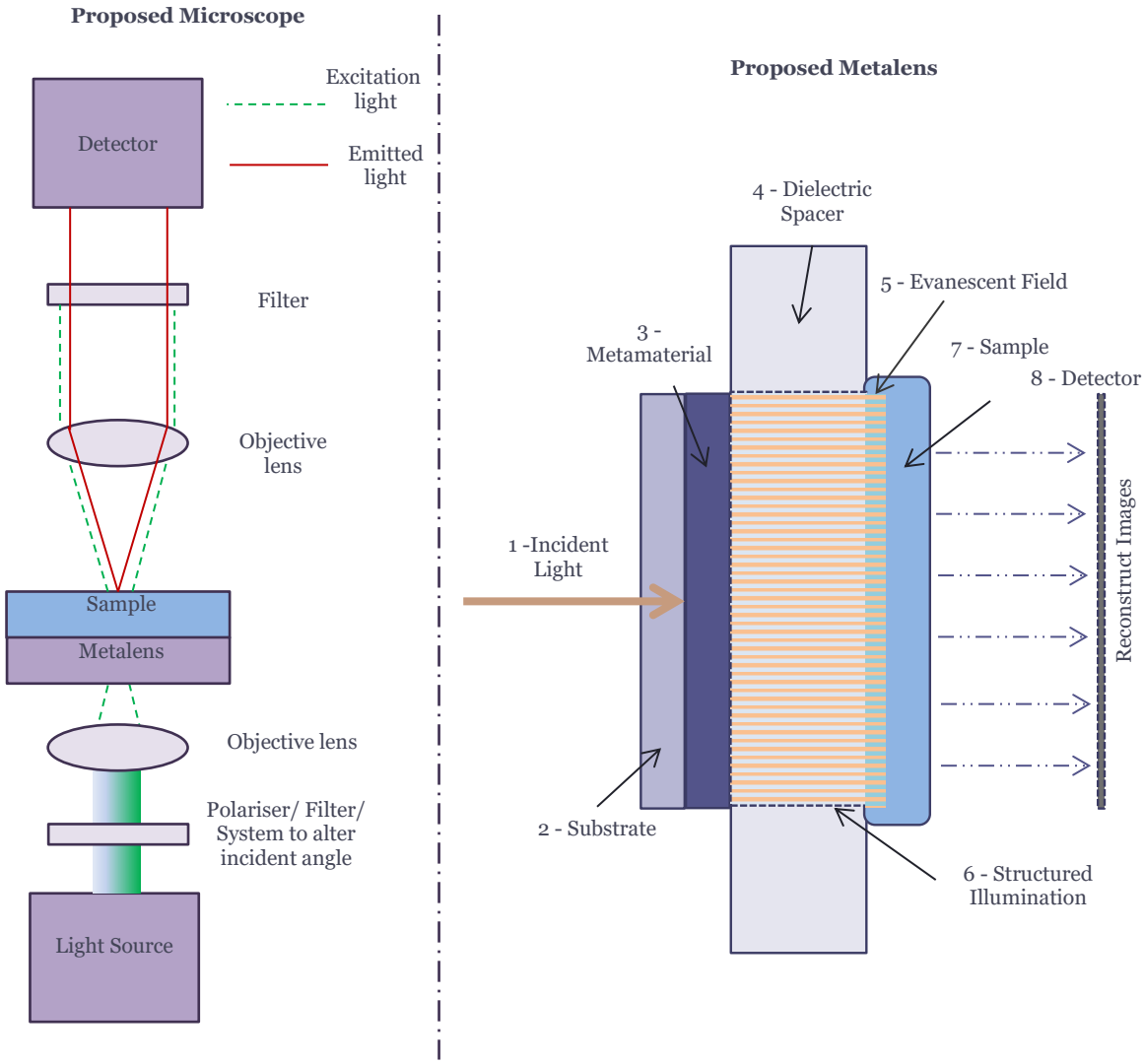

Figure 2.2: Diagram outlining the proposed microscope and metalens, including light paths and key components.

The key aspects of the proposed metalens, as pictured in figure 2.2:

1 - A coherent light input is used of a wavelength appropriate to the metalens being used, which has been polarised and angled as required.

2 - Substrate for mounting the metamaterial, typically glass or SiO_2.

3 - The metamaterial, the design of which is described in detail below.

4 - Dielectric spacer, which is key to ensuring the sample is illuminated by a structured evanescent field, and not illuminated by the stronger unstructured fields immediately adjacent to the metamaterial.

5 - The evanescent field which is sinusoidally structured, resulting in a TIRF-SIM style illumination of the sample.

6 - The structured illumination, produced by the metamaterial, required for SIM style imaging.

7 - Sample, which can contain fluorophores for fluorescent imaging, but is not limited to this. Initial samples are metal strips, with the aim of expanding to biological, particularly platelet, samples.

8 - Detector, type to be determined by experimental constraints.

2.3 CST Microwave Studio

CST Microwave Studio® (CST MWS) is a software package that specialises in simulating electromagnetic interactions with materials. It is one program within a suite of CST software, each adapted to different areas of physics simulation. All use Maxwell's equations of electromagnetism as their scientific basis, and simulations are solved via finite element modelling, using an adaptable mesh throughout the simulation volume[209,210].

CST MWS is commonly used for the simulation of metamaterials, as the scale of the simulation elements and the frequency range of the electromagnetic waves are ideal for the nm to µm scale and the optical to infra-red frequencies typical of metamterials[209-211]. It is ideally suited for the simulations that form a key part of this study into the uses of metamaterials for biomedical imaging.

The advantages of CST MWS, compared to other simulation software packages, in this case are: the ability to create large arrays of shapes, which replicates how a metamaterial is fabricated; its use of finite element modelling, allowing very detailed simulation of the physics of the metamaterial design and its interaction with electromagnetic light, at all points in the simulation volume; the library of available materials including many biological samples, making it more relevant to biomedical orientated research; the ability to create complex 3-dimensional shapes, allowing for a wider range of potential designs of metamaterial; the adaptability of the software - to different frequency ranges, different sizes of simulation, different mesh shapes and resolutions which can be varied across the simulation volume; the 3D visualisation and animation of the electromagnetic fields, enabling greater understanding of the physical problem; the ability to output the data, 1D –

3D, as plain text format, so that it can then be further processed and utilised in other programmes, particularly MATLAB in the case of this study; ease of use, the software is very user friendly and well supported with online help. However CST MWS has its limitations, including: the proprietary nature of the software means that the fundamental workings of the software cannot be altered or adapted, nor can its source code be accessed; there is a size limitation to the simulation volume; the software is computationally memory expensive, and large simulations require a long time to solve. Despite its limitations, CST MWS is well suited to the type of metamaterial simulation required by this study.

Other methods were also considered, notably MATLAB and COMSOL MultiPhysics®. In particular, initial simulations of a basic dipole metamaterial unit cell, were carried out in MATLAB. However, MATLAB proved to be unsuitable as a simulation technique for these compared to CST MWS as it requires a completely ground up approach to the simulation of the electromagnetic and materials properties, which was unnecessarily complicated for very limited and inaccurate results. COMSOL MultiPhysics® is another software package similar to CST for the modelling and simulation of various physics-based problems from multiple fields including electromagnetism and optics. COMSOL is used in the field of metamaterials for simulation purposes and can be successful, but it proved to be less user-friendly than CST MWS; so any potential advantages in its sophisticated programming were outweighed by the greater usability of CST MWS leading to a lower potential for human error in its use. Moreover CST MWS is just as suitable as COMSOL in its ability to perform the type of simulations required, as described above.

The simulation work was thus carried out in CST MWS 2014, using the following parameters unless otherwise stated.

CST Simulation Parameters	Value used
Mesh type	Hexahedral, FPBA enhanced.
Boundary conditions	Periodic in x, y; Open in z.
Energy cut off point	-80dB.
Frequency range	0 – 700 THz.
Background material	Normal.
Incident wave	Linear plane wave, polarised in x: E_x.
Metal film material	Gold, defined in figure 2.5, 40nm thickness.
Simulation volume material	Air, defined within the CST MWS Materials Library.
E Field Probes	Used at end of simulation volume, also if relevant at metamaterial surface. Probe position does not affect the electromagnetic spectra produced by the simulations.
Electric Field Monitors	Depending on simulation: 200, 280, 310, 400, 470, 560, 640, 750THz.
Electric field component exported	Absolute value, E_{Abs}.
Data step size for exporting	10nm

Figure 2.3: Table of key CST MWS simulation parameters.

2.4 Processing CST MWS data

Although the CST MWS simulations themselves are very informative, with regards to the electromagnetic fields and frequency response of the metamaterials, being able to quantitatively analyse the data and convert it into a more universal format is crucial. Moreover, in order to be able to reconstruct images from the simulation data or utilising the simulated structured illumination, the simulation data needs to be processed.

The CST MWS simulation can be exported as plain text (.txt file format), at which point it is possible for it to be imported into many different computer programming packages and mathematical software systems. The software of choice for this research was MATLAB. Specifically, the code developed for processing the CST MWS simulation data was produced using MATLAB R2012a. MATLAB was chosen as it is suitable for handling and displaying images of many file formats, particularly with the Image Processing Toolbox, implementing mathematical functions necessary for the image reconstruction algorithms discussed in Chapter 3, importing data from CST MWS, and as it is widely utilised it makes any code produced easily accessible and useable by others.

Separate code was developed for processing the one-dimensional and two-dimensional CST MWS data, not only importing the data from the text file, but also then displaying it. For the two-dimensional data, the electric field data is exported to text as the following:

x (nm)	*y (nm)*	*z (nm)*	*Real E_x (V/m)*	*Real E_y (V/m)*	*Real E_z (V/m)*	*Imaginary E_x (V/m)*	*Imaginary E_y (V/m)*	*Imaginary E_z (V/m)*

Consequently, from this data the electromagnetic field intensity then needs to be calculated for each coordinate in (x, y, z), using the following formula:

$$I = \frac{c \cdot n \cdot \varepsilon_0}{2} \left| \underline{\boldsymbol{E}} \right|^2 \qquad [2.1]$$

Where: *c* is the speed of light in a vacuum, *n* is the refractive index of the medium, ε_0 is the electric permittivity of free space, and $\underline{\boldsymbol{E}}$ is the complex electric field.

In addition, line profiles at chosen positions and their Fast Fourier Transforms can also be generated. The code developed for processing the simulation data is included in Appendix 1.1.

2.5 Metamaterial Design

2.5.1 Introduction & Requirements

The initial simulation work performed was investigating potential metamaterial designs for use as a metamaterial lens for a TIRF-SIM biomedical imaging system.

Simulations were also carried out to explore: the effects of a unit cell versus a larger scale simulation, the effects of an imperfect design, the effects of different sample types – materials and shapes, the effects of different size samples, how the material of the metamaterial affects its electromagnetic properties.

2.5.2 Requirements of the Metamaterial Design

In order to achieve the structured evanescent illumination required for a TIRF-SIM imaging system, the metamaterial unit cell has to fulfil certain conditions. Ideally, it has to produce a sinusoidal stripe pattern or a close approximation, for SIM to be possible, and enhancement of the electromagnetic field incident on the sample, to aid in fluorescence enhancement and ensure that the evanescent structured illumination is incident on the sample. In order to achieve this, a metamaterial unit cell design comprised of two elements at 45° to the normal was proposed.

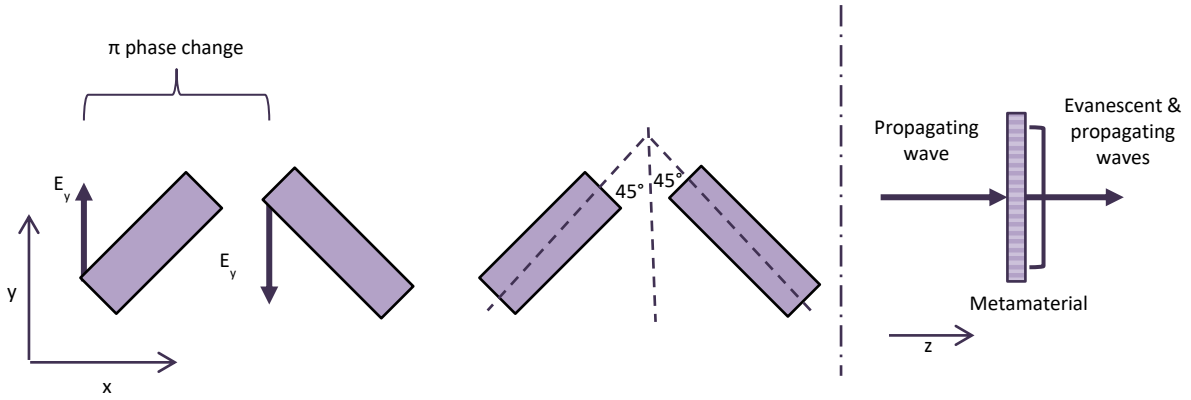

Figure 2.4: Schematic of the basic unit cell design and its geometry; schematic of the electromagnetic fields incident upon and produced by a metamaterial.

Each of these elements acts analogously to a spring, and resonates when an appropriate frequency is applied, which depends of the size and shape of the elements. The choice of this basic design is based on the π phase change in the electric field component between the two elements of the unit cell, see figure 2.4. This π phase change should result in an evanescent field instead of a propagating field being produced by the metamaterial, as the zero-order components of the electromagnetic field produced would be eliminated. Moreover an array of unit cells with this π phase change should result in the field being sinusoidal. Consequently, this type of design should therefore produce an approximately sinusoidally structured evanescent field.

Other types of metamaterial design have been proposed for metamaterial-based SIM imaging systems, including localised plasmonic SIM (LPSIM), although this is still a small field of research. Notable, is Ponsetto's work where a silver nano-disc array embedded in glass was used for LPSIM, imaging a fixed neuron cell. This design was able to able to achieve ~3× resolution, imaging with a resolution down to 75nm, using structured near-field excitation[118].

For this type of metamaterial design, other key considerations, besides the basic structural elements' shapes, are whether the unit cell design will be constructed as nano-holes, whereby the structures are cut out from a metal film, or nano-rods, whereby the structural elements are themselves metal and generally mounted on a dielectric. Moreover the choice of metal, generally between gold, silver, copper and aluminium, and the substrate it is mounted on are also important [152,195,212]. These design choices affect the properties of the metamaterial and have a great impact on the fabrication of it.

The two key materials considered for the design were gold and silver. Both are suitable in terms of their metamaterial properties, they can both achieve resonant frequencies and surface plasmon resonances in the optical and infra-red frequencies desired for imaging. However gold was chosen for the design, due to generally being easier to utilise in fabrication and therefore likely to have a better fabrication outcome. It generally proves to coat a substrate more evenly, making fabrication of a thin metal film more consistent[213,214]. The Drude model parameters used within CST MWS for the simulation of gold were as follows:

Drude Model Parameters	Definition	Values for Silver	Values for Gold
ε_∞	Electrical permittivity at infinite frequency	5.9	5.7
ω_p	Plasma frequency	1.37×10^{16} rad/s	1.37×10^{16} rad/s
γ	Collision frequency	1.2×10^{13} 1/s	1.22×10^{14} 1/s

Figure 2.5: Table of Drude model parameters used for silver and gold materials created within CST MWS.

An alternative to using a metal would be to create an entirely dielectric metamaterial, using dielectric resonators as the meta-atoms. Research into dielectric metamaterials has grown, as they offer a potential solution to the losses seen for metallic metamaterials, particularly at optical frequencies. Moreover, dielectric metamaterials can exhibit unusual optical phenomena similar to those of metallic metamaterials. This reduction in losses could lead to significantly higher device performance, and with a suitable design, could lead to greater resolution improvement for the proposed microscope. Even with reduced losses which could lead to enhanced resolution due to improved signal, the spatial frequency of the structured illumination would also have to be higher for further resolution improvements, which as for a metallic metamaterial would be dependent on the design and size of the meta-atoms/ resonators. However, very few all-dielectric metamaterials have been reported due to the limitations of current nano-fabrication technologies. In addition, their use has not been demonstrated for plasmonic SIM. Consequently, only metallic metamaterial designs were considered for the proposed microscope design[215].

A nano-hole design was chosen over a nano-rod design. Both designs act as viable metamaterials, but because of fabrication constraints, nano-holes were more suitable. Individual nano-rods would be more challenging to fabricate successfully with the facilities available. The dielectric substrate chosen was silicon dioxide glass. This is a suitable dielectric substrate for optical imaging, and it was suitable for the fabrication techniques chosen.

The key fabrication techniques chosen were electron-beam lithography and etching. Electron-beam lithography is micro/nano-fabrication technique that writes a pattern onto a resist on top of a substrate, using a focussed beam of electrons. The exposed areas can then

be developed, and in this case then etched, thus producing the 'H' shape cut-outs from the gold film. Feature sizes of a few nm's can be patterned depending on the instrument and resists used, but areas of only ~100×100µm to 1×1mm can typically be patterned[216]. The alternative technique considered was focused ion beam lithography, which is very similar to electron-beam lithography but uses a beam of ions instead of electrons[208]. Electron-beam lithography was chosen due to the facilities available.

2.5.3 Potential Unit Cell Designs

Based upon the constraints described above in Section 2.2.2 and the basic design concept described in Section 2.5.2, the initial design tested was a simple double dipole cut out design, with the two dipoles angled at ±45° to the normal, see figure 2.6.

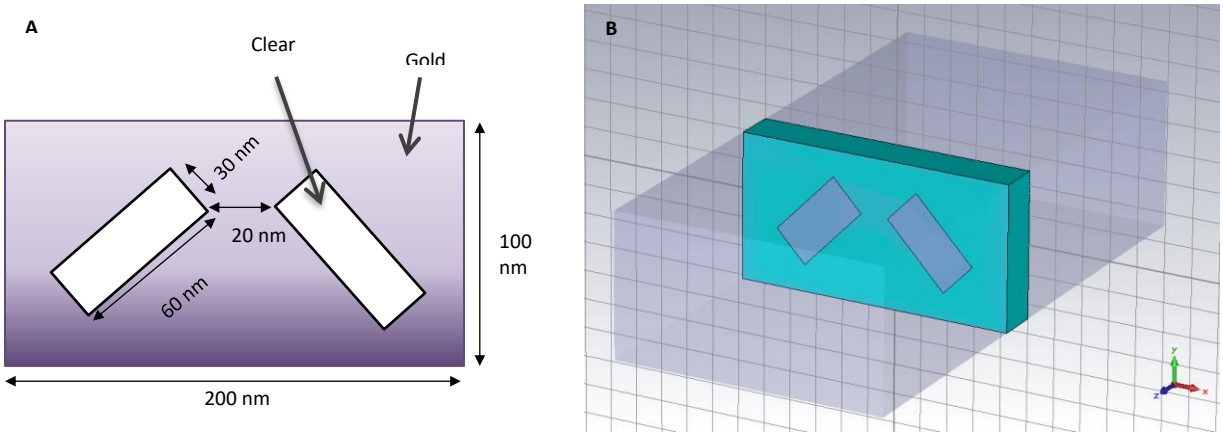

Figure 2.6: A – Schematic of initial basic unit cell, comprised of two rectangular nano-holes at ±45° to the normal; B – Basic unit cell in CST MWS.

The efficacy of this basic two dipole design was then evaluated using CST MWS. The key feature examined was the resonant frequency plot for the simulation, which for a simulation comprised just of the unit cell and a simulation volume, describes the frequency response of the unit cell. For user chosen co-ordinate locations within the simulation volume, the resonant frequency plot cycles through the frequency range of the simulation, and any peaks demonstrate resonant frequencies. These resonant frequency peaks are determined by the size and shape of the metamaterial unit cell, and demonstrate where there will be strong surface plasmon resonance, and thus strong field enhancement and an efficient electromagnetic response by the metamaterial.

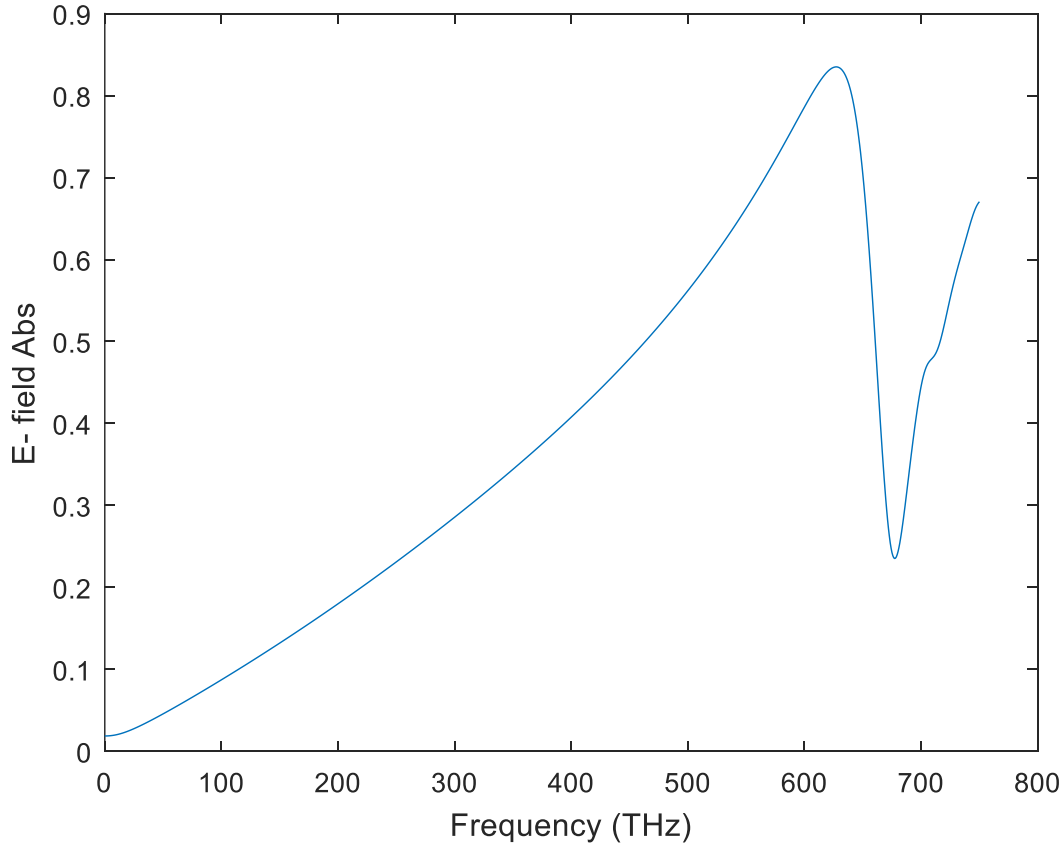

Figure 2.7: 1D plot of the frequency response of the basic dipole unit cell across the frequencies 0-750THz against the absolute electric field, data extracted from CST MWS and plotted in MATLAB.

The key resonant peak seen is at 627 THz (478.47nm). The peak seen in this resonant frequency plot are due to periodicity of the unit cells and the shape of the dipoles, and demonstrate strong transmission by the metamaterial.

In addition, the three-dimensional electromagnetic fields were also examined. The three-dimensional electromagnetic fields are analysed at user chosen frequencies (using the field monitor tool, see figure 2.3), determined by the field monitors chosen to be used in the simulation. By including field monitors across a wide range of frequencies, particularly at

resonant frequencies determined by the resonant frequency plot, the electromagnetic response of the metamaterial unit cell can be examined.

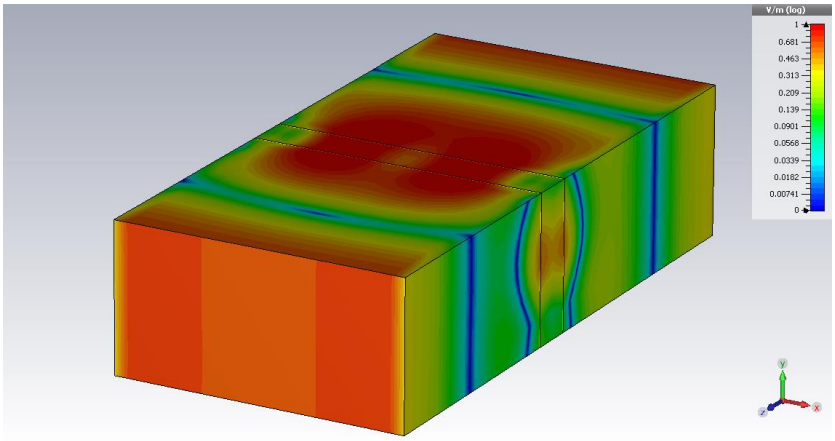

Figure 2.8: Image of the basic unit cell simulation in CST MWS, looking at the absolute electromagnetic fields produced from an x-polarised plane wave at 640THz within the resonant peak.

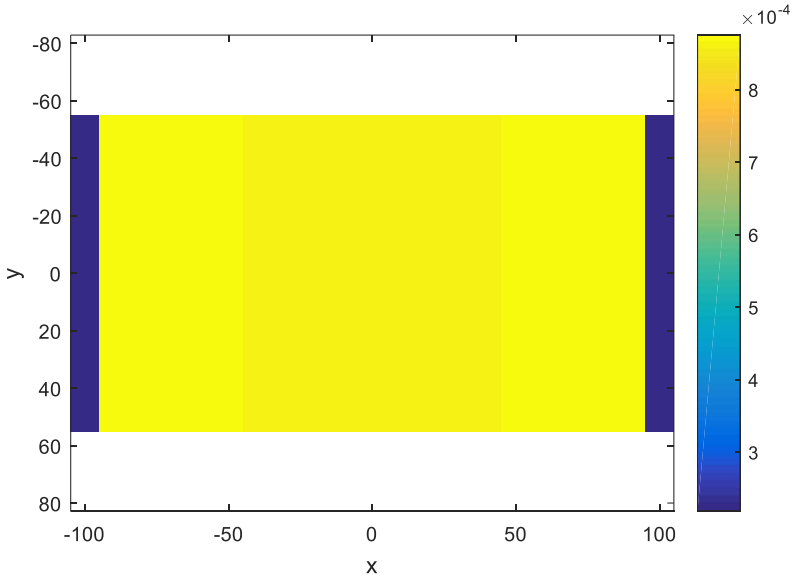

Figure 2.9: 2D MATLAB plot of the basic unit cell simulation from CST MWS, looking at the absolute electromagnetic fields produced from an x-polarised plane wave at 640THz within the resonant peak, at the end of the simulation volume: z=200nm .

It can be seen that the electromagnetic field is strong and non-uniform at the metamaterial surface. In addition, at z = 200nm, as seen in figure 2.9, the strong central stripe shows promise for producing structured illumination. However, in order to see any structured

illumination, an array of unit cells is required as the simulation volume around a single unit cell is not sufficiently large. Arrays of unit cells and the electromagnetic fields produced are explored further below, see Section 2.5.7.

However, this basic design has demonstrated that it has a strong resonant peak, meaning it is has a frequency-specific response; and it shows promise for producing structured illumination, which requires larger simulations to confirm. More resonant peaks would give more working flexibility, as multiple frequencies could be utilised and still get a resonant response, which is desirable. Consequently, a more complex unit cell design was developed.

Having demonstrated the efficacy of the basic design, a more complex unit cell design was proposed. However, more complex shapes tend to be harder to fabricate successfully due to the added complexity of the shapes. The evolution of the basic metamaterial unit cell design needed to contain two elements at ±45° to the normal, in order to preserve the desired properties of producing a structured evanescent field. In addition, the design still had to be simple enough to be readily fabricated. The simple rectangular dipole was thus altered to an 'H' shape.

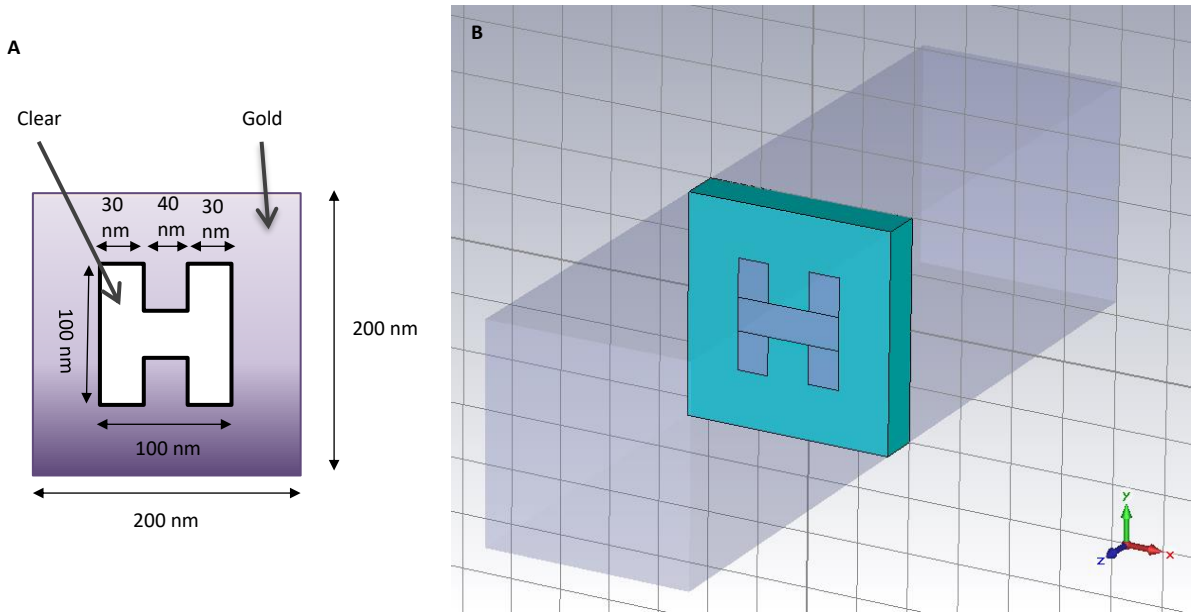

Figure 2.10: A – Schematic of initial basic 'H' shape, with dimensions comparable to the basic dipole; B – Basic 'H' shape in CST MWS.

These 'H' shapes have been utilised in metamaterials, but are uncommon, and have not been utilised for imaging. An example is the work by Choi, where 'H' shape (described as 'I' in text) gold nanostructures are used in the terahertz frequency range to produce a high refractive index material[217].

It can be seen that the dimensions and feature sizes are consistent with the original dipole. However this presented challenges in terms of fabrication, and the smallest feature size achievable with the lithography equipment available. With the electron-beam lithography equipment available at the School of Physics & Astronomy, University of Birmingham, U.K., the smallest feature size reliably achievable is ~50nm. Consequently, the 'H' shape design was scaled up when creating the unit cell, see figure 2.11. Yet by altering the unit cell design, this then impacts upon the metamaterial unit cell properties. Moreover, in order to be operating in super-resolution range, the wavelength of light used should be ~2 times greater

than the unit cell size, for the imaging system to be beyond the diffraction limit, as the unit cell acts as the diffracting element in the system. For the original 200nm size unit cell, this is >400nm wavelength, which is in the visible range. This then means that longer wavelengths of light need to be utilised for the metamaterial to be operating as a super-resolution lens. The unit cell design was as follows:

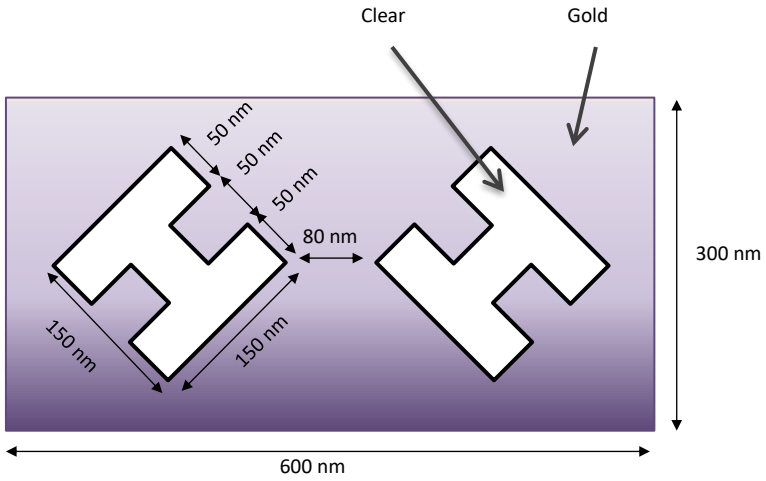

Figure 2.11: Schematic of two 'H' unit cell, comprised of two 'H' shape nano-holes at ±45° to the normal.

This design has the required smallest feature size of 50nm, but as a result the unit cell size is 600nm. Thus the super-resolution wavelength is >1200nm, which is in the infra-red range. Although this design was now able to be fabricated, the size is such that the super-resolution wavelength is now outside the visible range, which has implications for biomedical imaging, where fluorophores and optical imaging techniques are typically designed to operate in the visible range[41,67,70,83]. However, fluorophores that can operate at this excitation wavelength are available, particularly quantum dots[92]. Consequently, this larger unit cell design served as a prototype to test the overall design feasibility, and has the potential to be scaled down and operate in the visible range.

As a result, this design was chosen for the metamaterial design, and was carried forward. This design was chosen for multiple reasons. The geometry of the design is the two elements at ±45° to the normal, cut out from a gold film, which should produce a structured evanescent film; the size and shape of the unit cell is able to be fabricated with the facilities available; the comparative complexity of the design should produce more resonant frequency peaks, giving more options for frequencies that can be utilised with the design. The results that were produced to investigate these hypotheses are detailed below.

2.5.4 Resonant Frequency Profile

Below is the resonant frequency plot for the simulation, which describes the frequency response of the unit cell. Any peaks demonstrate resonant frequencies, which are determined by the size and shape of the metamaterial unit cell, and demonstrate where there will be strong surface plasmon resonance, and thus strong field enhancement and an efficient electromagnetic response by the metamaterial.

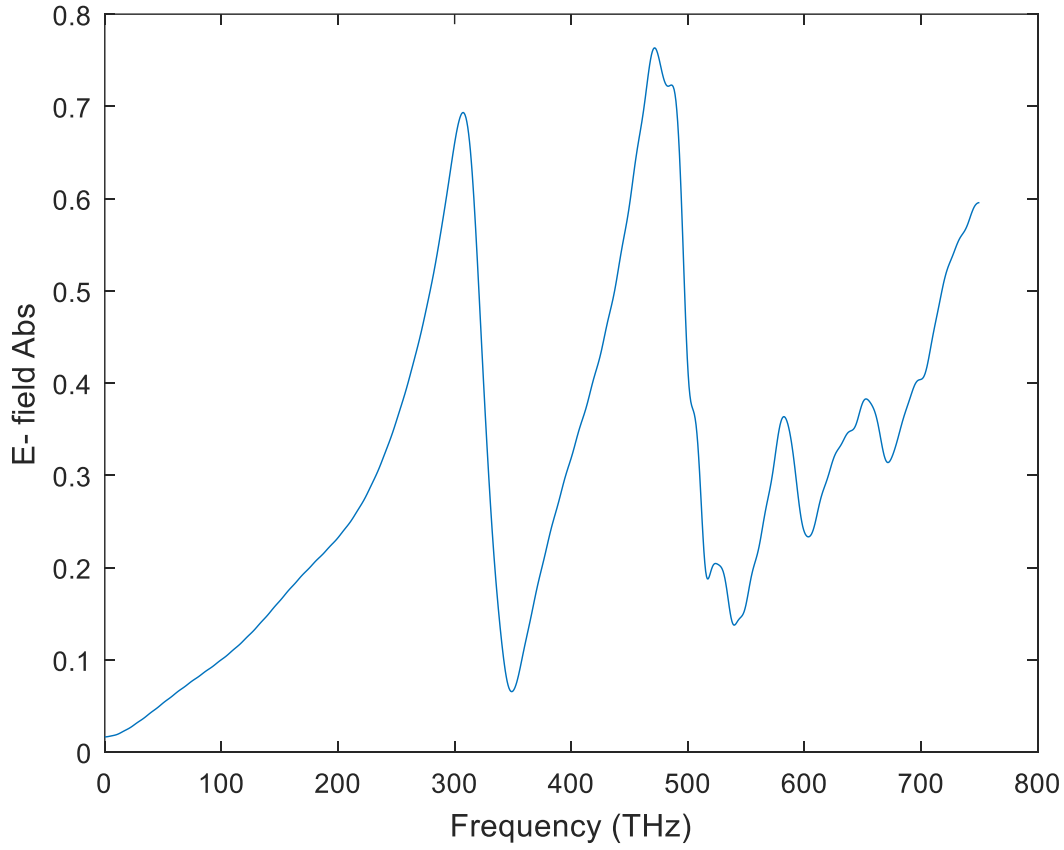

Figure 2.12: 1D plot of the frequency response of the two 'H' unit cell across the frequencies 0-750THz against the absolute electric field, data extracted from CST MWS and plotted in MATLAB.

It can be seen that the frequency profile is more complex than for the basic dipole unit cell, see figure 2.7, containing more peaks. The key peaks are at 307 THz (977.2nm) and 472 THz

(635.59nm). Consequently, field monitors were present in simulations at 310THz and 470THz, alongside others including 200THz. 200THz gives frequency information at a frequency which is greater than two times the unit cell size, so into the super-resolution range.

2.5.5 Electromagnetic Field

The electromagnetic fields as shown in CST MWS demonstrate what can be expected experimentally, and can be used to inform the proposed microscope design and ensure that the desired structured evanescent field is produced and under what conditions.

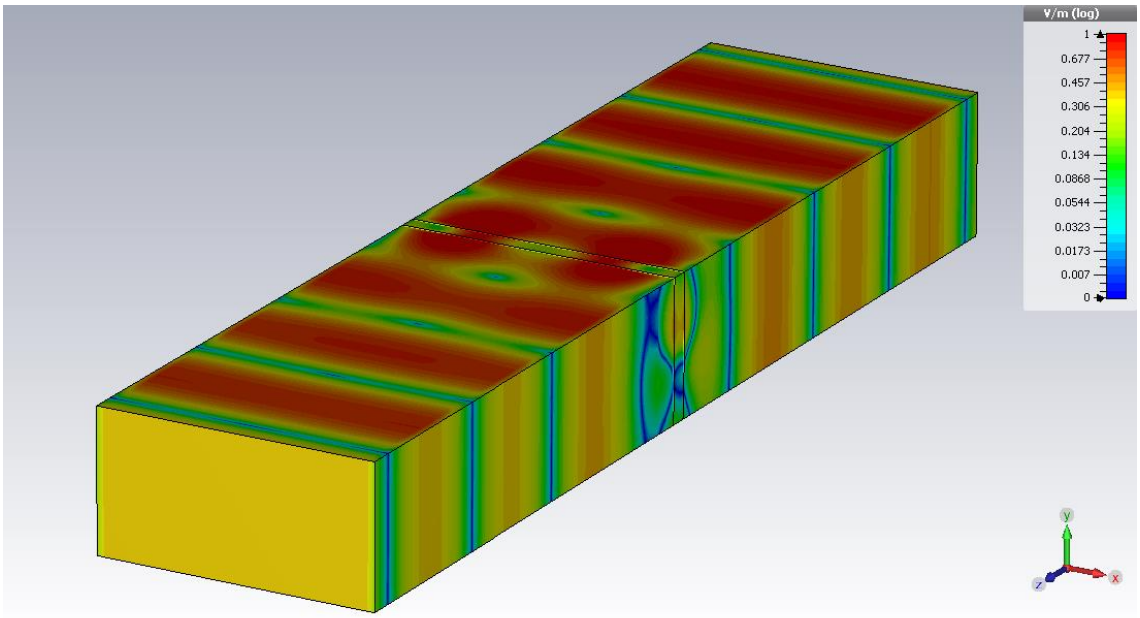

Figure 2.13: Image of the two 'H' unit cell simulation in CST MWS, looking at the absolute electromagnetic fields produced from an x-polarised plane wave at 470THz within the resonant peak.

It can be seen that the electromagnetic field produced by the metamaterial design is distorted directly around the metamaterial. Hence, a dielectric spacer would be required between the metamaterial and the sample.This electromagnetic field profile dictated the size of dielectric spacer required to protect the sample from photo-damage, whilst still illuminating it with the structured evanescent field, and illuminating where the evanescent field has formed the structured pattern.

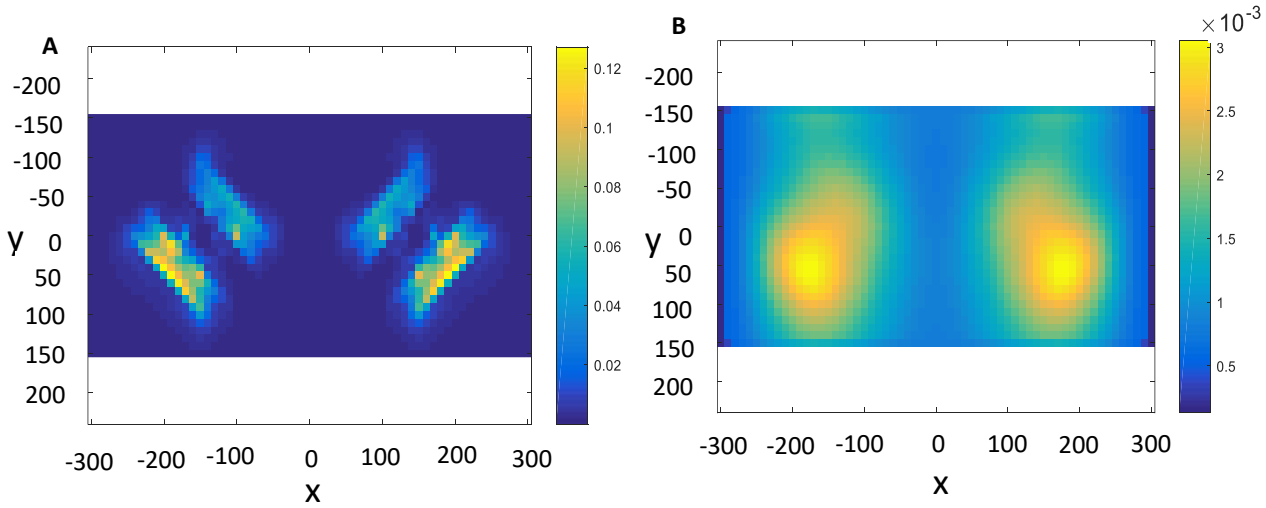

Figure 2.14: MATLAB plots of the two 'H' unit cell simulation in CST MWS, looking at the absolute electromagnetic fields produced from an x-polarised plane wave at 470THz within the resonant peak, at: A – z = 40nm, at the surface of the metamaterial; B - z = 140nm, 100nm beyond the surface of the metamaterial.

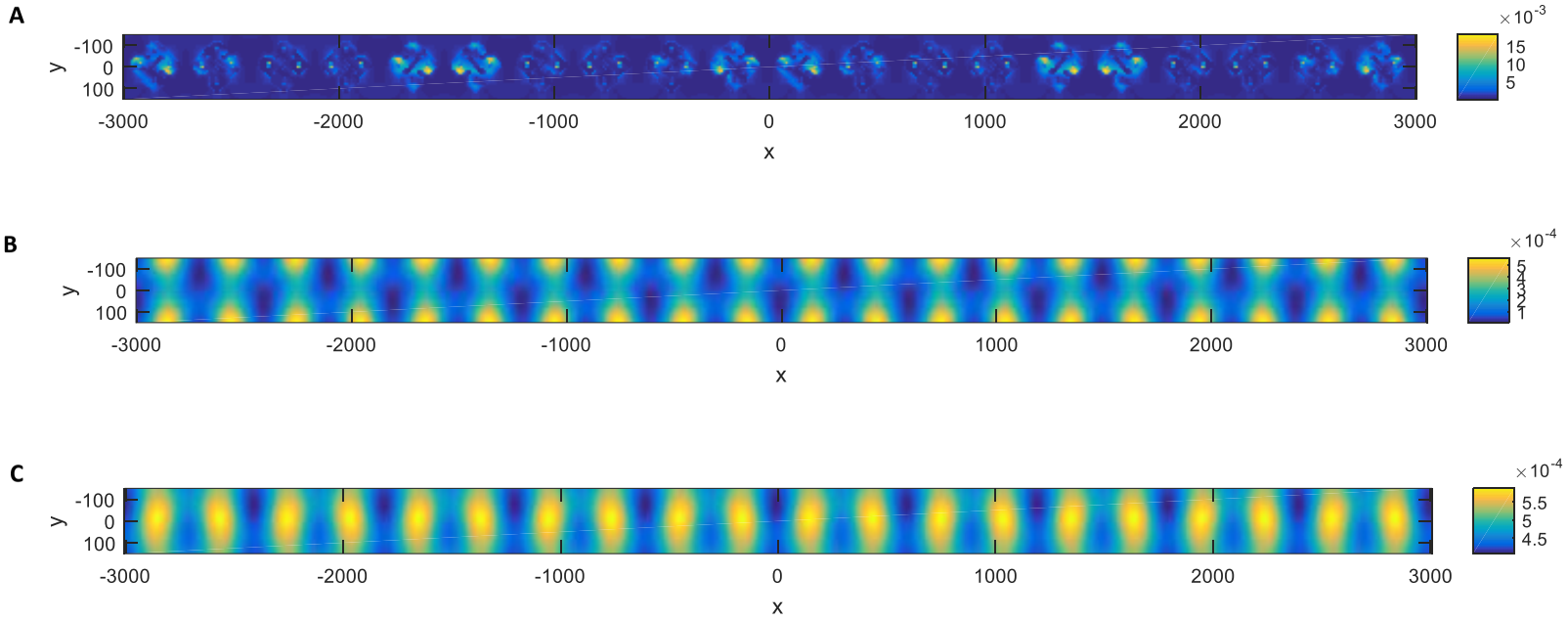

Figure 2.15: MATLAB plots of a one by ten array of the two 'H' unit cell simulation in CST MWS, looking at the absolute electromagnetic fields produced from an x-polarised plane wave at 470THz within the resonant peak, at: A – z = 40nm; B - z = 140nm; C - z = 200nm.

As a result of these simulations a dielectric spacer of 100nm depth was chosen, to be reviewed with the addition of experimental results.

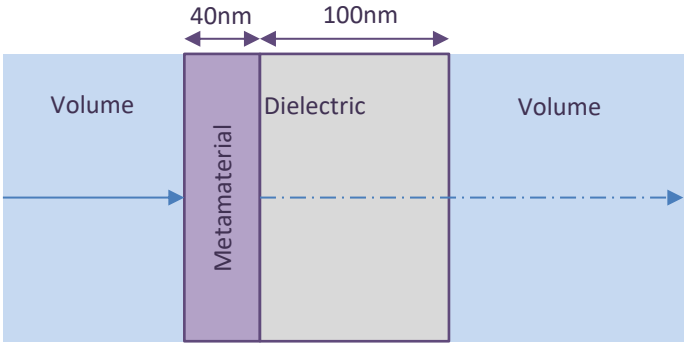

Figure 2.16: Schematic of the metamaterial and chosen spacer

2.5.6 Structured Illumination of the Metamaterial

Testing that the metamaterial produces structured illumination is critical. If it does not, then a new design would be required. Of particular interest is the spatial frequency of the structured illumination, which is important to be fully characterised. Ideally, the structured illumination is approximately sinusoidal. By exporting the electromagnetic field data as a text file and importing it into MATLAB, it was possible to analyse quantitatively the structured evanescent field. In order to evaluate the structured illumination, simulations of an array of unit cells were required, so that the full profile could be seen. Data was recorded at 200, 310, and 470THz based upon the unit cell frequency response, see Section 2.5.4, and collected at the end of the simulation volume.

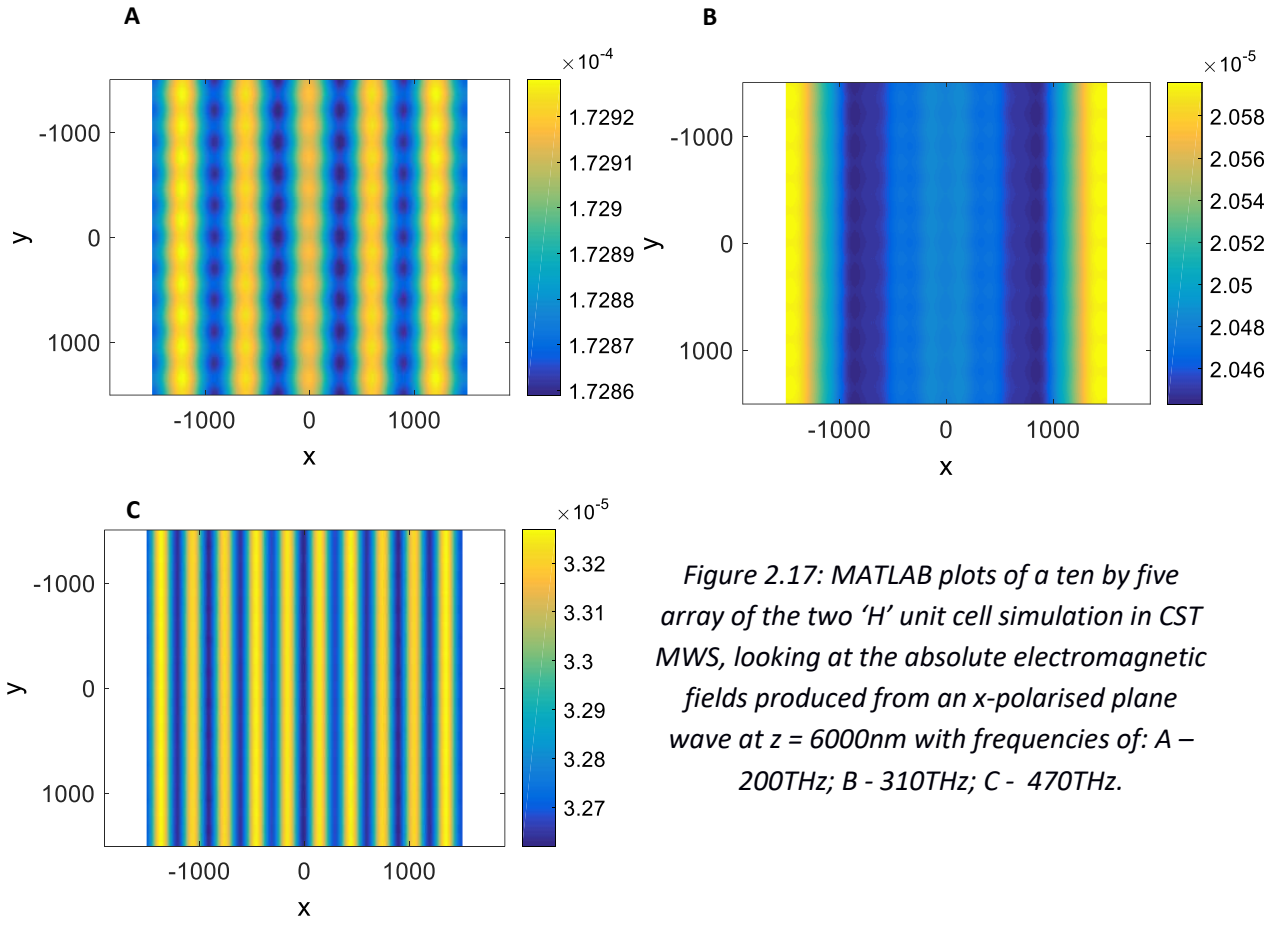

Figure 2.17: MATLAB plots of a ten by five array of the two 'H' unit cell simulation in CST MWS, looking at the absolute electromagnetic fields produced from an x-polarised plane wave at z = 6000nm with frequencies of: A – 200THz; B - 310THz; C - 470THz.

The structured illumination can be clearly seen in A and C for 200THz and 470THz respectively, although it is not present for B (310THz). This is even more evident in line plots taken across data, from which the spatial frequencies of the structured illumination can be calculated.

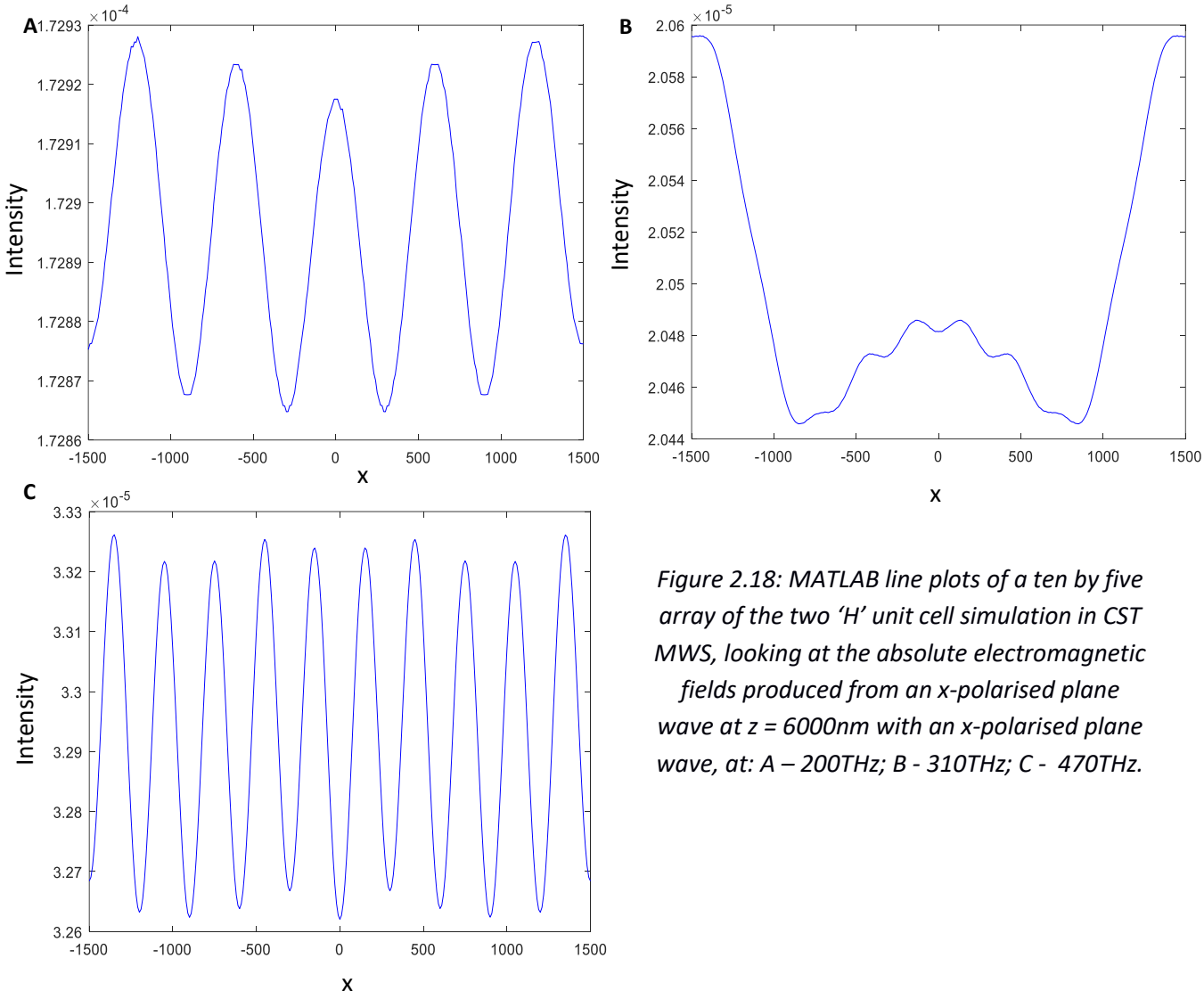

Figure 2.18: MATLAB line plots of a ten by five array of the two 'H' unit cell simulation in CST MWS, looking at the absolute electromagnetic fields produced from an x-polarised plane wave at z = 6000nm with an x-polarised plane wave, at: A – 200THz; B - 310THz; C - 470THz.

The periodic nature of the illumination is evident for A and C, and not B. The spatial wavelength of A (200THz) is 600nm, which corresponds to the periodicity of the unit cell; moreover the periodicity seen within the main stripes has a spatial wavelength of 300nm, which also corresponds to the unit cell size. The spatial wavelength of C (470THz) is 300nm, which may arise from the unit cell 'H' shapes as opposed to the overall unit cell.

2.6 Testing the Metamaterial Design

2.6.1 Introduction & Requirements

Having established that the chosen metamaterial design can produce structured illumination at multiple frequencies, the design required further investigation into its functionality.

2.6.2 Demonstrating the phase and orientation requirements of SIM

In order for SIM to be implemented by this proposed microscope, it is necessary to capture multiple images of the sample with the structured illumination at multiple orientations and phases.

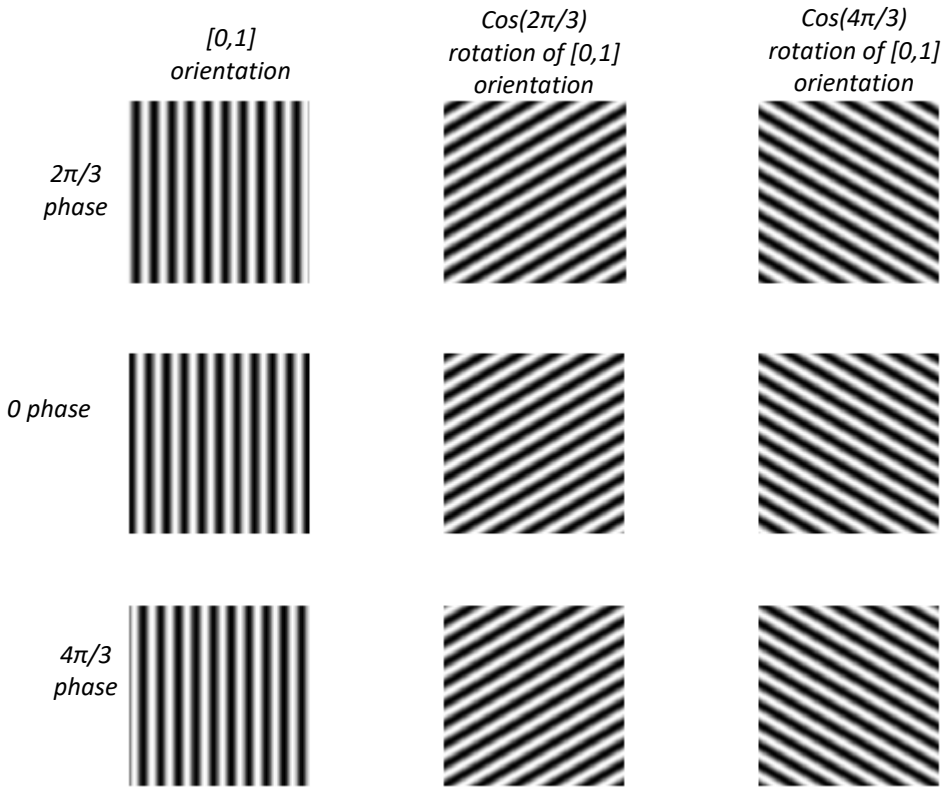

Figure 2.19: Typical sinusoidal structured illumination patterns, generated in MATLAB, showing the use of three phases (0, 2π/3, and 4π/3) and three orientations ([0,1], cos(2π/3) rotation of [0,1], and cos(4π/3) rotation of [0,1]).

In order to achieve this with a metalens, as opposed to with separately projected pattern as in standard SIM, a different approach is required. To produce the different phases, the light incident on the metalens has its polarisation varied; to produce the different orientations, the light incident on the metalens has its incident angle varied, as described in Ponsetto's work[118]. The simulations, for investigating the generation of the required phases and orientations for SIM, were conducted using a ten by five array of unit cells to produce a square volume cross-section. This was in order to make future image reconstructions from the simulation data simpler. Data was recorded at 200 and 470THz based upon the unit cell frequency response, see Section 2.5.4, and the results in Section 2.5.6.

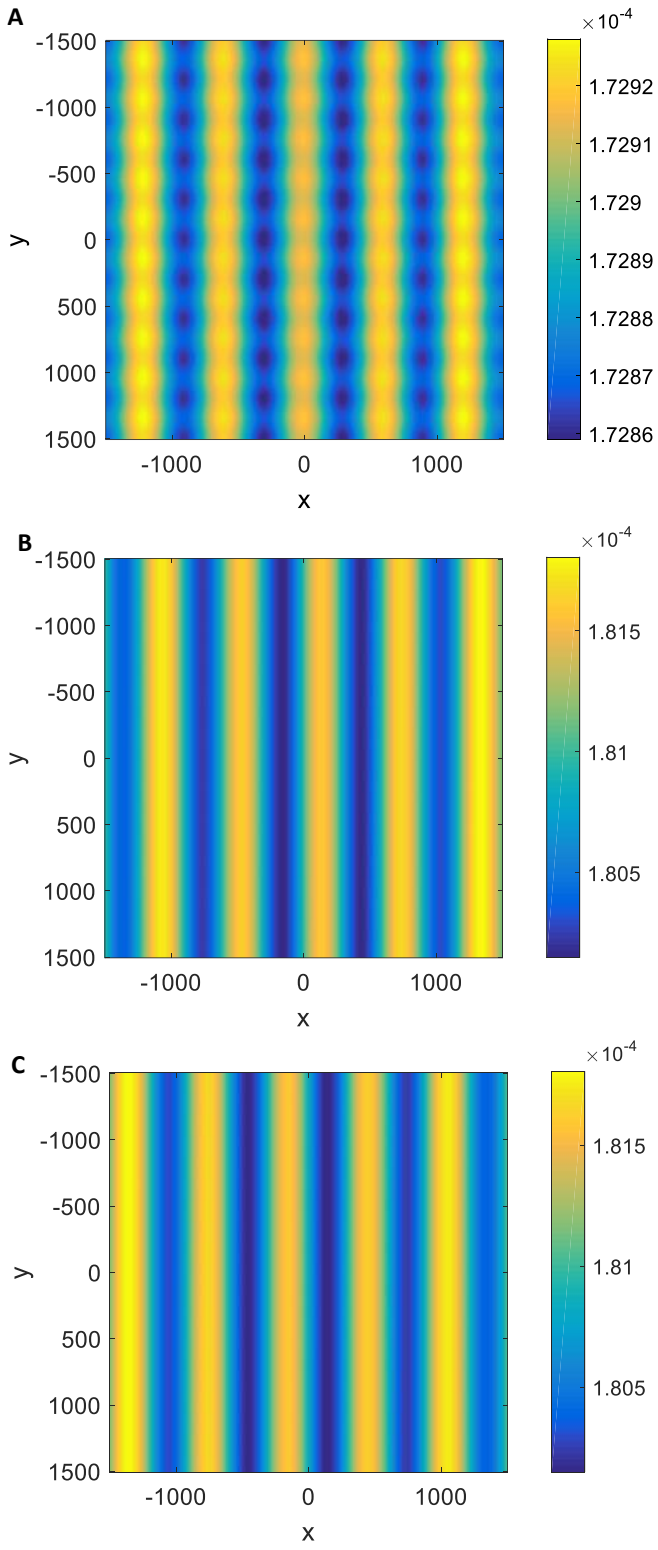

Figure 2.20: MATLAB plots of a ten by five array of the two 'H' unit cell simulation in CST MWS, looking at the absolute electromagnetic fields produced at 200THz, with: A – an x-polarised plane wave (0); B - 2π/3 polarised relative to the x-polarised zero-point; C - 4π/3 polarised relative to the x-polarised zero-point.

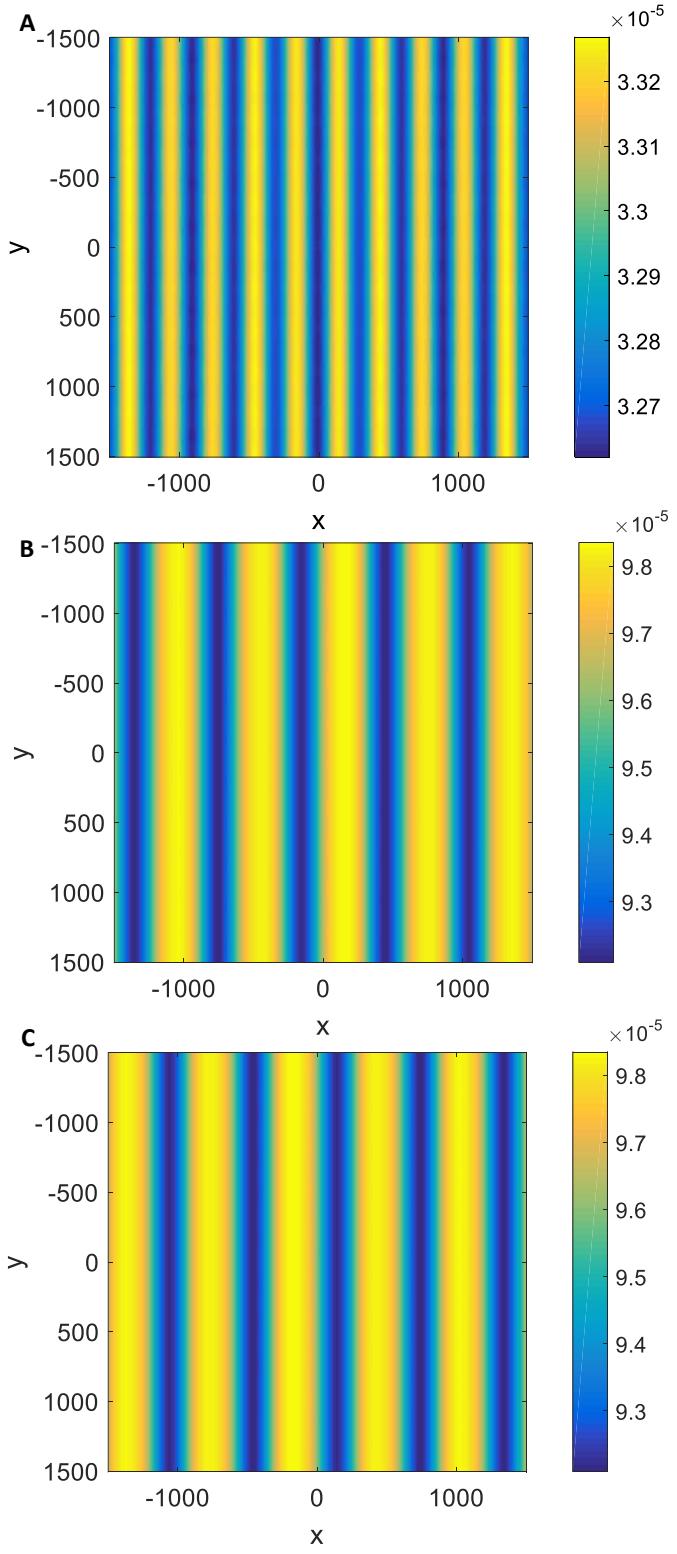

Figure 2.21: MATLAB plots of a ten by five array of the two 'H' unit cell simulation in CST MWS, looking at the absolute electromagnetic fields produced at 470THz, with: A – an x-polarised plane wave (0); B - 2π/3 polarised relative to the x-polarised zero-point; C - 4π/3 polarised relative to the x-polarised zero-point.

It can be seen that the necessary phases for SIM are produced, by changing the incident plane wave's polarisation from x-polarised (0) to $2\pi/3$ and $4\pi/3$ polarised relative to x-polarised as the zero-point, the phase of the structured illumination also changed from 0 to $2\pi/3$ and $4\pi/3$. In the case for 470THz, altering the polarisation and thus the phase has also changed the spatial wavelength from 300nm to 600nm, which is not the case for 200THz. This has an impact on any SIM-based image reconstruction, as the spatial wavelength of the illumination patterns should be consistent across all of the masks, making the 470THz data potentially not useable in a standard SIM reconstruction algorithm. Conversely, the 200THz data, which has consistent spatial phase, is less perfectly sinusoidal than for 470THz, indeed it contains two strong sinusoidal components, although the extra sinusoid is less apparent in the shifted patterns. This also has implications for image reconstruction, as any deviation from a perfectly sinusoidal mask deteriorates the final SIM image reconstruction quality, yet this can potentially be addressed by adapting the standard SIM reconstruction algorithm, see Chapter 3.

However, simulating the change in incident angle suggested for creating a change in orientation was not able to be successfully simulated. Nevertheless, this aspect could be tested experimentally should fabrication of the metamaterial be successful. In order to create a different orientation so that the simulation data could be tested within image reconstruction algorithms, the metamaterial array was rotated and illuminated with y-polarised plane waves. Then to create phase changes in this different orientation, the polarisation was varied from y-polarised (0) to 2π/3 and 4π/3 polarised relative to y-polarised as the zero-point. This orientation change would be equivalent to physically rotating the metalens, which would not be experimental valid as the sample would also rotate with the metalens, meaning no orientation change would be achieved. Nonetheless, this allowed a basis for testing the simulation data within image reconstruction algorithms, although with fewer orientations (two instead of three) than originally desired.

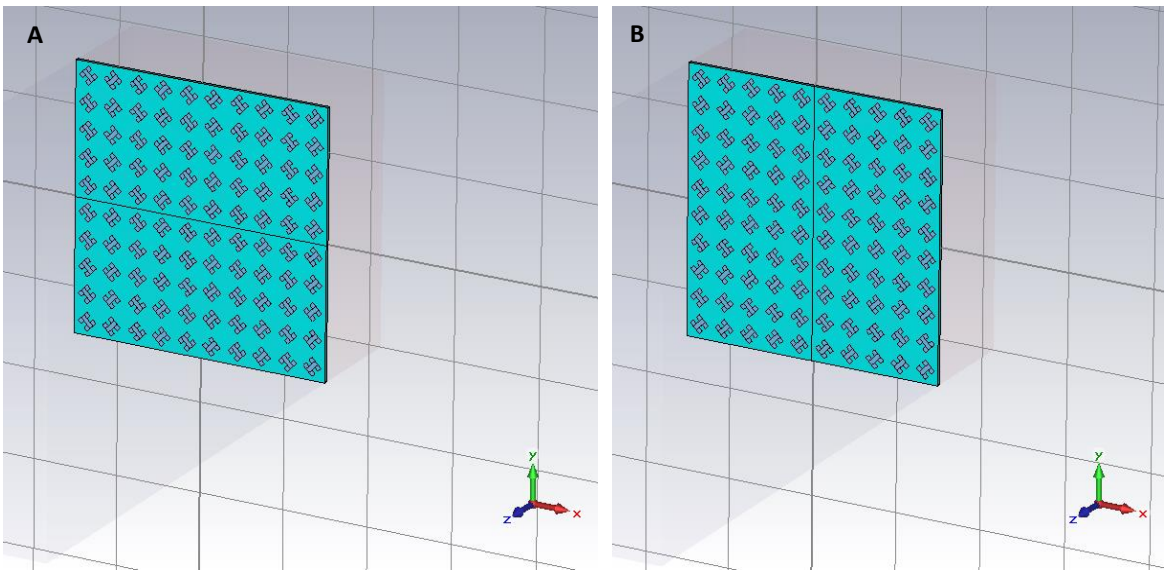

Figure 2.22: 10 by 5 arrays of unit cells in CST MWS, rotated: A - 0°, B - 90°.

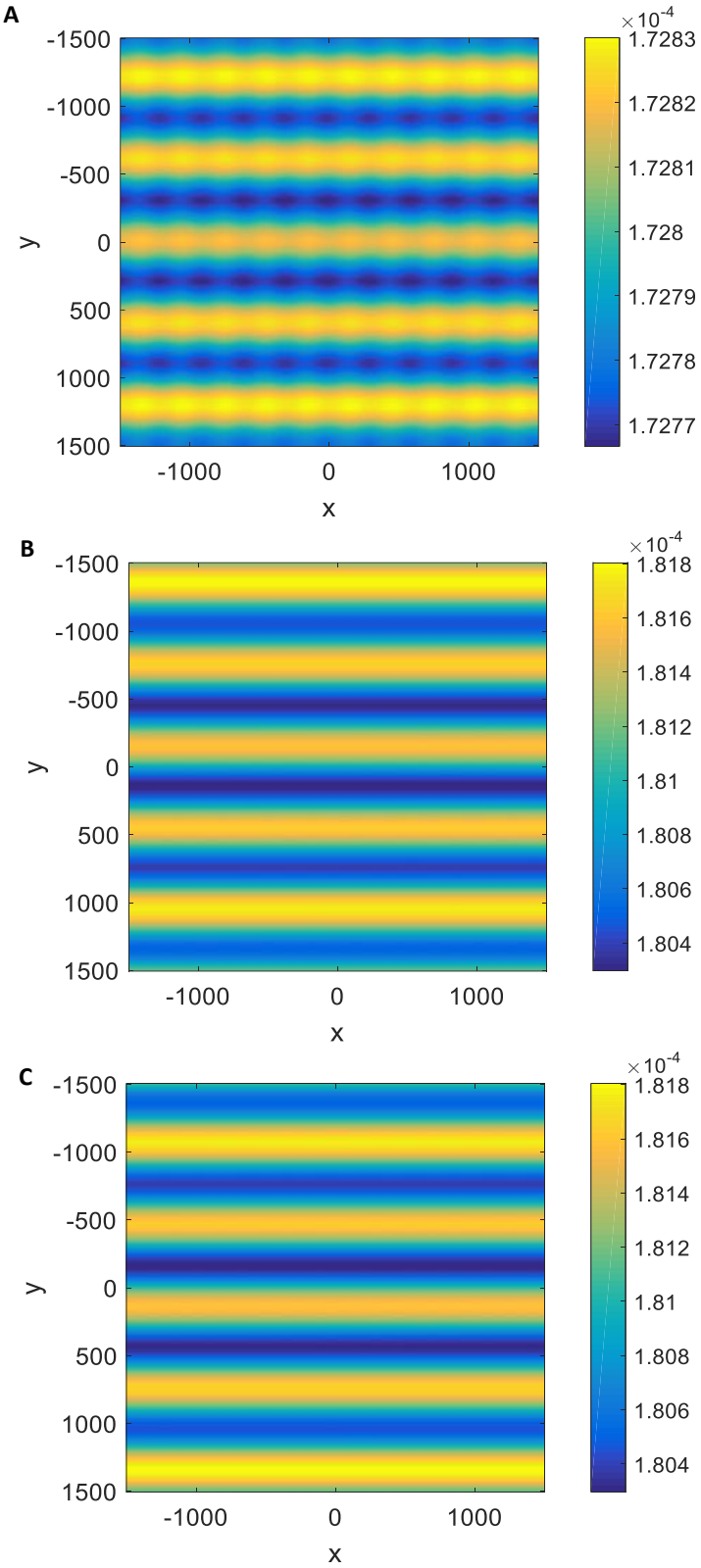

Figure 2.23: MATLAB plots of a ten by five array of the two 'H' unit cell simulation in CST MWS rotated 90°, looking at the absolute electromagnetic fields produced from a y-polarised plane wave at 200THz, at phases: A – 0; B - 2π/3; C - 4π/3.

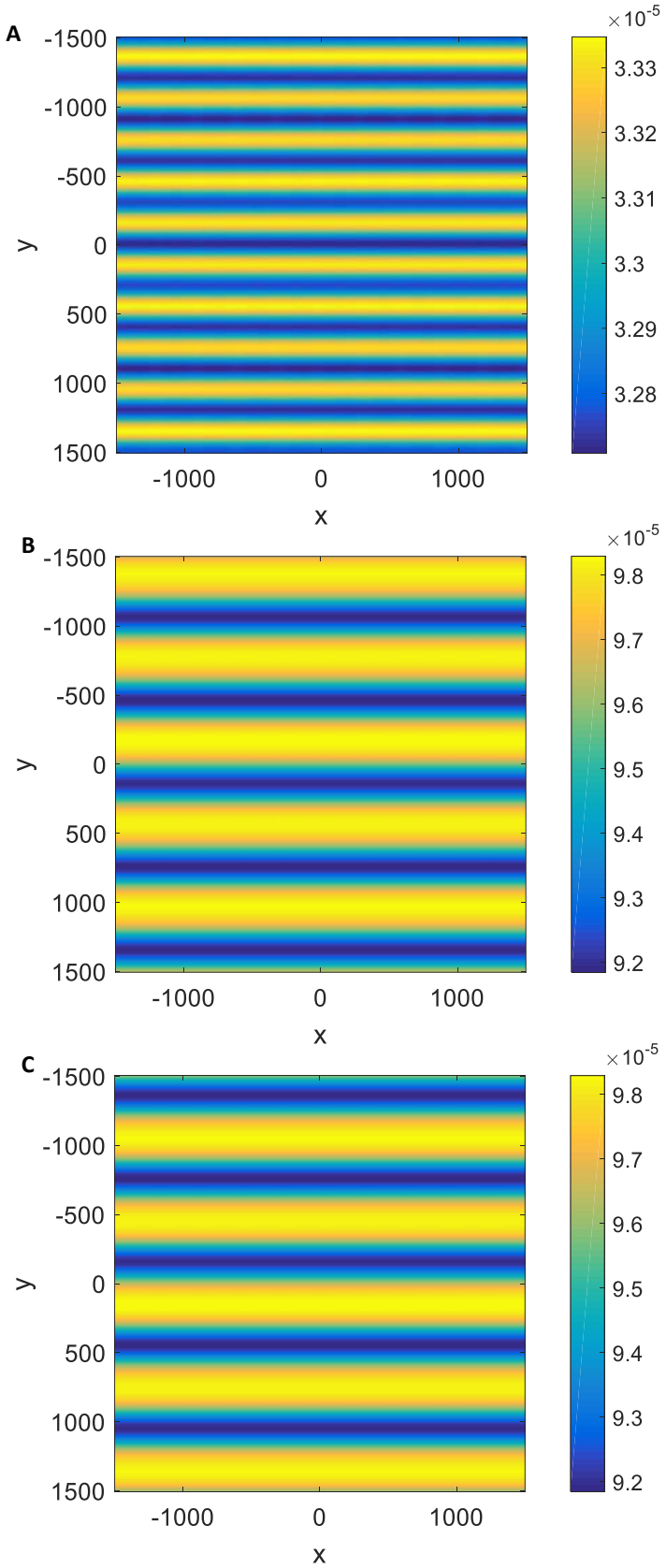

Figure 2.24: MATLAB plots of a ten by five array of the two 'H' unit cell simulation in CST MWS rotated 90°, looking at the absolute electromagnetic fields produced from a y-polarised plane wave at 470THz, at phases: A – 0; B - 2π/3; C - 4π/3.

It can be seen that different phases can be successfully produced by altering the polarisation of the incident plane wave, and that for image reconstruction purposes, two different orientations were achieved by rotating the metamaterial and using polarised incident light to match the rotation (x-polarised light for 0° rotation, and y-polarised light for 90° rotation). Moreover, by varying the frequency of the incident light, the structured illumination is altered. The structured illumination for 200THz has a spatial wavelength of 600nm, but the 0 phase patterns, see figures 2.20A and 2.23A, have a distinct secondary sinusoidal component with a spatial wavelength of 300nm. Whereas for the 470THz structured illumination, the spatial wavelength is 300nm for the 0 phase patterns, see figures 2.21A and 2.24A, but is 600nm for the $2\pi/3$ and $4\pi/3$ phases. These changes in the patterns across the different phases, will potentially negatively impact upon the image reconstruction.

2.6.3 Simulations with samples

Once simulations to choose a unit cell design and characterise it had been conducted, it was then necessary to test the theoretical sensitivity of the design's emitted light to a sample, ensuring that a sample could be detected and that the metamaterial design is potentially suitable for an imaging system. This was done by adding different samples, including metallic strips and gratings of various sizes, after the dielectric spacer into the CST simulations, and examining the electromagnetic fields at the end of the simulation volume and comparing them to a simulation with no sample. The setups and key results are described below.

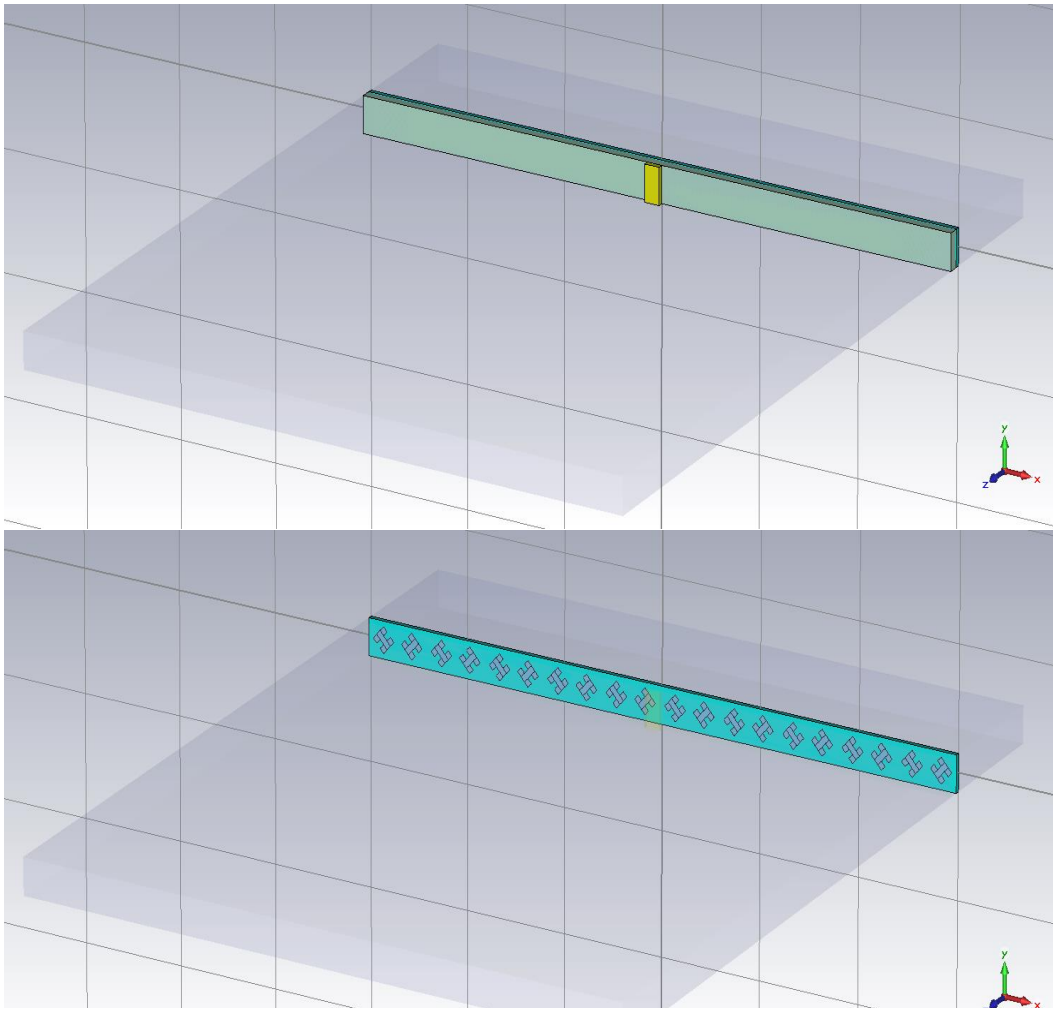

Figure 2.25: Images of a 1 by 10 array of unit cells with dielectric spacer and a gold strip sample (150×300×50nm in size), in CST MWS.

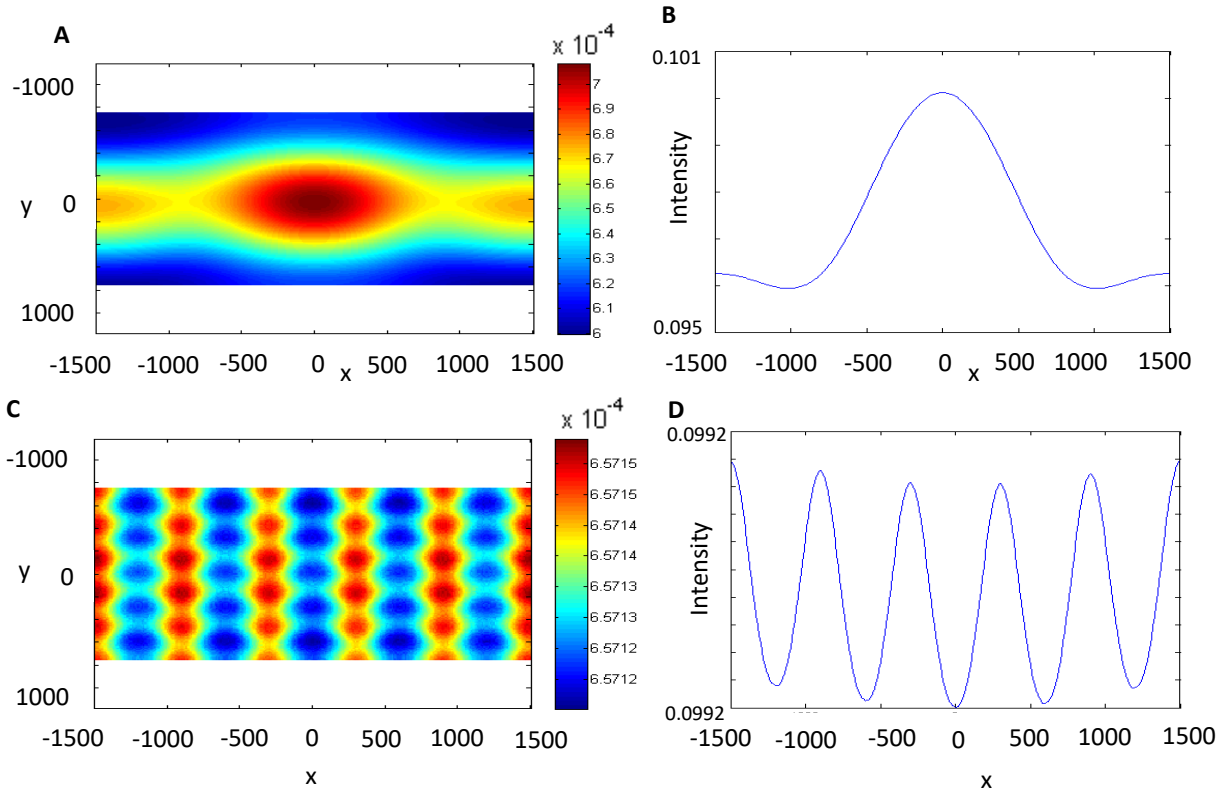

Figure 2.26: MATLAB plots of the intensity of the absolute E-field at 200 THz for the metalens simulation of a 5 by 5 array of unit cells at z = 6000nm for a CST MWS simulation with: ***A, B*** *– a 150×400×50nm strip of gold as a sample, shown as an intensity plot (****A****) and as a line plot (****B****);* ***C, D*** *- no sample, shown as an intensity plot (****C****) and as a line plot (****D****).*

The impact of the sample on the electromagnetic field is clear, demonstrating that a sample will be detectable. These metallic sample represents the type of test sample that can be used experimentally to characterise the resolution and sensitivity of the proposed imaging system.

2.6.4 Imperfect design simulations

The metamaterial design was fabricated using electron beam lithography and etching techniques, see Chapter 4 for details. Unlike in simulation, these fabrication processes do not produce perfectly defined shapes, there is surface roughness, edges are not perfectly straight and there are defects. Consequently, simulations were carried out in CST MWS to investigate the potential effects on the electromagnetic properties of the metamaterial lens. The key features looked at were the effects on the resonant frequencies of the metamaterial, and the effects on the structured illumination produced by the metamaterial.

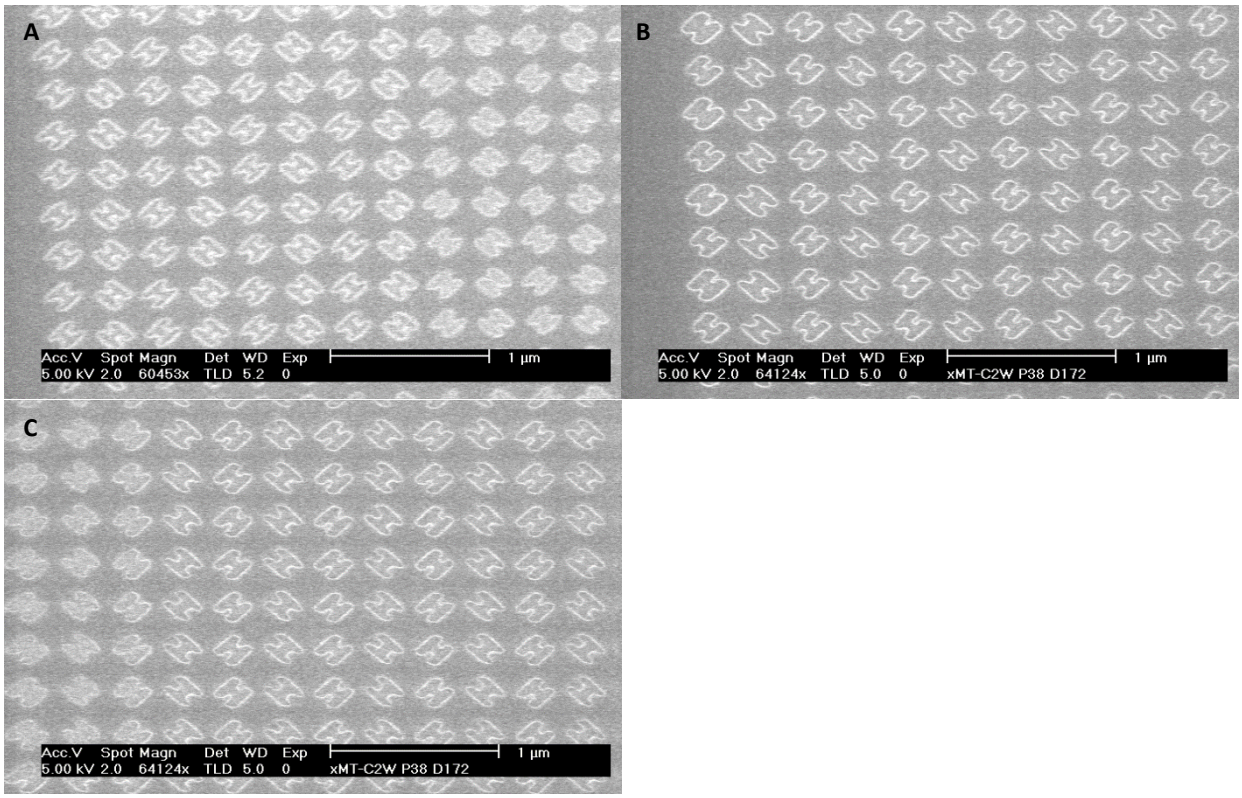

Figure 2.27: Prototype metamaterial fabrications demonstrating fabrication defects: metamterial fabricated using PMMA on a glass substrate (~6×6µm in size) were trialled and imaged using the non-commercial electron beam lithography system (combines a Philips XL 30 field emission SEM with Raith Elphy Plus hardware that interfaces with the SEM to run the patterns) at the School of Physics & Astronomy, University of Birmingham, UK.

As demonstrated by the SEM images of the fabricated ‘H’ shapes, see figure 2.27, the imperfections seen tend to be rounding or smoothing of the corners and jaggedness to the corners, so the ‘H’ shapes lack right-angled corners. Both of these effects were investigated. The corners of the uprights of the ‘H’ shapes were altered to be rounded or stepped, and the area to be altered on each corner was either 10nm by 10nm or 20nm by 20nm. This was done for each in five stages of alteration, and each of these imperfect unit cells could thus be referred to as: ‘Rounded/Stepped 10/20nm-1,2,3,4,5’. In fabrication, often larger scale defects are seen where large areas of the metal film are incorrectly patterned or are missing, however this will almost always make the metamaterial non-functional, so it has to be fabricated again. As a result, this large scale type of defect was not investigated.

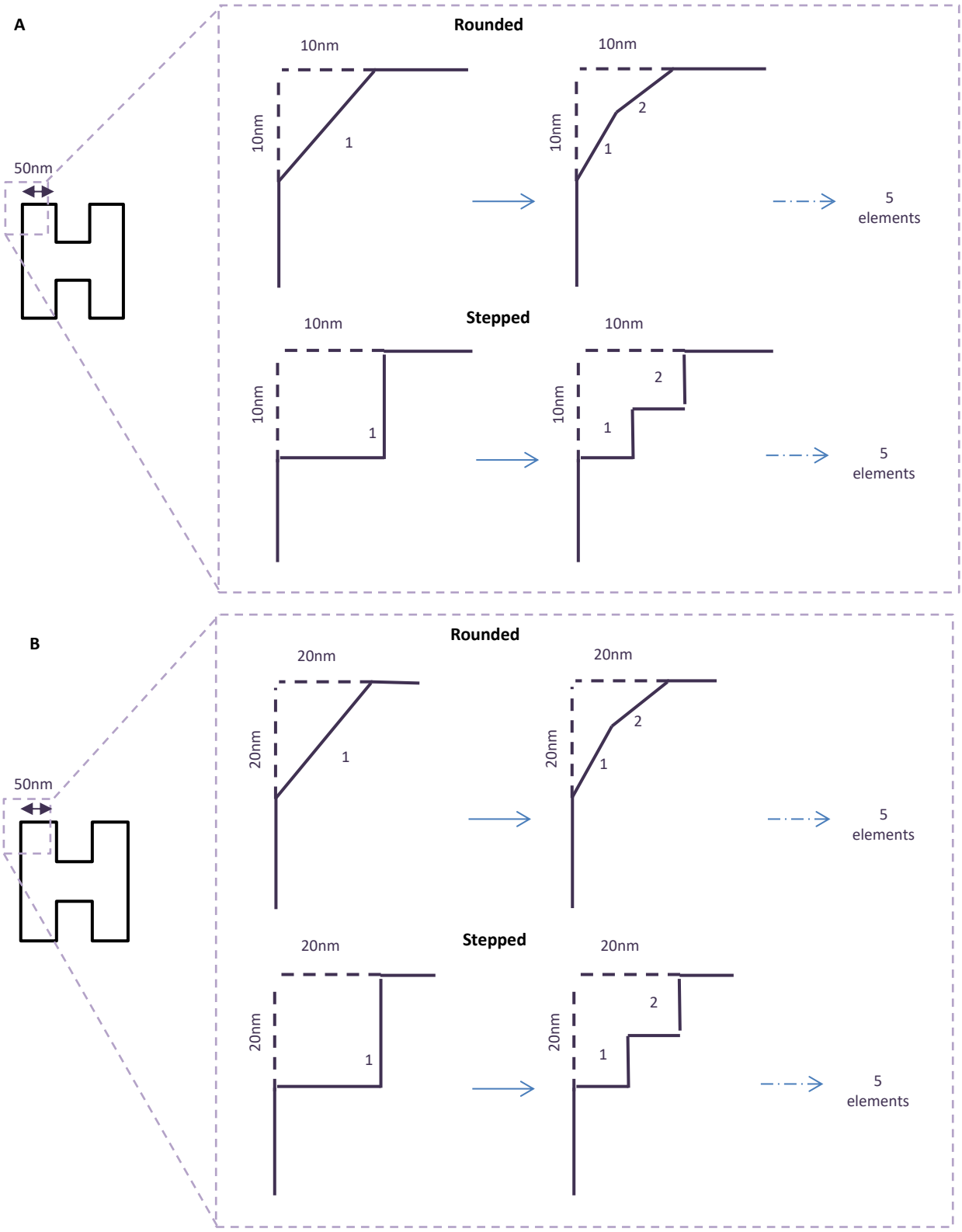

Figure 2.28: Schematic of the imperfect 'H' shape defects investigated, both rounded and stepped profiles, applied to all corners on the uprights of the 'H' shapes, with: A – a 10nm by 10nm corner cut-out area; B – a 20nm by 20nm corner cut-out area.

All of these defects were simulated for a unit cell, and the results are as follows:

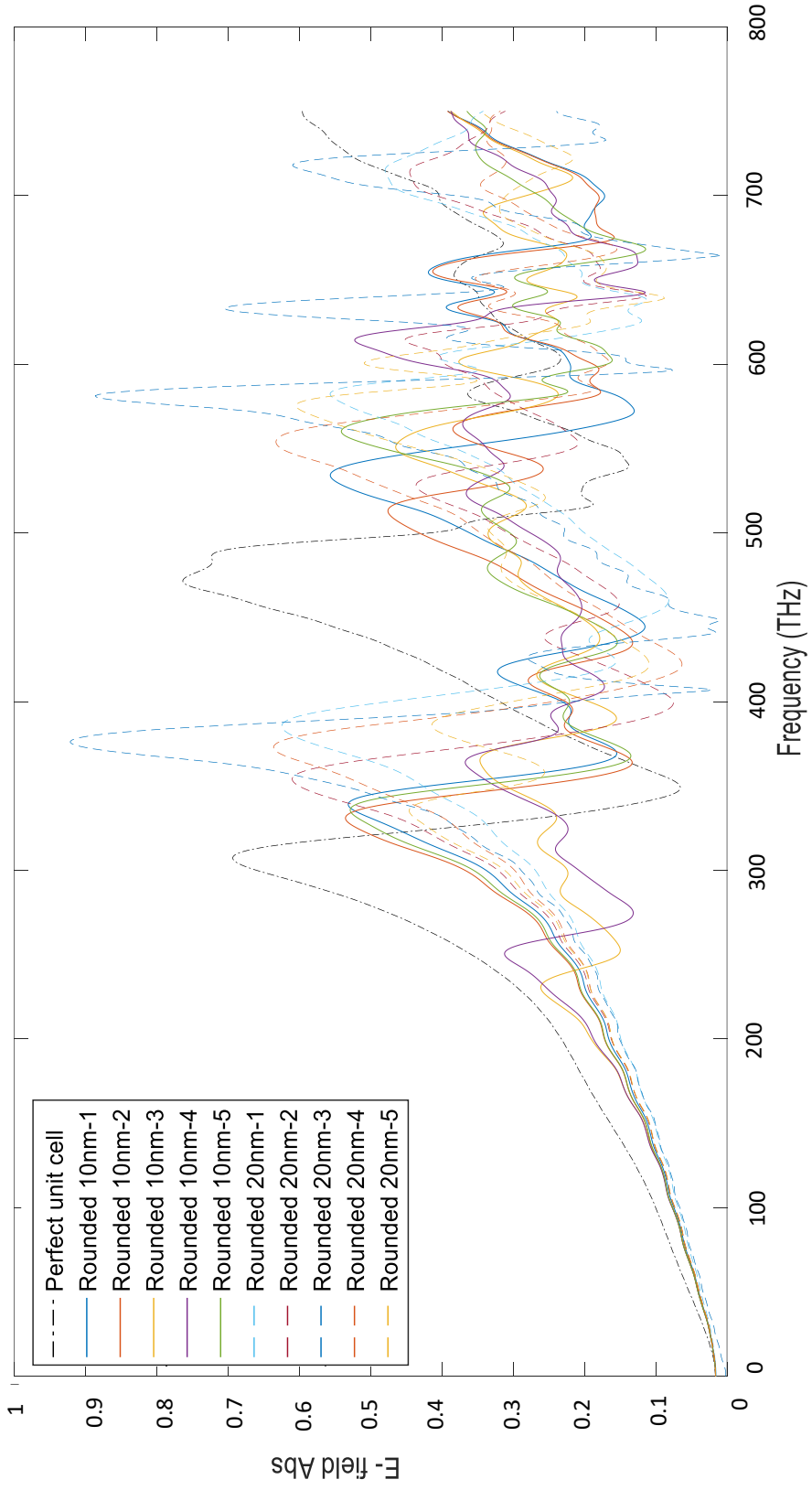

Figure 2.29: MATLAB plot of the frequency response of the imperfect rounded metamaterial 'H' shapes and the perfect 'H' shape.

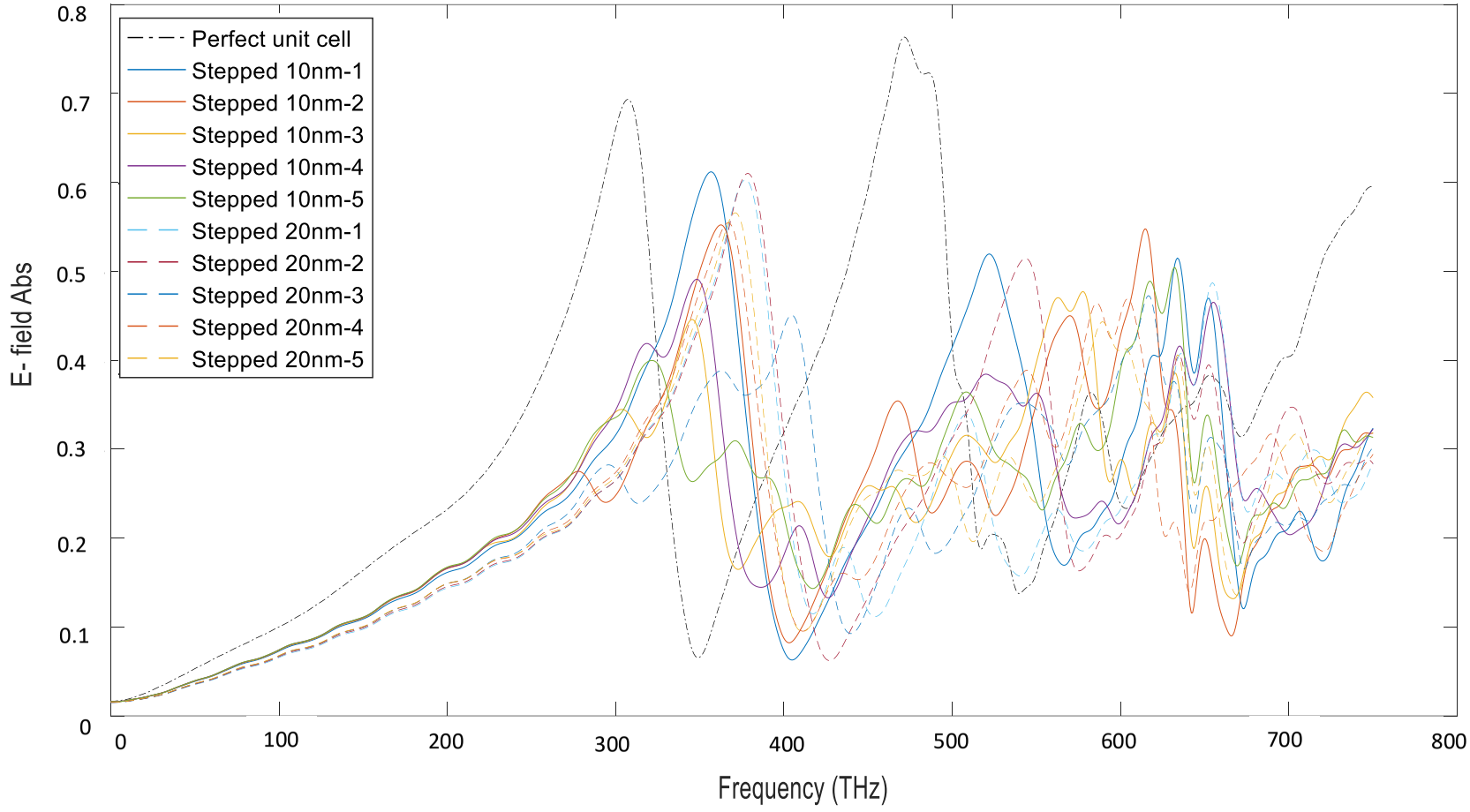

Figure 2.30: MATLAB plot of the frequency response of the imperfect stepped metamaterial 'H' shapes and the perfect 'H' shape.

It can be seen that the different defects do have an effect on the resonant frequency profiles and on the electromagnetic fields. There is a distinct shifting of the main peaks to higher frequencies compared to the perfect unit cell, the peaks have sub-peaks within themselves, and more peaks are present in the spectra. Furthermore, the amplitudes of the peaks have decreased compared to the perfect unit cell in the case of the stepped defects and most of the rounded defects, but some peaks have greater amplitude for the rounded defects, particularly the 20nm-1 rounded unit cell. However, there does not appear to be a definite enough trend between the different defects, or degree of defect, compared to the 'perfect' unit cell. Beyond the main peaks shifting to higher frequencies, the trends are too inconsistent to be able to predict the effects of imperfect fabrication on the metamaterial produced, beyond saying that there will be an effect. Consequently, after fabrication of the metamaterial, it requires imaging with SEM to see how well it has been fabricated, and then extensive characterisation of the electromagnetic fields with methods including FTIR to investigate its properties and allow for adaptation of the spacer layer and the light source if required.

2.7 Conclusions

The research presented in this Chapter has shown, via simulations in CST MWS, the development of a suitable metamaterial unit cell design, comprised of two nano-hole 'H' shapes at ±45° to the normal, cut out from a gold film. The efficacy of this design for producing a structured evanescent field suitable for TIRF-SIM type imaging was also investigated. Structured illumination was produced with a spatial wavelength of 600nm, and three different phases (0, $2\pi/3$ and $4\pi/3$) produced by changing the polarisation of the incident light. The three or more structured pattern orientations typically required for SIM imaging were not achieved. Although, two orientations ([0, 1] and [1, 0]) of the structured patterns were produced by rotating the metamaterial, suitable for testing a SIM image reconstruction algorithm. However, due to imperfections in the structured patterns produced, a standard SIM image reconstruction algorithm may not be suitable and may require adapting, which is investigated in Chapter 3.

In addition, simulations in CST MWS have demonstrated that a sample can be detected in the electromagnetic fields produced by the chosen metamaterial design. The effects of imperfect fabrication on the metamaterial were also investigated, and although few clear trends were seen, any defects to the metamaterial design have a great impact on the functionality of the metamaterial. Consequently, this has to be taken into account when fabricating the metamaterial, see Chapter 4, and characterising the metamaterial using techniques such as SEM to visualise the material, and FTIR to investigate the frequency response of the metamaterial, is of even greater importance.

Chapter 3: Image Reconstruction

3.1 Introduction

This Chapter details the image reconstruction necessary to accompany the proposed metamaterial TIRF-SIM design, and the process of developing such an algorithm. As previously discussed, the basic premise of the image reconstruction algorithm was based on well-established SIM reconstruction algorithms. Consequently, a standard SIM reconstruction algorithm, described below, was developed and then tested with the metamaterial-produced structured illumination patterns. Furthermore, an image reconstruction method was developed for the structured light source that extends standard SIM methods, to optimise it for the metamaterial, and thus other non-standard SIM reconstruction applications.

3.1.1 Aims

The aims of the image reconstruction part of this thesis were as follows:

- Implement a standard SIM image reconstruction algorithm in MATLAB, using typical, ideal structured illumination patterns.
- Implement this standard SIM image reconstruction algorithm in MATLAB, using metamaterial structured illumination patterns, based upon the CST MWS simulations detailed in Chapter 2.
- Determine whether a standard SIM reconstruction algorithm is suitable for these atypical patterns, based on the quality of reconstruction, as judged by any resolution improvement and artefacts in the reconstructed image.

- If necessary, develop new image reconstruction algorithms in order to accommodate these atypical metamaterial structured illumination patterns.
- Implement the novel SIM image reconstruction algorithms in MATLAB, using simulated, ideal metamaterial structured illumination patterns.
- Implement the novel SIM image reconstruction algorithms in MATLAB, using the actual simulated metamaterial structured illumination patterns.
- Determine whether the novel SIM reconstruction algorithms are suitable for these atypical patterns.

3.1.2 MATLAB

The programming environment chosen for developing the SIM reconstruction algorithms was MATLAB. Specifically, the code developed was produced using MATLAB R2012a. MATLAB was chosen as it is suitable for handling and displaying images of many file formats, particularly with the Image Processing Toolbox, implementing mathematical functions necessary for the image reconstruction algorithm, importing data from CST MWS, and as it is widely utilised it makes any code produced easily accessible and useable by others.

3.2 SIM reconstruction

3.2.1 Introduction & Requirements

The SIM image reconstruction described below is referred to as 'standard SIM' in this thesis. This standard SIM is what was originally proposed by M.G.L. Gustafsson[33], whereby a series of images of the same sample are acquired, each with a different projected pattern on the sample, and are then post-processed to produce a super-resolution image. In standard SIM, these patterns are sinusoidal and therefore appear as stripes across the image, and for a 2D image, nine different images are required with more images theoretically producing further resolution improvement, each with a different structured illumination pattern[33,35,36].

These nine different structured illumination patterns are based on three orientations and three phases of the basic sinusoidal stripes. By applying the structured patterns to the sample, higher frequency and thus higher resolution information is retained for the final image. Then by combining the nine or more images in the method described in *Section 3.2.3*, this higher resolution information is seen in the final image and the structured patterns are removed, producing a super-resolution image of ~2× resolution[33]. The sample to be imaged and the sinusoidal structured illumination incident upon it, act as the two patterns that are superposed, and as a result Moiré fringes appear which are coarser than either of the original patterns; these fringes represent information from the patterns that has been shifted in Fourier space as a result of the superposition. The observed image is the product of the mask and the sample, and contains the Moiré fringes. These fringes are easily observable, but contain information about the fine detail of the sample that is not observable because of the diffraction limit. Thus, in standard SIM, if the illumination pattern

is known, this higher resolution information from the sample can be accessed, creating a super-resolution imaging technique[33,35,36].

The final resolution improvement produced can depend on multiple factors. A primary factor is the number of structured illumination patterns and thus images used to produce the final image, generally the fewer used, the lower the final resolution, as less high resolution information will be retained for the final image. The design of the structured illumination is also important. Artefacts in the structured illumination patterns that make it deviate from being a perfect sinusoid generally result in artefacts and lower resolution in the final image. Moreover the spatial frequency of the structured illumination has an impact; the smaller the spatial frequency, the higher the final resolution, but with a greater potential for artefacts.

Accurately describing the point spread function of the imaging instrument and the structured illumination patterns is key to producing a well-resolved, artefact free final image. The sample image can also impact the final image, as very structured or rectilinear images such as a chequerboard tends to result in artefacts and a bad final reconstruction, due to being very similar to the structured illumination patterns. Finally, parameters within the image reconstruction algorithm, such as the parameter that estimates the noise, can greatly impact upon the final image quality, but this impact depends on the sample image and structured patterns used, so has to investigated and ideal values determined on a case-by-case basis.

Based upon these factors that can affect image reconstruction quality, it was expected that performing a standard SIM reconstruction with atypical structured illumination patterns produced by metamaterials would not be successful. However, as the metamaterial-

produced structured illumination patterns were predominantly sinusoidal, a standard SIM image reconstruction method was still potentially viable. Then, if this was not the case, standard SIM image reconstruction could form the basis for an algorithm optimised for the atypical patterns.

3.2.2 Current Extant Software

There is now open-access SIM reconstruction software, which has been developed and become available over the past few years. This software is designed to allow researchers utilising standard SIM to reconstruct their images outside of proprietary software attached to commercial SIM instruments[34,218-221]. The two main software packages available are FairSIM, developed by M. Müller, for use with ImageJ or FIJI[220,221], and SIMToolbox, developed by P. Křížek et al, for use in MATLAB[218,219]. Both are effective, however as the intent of this research was to potentially develop new or adapted algorithms, starting from the fundamental mathematics was deemed necessary and therefore a basic SIM reconstruction algorithm was developed, as opposed to working with pre-existing software.

3.2.3 Theory & Mathematics

Although SIM was first proposed by M.G.L Gustafsson[33], the mathematics for its reconstruction is comprehensively described by T. Lukeš et al. in the paper 'Comparison of image reconstruction methods for structured illumination microscopy'[34]. It is this paper that forms the mathematical basis for this research into SIM image reconstruction.

The initial expression of the collection of SIM images, that are comprised of the sample, the microscope's point spread function, and the structured illumination pattern masks, forms the basis for the mathematical description of the image reconstruction process.

$$g_n(\underline{\boldsymbol{x}}) = [m_n(\underline{\boldsymbol{x}})f(\underline{\boldsymbol{x}})] \otimes h(\underline{\boldsymbol{x}}) \qquad [3.1]$$

Where: $g_n(\underline{\boldsymbol{x}})$ are the *n* SIM images, $m_n(\underline{\boldsymbol{x}})$ are the structured illumination pattern masks, $f(\underline{\boldsymbol{x}})$ is the sample, $h(\underline{\boldsymbol{x}})$ is the microscope's point spread function, $\underline{\boldsymbol{x}}$ is a vector in the image plane, and $\otimes$ is the convolution operator. Therefore the images are formed from the sample multiplied by the masks, and then this is convolved with the PSF. This forms a set of n diffraction limited images, where the 'perfect' sample information is blurred by the PSF and is overlaid with the masks.

By Fourier transforming this expression, it can be expressed in Fourier space as:

$$G_n(\underline{\boldsymbol{k}}) = H(\underline{\boldsymbol{k}})[F(\underline{\boldsymbol{k}}) \otimes M_n(\underline{\boldsymbol{k}})] \qquad [3.2]$$

Where: $G_n(\underline{\boldsymbol{k}})$, $H(\underline{\boldsymbol{k}})$, $F(\underline{\boldsymbol{k}})$, $M_n(\underline{\boldsymbol{k}})$ are the Fourier transforms of $g_n(\underline{\boldsymbol{x}})$, $h(\underline{\boldsymbol{x}})$, $f(\underline{\boldsymbol{x}})$, $m_n(\underline{\boldsymbol{x}})$ respectively, and $\underline{\boldsymbol{k}}$ is (k_x,k_y) is a vector in the image plane in k-space. The matrix multiplication in real space has become a convolution, and vice-versa. The expression in Fourier space is useful as much of the image reconstruction algorithm is performed in Fourier space.

This reconstruction method relies on prior knowledge of both the PSF, which can be modelled as a Gaussian or Airy function, and of the masks used. Thus a mathematical expression of the masks is required. In the case of a sinusoidal mask, it is as follows:

$$m_n(\underline{\boldsymbol{x}}) = 1 + \alpha \cos(2\pi(\underline{\boldsymbol{p}} \cdot \underline{\boldsymbol{x}}) + \varphi_i) \qquad [3.3]$$

Where: α is amplitude of the sinusoid, $\underline{\boldsymbol{p}}$ is the modulation vector that describes the orientation and wavelength of the sinusoid, and φ_i is the spatial phase of the sinusoid, typically $\varphi_i = 0, 2\pi/3, 4\pi/3$. The use of a sinusoidal expression also means that it can be expanded to potentially describe any mask as a sum of sinusoids.

In Fourier space, this can be expressed as:

$$M(\underline{\boldsymbol{k}}) = \int_{-\infty}^{\infty} m_i(\underline{\boldsymbol{x}}) \cdot e^{-2\pi i \underline{\boldsymbol{x}} \cdot \underline{\boldsymbol{k}}} \, d\underline{\boldsymbol{x}}$$

$$= \int_{-\infty}^{\infty} (1 + \tfrac{\alpha}{2}\left(e^{2\pi i(\underline{\boldsymbol{p}} \cdot \underline{\boldsymbol{x}} + \varphi_i)} + e^{-2\pi i(\underline{\boldsymbol{p}} \cdot \underline{\boldsymbol{x}} + \varphi_i)}\right) \cdot e^{-2\pi i \underline{\boldsymbol{x}} \cdot \underline{\boldsymbol{k}}} \, d\underline{\boldsymbol{x}}$$

$$= \int_{-\infty}^{\infty} (e^{-2\pi i \underline{\boldsymbol{x}} \cdot \underline{\boldsymbol{k}}} + \tfrac{\alpha}{2}\left(e^{2\pi i \varphi_i} e^{-2\pi i \left(\underline{\boldsymbol{k}} - \underline{\boldsymbol{p}}\right) \cdot \underline{\boldsymbol{x}}} + e^{-2\pi i \varphi_i} e^{-2\pi i \left(\underline{\boldsymbol{k}} + \underline{\boldsymbol{p}}\right) \cdot \underline{\boldsymbol{x}}}\right)) \cdot e^{-2\pi i \underline{\boldsymbol{x}} \cdot \underline{\boldsymbol{k}}} \, d\underline{\boldsymbol{x}}$$

$$= \delta(\underline{\boldsymbol{k}}) + \tfrac{\alpha}{2}\delta\left(\underline{\boldsymbol{k}} - \underline{\boldsymbol{p}}\right) e^{2\pi i \varphi_i} + \tfrac{\alpha}{2}\delta\left(\underline{\boldsymbol{k}} + \underline{\boldsymbol{p}}\right) e^{-2\pi i \varphi_i}$$

$$M_n(\underline{\boldsymbol{k}}) = \delta(\underline{\boldsymbol{k}}) + \tfrac{\alpha}{2}\delta\left(\underline{\boldsymbol{k}} - \underline{\boldsymbol{p}}\right) e^{2\pi i \varphi_i} + \tfrac{\alpha}{2}\delta\left(\underline{\boldsymbol{k}} + \underline{\boldsymbol{p}}\right) e^{-2\pi i \varphi_i} \qquad [3.4]$$

Substituting equation [3.4] into [3.2], the SIM images in Fourier space can be expressed in terms of the modulation vector, $\underline{\boldsymbol{p}}$, which describes the orientation and spatial frequency of the masks, and the spatial phases, φ_i. This allows the frequency information that describes the images to be shifted and separated, which means that the higher resolution (higher frequency) information that is not present in a standard diffraction limited image can be retained in the low frequency signal via spatial frequency mixing. Moreover the masks can be separated and removed from the final reconstructed super-resolution image. This is the process for super-resolution SIM reconstruction.

$$G_n(\underline{\boldsymbol{k}}) = H(\underline{\boldsymbol{k}})[F(\underline{\boldsymbol{k}}) + \tfrac{\alpha}{2}F\left(\underline{\boldsymbol{k}} - \underline{\boldsymbol{p}}\right) e^{2\pi i \varphi_i} + \tfrac{\alpha}{2}F\left(\underline{\boldsymbol{k}} + \underline{\boldsymbol{p}}\right) e^{-2\pi i \varphi_i} \qquad [3.5]$$

By expressing equation [3.5] in matrix form (equation [3.6]), it creates the framework for creating a computational algorithm to perform the image reconstruction, as the images and variables will be arrays of numbers. In matrix form, for each value of $\underline{\boldsymbol{p}}$ this becomes:

$$\begin{bmatrix} G_1(\underline{\boldsymbol{k}}) \\ G_2(\underline{\boldsymbol{k}}) \\ G_3(\underline{\boldsymbol{k}}) \end{bmatrix} = \begin{bmatrix} 1 & e^{2\pi i\varphi_1} & e^{-2\pi i\varphi_1} \\ 1 & e^{2\pi i\varphi_2} & e^{-2\pi i\varphi_2} \\ 1 & e^{2\pi i\varphi_3} & e^{-2\pi i\varphi_3} \end{bmatrix} \begin{bmatrix} H(\underline{\boldsymbol{k}})F(\underline{\boldsymbol{k}}) \\ \frac{\alpha}{2}H(\underline{\boldsymbol{k}})F(\underline{\boldsymbol{k}}-\underline{\boldsymbol{p}}) \\ \frac{\alpha}{2}H(\underline{\boldsymbol{k}})F(\underline{\boldsymbol{k}}+\underline{\boldsymbol{p}}) \end{bmatrix} \qquad [3.6]$$

Consequently, for three $\underline{\boldsymbol{p}}$'s there are three sets of this matrix equation [3.6], and n (nine) G_n's, as there are *i* (three) phases, and three orientations. More images can be used, thus the number of orientations and/ or phases is increased, and this can result in improved spatial resolution in the final reconstruction as there is improved frequency coverage, but in this example nine images are used.

The spectral components of these G_n's then need to be separated, which is done by multiplying the G_n's by the Hermitian conjugate of the central matrix containing the phases in equation [3.6]. Separating the components allows the masks to be removed from the final image and the higher resolution information to be retained.

Central matrix: $[\mathbf{3.7}] = [\mathbf{3.6}]^{T*} = [\mathbf{3.6}]^{H} \ \therefore$

$$\begin{bmatrix} C_1(\underline{\boldsymbol{k}}) \\ C_2(\underline{\boldsymbol{k}}) \\ C_3(\underline{\boldsymbol{k}}) \end{bmatrix} = \begin{bmatrix} 1 & 1 & 1 \\ e^{-2\pi i\varphi_1} & e^{-2\pi i\varphi_2} & e^{-2\pi i\varphi_3} \\ e^{2\pi i\varphi_1} & e^{2\pi i\varphi_2} & e^{2\pi i\varphi_3} \end{bmatrix} \begin{bmatrix} G_1(\underline{\boldsymbol{k}}) \\ G_2(\underline{\boldsymbol{k}}) \\ G_3(\underline{\boldsymbol{k}}) \end{bmatrix} \qquad [3.7]$$

Where C_n are the separated components, and again there are three sets of equation [3.7] to give the total nine C_n's. Unlike iterative methodologies for image reconstruction, such as Blind SIM, this method does not attempt to directly solve for the sample, $f(\underline{\boldsymbol{x}})$; instead, this reconstruction methodology uses the prior knowledge of the masks which have enabled retention of higher resolution information, and then separates and shifts the different

images to separate the higher resolution information from the masks and combine it with the lower resolution information. The masks are removed from the images and the multiple images are combined to create a final reconstruction of a single image that is a closer solution to $f(\underline{\boldsymbol{x}})$ than the diffraction-limited widefield image. Therefore, this SIM image reconstruction methodology is attempting to solve for $f(\underline{\boldsymbol{x}})$, but in an indirect manner, thus the $C_n(\underline{\boldsymbol{k}})$'s in equation [3.7] do not represent a direct solution for $f(\underline{\boldsymbol{x}})$.

After separating the components in equation [3.7], these separated components are then shifted in Fourier space by a factor dependent on the spatial wavelength that is a parameter of the $\underline{\boldsymbol{p}}$'s, this mixes spectral frequencies that are not observable due to the diffraction limit of the imaging system and its PSF with those that are observable. Thus, in Fourier space a greater area of spectral information is covered and thus more information is retained and a higher resolution final image can be produced. The shifts are $\underline{\boldsymbol{0}}$ and $\pm\underline{\boldsymbol{p}}$, for each $\underline{\boldsymbol{p}}$ value.

$$\begin{aligned} CS_1(\underline{\boldsymbol{k}}) &= C_1(\underline{\boldsymbol{k}}) \\ CS_2(\underline{\boldsymbol{k}}) &= C_2\left(\underline{\boldsymbol{k}} + \underline{\boldsymbol{p}}\right) \\ CS_3(\underline{\boldsymbol{k}}) &= C_3\left(\underline{\boldsymbol{k}} - \underline{\boldsymbol{p}}\right) \end{aligned} \qquad [3.8]$$

$$\begin{aligned} \therefore CS_1(\underline{\boldsymbol{k}}) &= G_1(\underline{\boldsymbol{k}}) + G_2(\underline{\boldsymbol{k}}) + G_3(\underline{\boldsymbol{k}}) \\ CS_2(\underline{\boldsymbol{k}}) &= e^{-2\pi i\varphi_1} G_1\left(\underline{\boldsymbol{k}} + \underline{\boldsymbol{p}}\right) + e^{-2\pi i\varphi_2} G_2\left(\underline{\boldsymbol{k}} + \underline{\boldsymbol{p}}\right) + e^{-2\pi i\varphi_3} G_3\left(\underline{\boldsymbol{k}} + \underline{\boldsymbol{p}}\right) \\ CS_3(\underline{\boldsymbol{k}}) &= e^{2\pi i\varphi_1} G_1\left(\underline{\boldsymbol{k}} + \underline{\boldsymbol{p}}\right) + e^{2\pi i\varphi_2} G_2\left(\underline{\boldsymbol{k}} + \underline{\boldsymbol{p}}\right) + e^{2\pi i\varphi_3} G_3\left(\underline{\boldsymbol{k}} + \underline{\boldsymbol{p}}\right) \end{aligned} \qquad [3.8b]$$

These shifted, separated components are then combined via a Wiener filter:

$$S(\underline{\boldsymbol{k}}) = \frac{\sum_{n=1}^{N} OTF_n(\underline{\boldsymbol{k}})^* CS_n(\underline{\boldsymbol{k}})}{\sum_{n=1}^{N} \left|OTF_n(\underline{\boldsymbol{k}})\right|^2 + w} \qquad [3.9]$$

Where: $S(\underline{\boldsymbol{k}})$ is the reassembled image in Fourier space; OTF_n is the n-th shifted OTF (Optical Transfer Function which is the PSF in Fourier space), shifted in the same way as the C_n's are in equation [3.8]; * is the complex conjugate function; N is the total number of image components, typically nine; and w is a noise constant. A Wiener filter was used as it has been proven widely effective for image reconstruction, including for SIM, as it offers an optimal balance between reconstructing a higher resolution image and noise smoothing.

This reassembled image in Fourier space is then apodized, which is a mathematical optical filtering technique to smooth discontinuities and particularly ringing artefacts common to SIM imaging, with the desired OTF. In this case, the desired OTF is the desired PSF of the system, so by reducing the width of the PSF by half, it should produce 2× resolution compared to the original widefield image. Finally, the image is then converted from Fourier space to real space, giving a super-resolution reconstructed SIM image. The aim of this is to get as close to the sample f($\underline{x}$), which would be a 'perfect' image, as possible.

3.2.4 MATLAB algorithm

This mathematical process was converted into a MATLAB based algorithm. The algorithm is adaptable to different images, and can be used with simulated masks, or utilise inputted masks or images already overlaid with masks. The input image can be rescaled to match the size of inputted masks, and can be in any file format compatible with MATLAB. The PSF is based upon the Gaussian approximation of an Airy disc and is created using adjustable parameters for the simulated microscope's wavelength, λ, numerical aperture, *NA*, and refractive index, *n*.

$$PSF(x,y) \approx e^{-(x^2+y^2)/\left(2\cdot\left(0.45\cdot\lambda\cdot\frac{n}{2\cdot NA}\right)^2\right)} \qquad [3.10]$$

The masks and the original image need to be the same size in order for the matrix mathematics to be possible. The final image is reassembled via a Wiener filter. The shifts are achieved by multiplying the appropriate C_n's by a Fourier kernel:

$$K(\underline{\boldsymbol{x}}) = e^{\pm i(\underline{\boldsymbol{p}}\cdot\underline{\boldsymbol{x}})} \qquad [3.11]$$

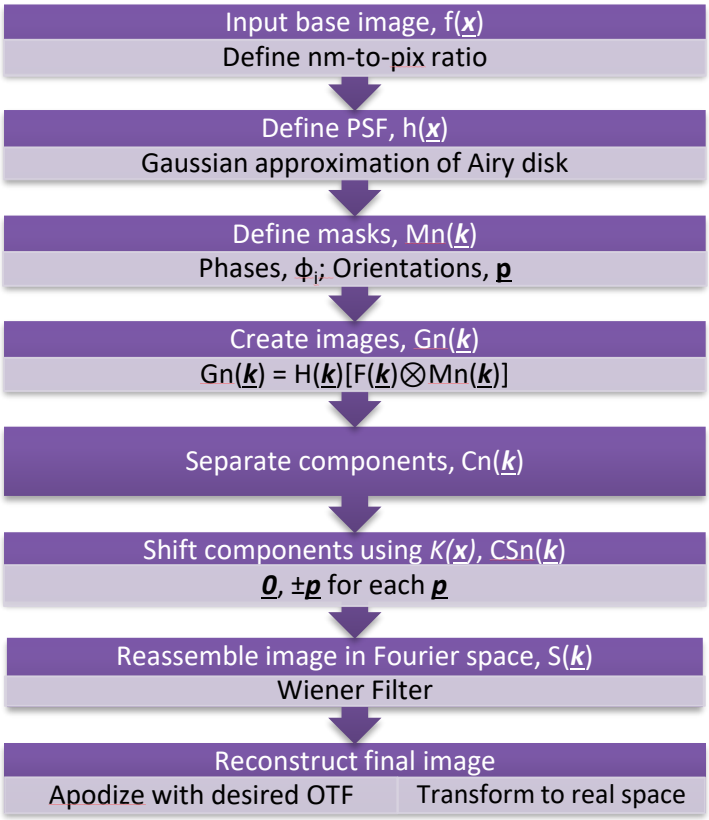

Figure 3.1: Diagram of SIM reconstruction key stages and parameters

Key parameters are: the nm-to-pixel ratio which describes the size of each pixel in nm, the PSF parameters described above, the mask phases φ_i, the mask orientations $\boldsymbol{p}$, the spatial frequency of the masks, the noise parameter w, and the width of the desired OTF. The algorithm is presented in full in Appendix 2.

3.2.5 Implementing the standard SIM image reconstruction algorithm

The mathematical process of standard SIM described above, is now explained visually with an example image, simulated microscope PSF, and nine simulated sinusoidal masks, utilising the algorithm in Appendix 2. Using a laptop with an Intel® Core™ i5-2410M CPU@2.30 GHz and 6.00GB RAM and running Windows 7 (64 bit), image reconstructions typically took

approximately 1 - 2 minutes to run, depending on sample image size and the number of figures to be outputted by the MATLAB algorithm.

The example image was the inbuilt MATLAB 'Modified Shepp-Logan' head phantom which is often used to test 2-dimensional image reconstruction algorithms[222,223], image size was 256×256 pixels. The nm-to-pixel ratio was 20; the PSF was defined by the parameters: λ = 500nm, n = 1, NA = 1.49; three mask phases were used, φ_i = 0, $2\pi/3$, $4\pi/3$; three mask orientations were used, $\boldsymbol{p}$ = [1,0; cos(π/3),sin(π/3); cos(2π/3), sin(2π/3)]; the spatial wavelength of the masks was 50nm; the noise parameter, w = 0.1 ; and the width of the desired OTF was half that of the original PSF. These parameters were chosen to optimise the resolution improvement in the final image.

The example image was treated as the ground-truth sample for this algorithm.

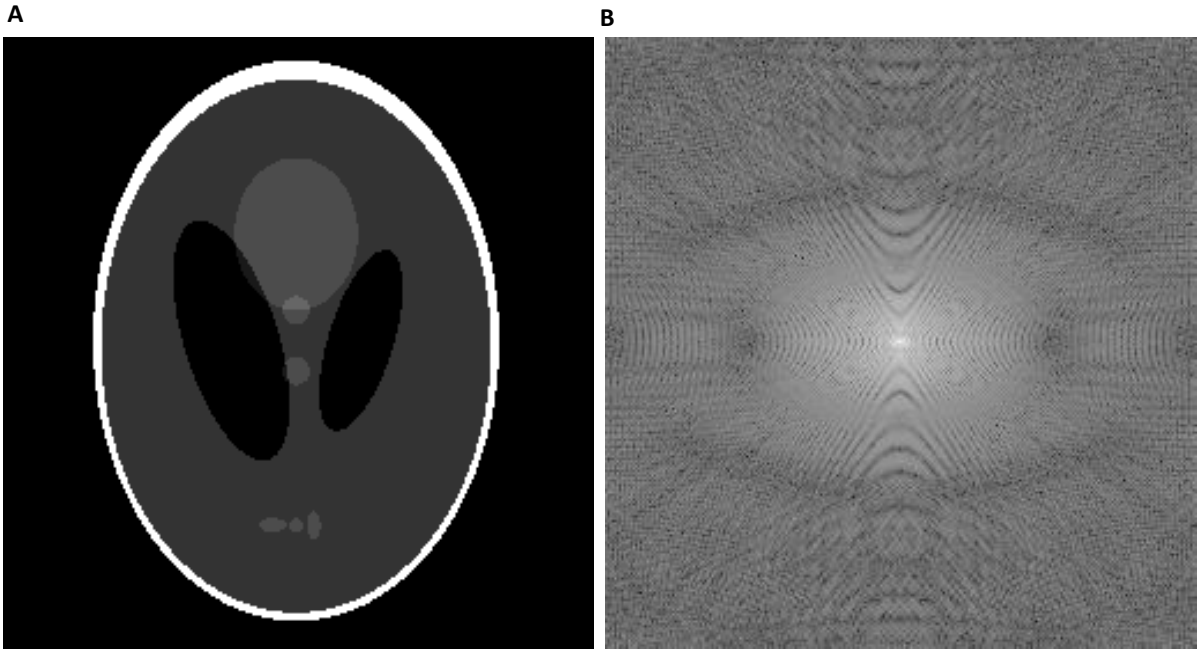

Figure 3.2: A – Ground truth image, 256×256 modified Shepp-Logan phantom from MATLAB; B – Fast Fourier Transform (FFT) of the ground truth image (256×256 pixels).

It was then convolved with the PSF to demonstrate how the sample would appear under a brightfield microscope, the widefield image.

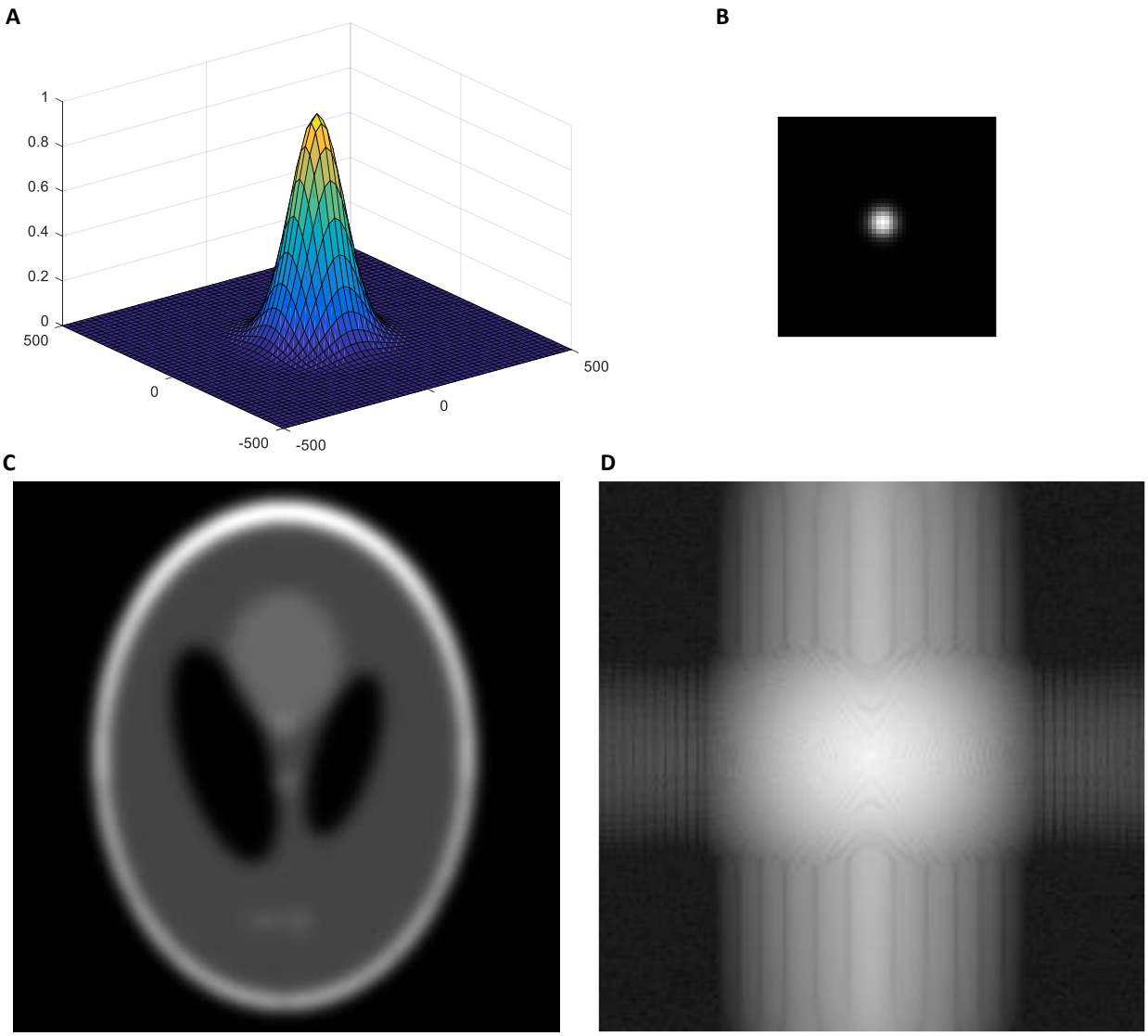

Figure 3.3: A – Point spread function (PSF) used to blur the ground truth image, plotted in units of nm (51×51 pixels); B – FFT of the PSF, giving the optical transfer function (OTF) (51×51 pixels); C – the widefield image, created by convolving the ground truth image with the PSF (256×256 pixels); D – FFT of the widefield image(256×256 pixels).

The masks were then created as sinusoids for the different orientations and phases.

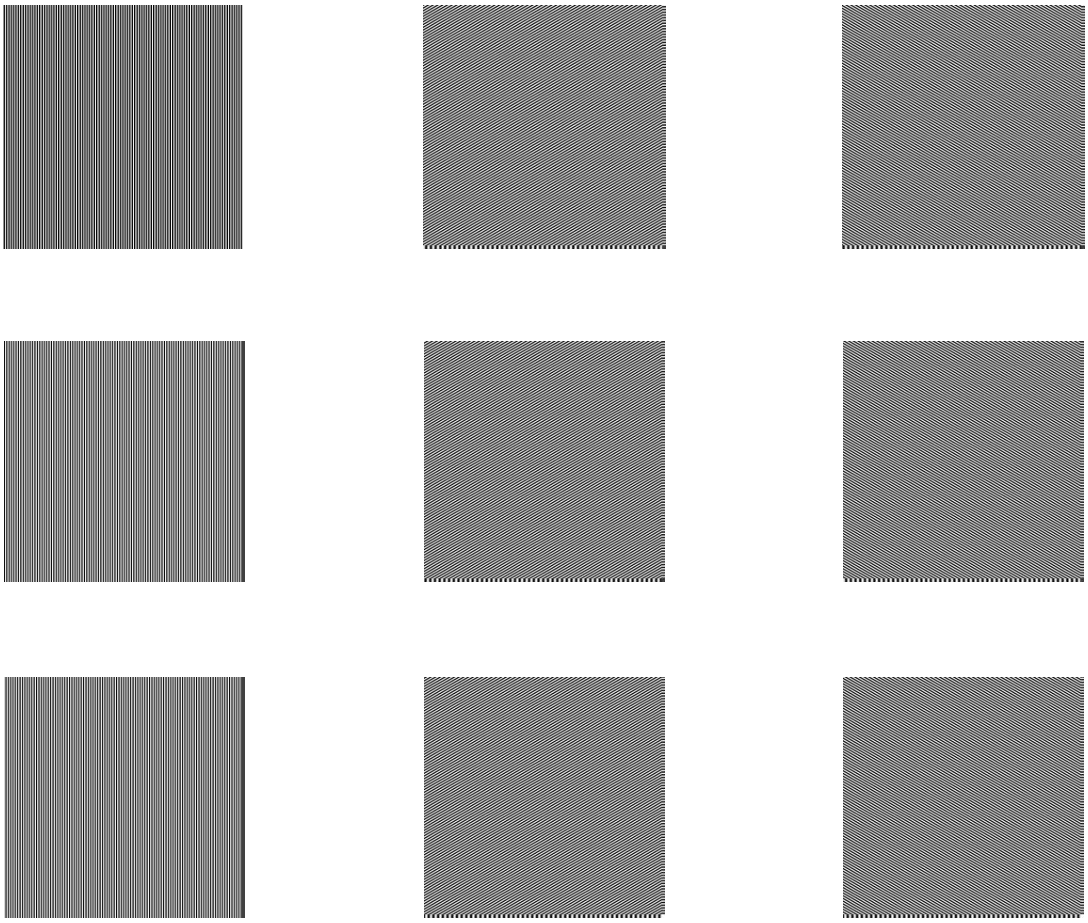

Figure 3.4: The nine masks used (256×256 pixels), created as standard sinusoids using the following parameters: three phases were used, $\varphi_i = 0, 2\pi/3, 4\pi/3$; three mask orientations were used, $\underline{\boldsymbol{p}} = [1,0; \cos(\pi/3),\sin(\pi/3); \cos(2\pi/3), \sin(2\pi/3)]$; the spatial wavelength of the masks was 50nm.

Then the nine images of the masks combined with the widefield image are created, $g_n(\underline{\boldsymbol{x}})$ and $G_n(\underline{\boldsymbol{k}})$.

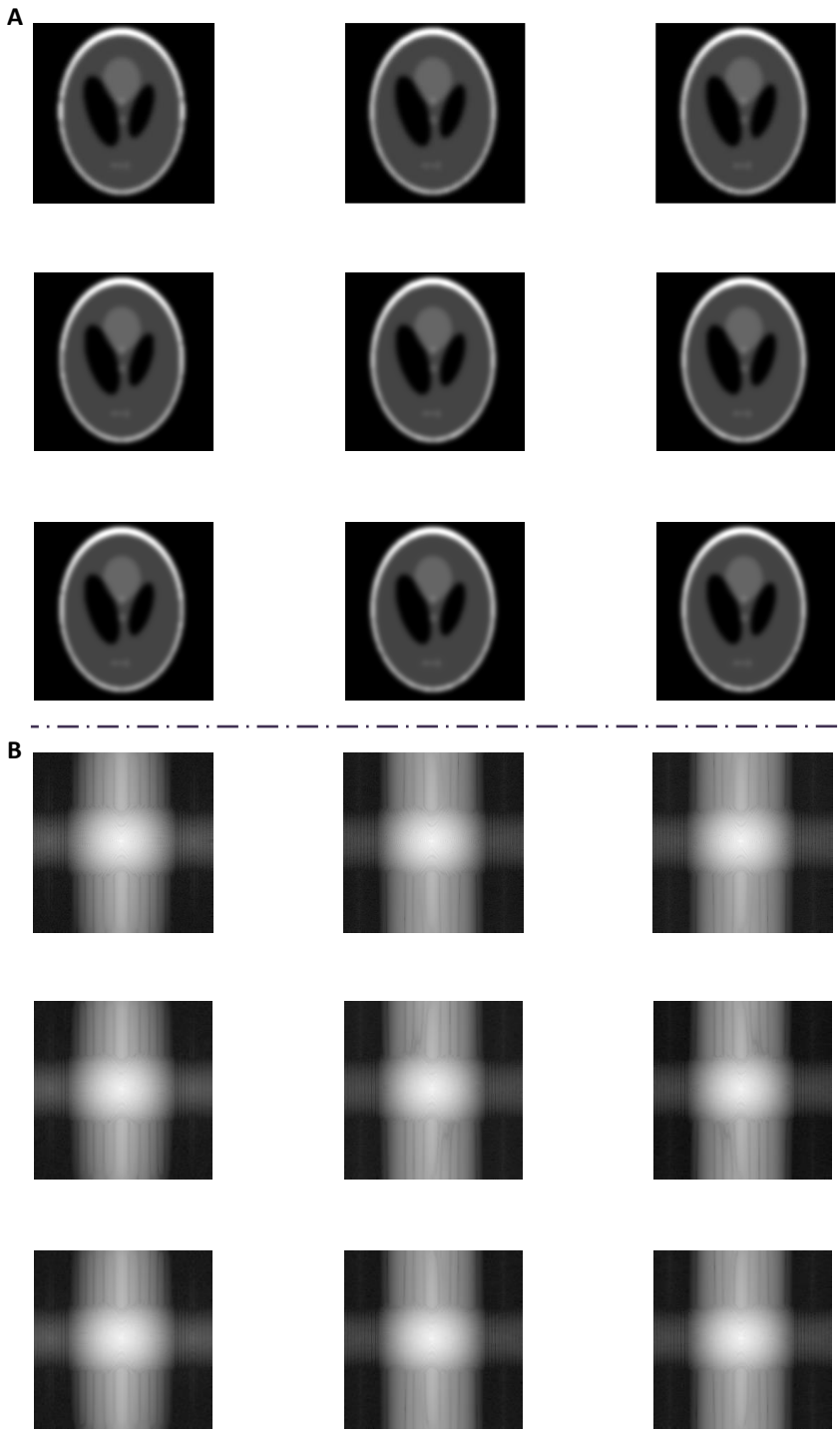

Figure 3.5: A – The nine acquired images (256×256 pixels), created by multiplying the masks and the ground truth image, and then convolving with the PSF; B – Fast Fourier Transform (FFT) of the acquired images (256×256 pixels).

The spectral components of the images in Fourier space can be clearly seen. These components are separated and then shifted, to give the nine $CS_n(\underline{\boldsymbol{k}})$.

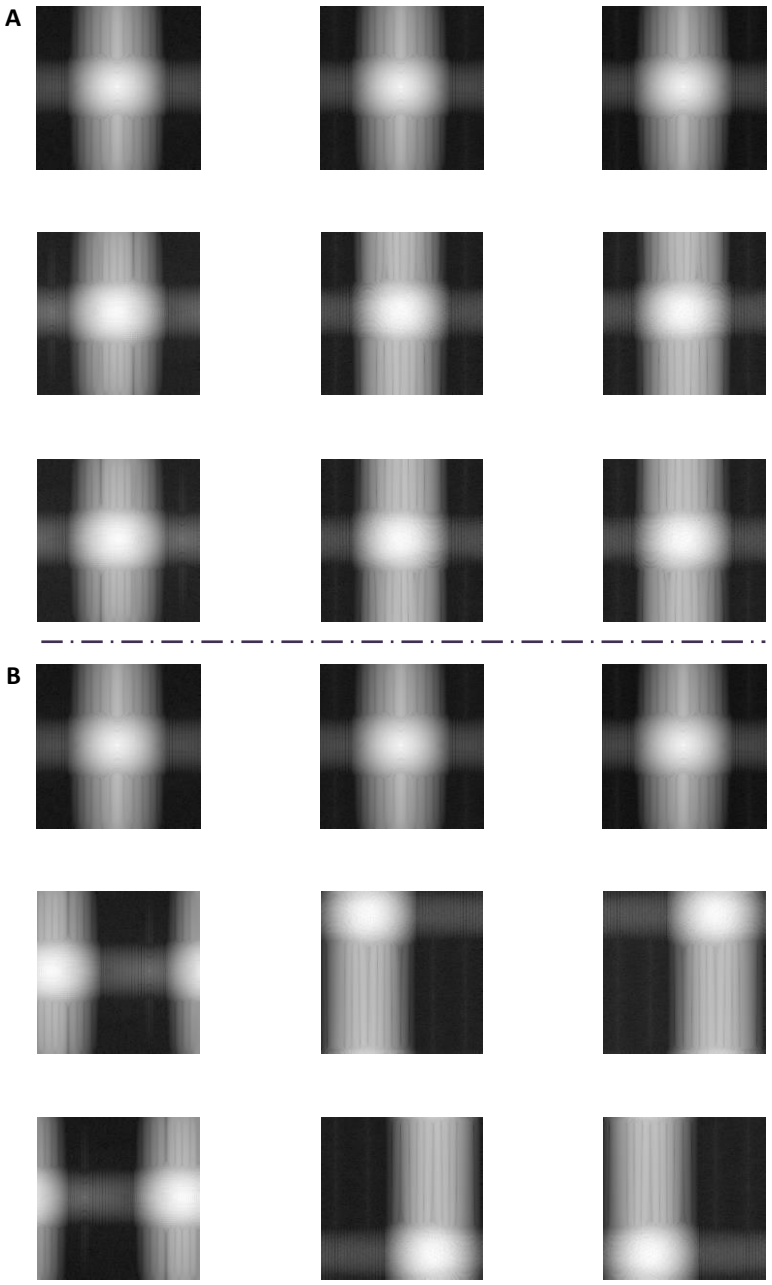

Figure 3.6: A – The nine separated spectral components of the acquired images in Fourier space (256×256 pixels); B – the shifted, separated spectral components of the acquired images in Fourier space (256×256 pixels).

The OTF is also shifted in Fourier space.

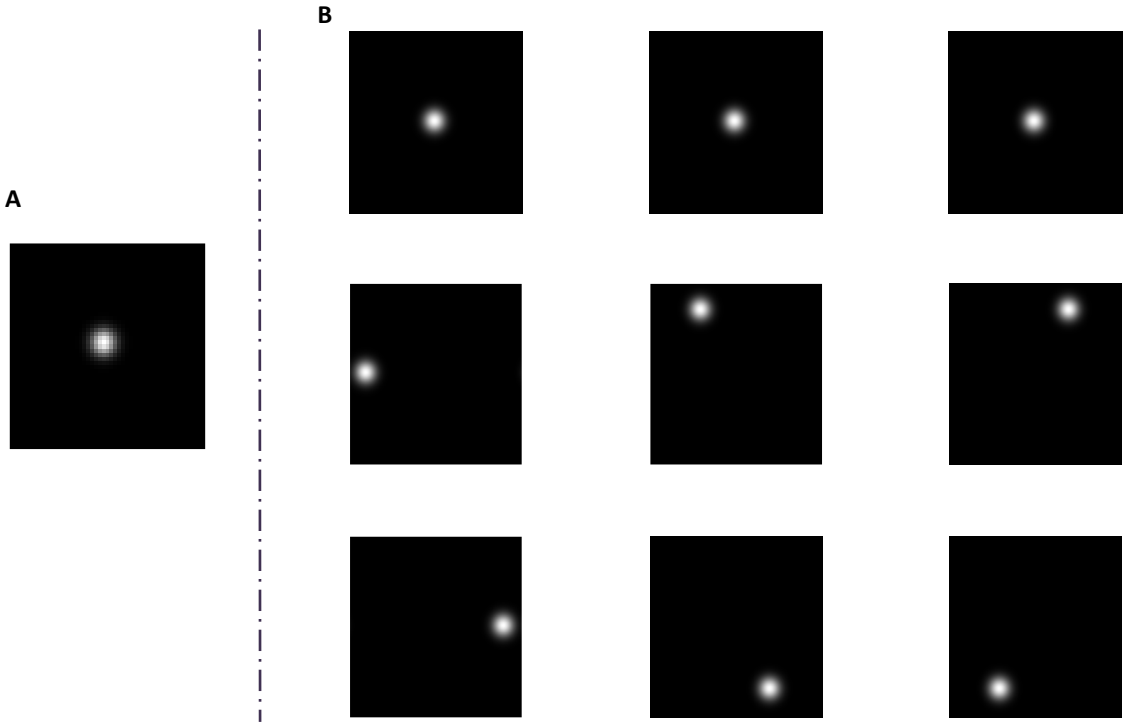

Figure 3.7: A – The original OTF (51×51 pixels); B – the shifted OTFs (256×256 pixels).

The components of the Wiener filter required to reassemble the image are then created.

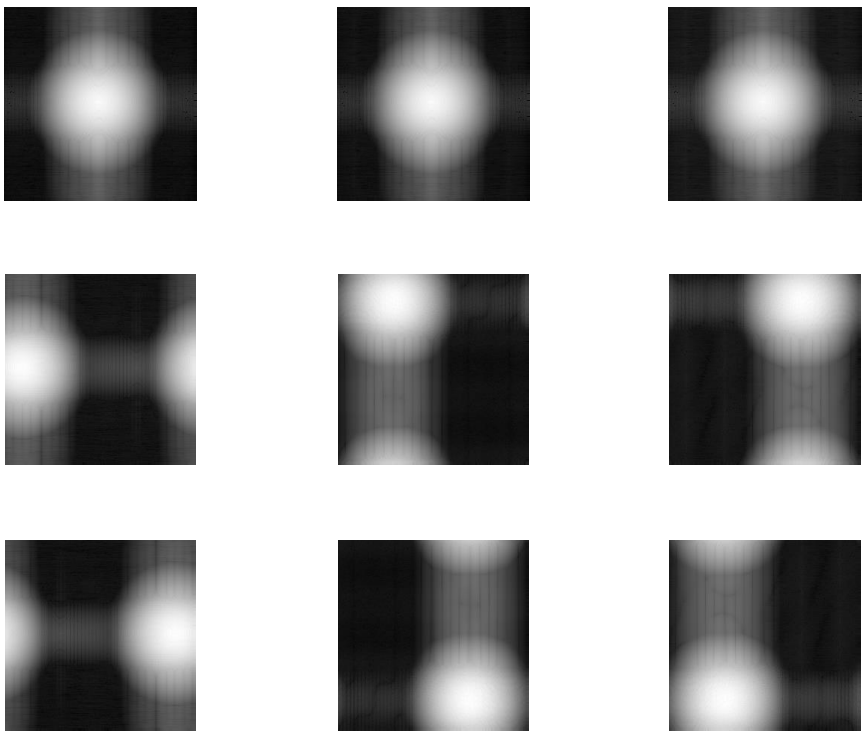

Figure 3.8: The components of the Wiener filter (256×256 pixels).

The image is then apodized with the desired OTF as described above, to give the reconstructed image in Fourier space. This should have a distinct 'flower' shape composed of the different shifted spectra. If the 'petals' of the 'flower' (the shifted components' do not meet around the central unshifted component, then there are gaps in the spectral frequencies that are in the final image, and there will be artefacts. If the 'flower' does not cover a larger area than the original widefield image in Fourier space, then there will not be any resolution improvement in the final image. This 'flower' shape is dictated by the number of images – the number of 'petals' and thus the spectral area covered in Fourier space, which is why at least nine images are recommended as this increases the spectral coverage and thus the amount of higher resolution information retained in the final image; the ***p*** values which dictate the shifts in Fourier space – and thus again the spectral coverage in Fourier space; and the spatial wavelength of the masks - too small a spatial wavelength results in gaps in the 'flower', and too large a spatial wavelength means that the 'flower' covers a smaller spectral area in Fourier space and the resolution improvement will be smaller.

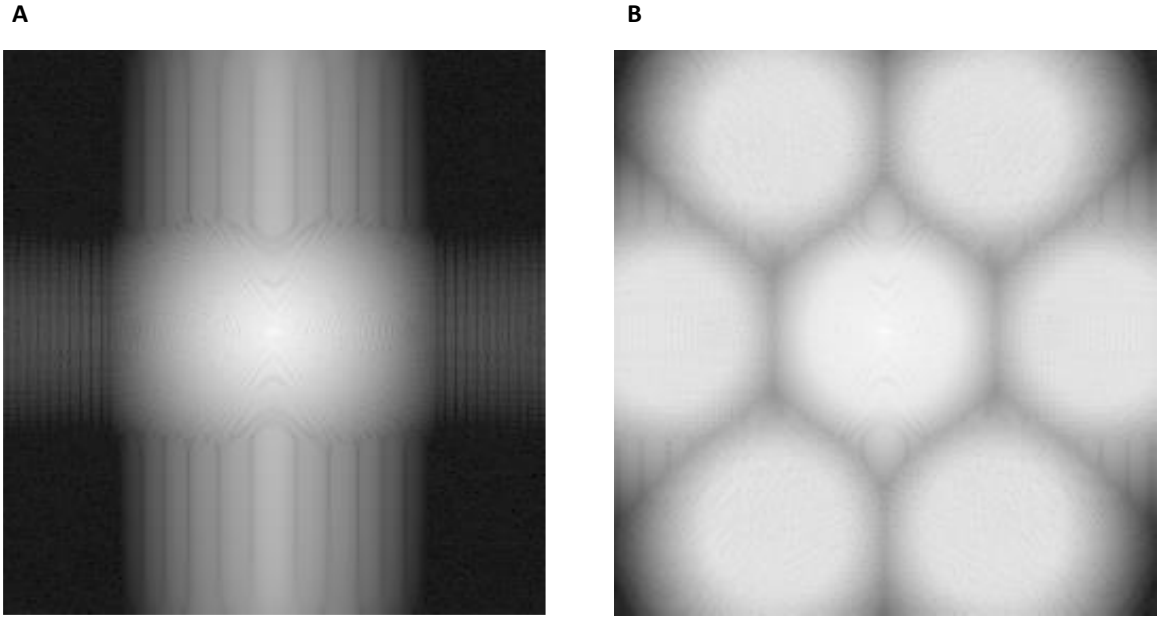

Figure 3.9: A – The widefield image in Fourier space (256×256 pixels); B – the reconstructed image in Fourier space (256×256 pixels).

This is then finally converted back into real space to give the reconstructed image with improved resolution.

Figure 3.10: The final reconstructed image (256×256 pixels).

By comparing the sample image, the widefield image, and the reconstructed image together, the resolution improvement is clear.

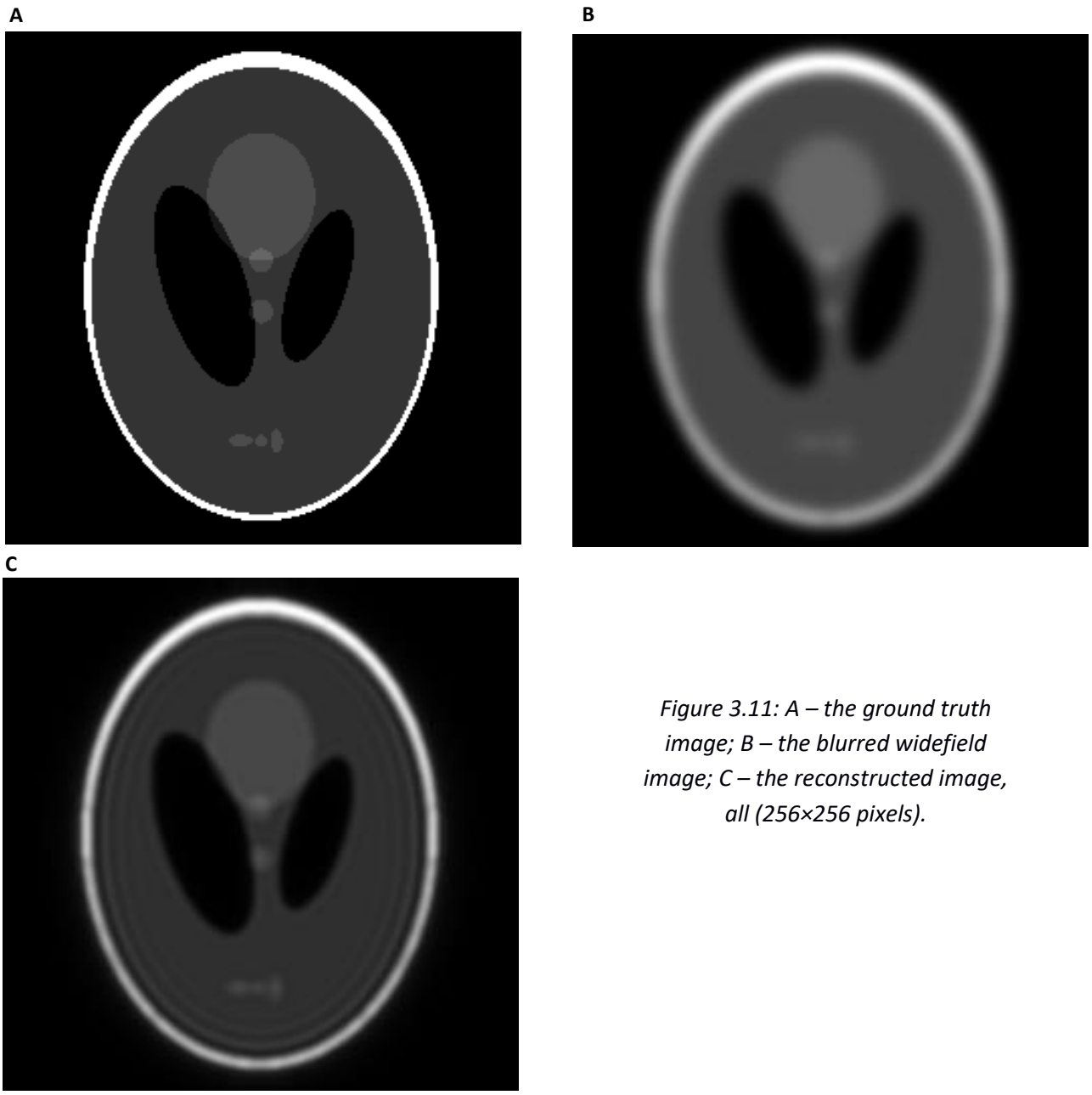

Figure 3.11: A – the ground truth image; B – the blurred widefield image; C – the reconstructed image, all (256×256 pixels).

There is definite resolution improvement in the reconstructed image compared to the widefield image, particularly in resolving the set of three grey shapes near the bottom of the image. However, there are distinct artefacts, a common problem in SIM

imaging[39,40,113,123,124]. Further image processing, or refining of the reconstruction parameters, could ameliorate the artefacts.

3.2.6 Further results

This standard SIM algorithm was then also tested using a more "realistic" sample image. The phantom used has an unusual structure in k-space because of it large blocky areas and sharp edges. This image is more typical: an image of a sample of human platelets spread on a glass coverslip and stained for F-actin using phalloidin, provided by Dr Steve Thomas of the Institute of Cardiovascular Sciences, Institute of Biomedical Research, University of Birmingham, UK. The image size was 256×256 pixels. The nm-to-pixel ratio was 20; the PSF was defined by the parameters: λ = 500nm, n = 1, NA = 1.49; three mask phases were used, φ_i = 0, $2\pi/3$, $4\pi/3$; two mask orientations were used, $\underline{\boldsymbol{p}}$ = [1,0; 0,1]; the spatial wavelength of the masks was 50nm; the noise parameter, w = 0.1 ; and the width of the desired OTF was half that of the original PSF. These parameters were chosen to optimise the resolution improvement in the final image.

The results are detailed below:

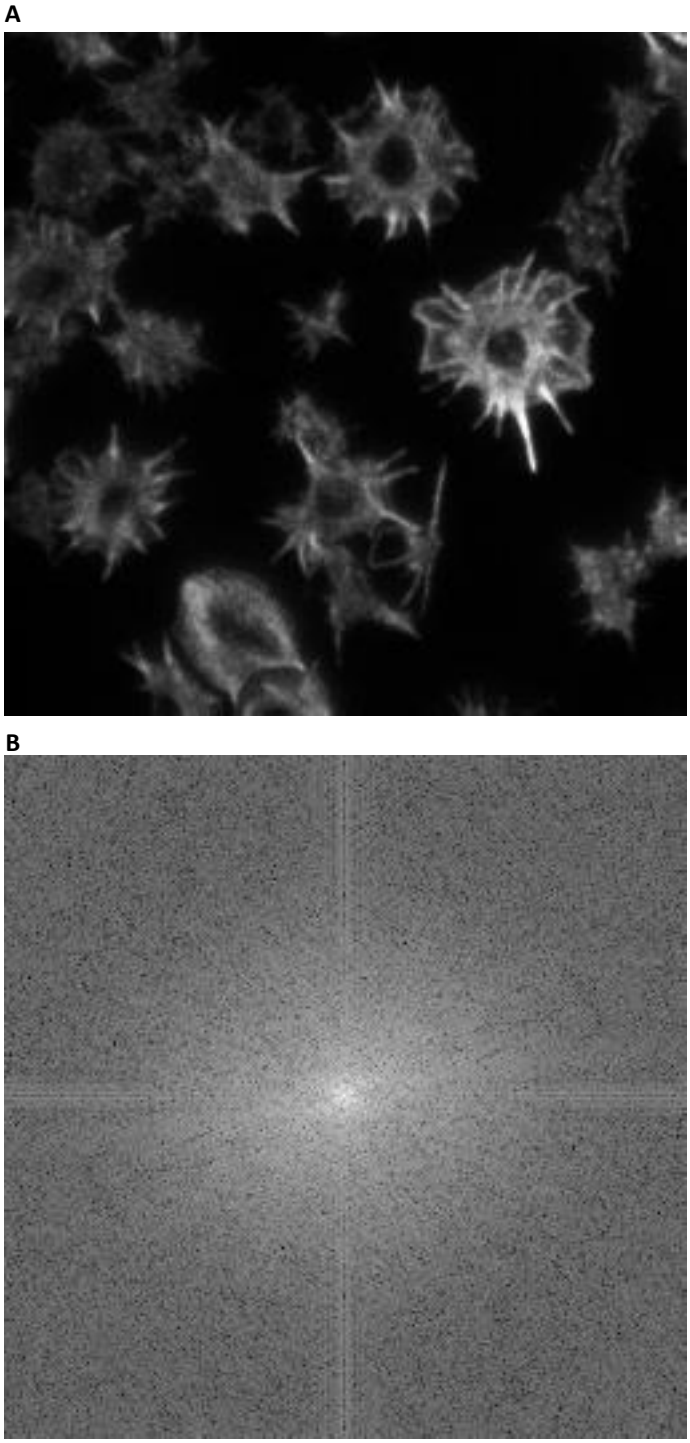

Figure 3.12: A – Ground truth image, 256×256 image of platelets courtesy of Dr Steve Thomas, University of Birmingham, UK; B – Fast Fourier Transform (FFT) of the ground truth image (256×256 pixels).

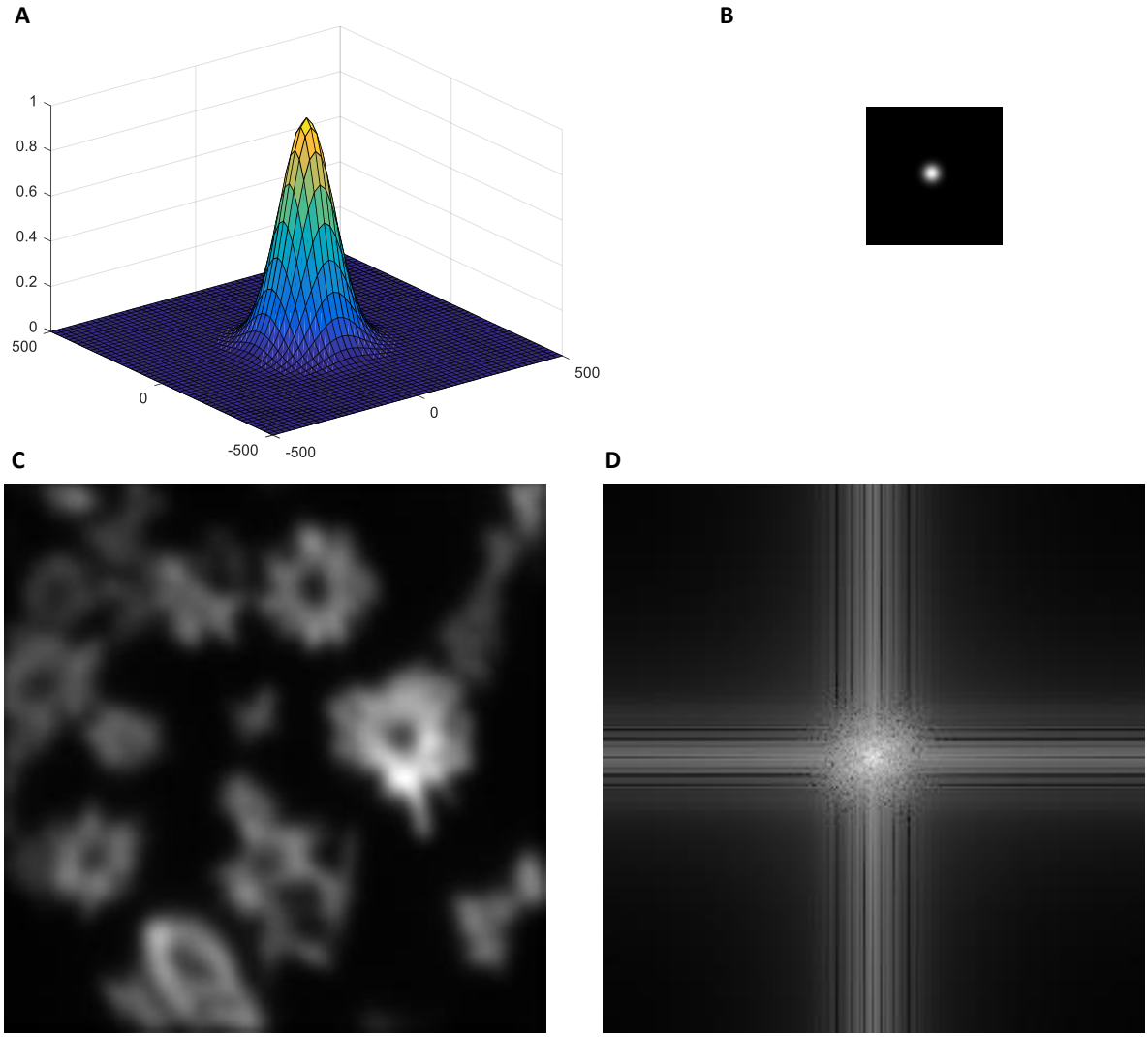

Figure 3.13: A – Point spread function (PSF) used to blur the ground truth image, plotted in units of nm (51×51 pixels); B – FFT of the PSF, giving the optical transfer function (OTF) (51×51 pixels); C – the widefield image, created by convolving the ground truth image with the PSF (256×256 pixels); D – FFT of the widefield image (256×256 pixels).

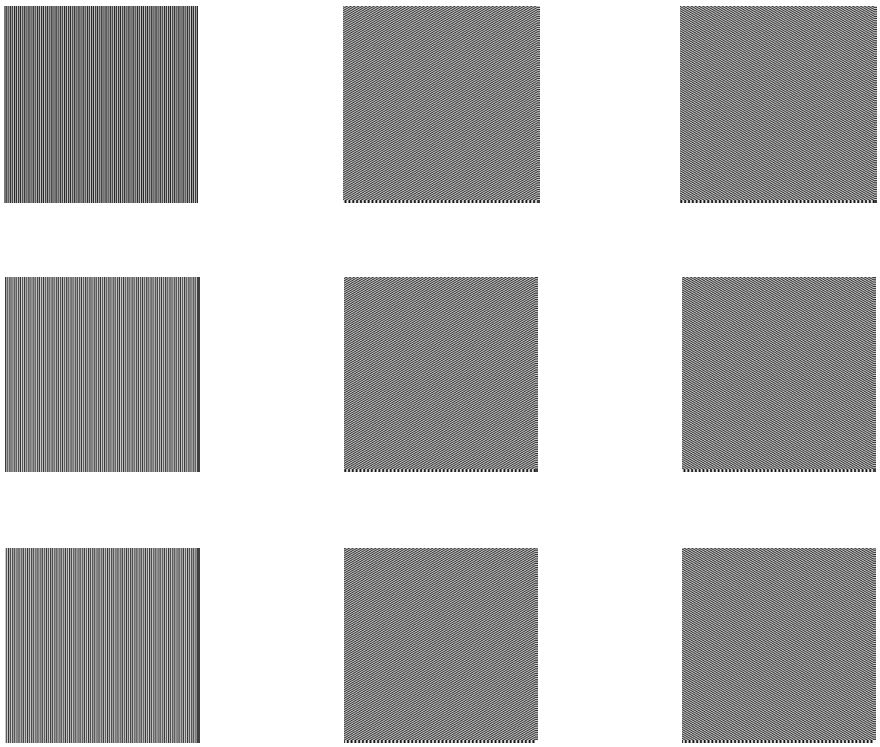

Figure 3.14: The nine masks used (256×256 pixels), created as standard sinusoids using the following parameters: three phases were used, $\varphi_i = 0, 2\pi/3, 4\pi/3$; three mask orientations were used, $\underline{\boldsymbol{p}} = [1,0; \cos(\pi/3),\sin(\pi/3); \cos(2\pi/3), \sin(2\pi/3)]$; the spatial wavelength of the masks is 50nm.

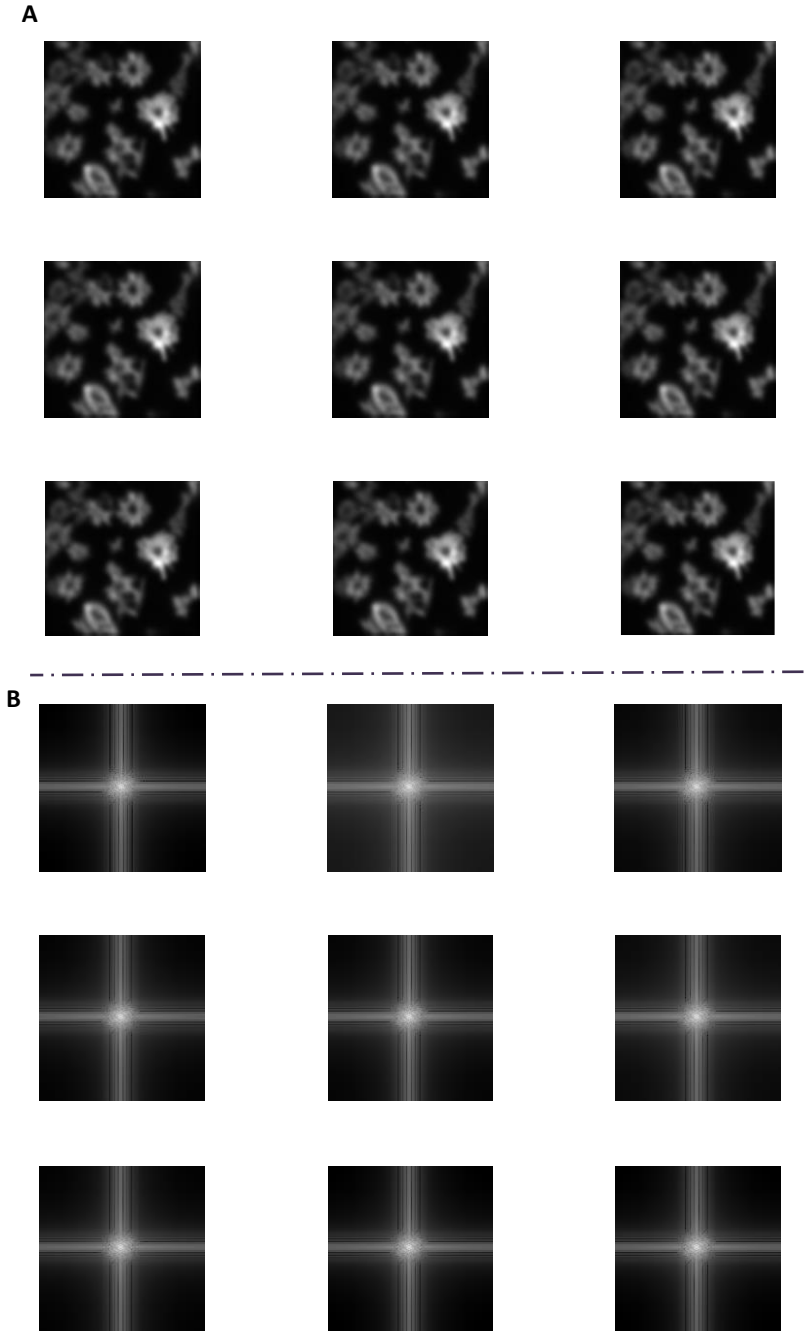

Figure 3.15: A – The nine acquired images (256×256 pixels), created by multiplying the masks and the ground truth image, and then convolving with the PSF; B – Fast Fourier Transform (FFT) of the acquired images (256×256 pixels).

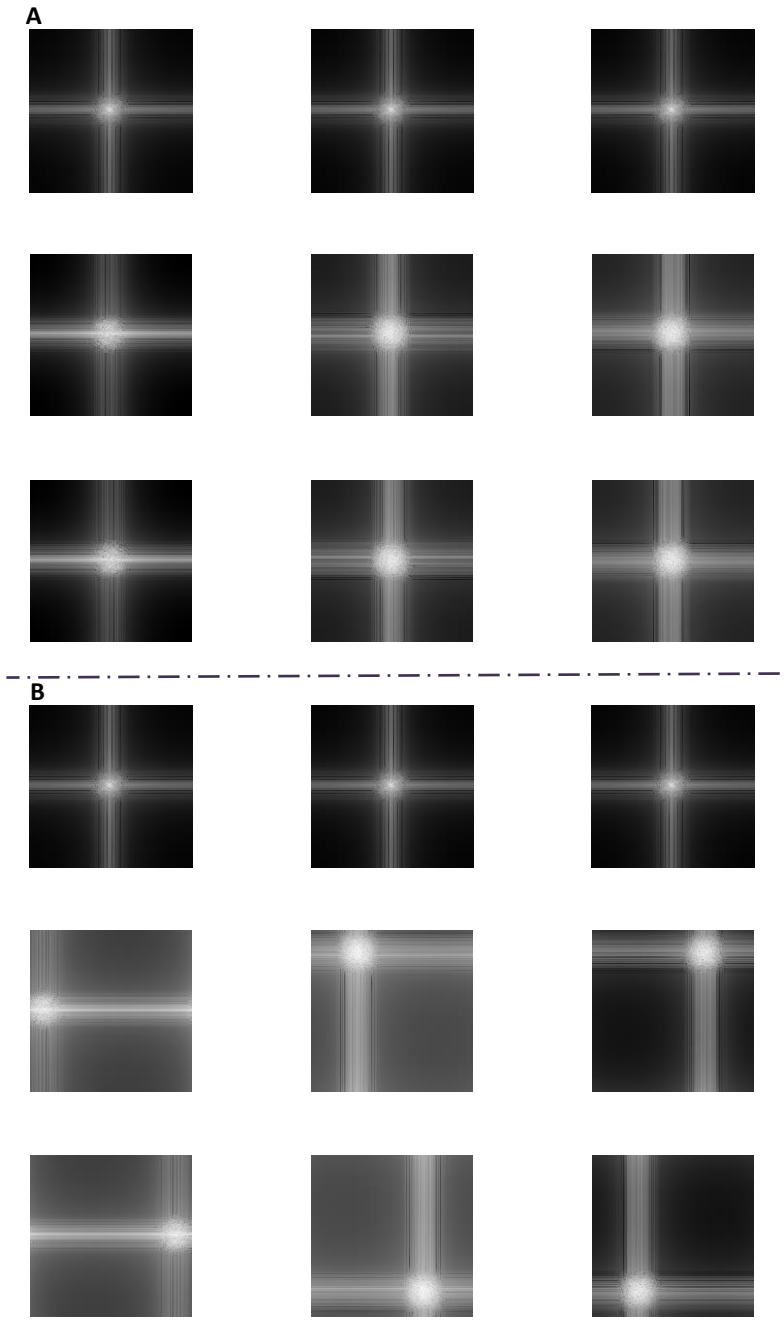

Figure 3.16: A – The nine separated spectral components of the acquired images in Fourier space (256×256 pixels); B – the shifted, separated spectral components of the acquired images in Fourier space (256×256 pixels).

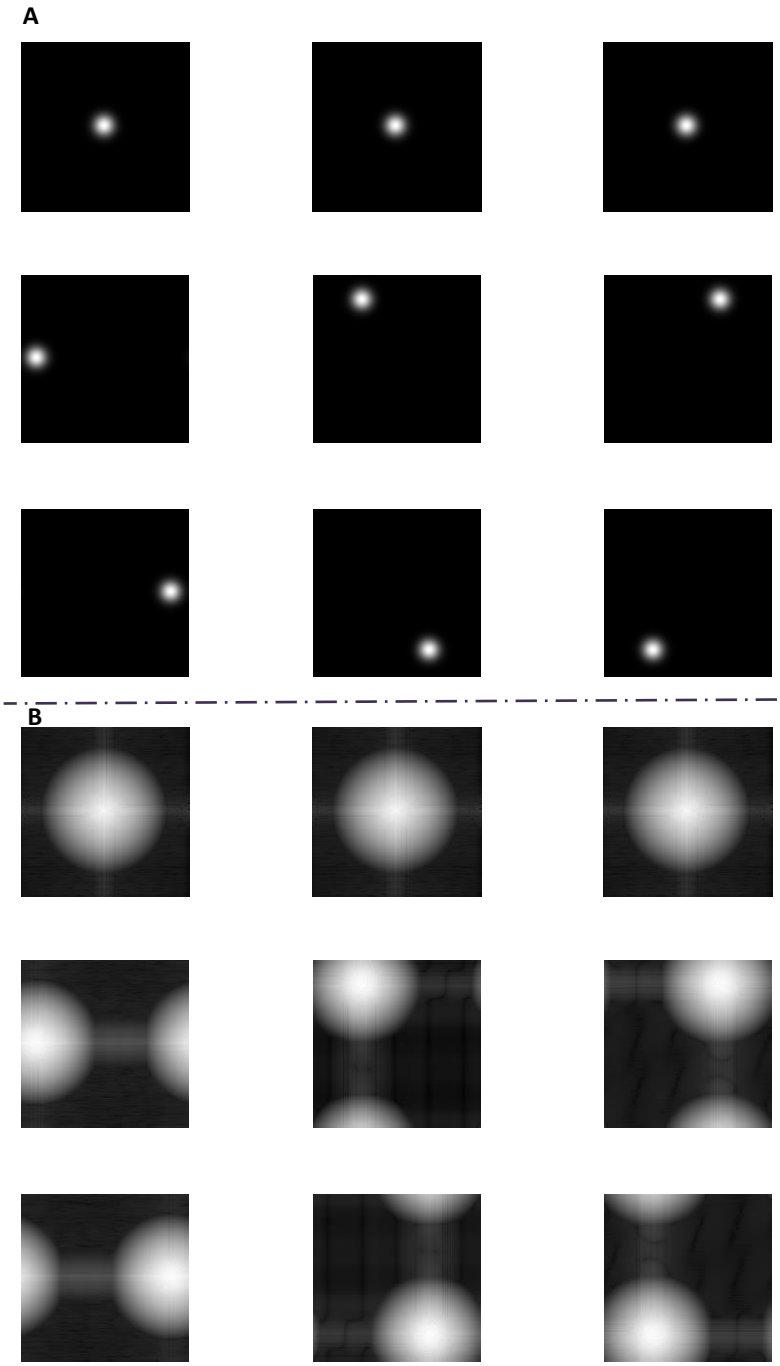

Figure 3.17: A – the shifted OTFs (256×256 pixels); B – the components of the Wiener filter (256×256 pixels).

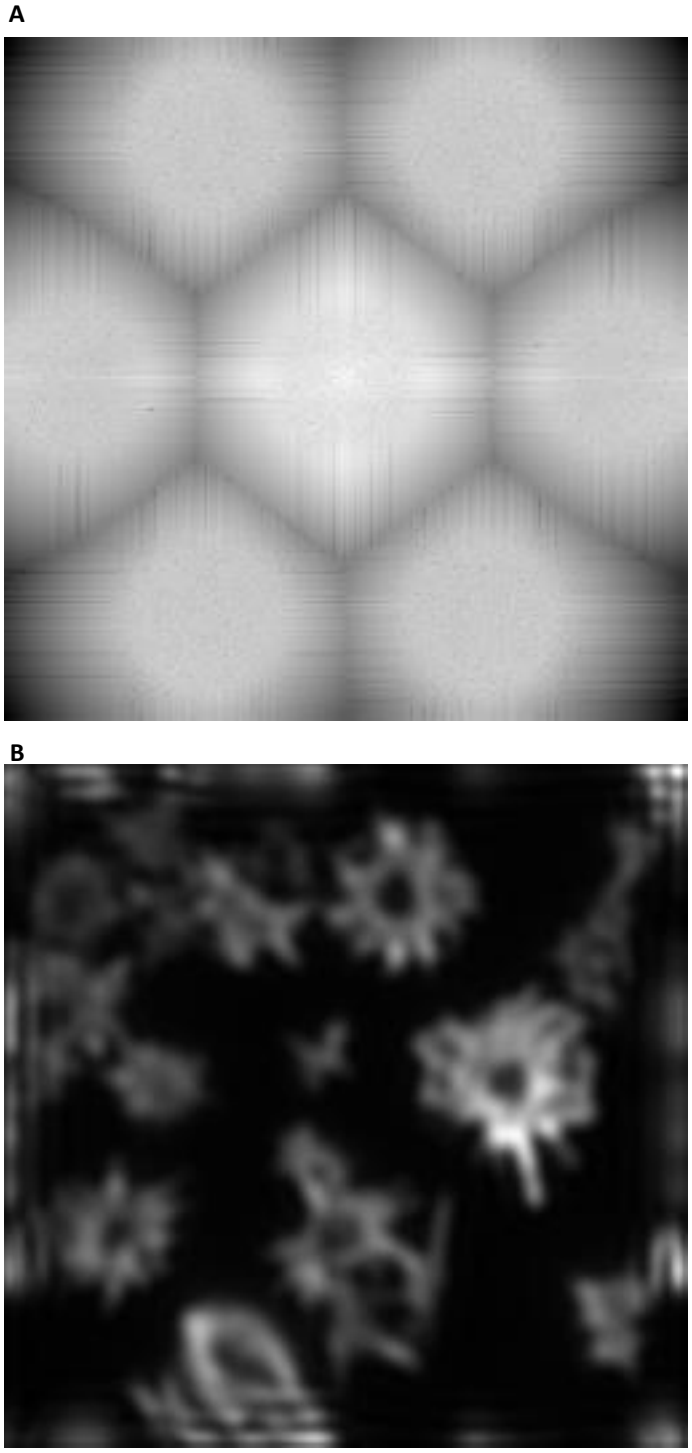

Figure 3.18: A - the reconstructed image in Fourier space (256×256 pixels); B – the final reconstructed image (256×256 pixels).

It can be seen that the nine components are successfully separated and shifted in Fourier space. This results in the typical ‘flower’ shape in the FFT of the reconstructed image, demonstrating a successful Sim reconstruction. Moreover, as more of Fourier space is covered by the reconstructed image than by the widefield image, as a result of the shifts, resolution improvement should be seen. An improvement in resolution can clearly be seen in the reconstructed image, and is further demonstrated below.

There is clear resolution improvement from the widefield image to the reconstructed image. Thus demonstrating the success of the standard SIM reconstruction algorithm.

A

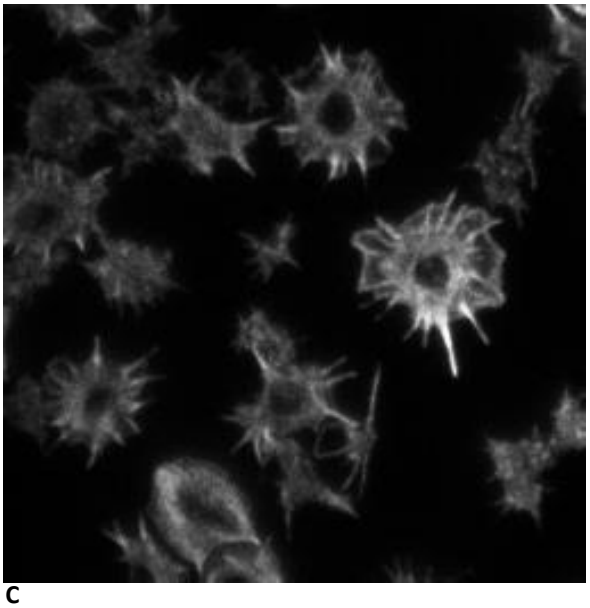

B

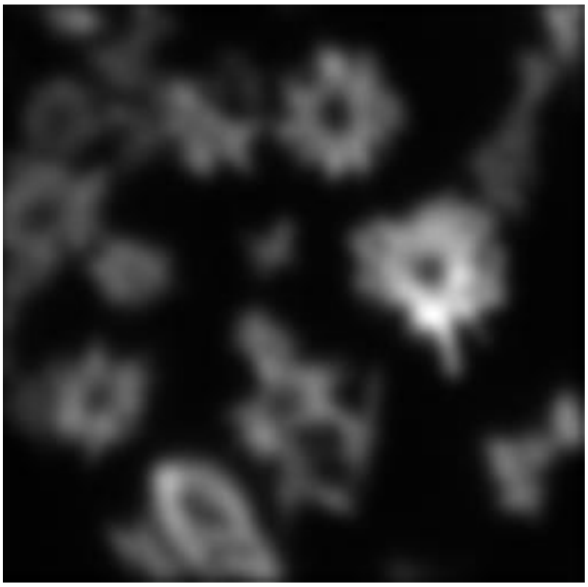

C

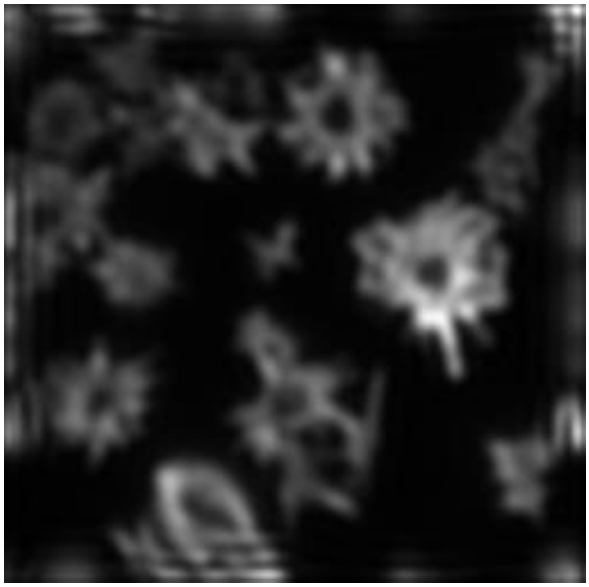

Figure 3.19: A – the ground truth image; B – the blurred widefield image; C – the reconstructed image, all (256×256 pixels).

3.2.7 The metamaterial patterns

The next stage in the research was to apply the masks produced by the metamaterial design in simulation. From the simulation work performed in CST MWS, it was possible to create six potential SIM masks. These comprise three phases, 0, 2π/3 and 4π/3, created by changing the polarisation of the incident light, 0, 2π/3 and 4π/3 with respect to the original linear polarised light, and two orientations, created by rotating the metamaterial 0° and 90°. Ideally nine such masks would have been produced, but it was not possible to achieve the three orientations required for this, discussed in greater detail in Chapter 2. However, the lack of patterns may be ameliorated somewhat by the increased complexity of the pattern. There were two sets of the six patterns, created using different frequencies of incident light – 200 and 470THz. These sets of masks are shown below, see figures 3.20 and 3.21.

It can be seen that for both sets of masks, they are very close to being the simple sinusoid typically used in SIM reconstruction, and demonstrated in *Section 3.2.5*. The masks produced at 470THz are sinusoidal in profile, however the spatial frequency of the sinusoid changes from 300nm for the 0 phase masks, to 600nm for the other two phases. This limits their use within a standard SIM reconstruction algorithm as the spatial wavelength should be constant, as it affects the coefficient of the orientations of the masks within the algorithm. In contrast, the spatial wavelength of the 200THz masks does not change, it is 600nm. Yet, the masks are not as sinusoidal as for 470THz. In particular the 0 phase masks have a distinct second component, spatial wavelength 300nm. This again makes SIM reconstruction challenging with the standard SIM reconstruction algorithm, as it models the masks as a simple sinusoid, which affects the separation and shifting of the components.

Both sets of masks have flaws that could potentially impact the quality of SIM reconstruction. It was decided to continue forward with the masks produced using 200THz incident light. This was because it was felt that the deviation from a simple sinusoid for some of the masks, would have less impact on the final reconstructed image than a change in spatial wavelength. However this did mean using a longer spatial wavelength overall, which means that resolution enhancement would be smaller.

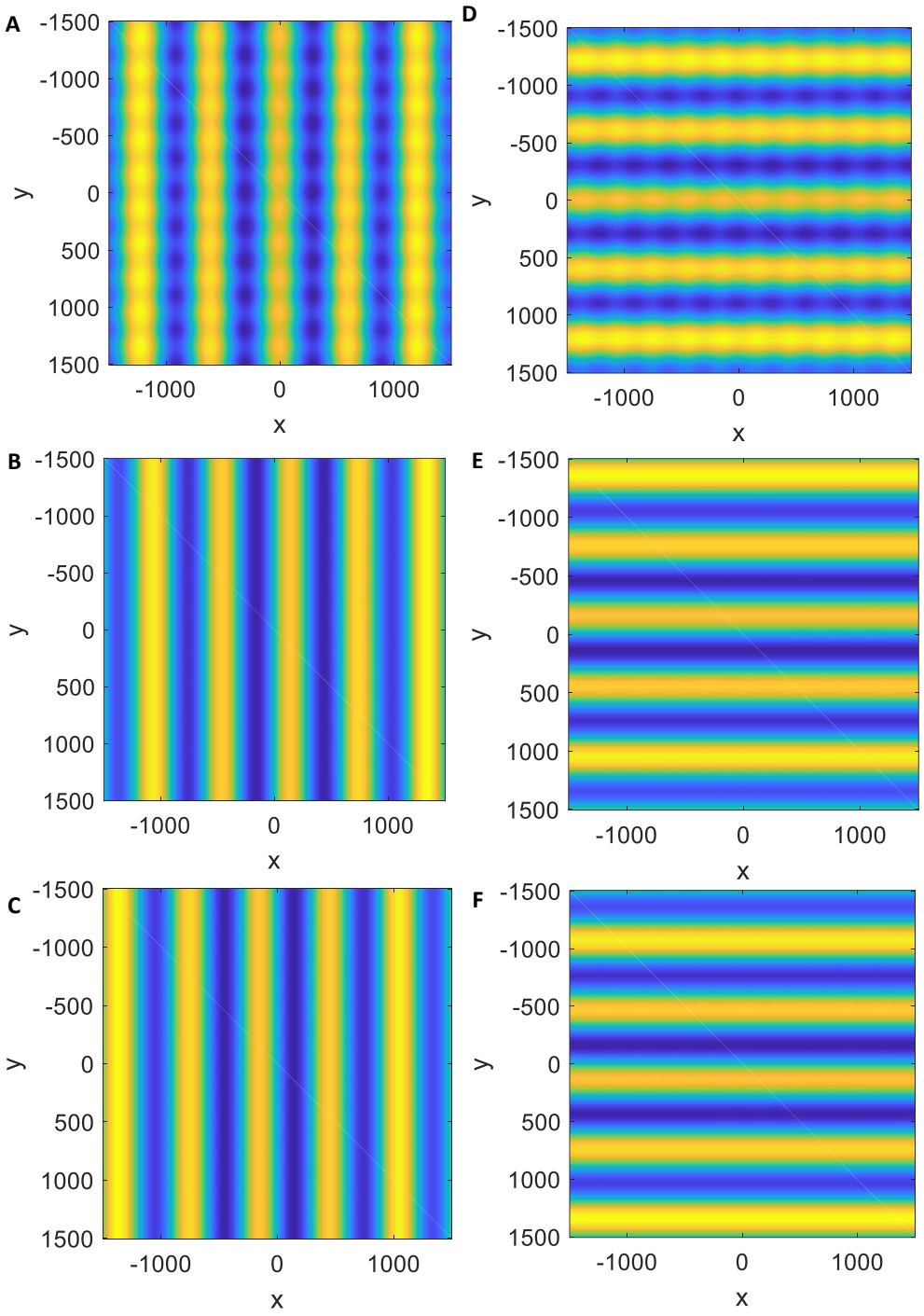

Figure 3.20: The set of six metamaterial produced SIM masks for incident frequency 200THz. A, B, C – are for 0° rotation, orientation [0,1], phases 0, 2π/3 and 4π/3 respectively; D, E, F – are for 90° rotation, orientation [1,0], phases 0, 2π/3 and 4π/3 respectively.

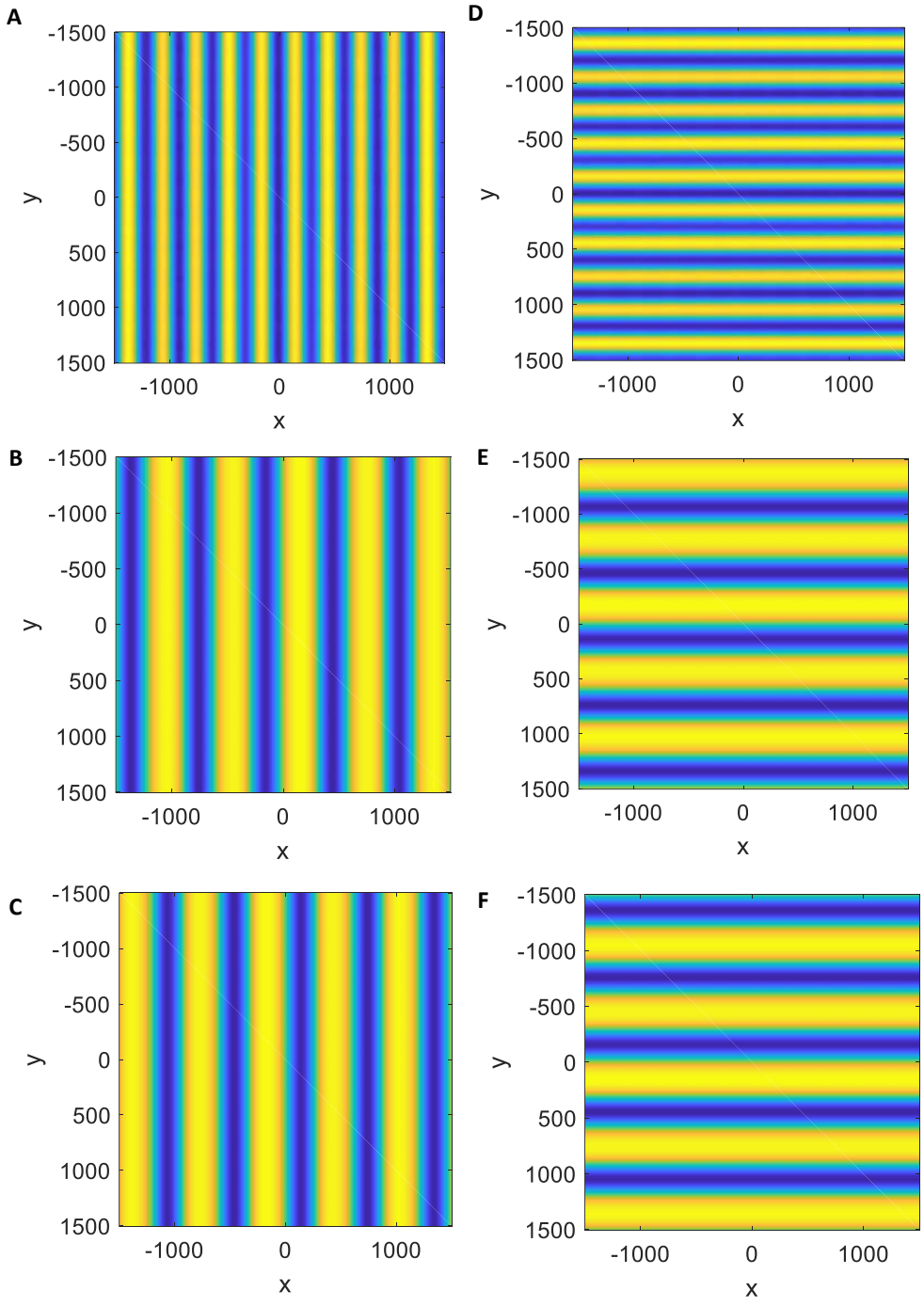

Figure 3.21: The set of six metamaterial produced SIM masks for incident frequency 470THz. A, B, C – are for 0° rotation, orientation [0,1], phases 0, 2π/3 and 4π/3 respectively; D, E, F – are for 90° rotation, orientation [1,0], phases 0, 2π/3 and 4π/3 respectively.

3.2.8 Using non-standard patterns in standard SIM

The standard SIM algorithm is now demonstrated using the atypical (non-sinusoidal) masks from the metamaterial patterns described in *Section* 3.2.7, specifically the 200THz x-polarised structured pattern, which has two distinct sinusoidal components, see figure 3.20 above. This was in order to determine how well the standard SIM reconstruction algorithm can reconstruct utilising masks that are not perfect sinusoids. The same example image scaled to the metamaterial masks, and simulated microscope PSF were used, utilising the algorithm in Appendix 3. However as the metamaterial only produces six patterns, fewer patterns were utilised, and the parameters were altered to match those of the metamaterial masks. The nm-to-pixel ratio was 20; the PSF was defined by the parameters: λ = 500nm, n = 1, NA = 1.49; three mask phases were used, $\varphi_i = 0, 2\pi/3, 4\pi/3$; two mask orientations were used, $\underline{\boldsymbol{p}} = [1,0; 0,1]$; the spatial wavelength of the masks was 600nm; the noise parameter, $w = 1$; and the width of the desired OTF was half that of the original PSF.

The results are as follows:

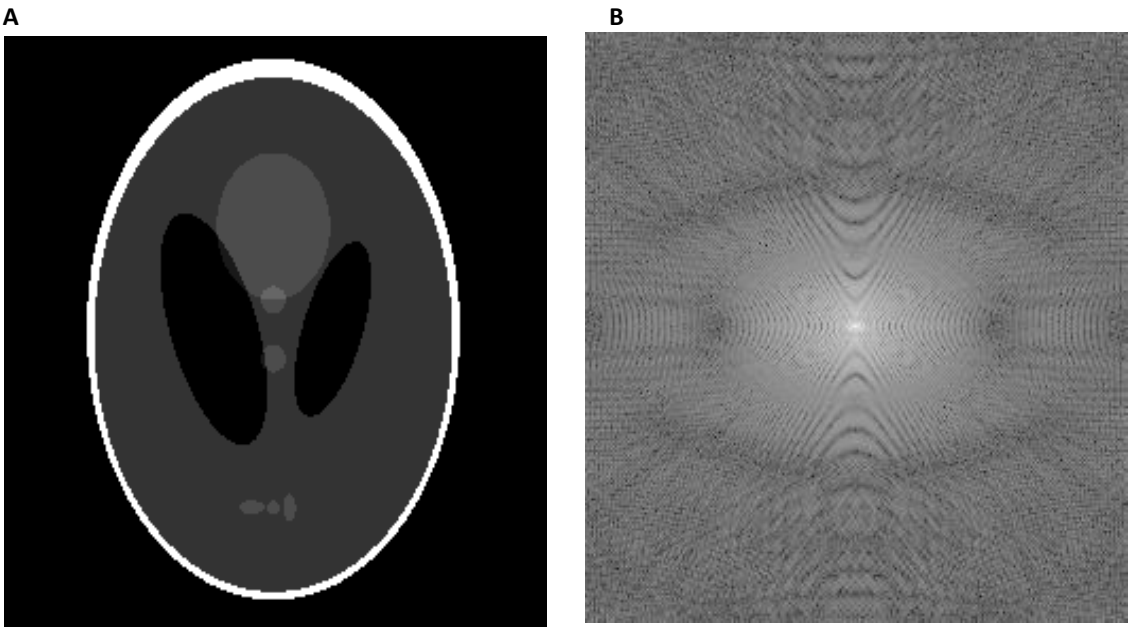

Figure 3.22: A – Ground truth image, 301×301 modified Shepp-Logan phantom from MATLAB; B – Fast Fourier Transform (FFT) of the ground truth image (301×301 pixels).

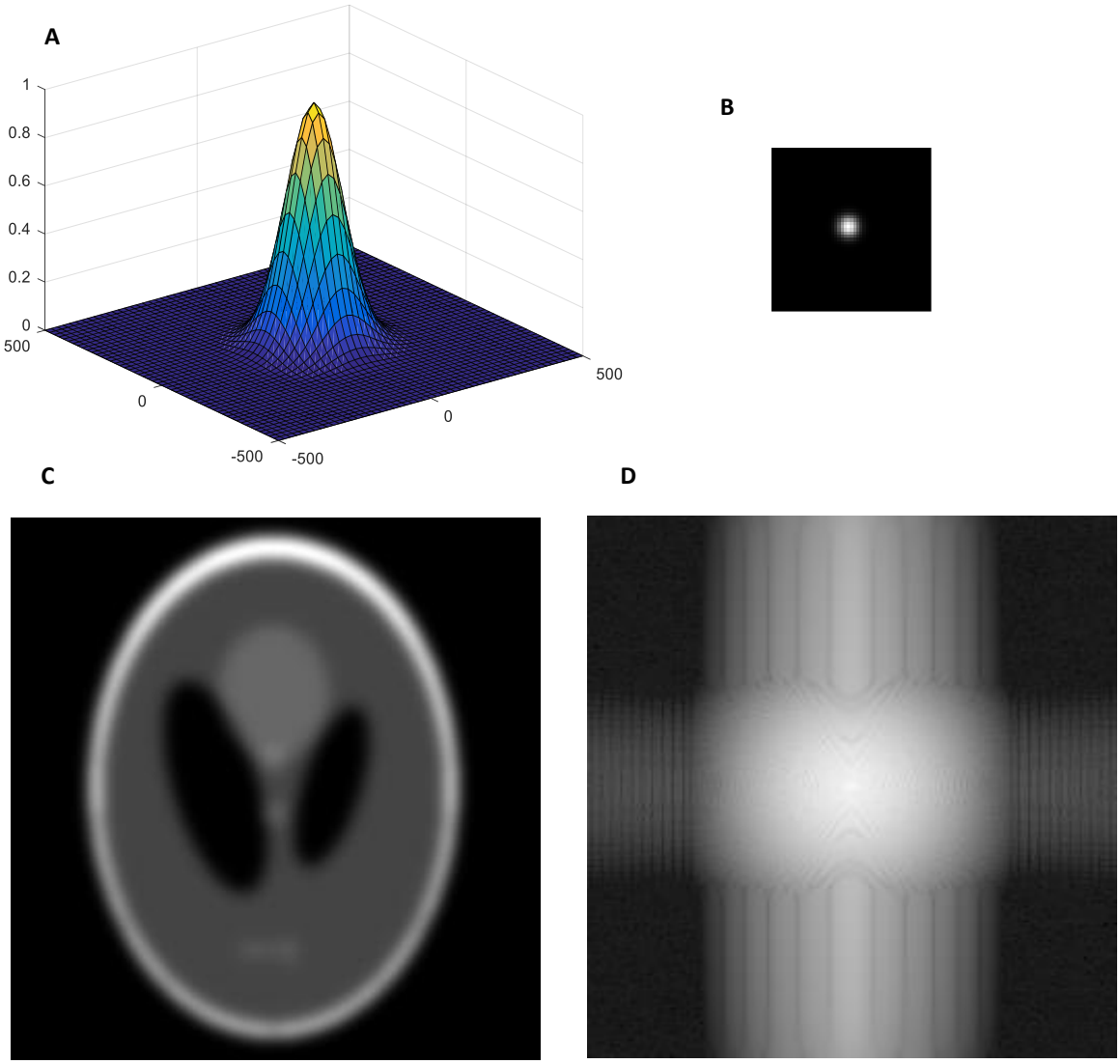

Figure 3.23: A – Point spread function (PSF) used to blur the ground truth image, plotted in units of nm (51×51 pixels); B – FFT of the PSF, giving the optical transfer function (OTF) (51×51 pixels); C – the widefield image, created by convolving the ground truth image with the PSF (301×301 pixels); D – FFT of the widefield image (301×301 pixels).

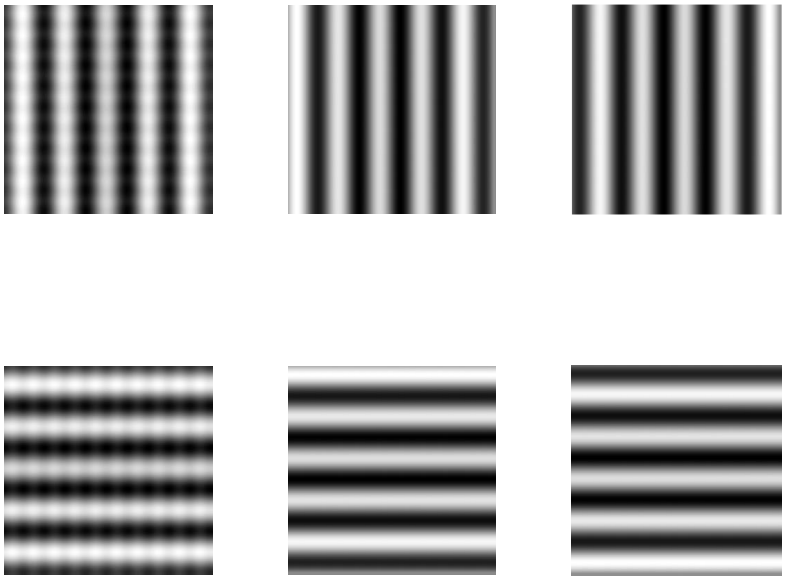

Figure 3.24: A - The six masks used (301×301 pixels), created in simulation using the metamaterial design seen in Chapter 2: three phases were used, $\varphi_i = 0, 2\pi/3, 4\pi/3$; two mask orientations were used, $\underline{\mathbf{p}} = [1,0; 0,1]$; the spatial wavelength of the masks was 600nm.

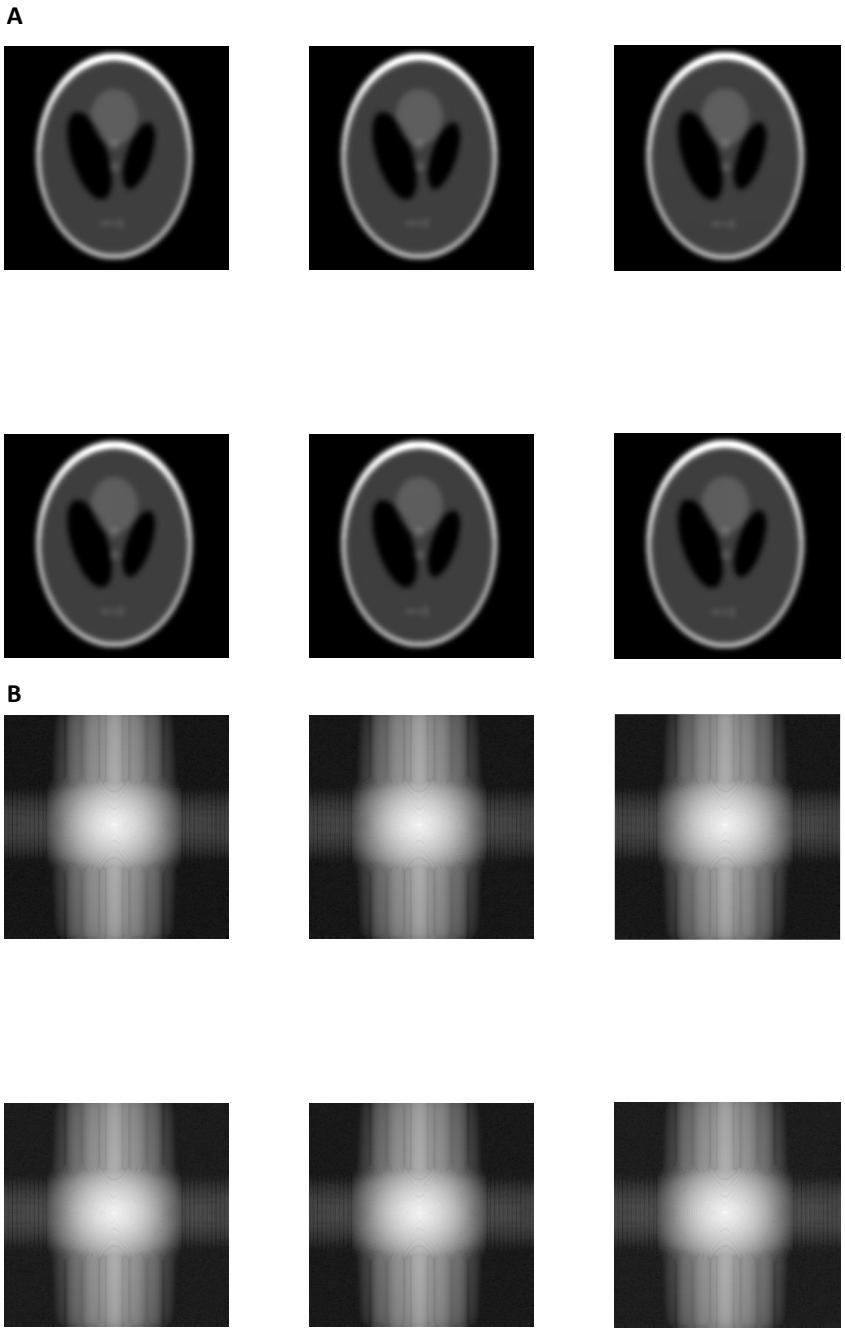

Figure 3.25: A – The six acquired images (301×301 pixels), created by multiplying the masks and the ground truth image, and then convolving with the PSF; B – Fast Fourier Transform (FFT) of the acquired images (301×301 pixels).

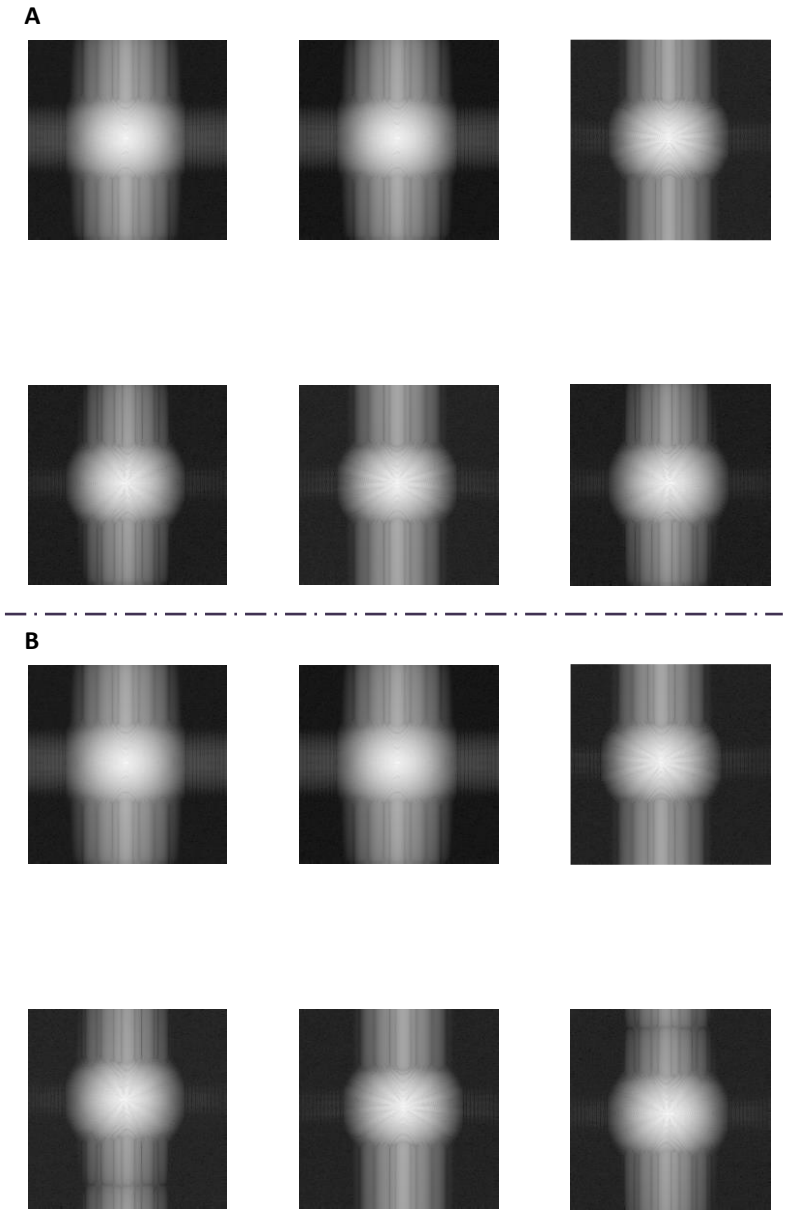

Figure 3.26: A – The six separated spectral components of the acquired images in Fourier space (301×301 pixels); B – the shifted, separated spectral components of the acquired images in Fourier space (301×301 pixels).

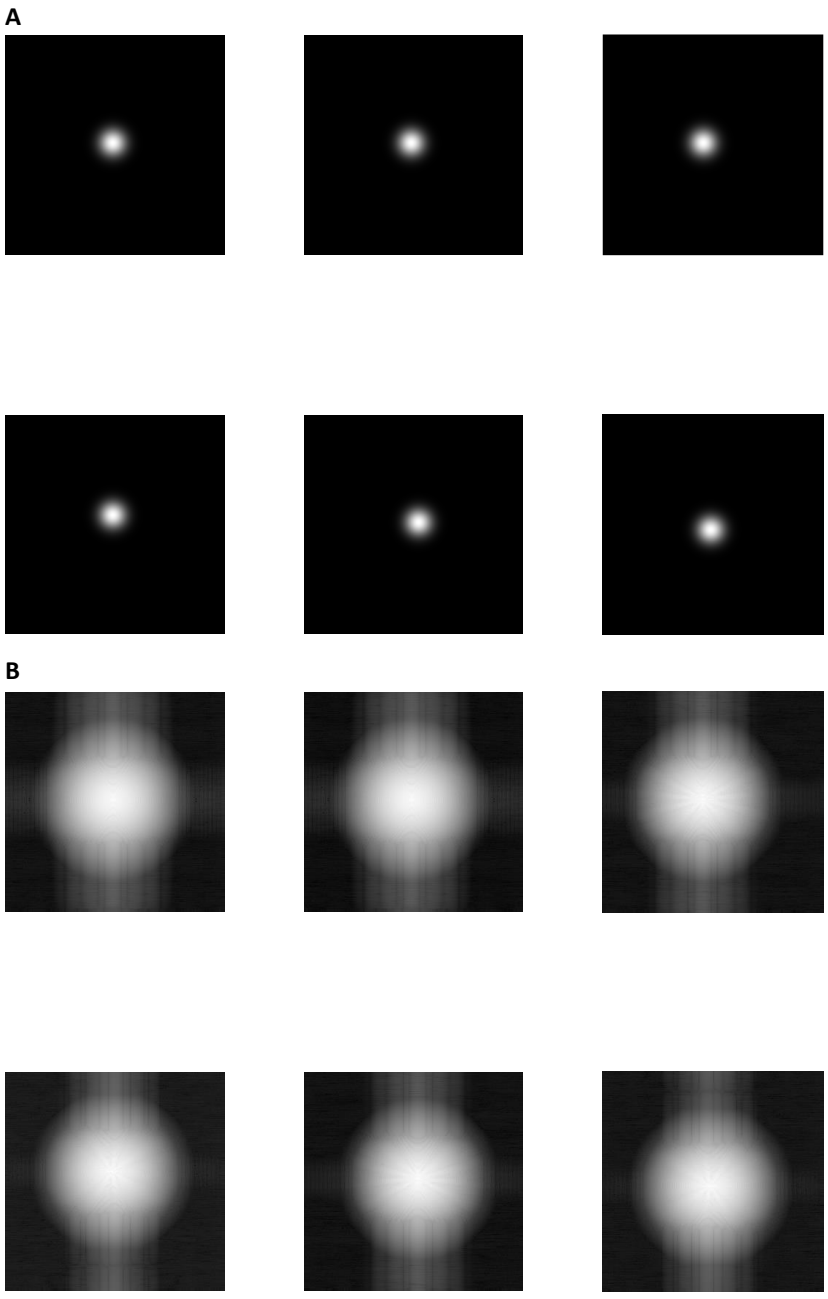

Figure 3.27: A - the shifted OTFs (301×301 pixels); B - the components of the Wiener filter (301×301 pixels).

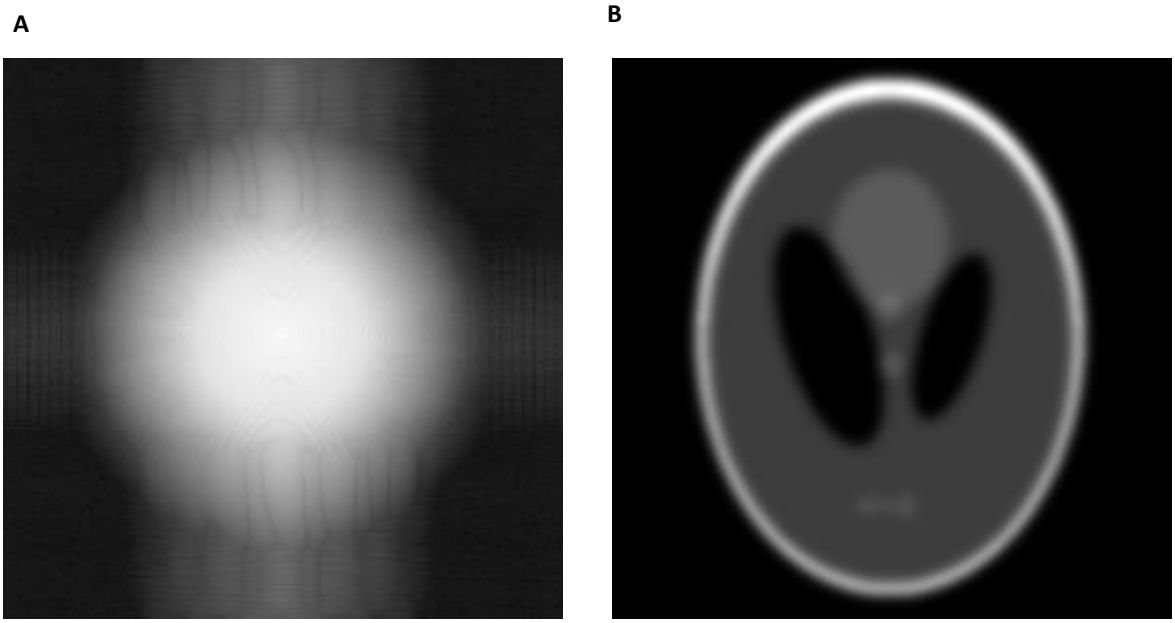

Figure 3.28: A - The reconstructed image in Fourier space (301×301 pixels); B - the final reconstructed image (301×301 pixels).

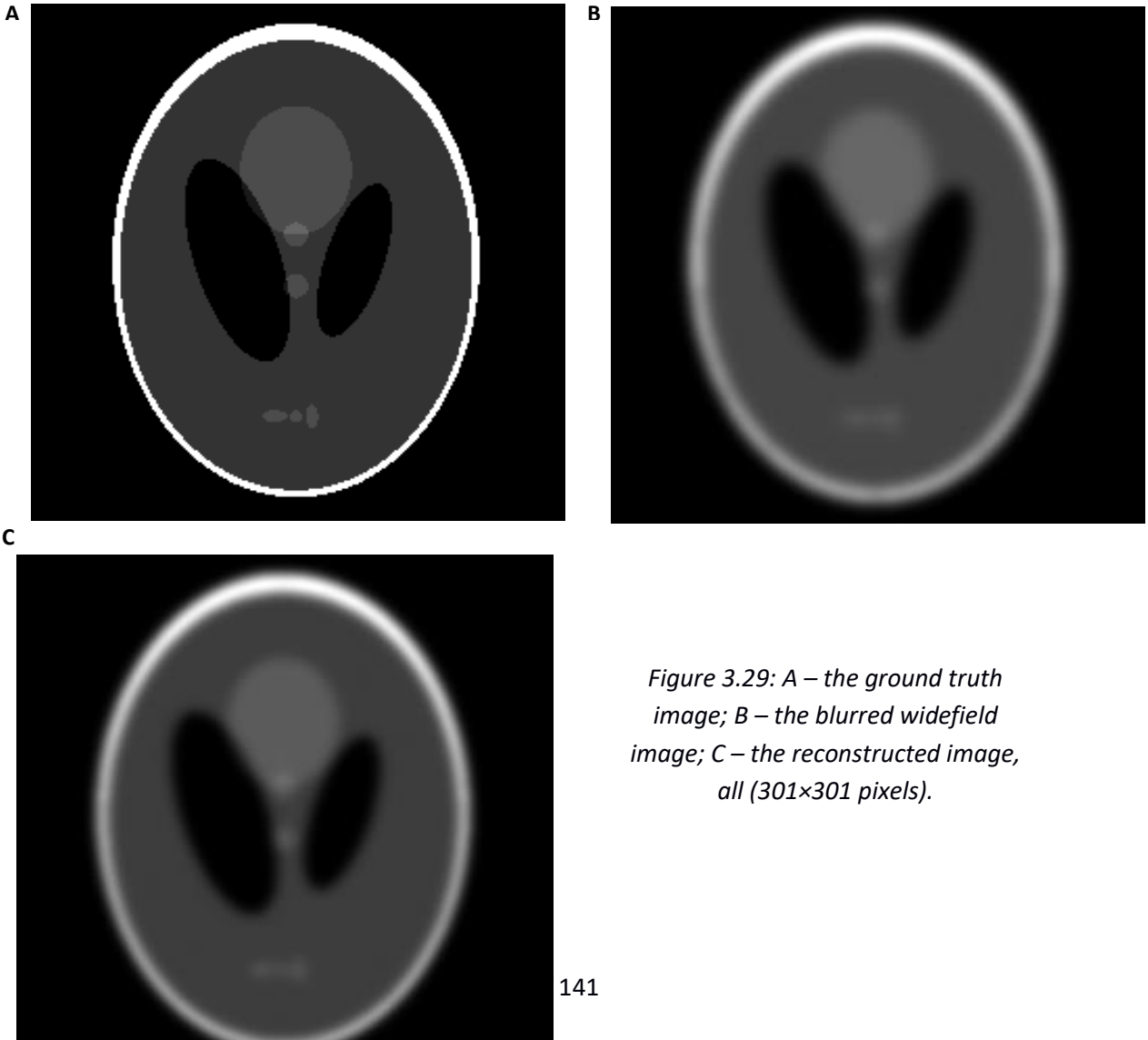

Figure 3.29: A – the ground truth image; B – the blurred widefield image; C – the reconstructed image, all (301×301 pixels).

It is clear that any resolution improvement is minimal, indeed the reconstructed image is only a slight improvement over the widefield image. The lack of resolution improvement is potentially due to utilising fewer masks with different spatial wavelengths or using non-sinusoidal masks. Another potential cause is the large spatial wavelength of the masks which would inhibit resolution improvement because the shift in Fourier space is very small. However there are few if any artefacts, which could potentially be expected due to reconstructing a non-sinusoidal mask with a standard SIM reconstruction algorithm.

This use of non-standard masks with a standard SIM reconstruction algorithm was further investigated using an image of a sample of human platelets. The image size was scaled to 301×301 pixels. The nm-to-pixel ratio was 20; the PSF was defined by the parameters: λ = 500nm, n = 1, NA = 1.49; three mask phases were used, φ_i = 0, $2\pi/3$, $4\pi/3$; two mask orientations were used, $\boldsymbol{p}$ = [1,0; 0,1]; the spatial wavelength of the masks was 600nm; the noise parameter, w = 1 ; and the width of the desired OTF was half that of the original PSF. These parameters were chosen to optimise the resolution improvement in the final image. The key results are shown below:

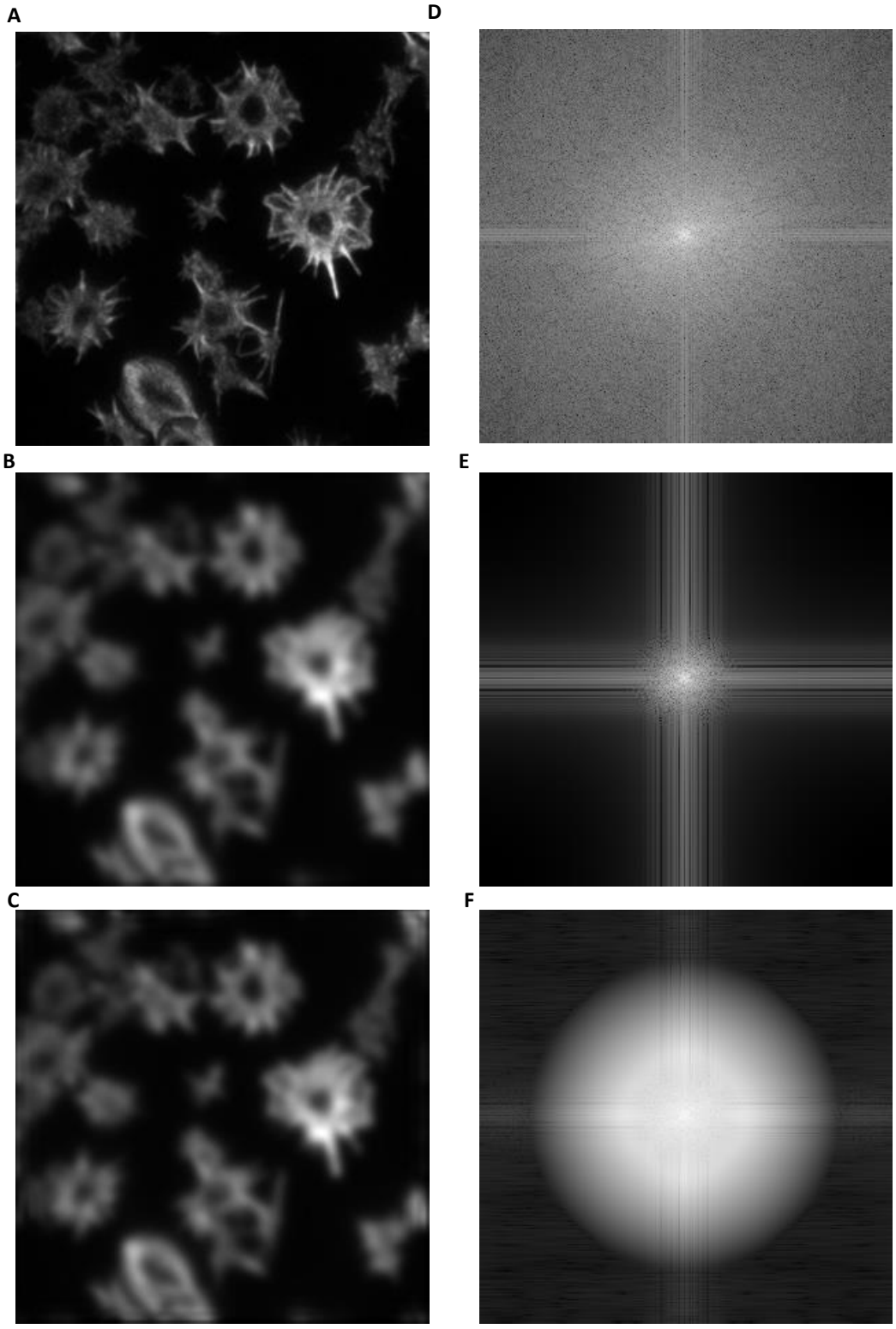

Figure 3.30: A - the ground truth image, 301×301 image of platelets courtesy of Dr Steve Thomas, University of Birmingham, UK; B - the widefield image, created by convolving the ground truth image with the PSF; C – the final reconstructed image; D, E, F – Fast Fourier Transforms of A, B & C respectively, all (301×301 pixels).

Again, as with the phantom image, it is clear that any resolution improvement between the widefield and the reconstructed image is minimal. The lack of resolution improvement is potentially due to utilising fewer masks with different spatial wavelengths or using non-sinusoidal masks. Another potential cause is the large spatial wavelength of the masks. However, as before, there are few if any artefacts, which could potentially be expected due to reconstructing a non-sinusoidal mask with a standard SIM reconstruction algorithm.

3.2.9 Discussion

It is clear that the standard SIM algorithm is effective for a set of simulated sinusoidal patterns. It produces the distinct 'flower' shape and there is clear resolution improvement, which could be potentially further optimised with altered parameters and masks.

However, it can be seen that the final reconstruction using the metamaterial patterns is very similar to the widefield image. This could be as a result of the fewer images. It is also possible that the non-sinusoidal components of the mask patterns are the cause. Consequently, in order to try and produce the desired resolution improvement with these metamaterial masks, alternative SIM image reconstruction algorithms adapted for the metamaterial masks were investigated, using two mathematical expansions to the expression for the masks.

3.3 Expanding SIM for non-standard patterns – Fourier Series

3.3.1 Introduction & Requirements

Although the standard SIM reconstruction algorithm proved successful with the typical sinusoidal masks used in SIM, it was not successful when the metamaterial patterns were used. Therefore, in order to accommodate these atypical patterns, the underlying model and thus the MATLAB algorithm needed to be adapted. The new approach needed to be able to encompass a more comprehensive mathematical description of the metamaterial masks, and ideally accommodate for the fewer masks than the nine or more typically used[1,3,7,16], and still provide resolution enhancement.

The metamaterial masks were inadequately modelled by simple sinusoids. A new model is therefore introduced to better model the masks. The mathematical expansion first trialled was a Fourier Expansion, which describes the masks as a sum of sinusoids. By substituting a new expression for the masks into the standard SIM mathematics, the mathematics can be altered to better accommodate the atypical metamaterial masks, and theoretically provide a better final image reconstruction.

3.3.2 Theory & Mathematics

As before, the mathematics for this novel approach to SIM reconstruction is still based upon the mathematics in the paper by T. Lukeš et al., 'Comparison of image reconstruction methods for structured illumination microscopy'[34]. However this mathematical basis for this research into SIM image reconstruction has been expanded to better describe the metamaterial masks, with a Fourier expansion of the original sinusoidal expression to give a Fourier series of summed sinusoids. The general expression for a Fourier Series, where: a_0,

a_n, and b_n are amplitude constants known as the Fourier coefficients; and *n =1,2,3…* numbers the terms in the series[224], is given in equation [3.12].

$$F(x) = \frac{a_0}{2} + \sum_{n=1}^{\infty}(a_n \cos nx) + \sum_{n=1}^{\infty}(b_n \sin nx) \qquad [3.12]$$

The initial expression of the collection of SIM images, that are comprised of the sample, the microscope's point spread function, and the structured illumination pattern masks, still forms the basis for the mathematical description of the image reconstruction process.

$$g_n(\underline{\boldsymbol{x}}) = [m_n(\underline{\boldsymbol{x}})f(\underline{\boldsymbol{x}})] \otimes h(\underline{\boldsymbol{x}}) \qquad [3.13]$$

Where: $g_n(\underline{\boldsymbol{x}})$ are the *n* SIM images, $m_n(\underline{\boldsymbol{x}})$ are the structured illumination pattern masks, $f(\underline{\boldsymbol{x}})$ is the sample, $h(\underline{\boldsymbol{x}})$ is the microscope's point spread function, $\underline{\boldsymbol{x}}$ is *(x,y)* is a vector in the image plane, and $\otimes$ is the convolution operator.

By Fourier transforming this expression, it can be described in Fourier space as:

$$G_n(\underline{\boldsymbol{k}}) = H(\underline{\boldsymbol{k}})[F(\underline{\boldsymbol{k}}) \otimes M_n(\underline{\boldsymbol{k}})] \qquad [3.14]$$

Where: $G_n(\underline{\boldsymbol{k}})$, $H(\underline{\boldsymbol{k}})$, $F(\underline{\boldsymbol{k}})$, $M_n(\underline{\boldsymbol{k}})$ are the Fourier transforms of $g_n(\underline{\boldsymbol{x}})$, $h(\underline{\boldsymbol{x}})$, $f(\underline{\boldsymbol{x}})$, $m_n(\underline{\boldsymbol{x}})$ respectively, and $\underline{\boldsymbol{k}}$ is (k_x,k_y) is a vector in the image plane in k-space.

Then a mathematical expression of the masks is required. In the case of a sinusoidal mask, it is as follows:

$$m_n(\underline{\boldsymbol{x}}) = 1 + \alpha \cos(2\pi(\underline{\boldsymbol{p}} \cdot \underline{\boldsymbol{x}}) + \varphi_i) \qquad [3.15]$$

Where: α is amplitude of the sinusoid, $\underline{\boldsymbol{p}}$ is the modulation vector that describes the orientation of the sinusoid, and φ_i is the spatial phase of the sinusoid, typically $\varphi_i = 0, 2\pi/3, 4\pi/3$.

However, in order to better describe the masks, a generalisation of this expression was developed to describe the masks as sums of sinusoids or Fourier Series.

$$m_n(x) = 1 + \alpha_{amp}\cos(2\pi(\alpha_{per}\underline{\boldsymbol{p}})\cdot\underline{\boldsymbol{x}} + \varphi_i) + \beta_{amp}\cos(2\pi(\beta_{per}\underline{\boldsymbol{p}})\cdot\underline{\boldsymbol{x}} + \theta_\beta) + \cdots \quad [3.16]$$

Where: α_{amp}, β_{amp} are the amplitude of the sinusoids; α_{per}, β_{per} are the periodicities of the sinusoids; and θ_β is the phase of the second sinusoid.

More generally:

$$m_n(x) = 1 + \sum_{n=1}^{N} Amp_n\cos(2\pi(Per_n\underline{\boldsymbol{p}})\cdot\underline{\boldsymbol{x}} + \theta_n) \quad [3.17]$$

In order to achieve the pattern produced by the metamaterial, which is comprised of a primary sinusoid and then a secondary sinusoid which is rotated 90° to the primary sinusoid, *Per* requires a rotation matrix to describe the secondary sinusoid, therefore:

$$Per_2 = \beta_{per} = \beta\cdot\underline{\boldsymbol{R}} \;\; where \;\; \underline{\boldsymbol{R}} = \begin{bmatrix} 0 & -1 \\ 1 & 0 \end{bmatrix} \quad [3.18]$$

In Fourier space, the masks can be described as follows:

$$M(\underline{\boldsymbol{k}}) = \delta(\underline{\boldsymbol{k}}) + \sum_{n=1}^{N} \frac{Amp_n}{2}\delta(\underline{\boldsymbol{k}} - Per_n\underline{\boldsymbol{p}})e^{2\pi i\theta_n} + \frac{Amp_n}{2}\delta(\underline{\boldsymbol{k}} + Per_n\underline{\boldsymbol{p}})e^{-2\pi i\theta_n} \quad [3.19]$$

Substituting equation [3.19] into [3.14], the SIM images in Fourier space can be expressed in terms of the modulation vector, $\underline{\boldsymbol{p}}$, and the spatial phases, φ_i, which allows the frequency information that describes the images to be shifted and separated, the process necessary for super-resolution reconstruction.

$$G(\underline{\boldsymbol{k}}) = H(\underline{\boldsymbol{k}})[F(\underline{\boldsymbol{k}}) + \sum_{n=1}^{N} \frac{Amp_n}{2}F(\underline{\boldsymbol{k}} - Per_n\underline{\boldsymbol{p}})e^{2\pi i\theta_n} + \frac{Amp_n}{2}F(\underline{\boldsymbol{k}} + Per_n\underline{\boldsymbol{p}})e^{-2\pi i\theta_n}] \quad [3.20]$$

In matrix form, for each value of $\underline{\boldsymbol{p}}$ for the metamaterial mask in equation [3.20], this becomes:

$$\begin{bmatrix} G_1(\underline{\boldsymbol{k}}) \\ G_2(\underline{\boldsymbol{k}}) \\ G_3(\underline{\boldsymbol{k}}) \end{bmatrix} = \begin{bmatrix} 1 & e^{2\pi i\varphi_1} & e^{-2\pi i\varphi_1} & e^{2\pi i\theta_\beta} & e^{-2\pi i\theta_\beta} \\ 1 & e^{2\pi i\varphi_2} & e^{-2\pi i\varphi_2} & e^{2\pi i\theta_\beta} & e^{-2\pi i\theta_\beta} \\ 1 & e^{2\pi i\varphi_3} & e^{-2\pi i\varphi_3} & e^{2\pi i\theta_\beta} & e^{-2\pi i\theta_\beta} \end{bmatrix} \begin{bmatrix} H(\underline{\boldsymbol{k}})F(\underline{\boldsymbol{k}}) \\ \frac{\alpha_{amp}}{2}H(\underline{\boldsymbol{k}})F(\underline{\boldsymbol{k}}-\alpha_{per}\underline{\boldsymbol{p}}) \\ \frac{\alpha_{amp}}{2}H(\underline{\boldsymbol{k}})F\left(\underline{\boldsymbol{k}}+\alpha_{per}\underline{\boldsymbol{p}}\right) \\ \frac{\beta_{amp}}{2}H(\underline{\boldsymbol{k}})F(\underline{\boldsymbol{k}}-\beta_{per}\underline{\boldsymbol{p}}) \\ \frac{\beta_{amp}}{2}H(\underline{\boldsymbol{k}})F(\underline{\boldsymbol{k}}+\beta_{per}\underline{\boldsymbol{p}}) \end{bmatrix} \quad [3.21]$$

Consequently, for three $\underline{\boldsymbol{p}}$'s there are three sets of this matrix equation [3.21], and the total G_n's. The spectral components of these G_n's then need to be separated, which is done by multiplying the G_n's by the Hermitian conjugate of the central matrix containing the phases. Separating the components allows the masks to be removed from the final image and the higher resolution information to be retained.

$$\begin{bmatrix} C_1(\underline{\boldsymbol{k}}) \\ C_2(\underline{\boldsymbol{k}}) \\ C_3(\underline{\boldsymbol{k}}) \\ C_4(\underline{\boldsymbol{k}}) \\ C_5(\underline{\boldsymbol{k}}) \end{bmatrix} = \begin{bmatrix} 1 & 1 & 1 \\ e^{-2\pi i\varphi_1} & e^{-2\pi i\varphi_2} & e^{-2\pi i\varphi_3} \\ e^{2\pi i\varphi_1} & e^{2\pi i\varphi_2} & e^{2\pi i\varphi_3} \\ e^{-2\pi i\theta_\beta} & e^{-2\pi i\theta_\beta} & e^{-2\pi i\theta_\beta} \\ e^{2\pi i\theta_\beta} & e^{2\pi i\theta_\beta} & e^{2\pi i\theta_\beta} \end{bmatrix} \begin{bmatrix} G_1(\underline{\boldsymbol{k}}) \\ G_2(\underline{\boldsymbol{k}}) \\ G_3(\underline{\boldsymbol{k}}) \end{bmatrix} \quad [3.22]$$

Where C_n are the separated components, and again there are three sets of equation [3.22] to give the C_n's. This gives more C_n's than for standard SIM, however if $\theta_\beta = 0$, so there is no additional phase shift, and it can be simplified to the standard three C_n's. These separated components are then shifted, this mixes spectral frequencies that are not observable due to the diffraction limit of the imaging system and its PSF with those that are observable. Thus, in Fourier space a greater area of spectral information is covered and thus more information is retained and a higher resolution final image can be produced. The shifts are $\underline{\boldsymbol{0}}$ and $\pm\underline{\boldsymbol{p}}$, for each $\underline{\boldsymbol{p}}$ value.

$$CS_1(\underline{\boldsymbol{k}}) = C_1(\underline{\boldsymbol{k}})$$
$$CS_2(\underline{\boldsymbol{k}}) = C_2\left(\underline{\boldsymbol{k}} + \underline{\boldsymbol{p}}\right)$$
$$CS_3(\underline{\boldsymbol{k}}) = C_3\left(\underline{\boldsymbol{k}} - \underline{\boldsymbol{p}}\right) \qquad [3.23]$$

For this expanded SIM, the Fourier kernels that achieve these shifts need to be adjusted:

$$K(\underline{\boldsymbol{x}}) = e^{\pm i(((\alpha_{per}+\beta_{per})\underline{\boldsymbol{p}})\cdot\underline{\boldsymbol{x}})} \qquad [3.24]$$

These shifted, separated components are then combined via a Wiener filter:

$$S(\underline{\boldsymbol{k}}) = \frac{\sum_{n=1}^{N} OTF_n(\underline{\boldsymbol{k}})^* CS_n(\underline{\boldsymbol{k}})}{\sum_{n=1}^{N} \left|OTF_n(\underline{\boldsymbol{k}})\right|^2 + w} \qquad [3.25]$$

Where: $S(\underline{\boldsymbol{k}})$ is the reassembled image in Fourier space; OTF_n is the n-th shifted OTF (Optical Transfer Function which is the PSF in Fourier space), shifted in the same way as the C_n's are in equation [3.23]; * is the complex conjugate function; N is the total number of image components, typically nine; and w is a noise constant.

This reassembled image in Fourier space is then apodized, which is a mathematical optical filtering technique to smooth discontinuities and particularly ringing artefacts common to SIM imaging, with the desired OTF. In this case, the desired OTF is the desired PSF of the system, so by reducing the width of the PSF by half, it should produce 2× resolution compared to the original widefield image. Finally, the image is then converted from Fourier space to real space, giving a super-resolution reconstructed SIM image.

The MATLAB algorithm for this Fourier Series SIM is presented in Appendix 4 and 5.

3.3.3 Simulating the patterns

The patterns were simulated as a sum of two sinusoids. The primary sinusoid that forms the main ‘stripes’ had a spatial wavelength of 600nm. The secondary sinusoid that forms the blocks within the main stripes had a spatial wavelength of 300nm, and was rotated to be perpendicular the primary sinusoid. Both of the sinusoids were formed on the basis to provide the two orientations, [1, 0] and [0, 1], and three phases, 0, $2\pi/3$ and $4\pi/3$, seen in the metamaterial masks. The simulated masks and actual masks are compared below.

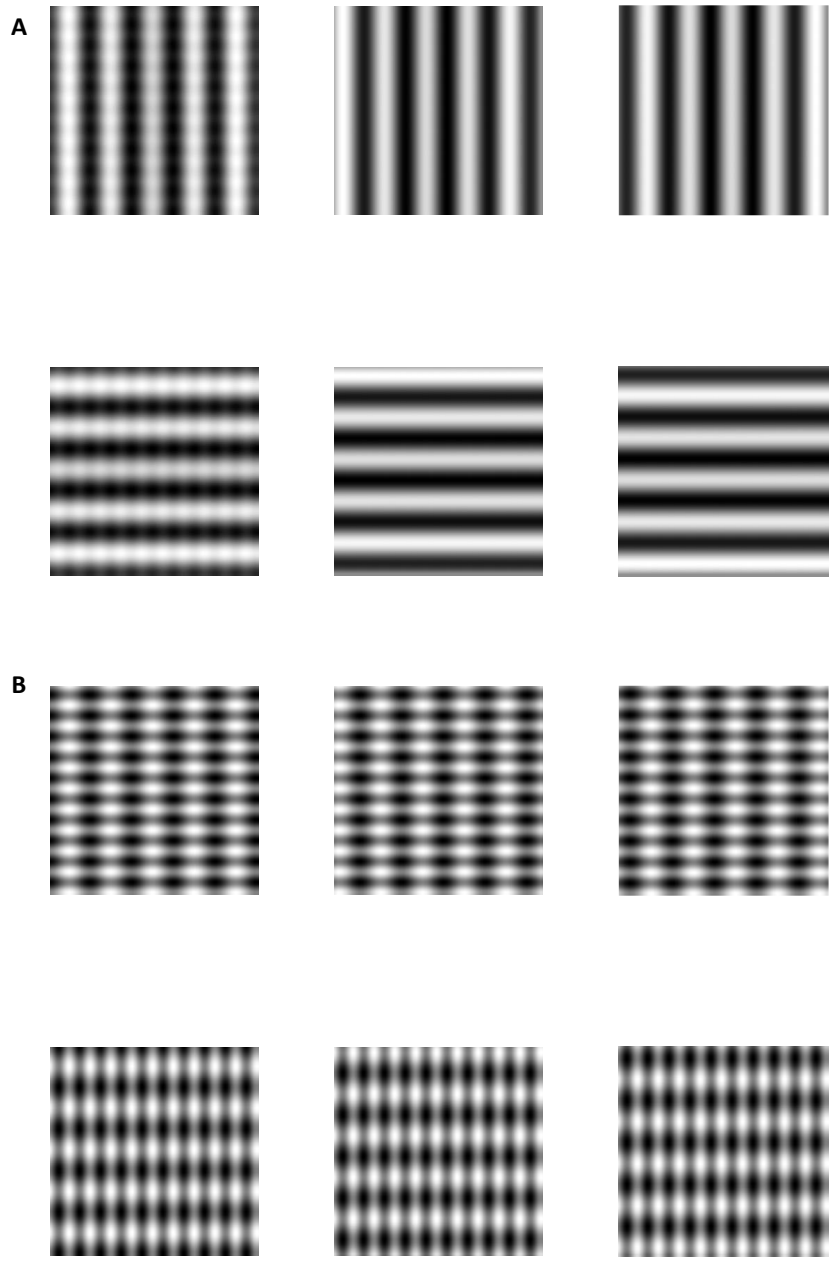

Figure 3.31: A - The six metamaterial masks created in simulation using the metamaterial design (301×301 pixels); B – the six simulated masks created using a Fourier Series of two sinusoids (301×301 pixels).

The simulated masks represent how the image reconstruction algorithm models the masks when reconstructing, and the closer this is to the metamaterial masks, the better the image reconstruction quality.

It can be seen that the key 'stripes' and 'blocks' are achieved, as well as the phases and orientations of the patterns. Moreover, the 'stripes' and 'blocks' are matched in terms of positioning between the metamaterial and simulated masks. However, the simulated masks have wider, more continuous stripes compared to the metamaterial masks. Moreover, only two of the metamaterial patterns have the extra sinusoidal component, whereas the simulated masks all contain the expanded description. This means that the simulation is not identical to the metamaterial masks, but they are potentially more similar than a simple sinusoid and the metamaterial masks. This may impact the reconstruction quality, as was the case when using standard SIM image reconstruction, but as the masks are a closer estimate to the actual masks, the image reconstruction quality should be improved.

3.3.4 Using simulated patterns

The mathematical process of Fourier Series SIM described above, is now demonstrated with an example image, simulated microscope PSF, and six simulated Fourier Series masks based upon the metamaterial masks described in *Section* 3.3.3, utilising the algorithm in Appendix 4.

The example image was that of a sample of human platelets previously used. The nm-to-pixel ratio was 20; the PSF was defined by the parameters: $\lambda = 500$nm, $n = 1$, $NA = 1.49$; three mask phases were used, $\varphi_i = 0, 2\pi/3, 4\pi/3$; two mask orientations were used, $\boldsymbol{p} = [1,0; 0,1]$; the spatial wavelengths of the masks were 600nm and 300nm; the noise parameter, $w = 1$; and the width of the desired OTF was half that of the original PSF. These parameters were chosen to optimise the resolution improvement in the final image, see figures 3.23, 3.30 for details of the ground truth image and PSF used.

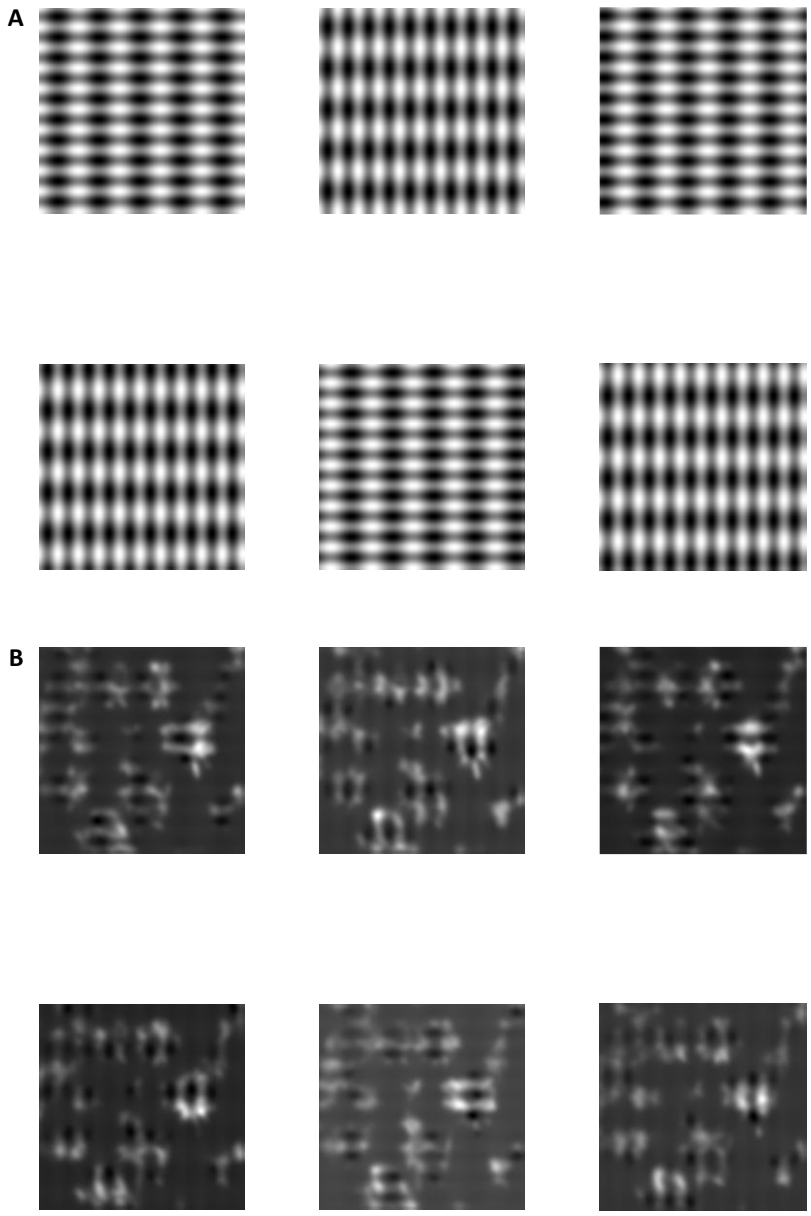

Figure 3.32: A - The six masks used (301×301 pixels), simulating the masks produced by the metamaterial design, three phases were used, φ_i = 0, 2π/3, 4π/3, two mask orientations were used, $\underline{\boldsymbol{p}}$ = [1,0; 0,1]; B – the six acquired images (301×301 pixels), created by multiplying the masks and the ground truth image, and then convolving with the PSF.

A

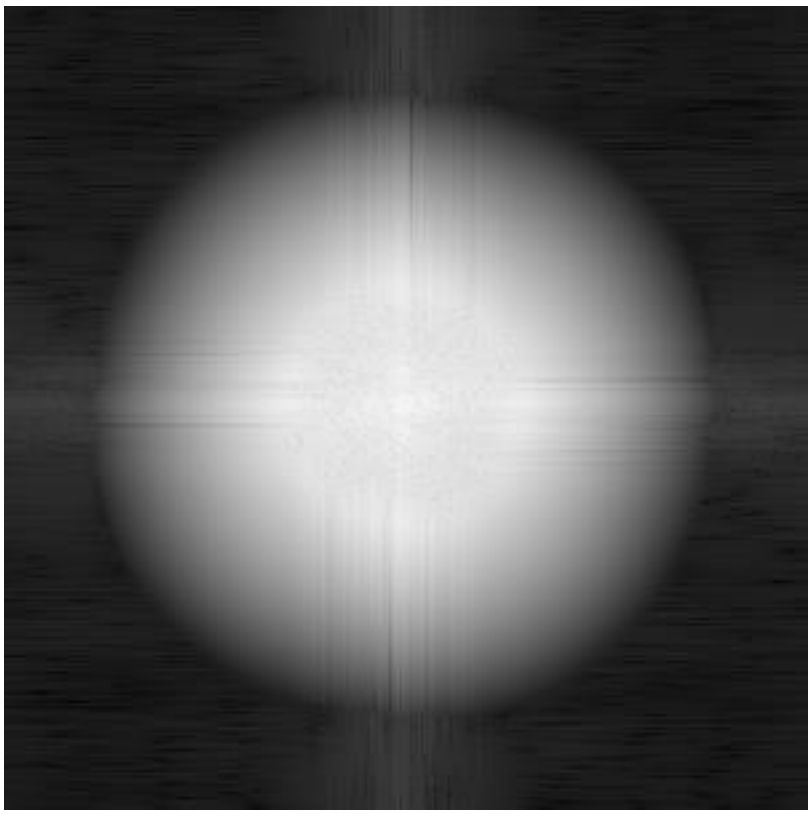

B

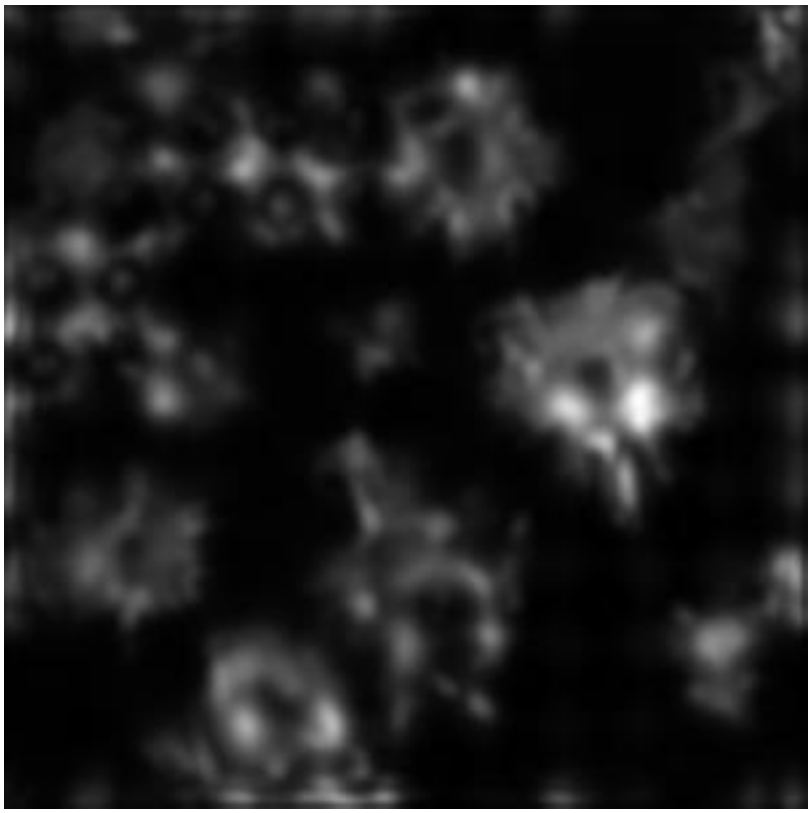

Figure 3.33: A – The reconstructed image in Fourier space (301×301 pixels); B – the final reconstructed image (301×301 pixels).

These simulated masks were also used within the standard SIM reconstruction algorithm, to provide a basis of comparison when using a set of atypical masks, as opposed to the set of metamaterial masks where only two of the masks clearly contain additional components beyond a simple sinusoid.

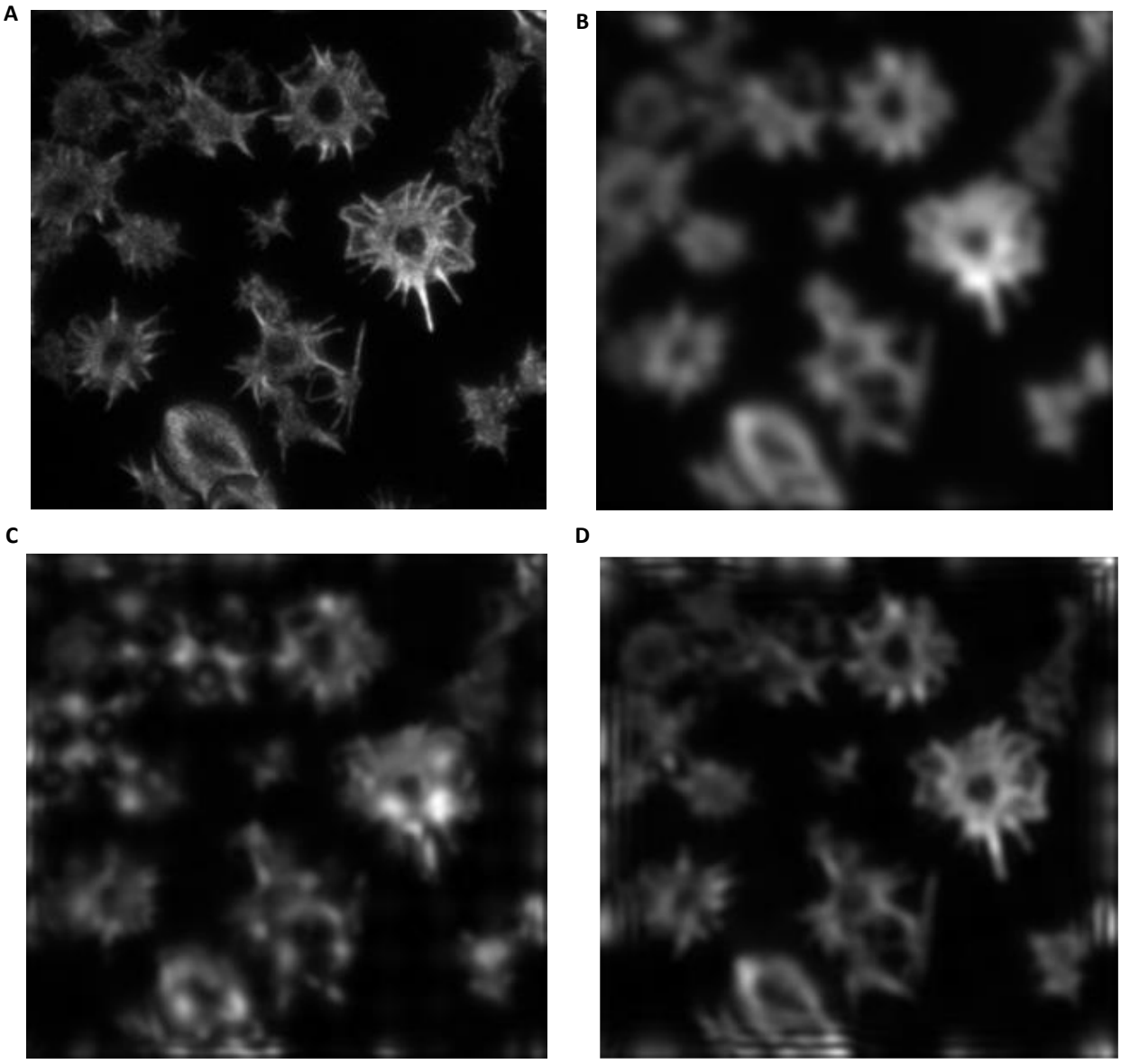

Figure 3.34: A – Ground truth image of platelets, courtesy of Dr Steve Thomas, University of Birmingham, UK; B – the widefield image, created by convolving the ground truth image with the PSF; C – the image as reconstructed using the Fourier Series SIM reconstruction algorithm; D – the image as reconstructed using the standard SIM reconstruction algorithm, all (301×301 pixels).

It can be seen that there are strong artefacts in the Fourier Series based reconstruction, whereas the standard SIM reconstruction has produced clear resolution improvement, with minimal artefacts at the image edges. Furthermore, the use of the more complex masks has produced greater resolution improvement than the use of the actual metamaterial masks, see figure 3.34, with standard SIM image reconstruction. This could be because the extra sinusoidal term in the expanded simulated masks has expanded the coverage of the masks in Fourier space, meaning more high resolution information is retained in the reconstructed image. Thus compensating for only six images being used to reconstruct from as opposed to the typical nine required for resolution enhancement. The Fourier Series SIM reconstruction method was further investigated to see if it was suitable as a SIM image reconstruction method.

3.3.5 Using the metamaterial patterns

The mathematical process of Fourier Series SIM described above, is now demonstrated with an example image, simulated microscope PSF, and the six metamaterial masks described in Section 3.3.3, utilising the algorithm in Appendix 5.

The example image was that of a sample of human platelets previously used. The nm-to-pixel ratio was 20; the PSF was defined by the parameters: $\lambda = 500$nm, $n = 1$, $NA = 1.49$; three mask phases were used, $\varphi_i = 0, 2\pi/3, 4\pi/3$; two mask orientations were used, $\underline{\boldsymbol{p}} = [1,0; 0,1]$; the spatial wavelength of the masks was 600nm; the noise parameter, $w = 1$; and the width of the desired OTF was half that of the original PSF. These parameters were chosen to optimise the resolution improvement in the final image.

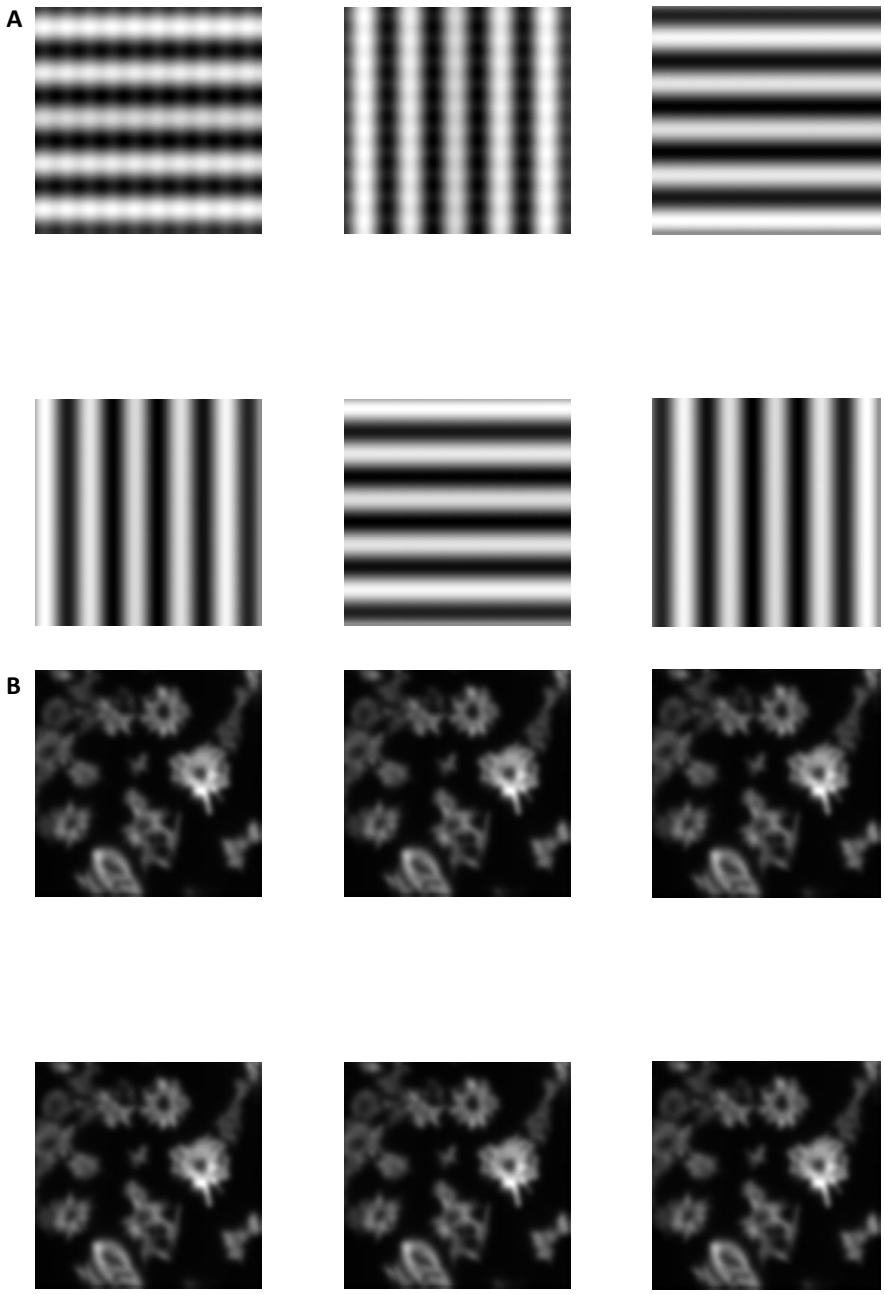

Figure 3.35: A - The six masks used (301×301 pixels), produced by the metamaterial design, three phases were used, $\varphi_i = 0, 2\pi/3, 4\pi/3$, two mask orientations were used, $\underline{\mathbf{p}} = [1,0; 0,1]$; B – the six acquired images (301×301 pixels), created by multiplying the masks and the ground truth image, and then convolving with the PSF.

A

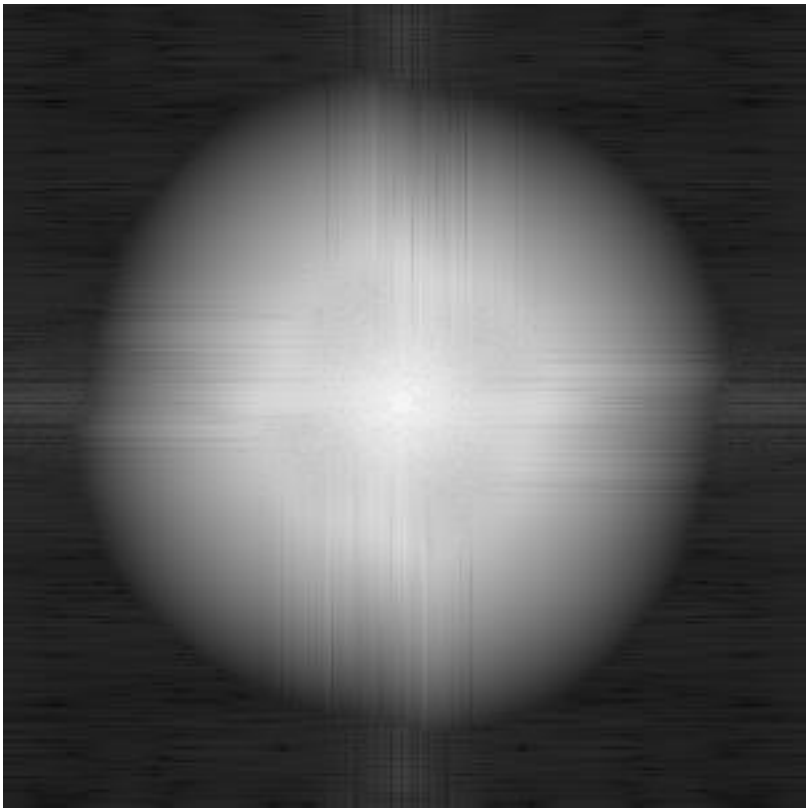

B

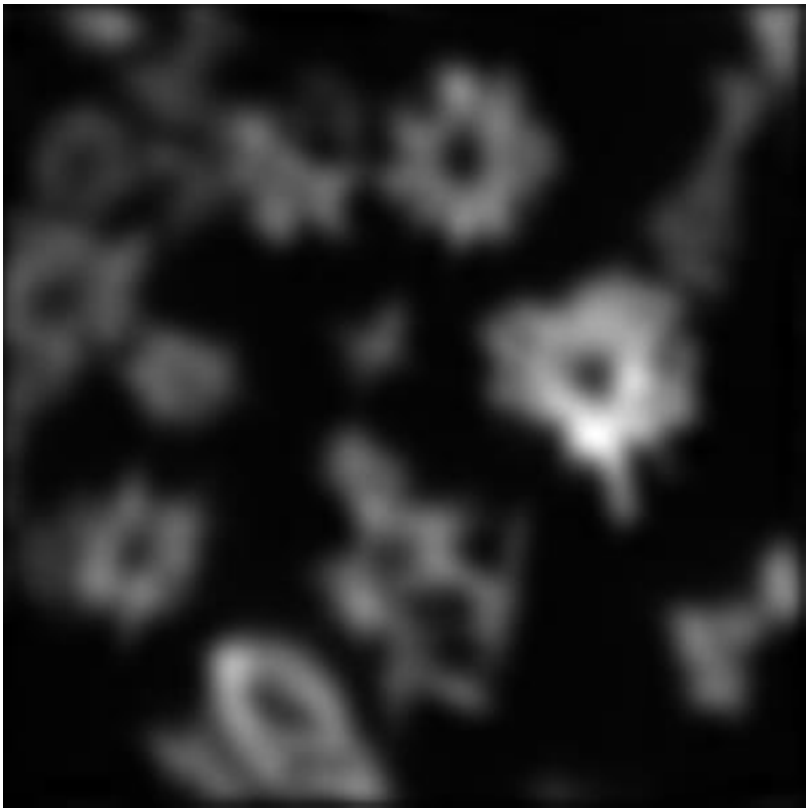

Figure 3.36: A – The reconstructed image in Fourier space (301×301 pixels); B – the final reconstructed image (301×301 pixels).

The metamaterial masks were also used within the standard SIM reconstruction algorithm, see Section 3.2.8. This reconstruction is shown alongside the Fourier Series reconstruction to provide a basis of comparison between the two methods when using the metamaterial masks.

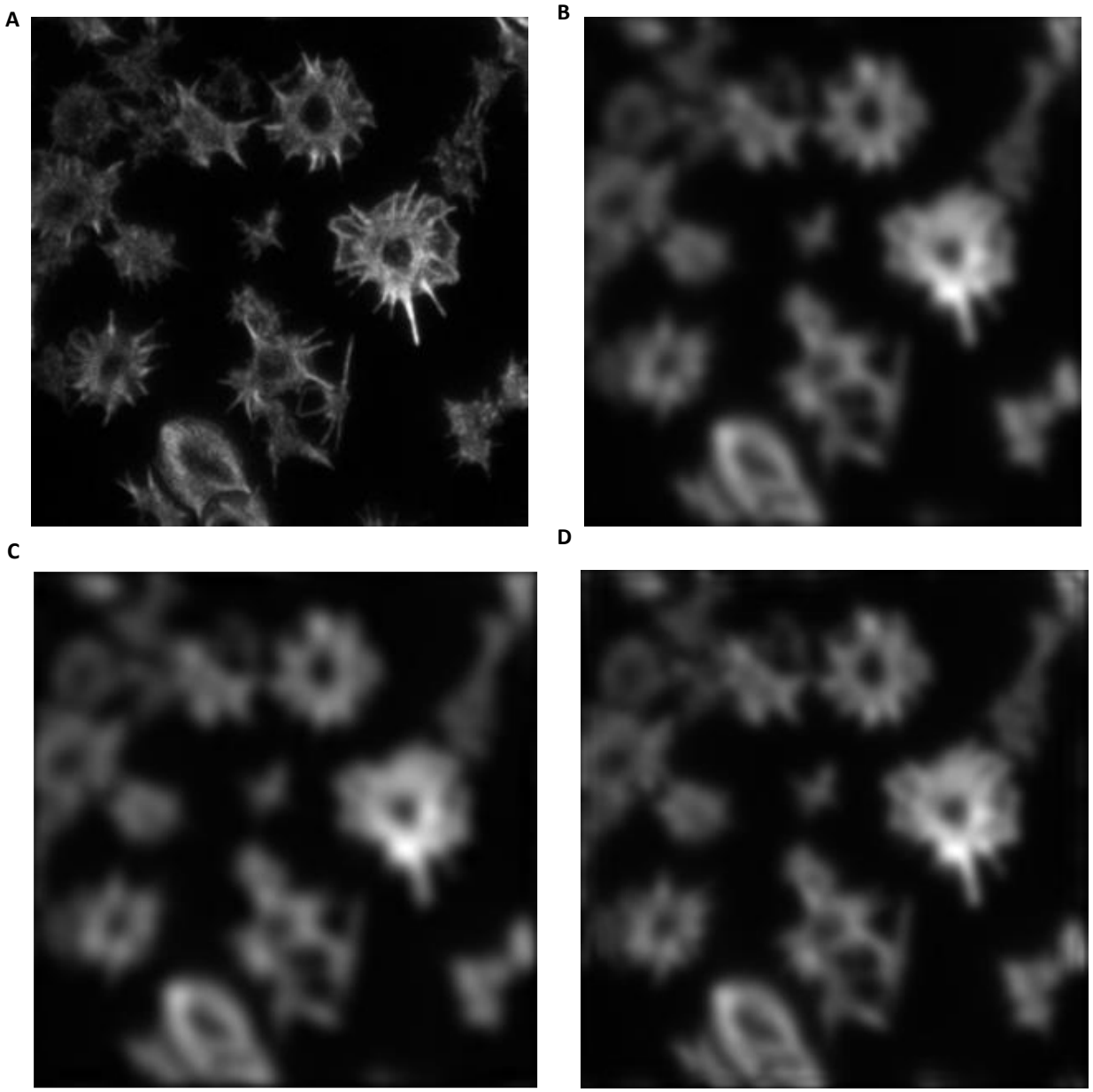

Figure 3.37: A – Ground truth image of platelets, courtesy of Dr Steve Thomas, University of Birmingham, UK; B – the widefield image, created by convolving the ground truth image with the PSF; C - the image as reconstructed using the Fourier Series SIM reconstruction algorithm; D – the image as reconstructed using the standard SIM reconstruction algorithm, all (301×301 pixels).

It can be seen that the standard SIM reconstruction method was more successful than the Fourier Series method, although any resolution improvement is minimal. Indeed the Fourier Series method has produced an image reconstruction worse than the widefield image. This is probably due to the metamaterial patterns being more similar to a standard sinusoid than the Fourier Series expansion, meaning the expanded algorithm produced artefacts as the masks and the description in the algorithm were not sufficiently similar. In addition, the metamaterial masks show little impact on the acquired images, see figure 3.35. This may be because there is not sufficient contrast between the peaks and troughs of the pattern; this would also lessen any resolution enhancement, as there would be a lesser interaction between the masks and the sample meaning less high resolution information would be retained in the final image. Moreover, the spatial wavelength may be too long to allow for super-resolution reconstruction.

3.3.6 Discussion

Although the mathematical theory of the Fourier Series expansion to the SIM reconstruction algorithm was robust, it has not proved successful when used with the metamaterial masks. This is potentially because the metamaterial masks are too close to being a simple sinusoid, there being too few masks, or the spatial wavelength of the masks being too large. This was then further investigated using a second mathematical expansion to the expression for the masks, as described below, see *Section 3.4*.

However, the use of simulated masks based upon the metamaterial masks was able to produce resolution enhancement, particularly when used in the standard SIM image

reconstruction algorithm. This was in spite of only six masks being used and could have potential for reducing the number of masks needed for standard SIM image reconstruction.

3.4 Expanding SIM for non-standard patterns – Sinusoid Product-based SIM

3.4.1 Introduction & Requirements

Although the standard SIM reconstruction algorithm proved successful with the typical sinusoidal masks used in SIM, it was not successful when the metamaterial patterns were used. The use of the Fourier Series expansion had proven mostly unsuccessful, see *Section 3.3*, so another mathematical expansion was investigated. As before, the new approach needed to be able to encompass a more comprehensive mathematical description of the metamaterial masks, and ideally accommodate for the fewer masks than the nine or more typically used[33,36,117,220], and still provide resolution enhancement.

The metamaterial masks were inadequately modelled by simple sinusoids. A new model is therefore introduced to better model the masks. The mathematical expansion first trialled was a Fourier Expansion, but this method showed distinct artefacts, despite being able to create a reasonable approximation of the metamaterial masks. Consequently, a different mathematical expansion was trialled, describing the masks based upon a product of sinusoids. This produces a chequerboard of peaks and troughs that can be rotated and scaled to produce an approximation to the metamaterial masks. By substituting a new expression for the masks into the standard SIM mathematics, the mathematics can be altered to better accommodate the atypical metamaterial masks, and theoretically provide a better final image reconstruction.

3.4.2 Theory & Mathematics

As before, the mathematics for this novel approach to SIM reconstruction is still based upon the mathematics in the paper by T. Lukeš et al., 'Comparison of image reconstruction methods for structured illumination microscopy'[34]. However, this mathematical basis for this research into SIM image reconstruction has been expanded to better describe the metamaterial masks, by describing the masks in terms of a product of sinusoids.

The initial expression of the collection of SIM images, that are comprised of the sample, the microscope's point spread function, and the structured illumination pattern masks, still forms the basis for the mathematical description of the image reconstruction process.

$$g_n(\underline{\boldsymbol{x}}) = [m_n(\underline{\boldsymbol{x}}) f(\underline{\boldsymbol{x}})] \otimes h(\underline{\boldsymbol{x}}) \quad [3.26]$$

Where: $g_n(\underline{\boldsymbol{x}})$ are the n SIM images, $m_n(\underline{\boldsymbol{x}})$ are the structured illumination pattern masks, $f(\underline{\boldsymbol{x}})$ is the sample, $h(\underline{\boldsymbol{x}})$ is the microscope's point spread function, $\underline{\boldsymbol{x}}$ is (x,y) is a vector in the image plane, and $\otimes$ is the convolution operator.

By Fourier transforming this expression, it can be described in Fourier space as:

$$G_n(\underline{\boldsymbol{k}}) = H(\underline{\boldsymbol{k}})[F(\underline{\boldsymbol{k}}) \otimes M_n(\underline{\boldsymbol{k}})] \quad [3.27]$$

Where: $G_n(\underline{\boldsymbol{k}})$, $H(\underline{\boldsymbol{k}})$, $F(\underline{\boldsymbol{k}})$, $M_n(\underline{\boldsymbol{k}})$ are the Fourier transforms of $g_n(\underline{\boldsymbol{x}})$, $h(\underline{\boldsymbol{x}})$, $f(\underline{\boldsymbol{x}})$, $m_n(\underline{\boldsymbol{x}})$ respectively, and $\underline{\boldsymbol{k}}$ is (k_x,k_y) is a vector in the image plane in k-space.

Then a mathematical expression of the masks is required. In the case of a sinusoidal mask, it is as follows:

$$m_n(\underline{\boldsymbol{x}}) = 1 + \alpha \cos(2\pi(\underline{\boldsymbol{p}} \cdot \underline{\boldsymbol{x}}) + \varphi_i) \quad [3.28]$$

Where: α is amplitude of the sinusoid, $\underline{\boldsymbol{p}}$ is the modulation vector that describes the orientation of the sinusoid, and φ_i is the spatial phase of the sinusoid, typically $\varphi_i = 0, 2\pi/3, 4\pi/3$.

However, in order to better describe the masks, this expression was developed to describe the masks as a product of sinusoids.

$$m_n(\underline{\boldsymbol{x}}) = 1 + \cos(2\pi(\alpha\underline{\boldsymbol{p}^{(1)}} \cdot \underline{\boldsymbol{x}})) \times \cos(2\pi(\alpha\underline{\boldsymbol{p}^{(2)}} \cdot \underline{\boldsymbol{x}} + \varphi_i)) \quad [3.29]$$

$$\underline{\boldsymbol{p}^{(1)}} = \begin{bmatrix}1\\1\end{bmatrix}; \underline{\boldsymbol{p}^{(2)}} = \begin{bmatrix}1\\-1\end{bmatrix}; \underline{\boldsymbol{p}^{(1)}} \cdot \underline{\boldsymbol{p}^{(2)}} = 0;\ \alpha = \begin{bmatrix}a\\b\end{bmatrix} \quad [3.30]$$

Where: φ_i, are the phases of the masks; $\underline{\boldsymbol{p}^{(1)}}$, $\underline{\boldsymbol{p}^{(2)}}$ are the orientations of the sinusoids and should be orthogonal, required to rotate the *cos(x)cos(y)* chequerboard into the stripes seen in the metamaterial masks; α is a periodicity constant; and *a*, *b* are the spatial frequencies of the sinusoids. The basic mask is orientated as $\underline{\boldsymbol{p}} = [1,0]$ and is rotated to produce other orientations.

This is a reasonable model as the product of two sinusoids forms a chequerboard of peaks and troughs that, once rotated, can replicate the 'blocks' seen in the stripes of the metamaterial masks, with the period of the sinusoids being adjusted to create the appropriate spatial frequencies of the metamaterial masks, see figure 3.38 below.

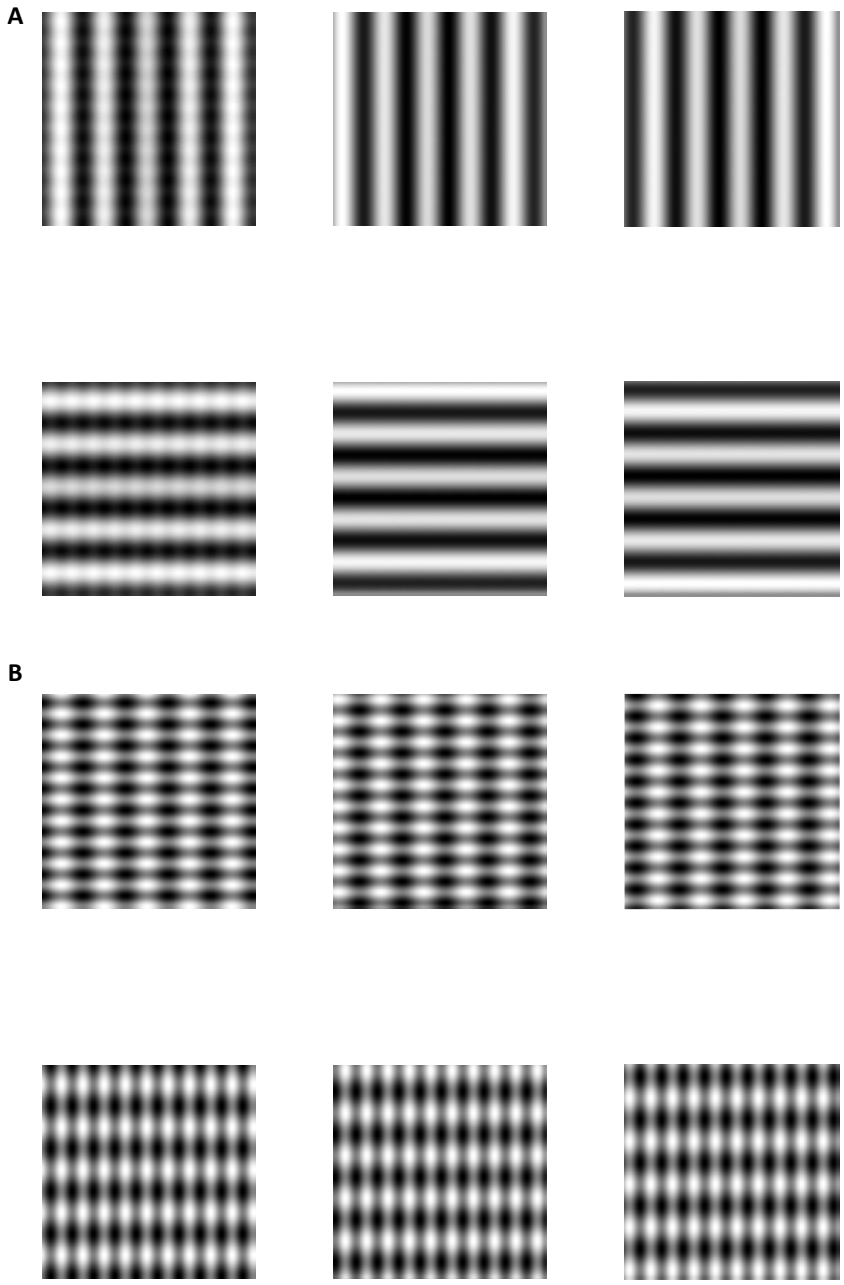

Figure 3.38: A - The six metamaterial masks created in simulation using the metamaterial design; B – the six simulated masks created using a product of two sinusoids.

In Fourier space, the masks can be described as follows:

$$M_n(\underline{\boldsymbol{k}}) = \delta(\underline{\boldsymbol{k}}) + \tfrac{1}{4}[\delta\left(\underline{\boldsymbol{k}} - \alpha\left(\underline{\boldsymbol{p}^{(1)}} - \underline{\boldsymbol{p}^{(2)}}\right)\right)e^{2\pi i\varphi_i} + \delta\left(\underline{\boldsymbol{k}} + \alpha\left(\underline{\boldsymbol{p}^{(1)}} - \underline{\boldsymbol{p}^{(2)}}\right)\right)e^{-2\pi i\varphi_i} + \delta\left(\underline{\boldsymbol{k}} - \alpha\left(\underline{\boldsymbol{p}^{(1)}} + \underline{\boldsymbol{p}^{(2)}}\right)\right)e^{2\pi i\varphi_i} + \delta\left(\underline{\boldsymbol{k}} + \alpha\left(\underline{\boldsymbol{p}^{(1)}} + \underline{\boldsymbol{p}^{(2)}}\right)\right)e^{-2\pi i\varphi_i}] \quad [3.31]$$

Substituting equation [3.31] into [3.27], the SIM images in Fourier space can be expressed in terms of the modulation vector, $\underline{\boldsymbol{p}}$, and the spatial phases, φ_i, which allows the frequency information that describes the images to be shifted and separated, the process necessary for super-resolution reconstruction.

$$G_n(\underline{\boldsymbol{k}}) = H(\underline{\boldsymbol{k}})[F(\underline{\boldsymbol{k}}) + \tfrac{1}{4}\Big[F\left(\underline{\boldsymbol{k}} - \alpha\left(\underline{\boldsymbol{p}^{(1)}} - \underline{\boldsymbol{p}^{(2)}}\right)\right)e^{2\pi i\varphi_i} + F\left(\underline{\boldsymbol{k}} + \alpha\left(\underline{\boldsymbol{p}^{(1)}} - \underline{\boldsymbol{p}^{(2)}}\right)\right)e^{-2\pi i\varphi_i} + F\left(\underline{\boldsymbol{k}} - \alpha\left(\underline{\boldsymbol{p}^{(1)}} + \underline{\boldsymbol{p}^{(2)}}\right)\right)e^{2\pi i\varphi_i} + F\left(\underline{\boldsymbol{k}} + \alpha\left(\underline{\boldsymbol{p}^{(1)}} + \underline{\boldsymbol{p}^{(2)}}\right)\right)e^{-2\pi i\varphi_i}\Big] \quad [3.32]$$

In matrix form, for each value of $\underline{\boldsymbol{p}}$ for the metamaterial mask in equation [3.32], this becomes:

$$\begin{bmatrix} G_1(\underline{\boldsymbol{k}}) \\ G_2(\underline{\boldsymbol{k}}) \\ G_3(\underline{\boldsymbol{k}}) \end{bmatrix} = \begin{bmatrix} 1 & e^{2\pi i\varphi_1} & e^{-2\pi i\varphi_1} & e^{2\pi i\varphi_1} & e^{-2\pi i\varphi_1} \\ 1 & e^{2\pi i\varphi_2} & e^{-2\pi i\varphi_2} & e^{2\pi i\varphi_2} & e^{-2\pi i\varphi_2} \\ 1 & e^{2\pi i\varphi_3} & e^{-2\pi i\varphi_3} & e^{2\pi i\varphi_3} & e^{-2\pi i\varphi_3} \end{bmatrix} \begin{bmatrix} H(\underline{\boldsymbol{k}})F(\underline{\boldsymbol{k}}) \\ \frac{1}{4}H(\underline{\boldsymbol{k}})F\left(\underline{\boldsymbol{k}} - \alpha\left(\underline{\boldsymbol{p}^{(1)}} - \underline{\boldsymbol{p}^{(2)}}\right)\right) \\ \frac{1}{4}H(\underline{\boldsymbol{k}})F\left(\underline{\boldsymbol{k}} + \boldsymbol{\alpha}\left(\underline{\boldsymbol{p}^{(1)}} - \underline{\boldsymbol{p}^{(2)}}\right)\right) \\ \frac{1}{4}H(\underline{\boldsymbol{k}})F\left(\underline{\boldsymbol{k}} - \boldsymbol{\alpha}\left(\underline{\boldsymbol{p}^{(1)}} + \underline{\boldsymbol{p}^{(2)}}\right)\right) \\ \frac{1}{4}H(\underline{\boldsymbol{k}})F\left(\underline{\boldsymbol{k}} + \alpha\left(\underline{\boldsymbol{p}^{(1)}} + \underline{\boldsymbol{p}^{(2)}}\right)\right) \end{bmatrix} \quad [3.33]$$

Consequently, for three orientations there are three sets of this matrix equation [3.33], and the total G_n's. The spectral components of these G_n's then need to be separated, which is done by multiplying the G_n's by the Hermitian conjugate of the central matrix containing the phases. Separating the components allows the masks to be removed from the final image and the higher resolution information to be retained.

$$\begin{bmatrix} C_1(\underline{\boldsymbol{k}}) \\ C_2(\underline{\boldsymbol{k}}) \\ C_3(\underline{\boldsymbol{k}}) \\ C_4(\underline{\boldsymbol{k}}) \\ C_5(\underline{\boldsymbol{k}}) \end{bmatrix} = \begin{bmatrix} 1 & 1 & 1 \\ e^{-2\pi i\varphi_1} & e^{-2\pi i\varphi_2} & e^{-2\pi i\varphi_3} \\ e^{2\pi i\varphi_1} & e^{2\pi i\varphi_2} & e^{2\pi i\varphi_3} \\ e^{-2\pi i\varphi_1} & e^{-2\pi i\varphi_2} & e^{-2\pi i\varphi_3} \\ e^{2\pi i\varphi_1} & e^{2\pi i\varphi_2} & e^{2\pi i\varphi_3} \end{bmatrix} \begin{bmatrix} G_1(\underline{\boldsymbol{k}}) \\ G_2(\underline{\boldsymbol{k}}) \\ G_3(\underline{\boldsymbol{k}}) \end{bmatrix} \quad [3.34]$$

Where C_n are the separated components, and again there are three sets of equation [3.34] to give the C_n's. This gives more C_n's than for standard SIM, however if $\theta_\beta = 0$, so there is no additional phase shift, and it can be simplified to the standard three C_n's. These separated components are then shifted, this mixes spectral frequencies that are not observable due to the diffraction limit of the imaging system and its PSF with those that are observable. Thus, in Fourier space a greater area of spectral information is covered and thus more information is retained and a higher resolution final image can be produced. The shifts are $\underline{\boldsymbol{0}}$ and $\pm\underline{\boldsymbol{p}}$, for each $\underline{\boldsymbol{p}}$ value, where the base orientation $\underline{\boldsymbol{p}}$ is described below, and the other $\underline{\boldsymbol{p}}$'s are rotations of this base $\underline{\boldsymbol{p}}$.

Where $\underline{\boldsymbol{p}}_j$ are the orientations, and R_j are the rotation matrices used to produce the other orientations.

$$\underline{\boldsymbol{p}} = \frac{1}{2}\alpha\left(\underline{\boldsymbol{p}^{(1)}} - \underline{\boldsymbol{p}^{(2)}}\right) = \alpha\begin{bmatrix}0\\1\end{bmatrix}; \qquad \underline{\boldsymbol{p}}_j = R_j[\tfrac{1}{2}\alpha\left(\underline{\boldsymbol{p}^{(1)}} - \underline{\boldsymbol{p}^{(2)}}\right)] = R_j(\alpha\begin{bmatrix}0\\1\end{bmatrix}) \qquad [3.35]$$

$$\begin{aligned} CS_1(\underline{\boldsymbol{k}}) &= C_1(\underline{\boldsymbol{k}}) \\ CS_2(\underline{\boldsymbol{k}}) &= C_2\left(\underline{\boldsymbol{k}} + \underline{\boldsymbol{p}}\right) \\ CS_3(\underline{\boldsymbol{k}}) &= C_3\left(\underline{\boldsymbol{k}} - \underline{\boldsymbol{p}}\right) \end{aligned} \qquad [3.36]$$

For this expanded SIM, the Fourier kernels that achieve these shifts are not adjusted, except for the different method of defining the $\underline{\boldsymbol{p}}$'s.

These shifted, separated components are then combined via a Wiener filter:

$$S(\underline{\boldsymbol{k}}) = \frac{\sum_{n=1}^{N} OTF_n(\underline{\boldsymbol{k}})^* CS_n(\underline{\boldsymbol{k}})}{\sum_{n=1}^{N}\left|OTF_n(\underline{\boldsymbol{k}})\right|^2 + w} \qquad [3.37]$$

Where: $S(\underline{\boldsymbol{k}})$ is the reassembled image in Fourier space; OTF_n is the n-th shifted OTF (Optical Transfer Function which is the PSF in Fourier space), shifted in the same way as the C_n's are in equation [3.36]; * is the complex conjugate function; N is the total number of image components, typically nine; and w is a noise constant.

This reassembled image in Fourier space is then apodized, which is a mathematical optical filtering technique to smooth discontinuities and particularly ringing artefacts common to SIM imaging, with the desired OTF. In this case, the desired OTF is the desired PSF of the system, so by reducing the width of the PSF by half, it should produce 2× resolution compared to the original widefield image. Finally, the image is then converted from Fourier space to real space, giving a super-resolution reconstructed SIM image.

The MATLAB algorithms for this Sinusoid Product-based SIM is presented in Appendix 6 and 7.

3.4.3 Simulating the patterns

The patterns were simulated as a product of two sinusoids. The primary sinusoid that forms the main ‘stripes’ had a spatial wavelength of 600nm. The secondary sinusoid that forms the blocks within the main stripes had a spatial wavelength of 300nm, and together they form a chequerboard of peaks and troughs. This was rotated to form the two orientations achieved by the metamaterial patterns. Both of the sinusoids were formed on the basis to provide the two orientations, [1, 0] and [0, 1], and three phases, 0, $2\pi/3$ and $4\pi/3$, seen in the metamaterial masks. The simulated masks and actual masks are compared in figure 3.38.

The simulated masks represent how the image reconstruction algorithm models the masks when reconstructing, and the closer this is to the metamaterial masks, the better the image reconstruction quality.

It can be seen that the key ‘stripes’ and ‘blocks’ are achieved, as well as the phases and orientations of the patterns. Moreover, the ‘stripes’ and ‘blocks’ are matched in terms of positioning between the metamaterial and simulated masks. However, the simulated masks have wider, more continuous stripes compared to the more continuous stripes compared to the metamaterial masks. Moreover, only two of the metamaterial patterns have the extra sinusoidal component, whereas the simulated masks all contain the expanded description. This means that the simulation is not identical to the metamaterial masks, but they are potentially more similar than simple sinusoid and the metamaterial masks. This may impact the reconstruction quality, as was the case when using standard SIM image reconstruction, but as the masks are a closer estimate to the actual masks, the image reconstruction quality should be improved. This simulation of the masks is very similar to that seen for the Fourier

Series approach, see figure 3.31, therefore similar results were expected for image reconstruction, however the different mathematical approach would potentially produce improved image reconstructions.

3.4.4 Using simulated patterns

The mathematical process of Sinusoid Product-based SIM described above, is now demonstrated with an example image, simulated microscope PSF, and six simulated Fourier Series masks based upon the metamaterial masks described in Section 3.4.3, utilising the algorithm in Appendix 6.

The example image was that of a sample of human platelets previously used. The nm-to-pixel ratio was 20; the PSF was defined by the parameters: λ = 500nm, n = 1, NA = 1.49; three mask phases were used, φ_i = 0, $2\pi/3$, $4\pi/3$; two mask orientations were used, $\underline{\boldsymbol{p}}$ = [1,0; 0,1]; the spatial wavelengths of the masks were 600nm and 300nm; the noise parameter, w = 1 ; and the width of the desired OTF was half that of the original PSF. These parameters were chosen to optimise the resolution improvement in the final image, see figures 3.23, 3.30 for details of the ground truth image and PSF used.

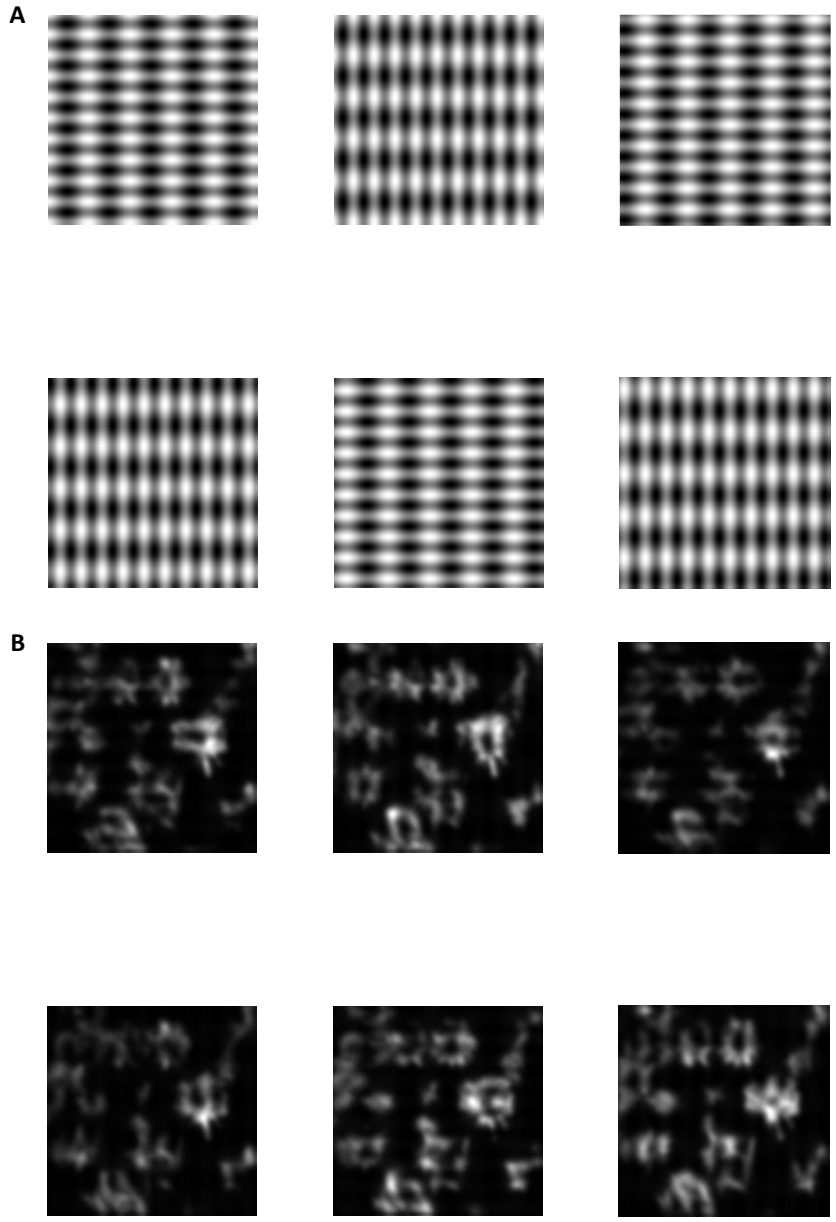

Figure 3.39: A - The six masks used (301×301 pixels), simulating the masks produced by the metamaterial design, three phases were used, φ_i = 0, 2π/3, 4π/3, two mask orientations were used, $\underline{\boldsymbol{p}}$ = [1,0; 0,1]; B – the six acquired images (301×301 pixels), created by multiplying the masks and the ground truth image, and then convolving with the PSF.

A

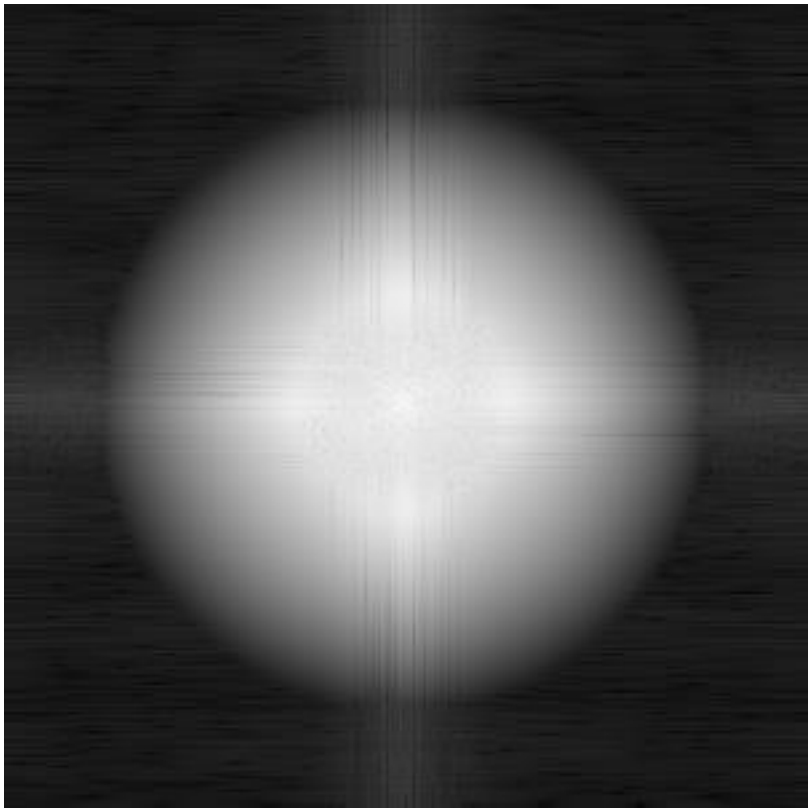

B

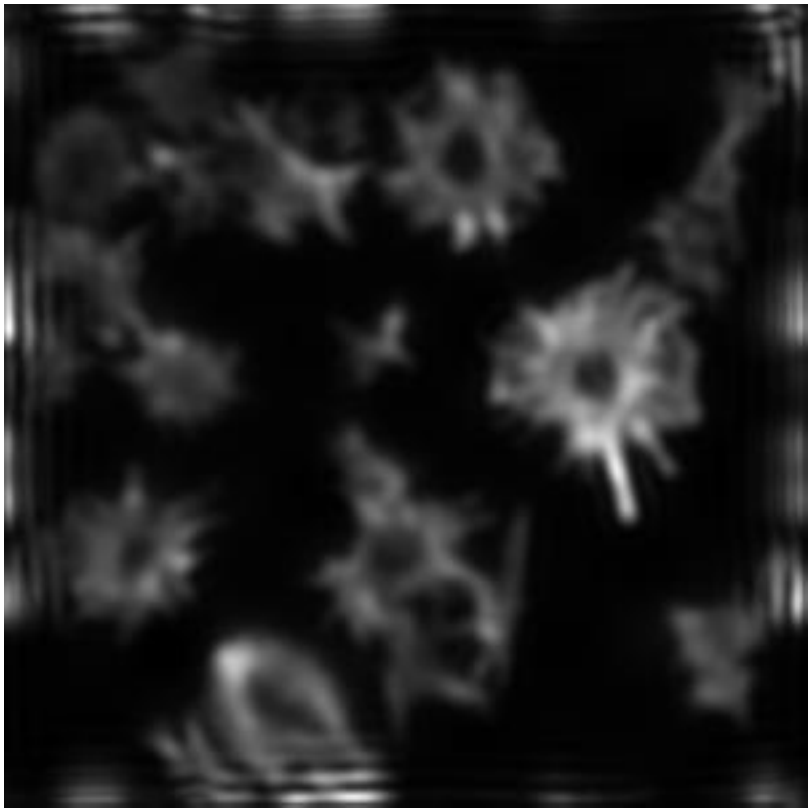

Figure 3.40: A – The reconstructed image in Fourier space (301×301 pixels); B – the final reconstructed image (301×301 pixels).

These simulated masks were also used within the standard SIM reconstruction algorithm, to provide a basis of comparison when using a set of atypical masks, as opposed to the set of metamaterial masks where only two of the masks clearly contain additional components beyond a simple sinusoid.

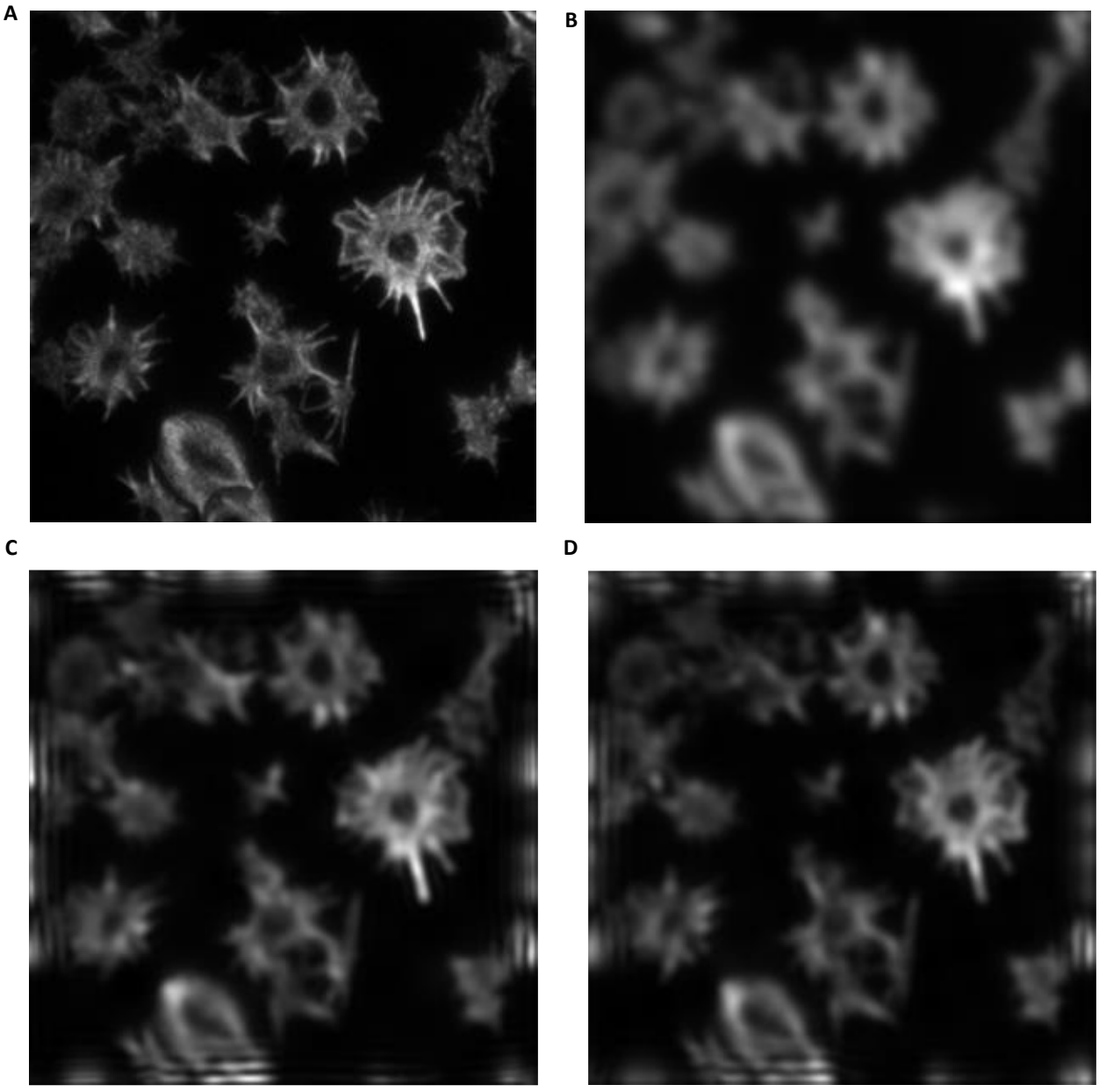

Figure 3.41: A – Ground truth image, platelet image, courtesy of Dr Steve Thomas, University of Birmingham, UK; B – the widefield image, created by convolving the ground truth image with the PSF; C – the image as reconstructed using the Sinusoid Product-based SIM reconstruction algorithm; D – the image as reconstructed using the standard SIM reconstruction algorithm, all (301×301 pixels).

It can be seen that there are artefacts in both the Sinusoid Product-based and the standard SIM reconstructions at the image edges. However there is also resolution improvement in both compared to the widefield image. There is minimal difference in image quality between the two reconstructions, although the Sinusoid Product-based image reconstruction is potentially marginally better. The use of the more complex masks has produced greater resolution improvement than the use of the actual metamaterial masks, see figure 3.41, with both standard SIM and Sinusoid Product-based image reconstruction. This could be because the extra sinusoidal term in the expanded simulated masks has expanded the coverage of the masks in Fourier space, meaning more high resolution information is retained in the reconstructed image. Thus compensating for only six images being used to reconstruct from as opposed to the typical nine required for resolution enhancement. The Sinusoid Product-based SIM reconstruction method was further investigated to see if it was suitable as a SIM image reconstruction method.

3.4.5 Using the metamaterial patterns

The mathematical process of Sinusoid Product-based SIM described above, is now demonstrated with an example image, simulated microscope PSF, and the six metamaterial masks described in Section 3.4.3, utilising the algorithm in Appendix 7.

The example image was that of a sample of human platelets previously used. The nm-to-pixel ratio was 20; the PSF was defined by the parameters: $\lambda = 500$nm, $n = 1$, $NA = 1.49$; three mask phases were used, $\varphi_i = 0, 2\pi/3, 4\pi/3$; two mask orientations were used, $\boldsymbol{p} = [1,0; 0,1]$; the spatial wavelengths of the masks were 600nm and 300nm; the noise parameter, $w = 1$; and the width of the desired OTF was half that of the original PSF. These parameters

were chosen to optimise the resolution improvement in the final image, see figures 3.23, 3.30 for details of the ground truth image and PSF used.

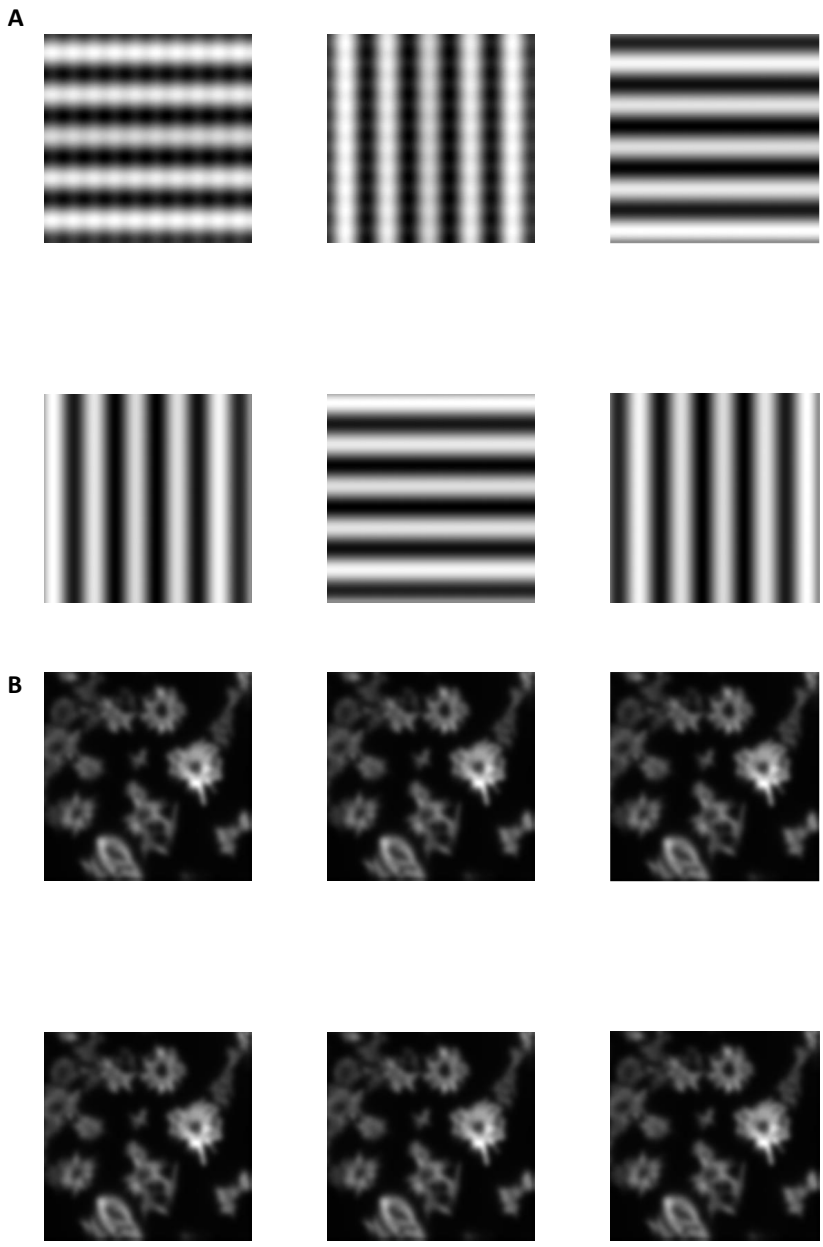

Figure 3.42: A - The six masks used (301×301 pixels), produced by the metamaterial design, three phases were used, $\varphi_i = 0, 2\pi/3, 4\pi/3$, two mask orientations were used, $\underline{\boldsymbol{p}} = [1,0; 0,1]$; B – the six acquired images (301×301 pixels), created by multiplying the masks and the ground truth image, and then convolving with the PSF.

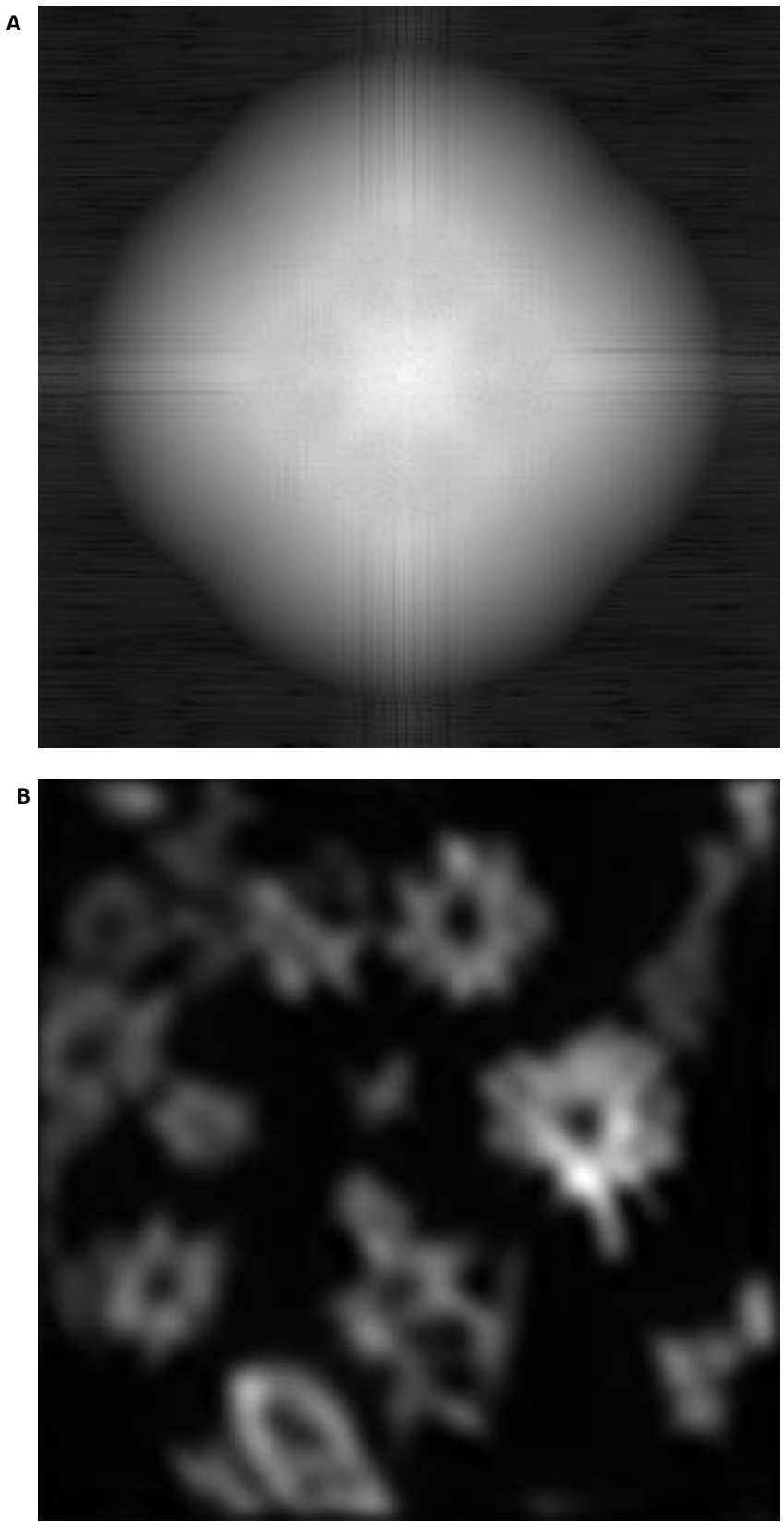

Figure 3.43: A – The reconstructed image in Fourier space (301×301 pixels); B – the final reconstructed image (301×301 pixels).

The metamaterial masks were also used within the standard SIM reconstruction algorithm, see Section 3.2.8. This reconstruction is shown alongside the Sinusoid Product-based reconstruction to provide a basis of comparison between the two methods when using the metamaterial masks.

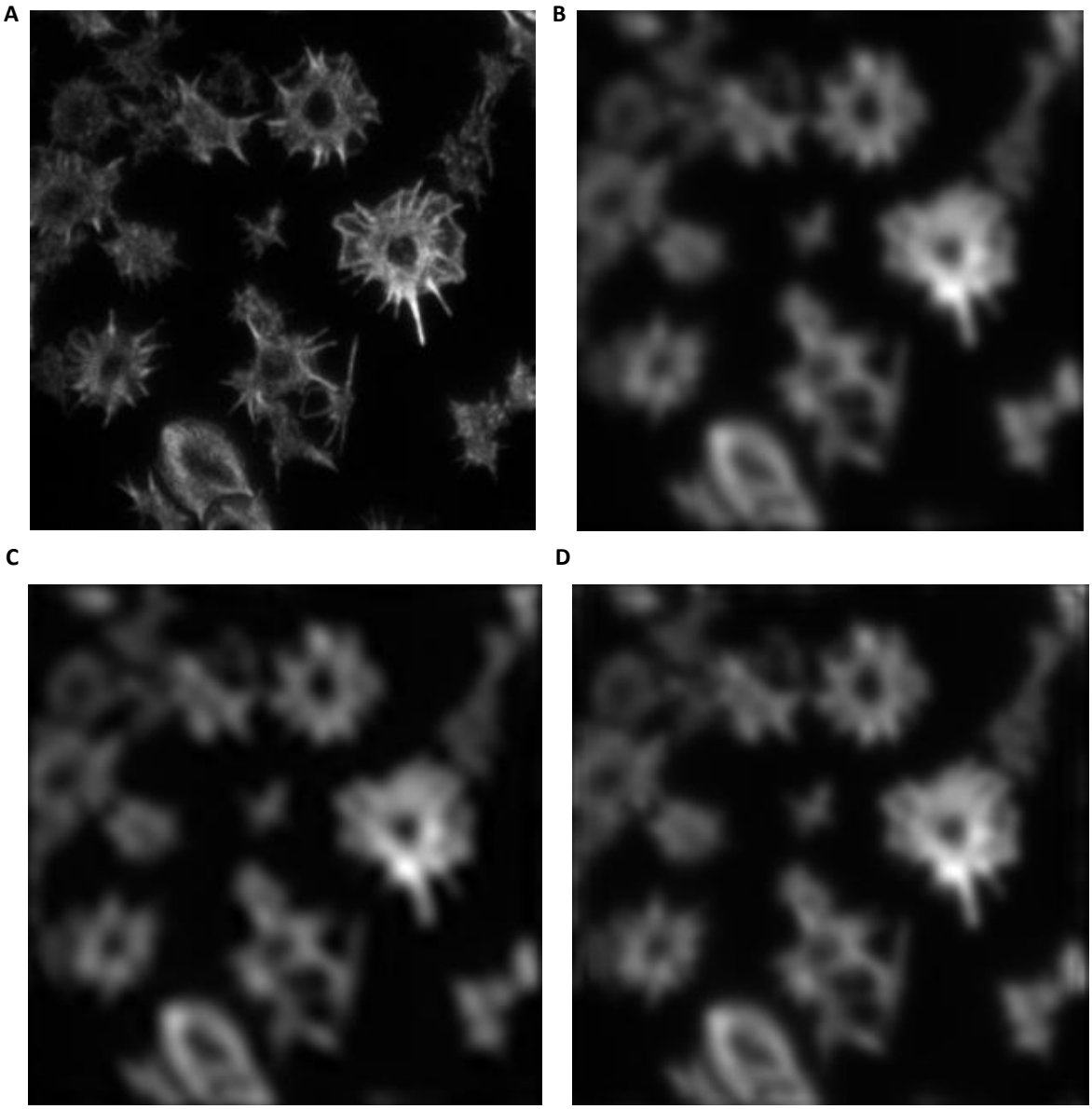

Figure 3.44: A – Ground truth image of platelets, courtesy of Dr Steve Thomas, University of Birmingham, UK; B – the widefield image, created by convolving the ground truth image with the PSF; C – the image as reconstructed using the Sinusoid Product-based SIM reconstruction algorithm; D –the image as reconstructed using the standard SIM reconstruction algorithm, all (301×301 pixels).

It can be seen that the standard SIM reconstruction method the Sinusoid Product-based method were both unsuccessful, as no resolution improvement can be seen. Indeed the Sinusoid Product-based method has produced an image reconstruction worse than the widefield image. This is probably due to the metamaterial patterns being more similar to a standard sinusoid than the Sinusoid Product-based expansion, meaning the expanded algorithm produced artefacts as the masks and the description in the algorithm were not sufficiently similar. In addition, as before for the Fourier Series expansion, the metamaterial masks show little impact on the acquired images, see figure 3.47. This may be because there is not sufficient contrast between the peaks and troughs of the pattern; this would also lessen any resolution enhancement, as there would be a lesser interaction between the masks and the sample meaning less high resolution information would be retained in the final image. Moreover, the spatial wavelength may be too long to allow for super-resolution reconstruction.

3.4.6 Discussion

Although the mathematical theory of the Sinusoid Product-based expansion to the SIM reconstruction algorithm was robust, it has not proved successful when used with the metamaterial masks. This is potentially because the metamaterial masks are too close to being a simple sinusoid, there being too few masks, or the spatial wavelength of the masks being too large.

However, the use of simulated masks based upon the metamaterial masks was able to produce resolution enhancement, both when used in the Sinusoid Product-based and the standard SIM image reconstruction algorithms. This was in contrast to the Fourier Series image reconstruction which had strong artefacts. This was in spite of only six masks being used and could have potential for reducing the number of masks needed for standard SIM image reconstruction. Furthermore, it shows there is potential for using expanded SIM reconstruction algorithms, although they may be of greater use with masks that are more different from the standard sinusoid.

3.5 Conclusions

The results of the various SIM image reconstruction methods, using both the metamaterial patterns produced in simulation, and those simulated in MATLAB, produced in this Chapter can be summarised as follows:

- The standard SIM image reconstruction algorithm was able to successfully reconstruct images using simulated sinusoidal masks, see figures 3.11 & 3.19.
- The image reconstructions in standard, Fourier Series and Sinusoid Product-based SIM, using the metamaterial masks were all unsuccessful, showing no resolution improvement compared to the widefield image, see figures 3.30, 3.36 & 3.37.
- The image reconstructions in standard SIM, using simulated approximations of the metamaterial masks simulated using both the Fourier Series and Sinusoid Product approaches, were successful. They showed distinct resolution improvement compared to the widefield image, although artefacts were present at the edges of the reconstructed images, see figures 3.34 & 3.41.
- The image reconstruction in Fourier Series SIM, using simulated approximations of the metamaterial masks simulated using the Fourier Series approach, was partially successful. It showed some resolution improvement compared to the widefield image, although strong artefacts were present across the reconstructed image, see figure 3.34.
- The image reconstruction in Sinusoid Product-based SIM, using simulated approximations of the metamaterial masks simulated using the Sinusoid Product approach, was successful. It showed distinct resolution improvement compared to the widefield image, although artefacts were present at the edges of the reconstructed

image. This resolution improvement was similar to that seen using the same masks in standard SIM, see figure 3.41.

The image reconstructions performed using the metamaterial masks or simulated approximations of the metamaterial masks used the same sample image, PSF parameters, number of masks, and spatial wavelengths. However, only the simulated approximations of the metamaterial masks successfully reconstructed across both standard SIM and the expanded SIM methods, the metamaterial masks were unsuccessful in all reconstruction methods. Consequently, the cause of the unsuccessful image reconstructions using the metamaterial masks is due to these masks. Thus, it is not due to the number of masks used or the spatial wavelength of the masks, as this was the same across all of the reconstructions.

Moreover, both the standard and the Sinusoid Product-based SIM image reconstruction methods were successful when using simulated approximations of the metamaterial masks, the Fourier Series method was less successful. Therefore, the method of modelling the masks is also not the cause of the unsuccessful image reconstructions using the metamaterial masks. Thus, it can be concluded that the metamaterial masks themselves are at fault, potentially due to the poor modulation of the patterns, something that the simulated approximations of the metamaterial masks did not suffer from. It could also be because the metamaterial masks are too close to being a simple sinusoid, and so the number of masks impacted the image reconstructions more than for the simulated patterns, which were more complex and thus their more complex Fourier components may have compensated for the number of masks used for reconstruction.

In conclusion, although the mathematical theory of the Fourier Series and Sinusoid Product-based expansions to the SIM reconstruction algorithm were robust, they did not prove successful when used with the metamaterial masks. The standard SIM reconstruction was also unsuccessful, as again no resolution improvement was seen. This could be because there being too few masks, six instead of nine, or the modulation of the masks being too small, both of which could have impacted the expanded SIM reconstructions. The expanded SIM methodology is limited as the masks need to be approximately the same, so changes in spatial wavelength or type of pattern between masks, are not able to be included. The use of the metamaterial masks and the best image reconstruction method could be further investigated experimentally, with a built metalens.

The results when using simulated masks based upon the metamaterial masks were more promising. In particular, resolution enhancement was seen with these masks both when used in the Sinusoid Product-based and the standard SIM image reconstruction algorithms. This was in contrast to the Fourier Series image reconstruction which had strong artefacts. This was in spite of only six masks being used and could have potential for reducing the number of masks needed for standard SIM image reconstruction. This could have a great impact in terms of computational time required to reconstruct the images, and the acquisition time for SIM images. Furthermore, it shows there is potential for using expanded SIM reconstruction algorithms, although they may be of greater use with masks that are more different from the standard sinusoid.

Chapter 4: Fabricating & Characterising the Metalens

4.1 Introduction

This Chapter covers the fabrication and subsequent characterisation of the metamaterial design, developed via simulation in CST MWS, and described in Chapter 2. The metamaterial is the main component of the metalens, which forms the crucial component of the proposed TIRF-SIM type microscope, that should allow for super-resolution imaging with a structured evanescent field. The fabrication of the metalens was done in collaboration with Dr Alex Robinson, School of Chemical Engineering, University of Birmingham, UK, in terms of fabrication protocol and design; and Dr Mark Rosamond and Professor Edmund Linfield of the School of Electronic and Electrical Engineering, University of Leeds, UK, in terms of fabrication work.

The principal techniques used in fabrication of the metamaterial were electron-beam lithography and etching, with both positive and negative resist techniques trialled. Small area (~6×6μm) prototypes of the metamaterial were initially created to optimise the fabrication parameters. These were then followed by larger area fabrication (~100×100μm) to test fabrication over large areas, and to scale up to the final area size of 100×100μm, suitable for testing the proposed microscope. This size could be potentially be scaled up further, should the prototypes prove successful, to create a larger metalens, suitable for a larger field of view of a sample. Subsequent characterisation involved imaging of the metamaterial with electron microscopy, testing with spectroscopy techniques to determine

the resonant frequency of the metamaterial, and optical testing within a brightfield microscopy setup to test the efficacy of the metalens for TIRF-SIM type imaging.

Successful fabrication of the metamaterial, as determined by the characterisation techniques, was aimed to be followed by implementation of the metalens within an optical setup to create the proposed TIRF-SIM type microscope.

4.1.1 Aims

The aims of this Chapter of the thesis were as follows:

- Demonstrate the feasibility of fabricating the metamaterial design.
- Develop a fabrication protocol.
- Image the metamaterial with SEM to determine how well it has been fabricated.
- Test the metamaterial with techniques including FTIR to determine its properties.
- Compare the experimental findings to the simulations.
- Evaluate the feasibility and efficacy of the metamaterial design, before implementing the proposed microscope.

4.2 Metalens Design

4.2.1 Introduction & Requirements

The design of metamaterial and dielectric spacer that form the metalens required for the proposed microscope design are discussed in Chapter 2. The key points that were considered in the design were ensuring the metamaterial produced approximately sinusoidally-structured evanescent light, that the dielectric spacer layer was sufficient to ensure that the sample would be exposed only to the structured light and not the stronger, distorted patterns at the metamaterial surface, as seen in the CST MWS simulation work in Chapter 2, and that the design was feasible in terms of fabrication. The fabrication techniques chosen when determining feasibility were electron-beam lithography and etching techniques.

Electron-beam lithography is a fabrication technique that uses a focussed beam of electrons to pattern onto a resist on top of a substrate. The exposed, or non-exposed, areas can then be developed, and in this case then etched. Feature sizes of a few nm's can be patterned depending on the instrument and resists used, but areas of only ~100×100μm to 1×1mm can typically be patterned[216]. The alternative technique considered was focused ion beam lithography, which is very similar to electron-beam lithography but uses a beam of ions instead of electrons[208]. Electron-beam lithography was chosen due to the facilities available and the small feature sizes that are achievable, additionally it was deemed more suitable for the patterning the 'H' shapes than focused ion beam lithography, due to the relative complexity of the design.

4.2.2 Design Schematics

The metamaterial and metalens designs are summarised in figure 4.1.

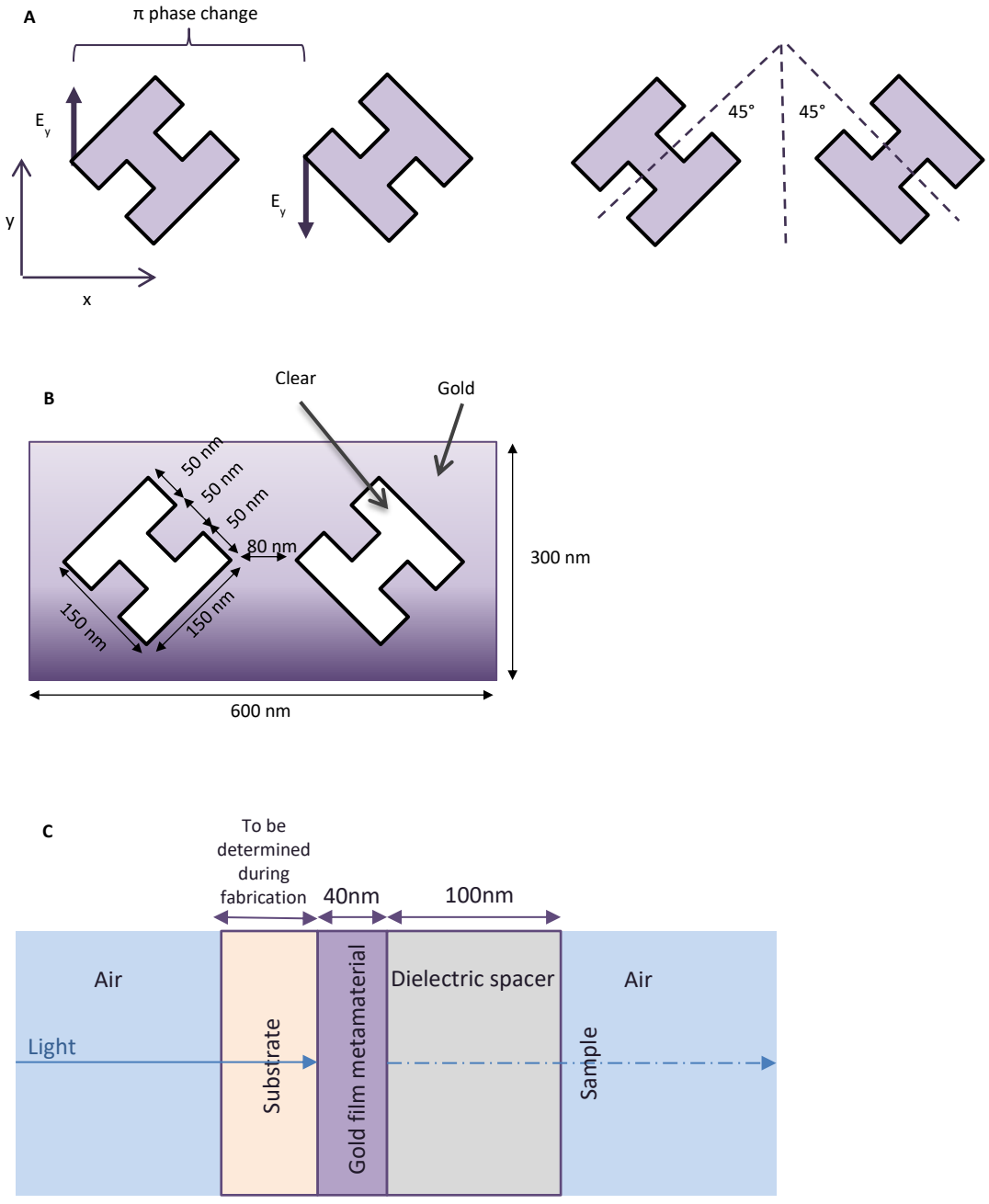

Figure 4.1: A – Schematic of the geometry of the 'H' shape unit cell; B – schematic of the dimensions of the unit cell; C – schematic of the metalens components.

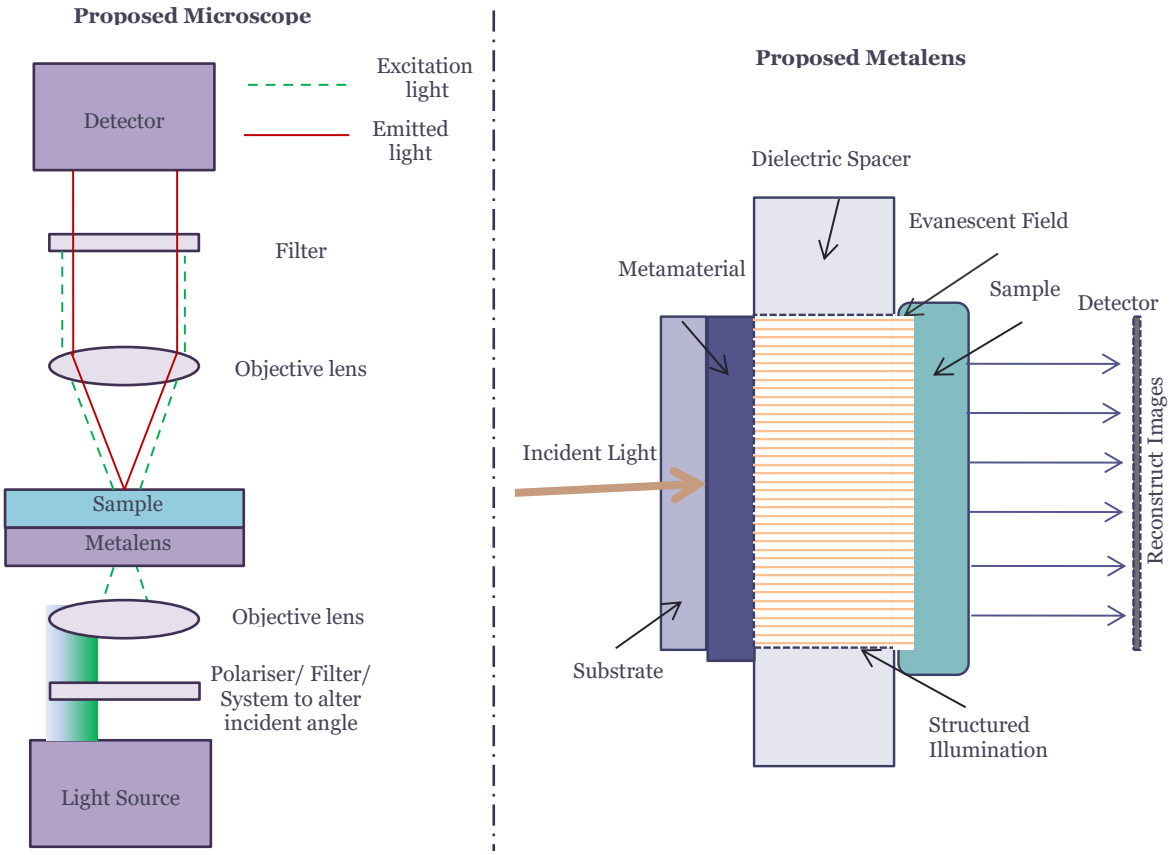

Figure 4.2: Diagram outlining the proposed microscope and metalens, including light paths and key components[1,2].

4.3 Metamaterial Fabrication

4.3.1 Introduction & Requirements

Correct fabrication of the metamaterial was key to its final functionality and fitness for purpose. As already discussed the key fabrication techniques utilised were electron-beam lithography and etching. The general fabrication process was to sputter coat the gold film onto the glass substrate, a layer of the resist was then added onto the gold-glass substrate and patterned with electron-beam lithography. This was then developed and the gold etched to produce the cut-out 'H' shapes. Initial prototypes of the design using PMMA on a glass substrate (~6×6μm in size) were trialled using the non-commercial electron beam lithography system (combines a Philips XL 30 field emission SEM with Raith Elphy Plus hardware that interfaces with the SEM to run the patterns, capable of achieving sub-50nm feature size) at the School of Physics & Astronomy, University of Birmingham, UK. This was done to investigate if this instrument was capable of achieving the desired 50nm feature size for the desired 'H' shapes, pattern areas of the 'H' shapes in general.

However, due to mechanical break-downs, the majority of fabrication work was carried out on the author's behalf by Dr Mark Rosamond and Professor Edmund Linfield of the School of Electronic and Electrical Engineering, University of Leeds, using a JEOL JBX-6300FS electron-beam lithography machine. As metamaterial fabrication was not done using gold at the University of Birmingham, these results were only used to inform the simulation work done to investigate the effects of imperfect fabrication on the metamaterial properties, see Chapter 2 Section 2.6.4.

The requirements of the fabrication were to achieve the 50nm feature size of the ‘H’ shapes, and successfully fabricate the metamaterial design outlined above as accurately as possible. Moreover, the gold film of the desired thickness (40nm) had to be successfully adhered to a dielectric substrate, and a dielectric spacer of appropriate depth (100nm) to be layered on top of the gold film. The fabrication of the metamaterial design needed to be uniform and consistent across the fabrication area, so that the structured illumination would be produced uniformly.

A further consideration was attaching a sample to the metalens design on the dielectric spacer layer. By directly attaching a sample, the imaging capacity of the metalens could be evaluated more easily, as a sample could be used to determine the sensitivity and resolution capabilities of the metalens. The metalens without a sample would not be able to tested in terms of resolution and sensitivity. Consequently, the fabrication design was amended to include a metal grating sample, with varying metal strips of known dimensions.

4.3.2 Metamaterial design with integrated sample

The amended metamaterial design with an integrated sample is shown in figure 4.3. The Chromium grating sample varies in pitch across the metamaterial, so that samples of different dimensions could be imaged, meaning that the resolution of the metalens and the resolution improvement of the SIM imaging could be evaluated. The inclusion of the grating required larger areas of metamaterial to be fabricated as prototypes, compared to the ~6×6µm prototypes fabricated at the University of Birmingham, these were 100×100µm.

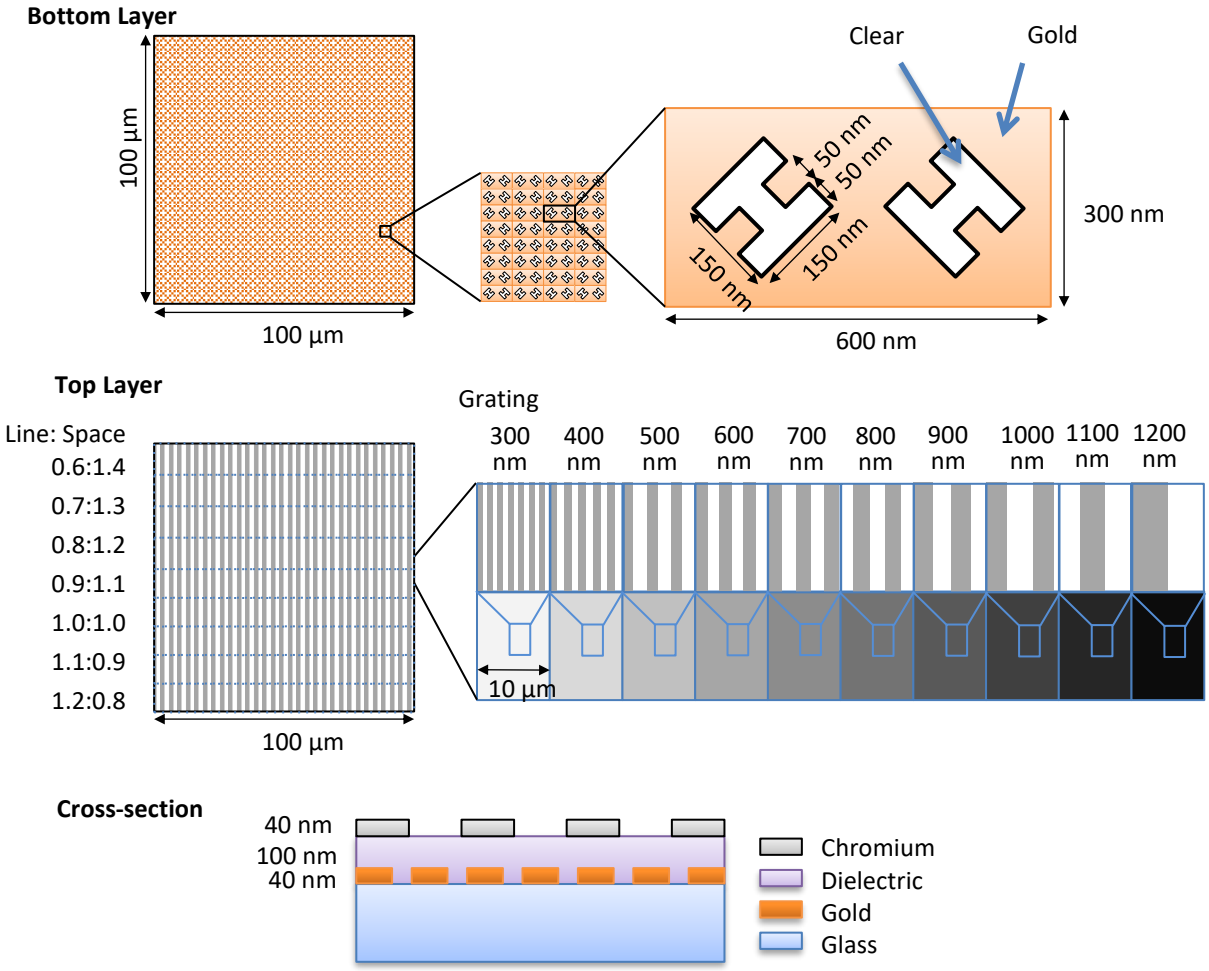

Figure 4.3: Diagram outlining the metamaterial design, the Chromium grating sample and the whole metalens fabrication, created in collaboration with Dr Alex Robinson, School of Chemical Engineering, University of Birmingham, UK.

4.3.3 Fabrication procedure

The basic fabrication procedure was as follows:

Forming the base of the metalens:

A) Gold coat the substrate by sputter coating it, forming the base for creating the metamaterial. A thin layer can be incorporated between the substrate and the gold to improve adhesion.

Creating the H-shapes that give the metalens its functionality sample:

B) Spin resist onto the gold. A thin anti-charging metal layer can be evaporated onto the resist to improve patterning of the gold, but must be removed with the resist.

C) Expose the H shapes in the resist using electron-beam lithography, to act as a template to create them in the gold.

D) Etch the gold, creating the metamaterial design. Remove the resist.

Creating a surface for a sample, and the dielectric spacer:

E) Spin coat Hydrogen Silsesquioxane (HSQ), which is a negative tone electron-beam resist, and use a fluorinated wafer to planarise the layer with pressure. This creates the flat surface required for the sample, and forms the dielectric spacer layer.

F) Bake HSQ and release planarising wafer. This removes unwanted components.

Creating the grating sample:

G) Spin positive resist (150 nm PMMA), to form a template for the grating sample.

H) Align and expose the gratings with electron-beam lithography, this also converts the HSQ

into silicon dioxide.

I) Chromium coat and lift-off, forming the grating sample.

The electron-beam lithography equipment used was the JEOL JBX-6300FS at the School of Electronic and Electrical Engineering, University of Leeds, UK. Fabrication was carried out by Dr Mark Rosamond and Professor Edmund Linfield of the School of Electronic and Electrical Engineering, University of Leeds, UK.

Variations upon this fabrication procedure were also investigated to optimise the fabrication. The original glass substrate was replaced with quartz, and the original 100nm PMMA resist was replaced by ma-N2403 (85 nm), and gold and aluminium (10 nm) were used as anti-charging layers added between the gold and the substrate. A chromium layer was also tried to improve adhesion of the gold to the substrate.

4.3.4 Fabrication issues

There were multiple issues with fabrication of the metamaterial that limited its success. Some of these problems that impacted the fabrication quality are detailed below, as imaged with SEM.

The fabrication protocol described above was mostly successful in producing the ‘H’ shape unit cell as a cut out from a gold film, with 50nm feature size, across 100×100μm areas, as can be seen in SEM images taken of the metamaterial, see figure 4.5. However, consistency of the fabrication was not achieved. The accuracy of the ‘H’ shapes was varied, with often ragged edges or parts of the ‘H’ not being patterned. These defects varied between different fabrication attempts and across the patterned areas, as can be seen in SEM images taken of the metamaterial, see figure 4.6.

There were also multiple issues with adherence between the gold and the substrate, resulting in sections of the gold not adhering and the subsequent stages of the fabrication then resulting in these sections being removed, leaving large voids in the metamaterial. This was attempted to be remedied by changing the substrate from glass to quartz and adding a chromium layer between the gold and the substrate, but with limited success as adhesion was still an issue.

Furthermore, the lift off stage required often deformed the gold film as seen in SEM images taken of the metamaterial samples, see figure 4.7, making the metamaterial unusable. Consequently, adding the chromium grating layer was not able to be achieved, making testing the metamaterial in an optical microscopy setup more challenging in terms of investigating resolution and sensitivity of the proposed imaging system. The prototypes fabricated consisted only of the substrate and the patterned gold film layer, and the results of these fabricated prototypes are discussed below.

4.4 Testing the Metamaterial Design

4.4.1 Introduction

Having fabricated prototype samples of the metamaterial, in spite of defects and problems with the fabrication, the metamaterial was then analysed to determine how much of an impact the defects had on the functionality of the metamaterial. This included: imaging with Scanning Electron Microscopy (SEM) to look at the fabrication quality, testing with Fourier Transform Infra-Red Spectroscopy (FTIR) to investigate the frequency response and find its resonant frequencies, and testing in a non-commercial optical microscopy setup to test its suitability for optical microscopy and SIM.

4.4.2 Sample Details

Early prototypes were fabricated that informed the fabrication process, the difference between the early prototypes and the final fabricated metamaterial are shown below, see figure 4.6. The first metamaterial fabrications at the University of Birmingham, were used to check that the metamaterial design could be patterned using electron-beam lithography which it could, but as they were fabricated not using gold, were then only used to inform the simulation work done to investigate the effects of imperfect fabrication on the metamaterial properties, see Chapter 2 Section 2.6.4. The first prototypes fabricated with gold, done at the University of Leeds, demonstrated that adhesion between the resist and the gold was a major challenge, but again showed that the metamaterial design could be patterned using electron-beam lithography and the general fabrication protocol, although the ‘H’ shapes were imperfect. This was improved by changing the dielectric substrate from glass to quartz, and adding an anti-charging layer on top of the resist.

The final metamaterial sample, as already discussed did not include the chromium grating for use as an imaging sample due to fabrication issues.

The final fabricated metamaterial sample consisted of 100×100μm areas of the 'H' shape unit cell metamaterial design repeated 160 times. The difference between each instance of the pattern was a combination of exposure dose and the programmed width of the 'H' shapes from the electron-beam lithography machine. The original metamaterial design was 50nm wide but this was patterning as larger than 50nm at all doses, suggesting overexposure of the resist. Therefore, the width of the 'H' was varied between 50nm and 22nm to reduce its width. This gave 20 doses each with 8 widths. This was done to find the optimal patterning parameters for the electron-beam lithography stage of fabrication.

The substrate used was a quartz substrate, onto which the metamaterial gold film (40nm) was coated, with a ma-N 2403 (a negative resist for electron beam lithography and etching metals, available from Micro Resist Technology[225]) (85nm) resist and aluminium (10nm) as an anti-charging layer. The ma-N 2403 resist was exposed using electron-beam lithography and then etching was used to create the metamaterial.

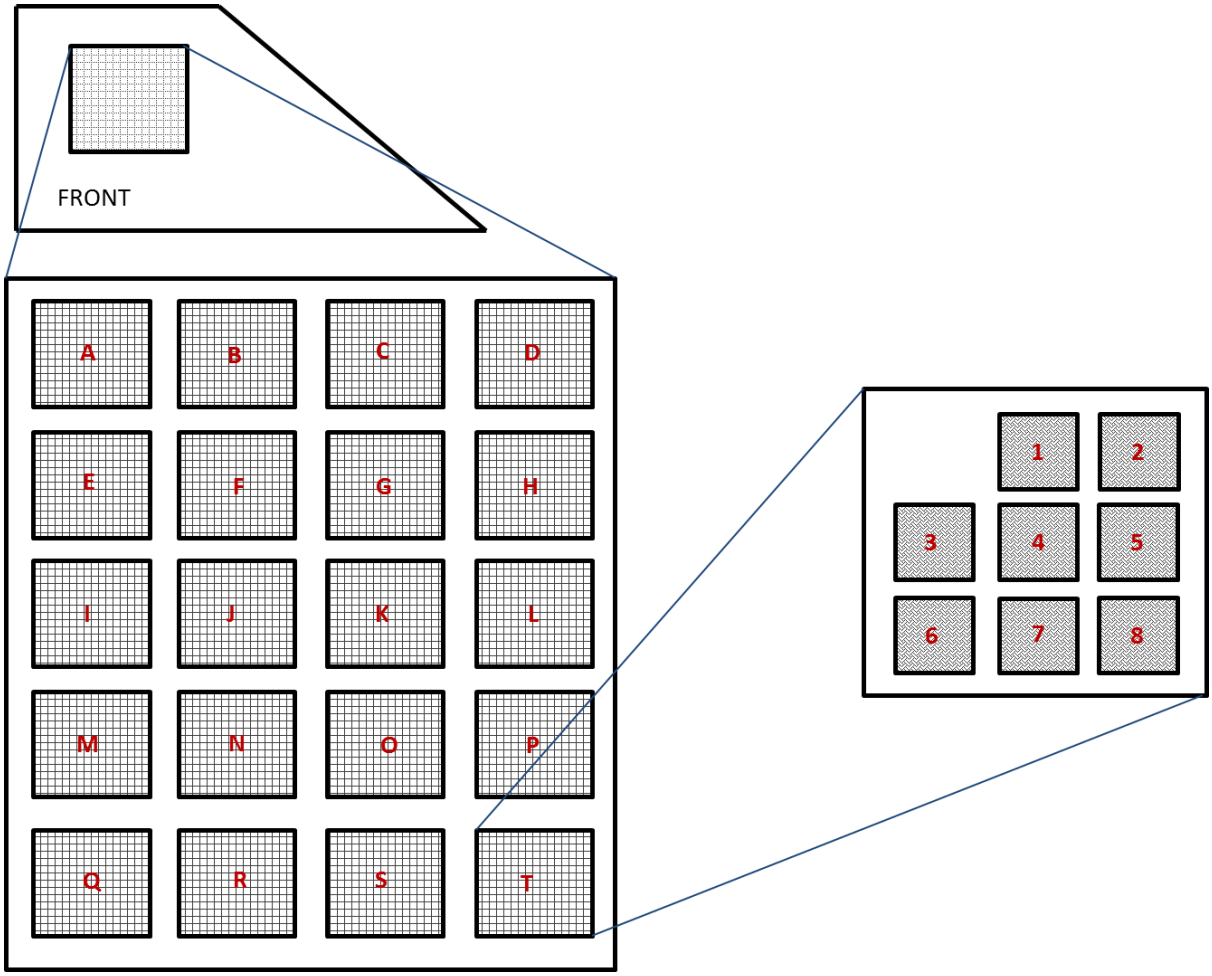

Figure 4.4: Diagram outlining the final metamaterial sample. The sample areas A – T are the different doses used during patterning with electron-beam lithography, with A the highest dose and T the lowest dose. Within the lettered sample areas are nine patterned areas of the metamaterial design, each 100×100μm in size. These nine areas are different programmed widths of the 'H' shapes, varying between 50nm (8) and 22nm (3).

4.4.3 SEM Imaging Results

The SEM images were taken in order to determine fabrication success. Key aspects that were looked at were the presence of defects across the whole metamaterial area, including over- or under-exposure of the metamaterial design, as well as areas of poor adhesion between the gold and the dielectric substrate, and areas where the patterning had not been successful. The accuracy of the metamaterial design at the individual 'H' shape level was also analysed, as deviation from a perfect 'H' shape impacts upon the metamaterials properties as seen in simulation, see *Chapter 2*.

SEM images were taken by the author using a Philips XL-30 ESEM at the Centre for Electron Microscopy, University of Birmingham, UK, and by Dr Mark Rosamond of the School of Electronic and Electrical Engineering, University of Leeds, UK using a Zeiss EVO MA15 SEM.

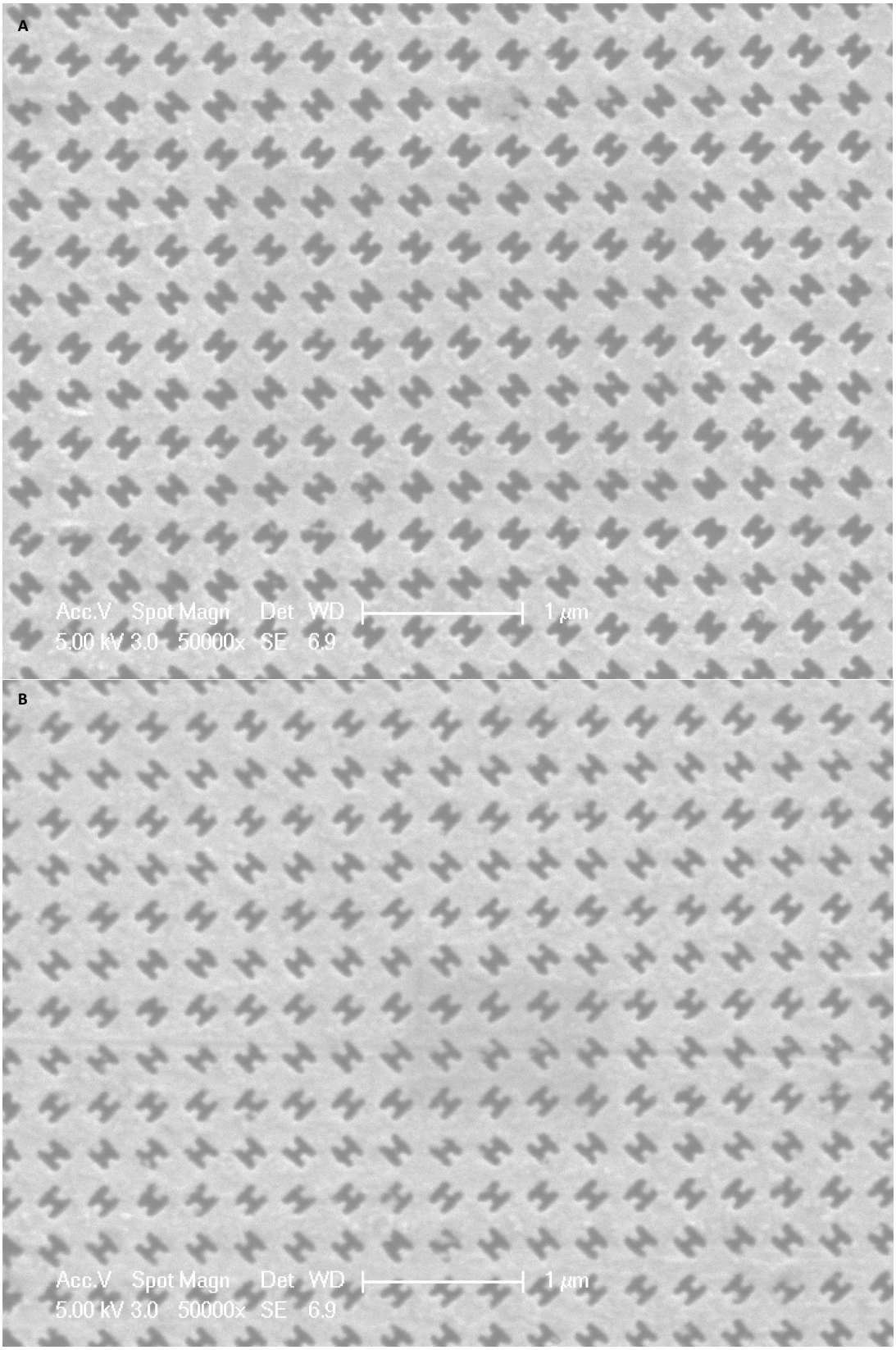

Figure 4.5: SEM images of the metamaterial sample, areas: A – G7, B – E3. Images were taken by the author using a Philips XL-30 ESEM at the Centre for Electron Microscopy, University of Birmingham, UK.

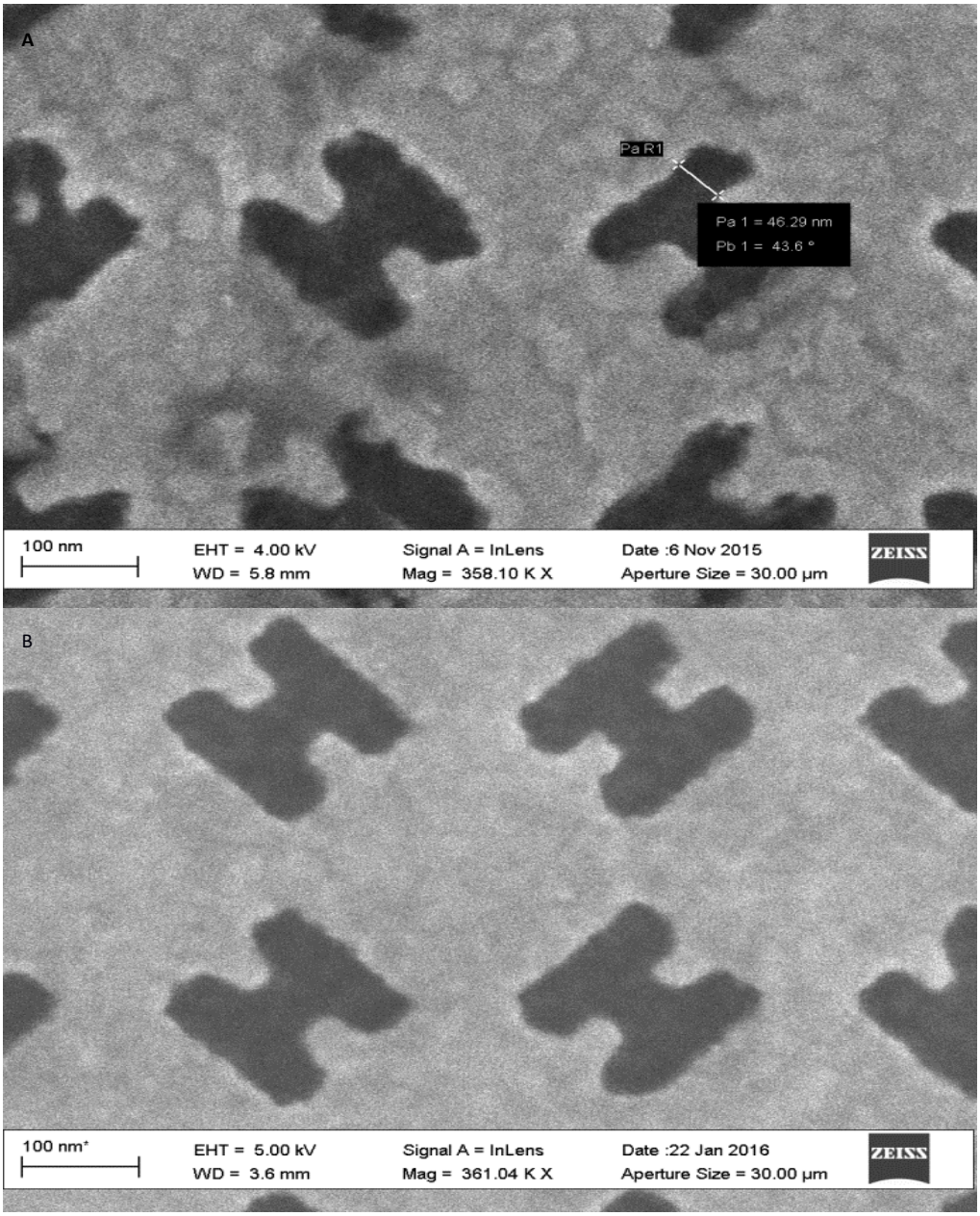

Figure 4.6: SEM images of the metamaterial samples demonstrating improvement in accuracy of the 'H' shape fabrication between A & B. A is an earlier prototype sample, not used for further results. The samples seen in A & B are equivalent except A used a gold charge dissolution layer and B used an aluminium charge dissolution layer, but B shows much more accurate fabrication of the 'H' shapes with fewer defects, both samples still suffered from large scale adhesion problems and defects. Images were taken by Dr Mark Rosamond of the School of Electronic and Electrical Engineering, University of Leeds, UK using a Zeiss EVO MA15 SEM.

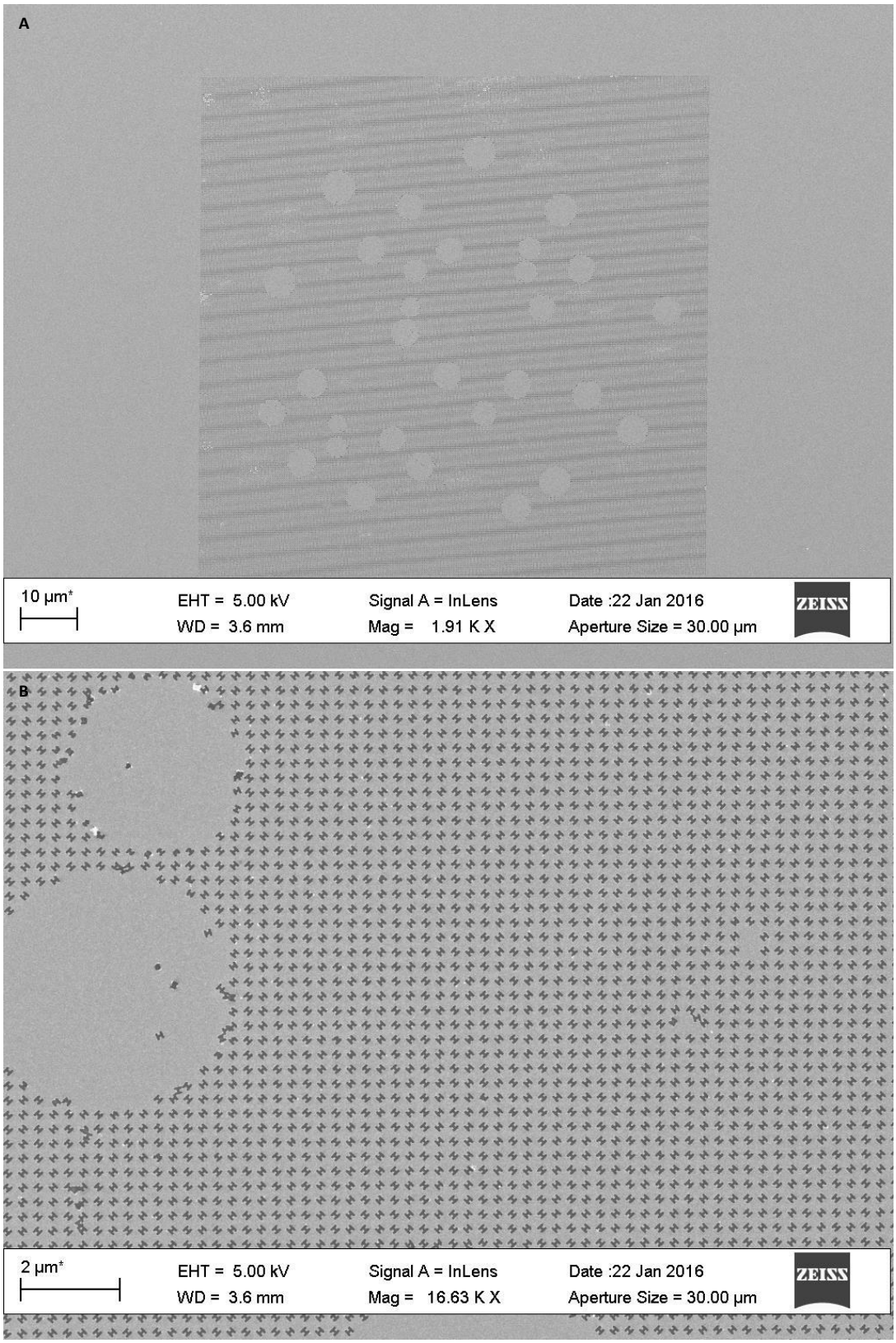

Figure 4.7: SEM images of the metamaterial sample demonstrating issues with fabrication, particularly adhesion between the gold film and the substrate. Images were taken by Dr Mark Rosamond of the School of Electronic and Electrical Engineering, University of Leeds, UK using a Zeiss EVO MA15 SEM.

It can be seen that the desired ‘H’ shape was able to achieved fairly accurately, although less crisply than in simulation. Moreover, that the aluminium anti-charging layer improved the patterning accuracy compared to a gold anti-charging layer, as seen in figure 4.6. However, ‘H’ shape was not consistently achieved, and even in the most successful fabrications, see figure 4.6B, the ‘H’ shapes were still rough around the edges.

In addition, large scale defects can be clearly seen, see figure 4.7. These defects are caused by poor adhesion between the resist and the gold film with substrate, and deformation of the gold film during lift-off of the resist and anti-charging layer. Further adjusting the fabrication procedure could ameliorate these defects, and to this end variations on the fabrication protocol and the materials used were tried. However, the best results were produced with the sample described here.

Nevertheless, the SEM images demonstrate that the metamaterial can be fabricated, and the effects of the roughness and defects can only be determined by testing the metamaterial with techniques such as FTIR.

4.4.4 FTIR Spectroscopy

The areas of the metamaterial prototype, as seen in figure 4.4, with the fewest defects were then tested using FTIR spectroscopy. FTIR was utilised to determine the frequency response of the metamaterial and look for its resonant frequencies. FTRIR measurements were taken using both horizontally (x) polarised and vertically (y) polarised light relative to the sample. This was in order to see if there is a difference between the two polarisations in terms of the frequency response. This FTRIR data was also compared to data produced by simulations in CST MWS. The CST MWS simulations were of a unit cells with periodic boundary conditions to simulate a larger (approximately infinite) area of metamaterial. The simulations included quartz (SiO_2) as the substrate and air as the rest of the simulation volume, thus matching the fabricated metamaterial as closely as possible. In addition, simulations were carried out for both x- and y-polarised light, and the frequency response data was collected at the extremity of the simulation volume to emulate the conditions in the FTIR.

The sample areas chosen for data collection with the FTIR were the areas with the least visible large-area defects, as determined by SEM imaging and imaging with the brightfield microscope integrated within the FTIR system.

FTIR data was acquired using a Vertex 70/70v FTIR spectrometer with HYPERION 1000 Microscope, with LN-MCT detector and CaF_2 beam splitter, in transmission mode, at the Metamaterials Research Centre, School of Physics & Astronomy, University of Birmingham, UK.

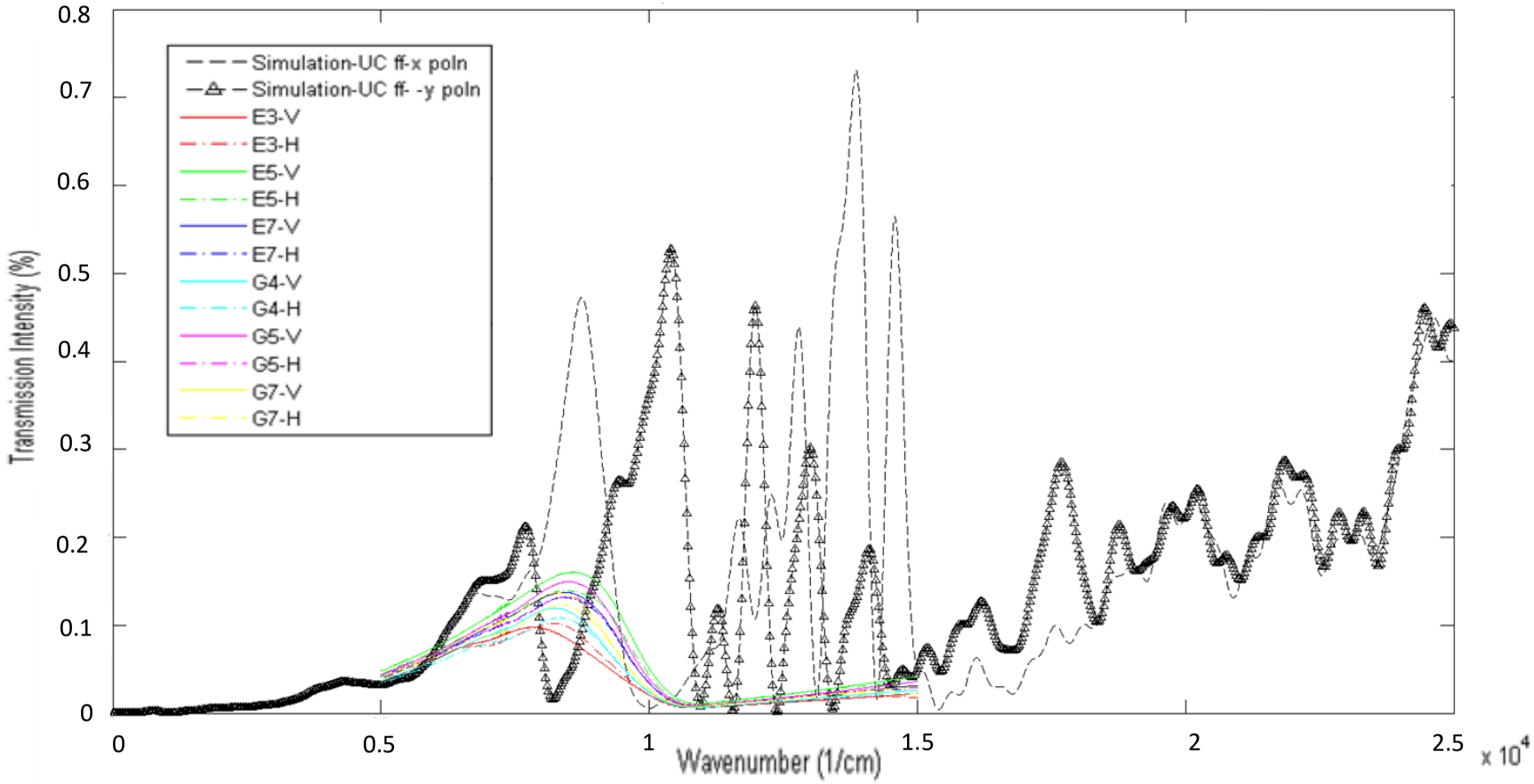

Figure 4.8: FTIR results for the best patterned areas of the metamaterial sample, (in colour) with legend titles corresponding to the sample map in figure 4.4 and H and V referring to horizontal (x-polarisation) and vertical (y-polarisation) polarised incident light respectively. The FTIR results are plotted against CST simulation results for both x- and y-polarised incident light, with data taken in the far-field of the simulation volume.

It can be seen that only one key peak is seen for all of the FTIR spectra collected, and that its amplitude is much smaller than for the simulated spectra (0.2 transmission compared to 0.5 for the nearest simulated spectra peak). In addition, the simulated spectra contain many peaks, although some fall outside the detector range of the FTIR, compared to the FTIR spectra. The simulated spectra also show potential peak shifting between the different polarisations, or very different spectra between the two polarisations. Some changes to the FTIR spectra for the different polarisations are seen, but they are minor compared to the differences seen in the simulated spectra.

The highest amplitude spectrum seen is for the metamaterial area E5, and the lowest amplitude is for the area E3. The higher amplitudes could relate to improved fabrication quality, however this is not born out by the SEM data.

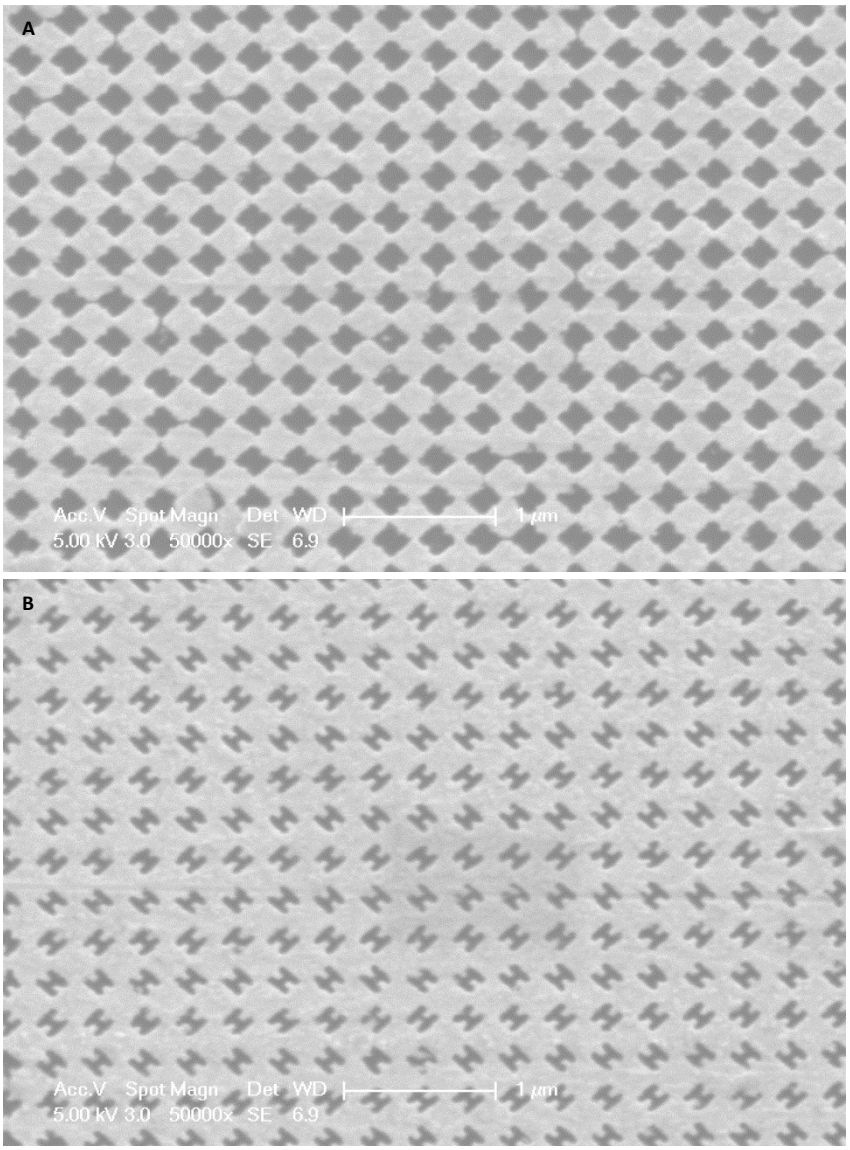

Figure 4.9: SEM images of the metamaterial sample areas, A – E5, B – E3. Images were taken by the author using a Philips XL-30 ESEM at the Centre for Electron Microscopy, University of Birmingham, UK.

The highest amplitude seen for sample area E5 corresponds to over-exposed patterning, where the ‘H’ shapes have become almost square. Whereas the low amplitude seen for sample area E3 corresponds to a well-patterned area where the ‘H’ shapes are clearly defined. Consequently, the higher transmission amplitude, instead of corresponding to a better plasmonic resonance due to the metamaterial’s plasmonic properties, corresponds to larger transparent areas in the metamaterial. This is in spite of the FTIR spectra peaks being positioned at the same frequency as a distinct peak in the x-polarised simulated spectrum.

Overall, the low amplitude and the limited number of peaks within the FTIR spectra compared to the simulated spectra, demonstrate that the fabrication of the metamaterial has been of limited success. Furthermore, the FTIR spectra do not indicate the plasmonic behaviour required for the metamaterial to have the plasmonic functionality required for it to be able to produce a structured evanescent field, as shown through there only being one peak in the spectra compared to many in the simulated spectra, and the higher amplitudes relating to a badly fabricated area of metamaterial.

The differences between the FTIR and the simulated spectra could be due to inaccurate or flawed fabrication. However, even the areas that when imaged with SEM appear to have been successfully fabricated, do not show comparable spectra to the simulation spectra and still share the same spectrum profile as the other FTIR spectra. Thus, the FTIR results show that the fabricated metamaterial is unlikely to be suitable as a metalens for the proposed microscope design, but optical testing was also carried out to confirm this.

4.4.5 Optical Testing & Characterisation

The metamaterial sample was placed within a non-commercial optical setup similar to a brightfield microscope, comprised primarily of an incident laser light source, objective lenses and CCD detector. This setup allowed the signal from the metamaterial sample to be investigated and imaging to be trialled.

Having successfully aligned a patterned section of the metamaterial sample within the optical setup and aligned the laser and other components, the signal was examined. However, only negligible signal was seen and very high noise was seen which overwhelmed the signal, meaning no data was able to be collected. Moreover, imaging was not possible without the chromium grating sample or similar to act as a sample to be imaged. Consequently, optical testing was not successful.

4.5 Conclusions

In conclusion, a fabrication protocol was developed to fabricate the metamaterial and fabrication was partly successful. The 'H' shapes were successfully patterned, but the edges were still rough compared to simulation, and the desired feature size of 50nm was achieved. The roughness of the fabrication, which was expected based upon the initial prototypes, does appear to have affected the metamaterial and its functionality, as predicted from the simulation work, see Chapter 2 Section 2.6.4. However, the fabrication also suffered from large scale defects and distortion, due to poor adhesion between the resist and the gold plus dielectric substrate. This was in spite of the addition of anti-charging layers between the resist and the gold film and adaptations to the fabrication protocol. The metamaterial was imaged using SEM to determine the fabrication quality visually.

Nevertheless, as some of the fabrication was successful, it was still tested using FTIR and within a non-commercial optical setup similar to a brightfield microscope. The optical testing was unsuccessful as there was negligible signal and high levels of noise. The FTIR spectra produced were very different from the spectra produced using CST MWS simulations. Only one broad peak was seen in the FTIR spectra compared to the simulation spectra, which did correspond to a simulation peak. However, the transmission amplitude was much smaller for the FTIR spectra, and the differences seen between different polarisations of incident light seen for the simulation spectra were not seen to any great extent for the FTIR spectra.

Consequently, the fabrication of the metamaterial was unsuccessful, both in terms of its visual appearance and in its functionality. Therefore, an alternative metamaterial design suitable for creating the structured illumination required for the proposed microscope was investigated, see Chapter 5.

Chapter 5: Alternative Metalens Design

5.1 Introduction

This Chapter covers the work to implement a metamaterial design developed in collaboration with Qilong Tan of the South China Normal University, Guangzhou, China, as an alternative to the design discussed in Chapters 2 & 4. As a result of being unable to successfully fabricate the 'H' shape based metamaterial, see Chapter 4, an alternative metamaterial of a simpler and thus more easily fabricated design was needed. This metamaterial could then be used to form the metalens, the crucial component of the proposed TIRF-SIM type microscope, that should allow for super-resolution imaging with a structured evanescent field.

Beyond discussing this alternative metamaterial design, this Chapter details the structured illumination produced by it, and thus its use within the image reconstruction algorithms detailed in Chapter 3. As previously discussed, the basic premise of the image reconstruction algorithm was based on well-established SIM reconstruction algorithms. The alternative design metamaterial's structured illumination patterns were applied in the standard SIM reconstruction algorithm, and in the adapted SIM reconstruction algorithms to optimise the image reconstruction for this metamaterial.

5.1.1 Aims

The aims of the alternative metamaterial design section of this thesis were as follows:

- Discuss the alternative metamaterial design and its functionality.

- Analyse the structured illumination patterns produced by this metamaterial.
- Implement these structured illumination patterns within the standard SIM image reconstruction algorithm in MATLAB, detailed in Chapter 3.
- Determine whether a standard SIM reconstruction algorithm is suitable for these structured illumination patterns.
- Implement these structured illumination patterns within the expanded Fourier Series SIM image reconstruction algorithm in MATLAB, if required, detailed in Chapter 3, using the metamaterial structured illumination patterns.
- Implement these structured illumination patterns within the expanded Sinusoid Product-based SIM image reconstruction algorithm in MATLAB, if required, detailed in Chapter 3, using the metamaterial structured illumination patterns.
- Determine whether the novel SIM reconstruction algorithms are suitable for these metamaterial structured illumination patterns.
- Compare the different image reconstruction algorithms used for their efficacy with these metamaterial structured illumination patterns.

5.2 Metalens Design

5.2.1 Introduction

The metamaterial design detailed below was designed as an alternative to the design developed and fabricated in Chapters 2 & 4. This original design, although in simulations in CST MWS was able to produce the structured illumination required, was not able to be successfully fabricated. Alongside defects in fabricated samples, prototype samples that were fabricated had frequency profiles that were inconsistent with the simulation data and

were unsuitable for the requirements of this research. Moreover, optical testing proved unsuccessful as only negligible signal and high noise was observed.

Consequently, an alternative metamaterial design was developed in collaboration with Qilong Tan of the South China Normal University, Guangzhou, China. This metamaterial was designed by Q. Tan and was shown to produced structured illumination. Thus, the design and results were analysed as a part of this research and applied to the development of a metamaterial based TIRF-SIM style microscope. This metamaterial is still in the simulation stage and has yet to be fabricated, thus all data is simulation based.

5.2.2 Concept

The original metamaterial design was formed of a periodic array of identical unit cells, each containing two 'H' shapes at ±45° to the normal, cut out from a gold film. By contrast, this alternative metamaterial design is formed from a substrate of silicon dioxide, with gold cuboids (30nm in height) of varying sizes arranged in unit cells, each unit cell containing nine of the gold cuboids, on top of it.

The structured illumination of the original design was produced by the periodicity of the unit cells and the π phase change between the two 'H' shapes of the unit cell, as well as the wavelength of incident light utilised, determining the spatial frequency of the structured illumination. The change to the phase of the incident light produced the phase changes in the structured illumination. However, change in orientation of the structured illumination was only able to be produced by rotating the metamaterial, which is not experimentally viable. Although, it has been suggested that changing the incident angle would produce the

change in orientation[118]; but this was able to be simulated successfully, and due to fabrication issues, could not be demonstrated experimentally.

The alternative metamaterial design's structured illumination's spatial wavelength is also dependent on the unit cell periodicity. The design of the unit cell is also important. The varying sizes of the gold cuboids in the unit cell provide the ability to alter the phase and orientation depending on the incident light. The alternative design of metamaterial has much simpler components to the unit cell, but the unit cell has more elements and thus is more complex.

5.2.3 Design Schematic

The metamaterial design is as follows:

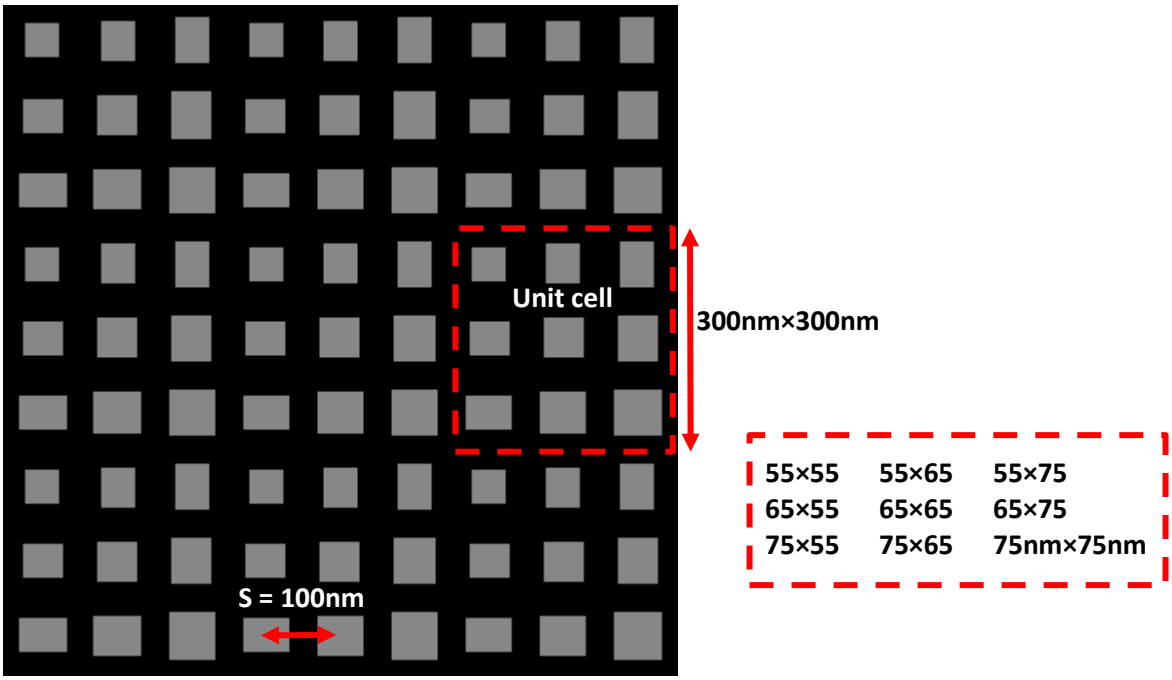

Figure 5.1: Schematic of alternative metamaterial design, including the unit cell (300nm×300nm in size), the sizes of the gold cuboids that comprise the unit cell, and the pitch of the unit cell components (S = 100nm). Image courtesy of Q. Tan, South China Normal University, Guangzhou, China.

5.2.4 Potential advantages

There are multiple advantages to this alternative metamaterial design. The key advantage is the more achievable fabrication, making this in the long-term a better design. This is due to the comparative simplicity of the unit cell elements. In addition, one of the key issues with the original design – potentially not being able to achieve different orientations of the structured illumination – is no longer an issue, having formed part of the metamaterial design, as shown in *Section 5.3.2* below.

5.3 Metalens Structured Illumination

5.3.1 Introduction & Requirements

This section describes the structured illumination produced by the alternative design. As previously stated, this metamaterial has yet to be fabricated, therefore the structured illumination is simulated.

As with the original metamaterial, if possible this metamaterial should produce approximately sinusoidal structured illumination, which can have its phase and orientation varied to produce the nine or more images ideally required by standard SIM imaging. However, as shown in Chapter 3, successful image reconstruction can be achieved using fewer than nine images using simulated atypical masks, and by adapting the standard SIM reconstruction algorithm, simulated atypical masks can be successfully utilised for SIM reconstruction. However, the masks created by the original 'H' shape based metamaterial design were unsuccessful in image reconstruction for all of the SIM image reconstruction methods.

In order to successfully model the patterns beyond a simple sinusoid, the metamaterial patterns need to be successfully characterised, and their mathematical components identified. This having been done, they can be tested within the SIM reconstruction algorithms detailed in Chapter 3.

5.3.2 Structured Illumination

The simulated structured illumination produced by the alternative metamaterial are shown below.

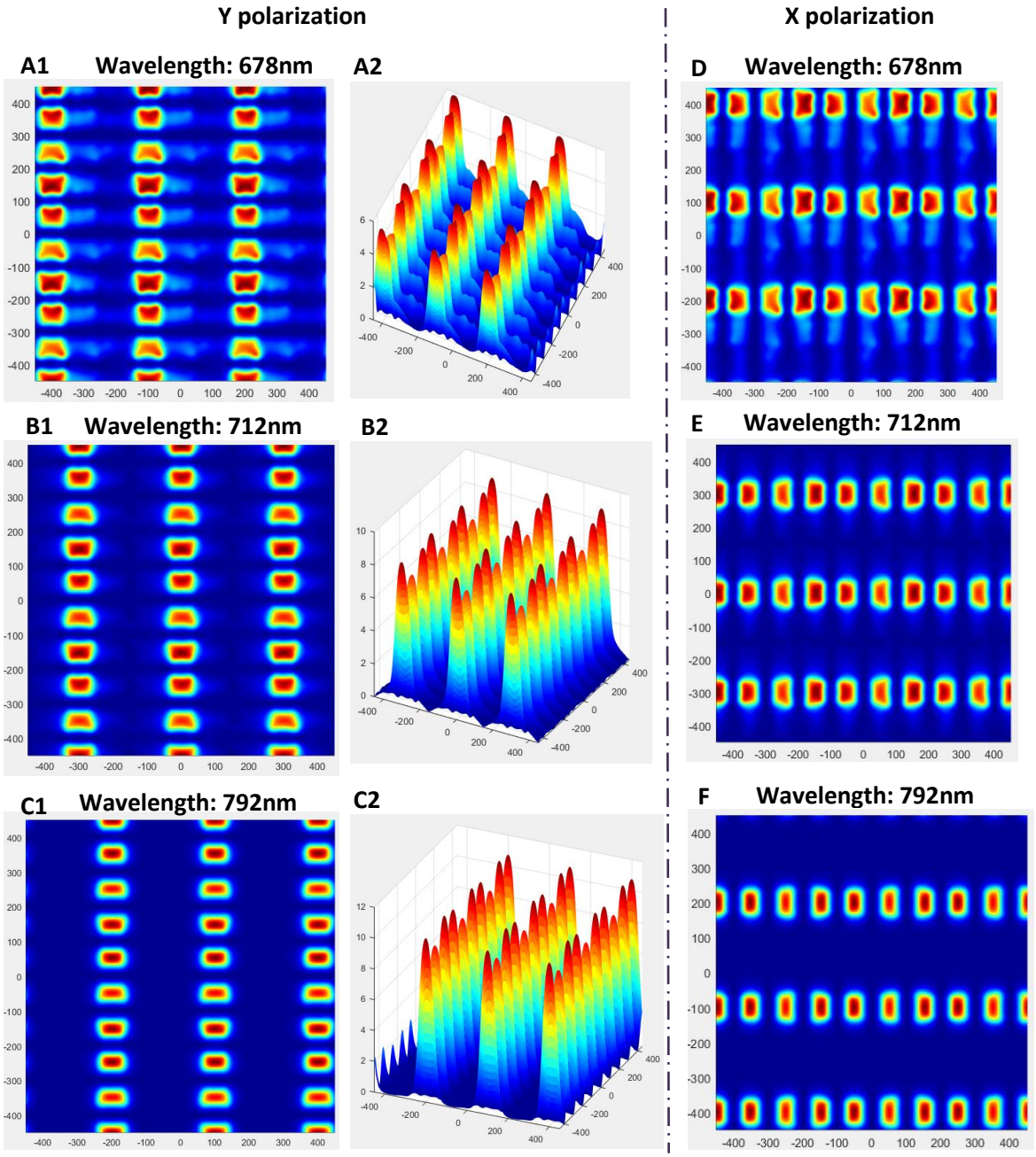

Figure 5.2: Simulated structured illumination produced by the alternative metamaterial design: A1 – 2D plot, A2 – 3D plot using y-polarised light, wavelength 678nm; B1 – 2D plot, B2 – 3D plot using y-polarised light, wavelength 712nm; C1 – 2D plot, C2 – 3D plot using y-polarised light, wavelength 792nm; D – 2D plot using x-polarised light, wavelength 678nm; E – 2D plot using x-polarised light, wavelength 712nm; F – 2D plot using x-polarised light, wavelength 792nm. Images courtesy of Q. Tan, South China Normal University, Guangzhou, China.

It can be seen that six structured illumination patterns have been produced successfully, which is fewer than ideally desired, but this can potentially be addressed in the image reconstruction algorithm. By switching between y-polarised and x-polarised light, two orientations of the structured illumination were achieved: [0, 1] and [1, 0] respectively. Furthermore, by switching between three different wavelengths of incident light - 678nm, 712nm, and 792nm – three different phases of the structured illumination were achieved: -2π/3, 0, and 2π/3 respectively. However, the structured illumination is not typically sinusoidal. Although there is a strong stripe pattern, each stripe is comprised of multiple discrete blocks, and for the 678nm wavelengths the stripes are asymmetric with a tail on one side of the stripe. Again, this deviation from a standard sinusoid could potentially be addressed within the adapted SIM reconstruction algorithms.

The structured illumination shown corresponds to an area of metamaterial equivalent to the nine unit cells seen in figure 5.2. The spatial wavelength of the main stripes is 300nm, which corresponds to the unit cell size; the spatial wavelength of the blocks within the stripes is 100nm, and probably results from the blocks that comprise the unit cells, as nine blocks are present in each row and column in the area of metamaterial used to produce the simulated structured illumination, and nine blocks are seen in each stripe of the structured illumination.

5.3.3 Discussion

The alternative metamaterial does produce structured illumination, however it has limitations. A potential limitation is that, like the original metamaterial design, the structured illumination is not perfectly sinusoidal, and instead has at least two main

sinusoidal components. However, this could also potentially be an advantage, if it results in a material with good optical properties. In addition, only six structured illumination patterns were produced, yet more could potentially be produced by further varying the polarisation of the incident light. However, non-x,y polarised light may not be compatible with the geometry of the metamaterial, due to the cuboid shapes of the unit cells only x-y polarised light may potentially produce suitable resonances for the structured illumination to be formed, which would require further investigation. Moreover, the adapted SIM reconstruction algorithms may compensate for the fewer patterns. As the patterns are not a simple sinusoid, they should have more Fourier components and thus cover a larger area in Fourier space. Thus meaning that when the images are shifted, a larger area of Fourier space will be present in the final reconstructed image, and thus more high-resolution information will be retained in the final image. Hence, the added complexity could still allow for resolution improvement in image reconstruction even with only six images, as was seen in Chapter 3.

5.4 Standard SIM Image Reconstruction

5.4.1 Introduction

The SIM image reconstruction described below is for what is referred to as 'standard SIM' in this thesis, and is discussed in greater detail in Chapter 3. In standard SIM, the patterns used are sinusoidal and therefore appear as stripes across the image, and for a 2D image, nine different images (three orientations and three phases of the basic sinusoidal stripes) are required with more images theoretically producing further resolution improvement, each with a different structured illumination pattern[33,34].

By applying the structured patterns to the sample, higher frequency and thus higher resolution information is retained for the final image. Then by combining the nine or more images in the method described in Chapter 3, this higher resolution information is seen in the final image and the structured patterns are removed, producing a super-resolution image of ~2× resolution[33].

It was expected that performing a standard SIM reconstruction with the atypical structured illumination patterns produced by this alternative metamaterial would not be very successful, as was seen with the original metamaterial. However, the adapted SIM reconstruction algorithms could be optimised for the atypical metamaterial patterns, and were expected to be more successful.

5.4.2 Results

The mathematical process and the different stages of standard SIM are described in Chapter 3. The image reconstruction has been performed with an example image, simulated microscope PSF, and the six metamaterial masks from the alternative design, utilising the algorithm in Appendix 3 and explained in detail in Chapter 3. The example image was the inbuilt MATLAB 'Modified Shepp-Logan' head phantom which is often used to test 2-dimensional image reconstruction algorithms[222,223], image size was 451×451 pixels. The nm-to-pixel ratio was 20; the PSF was defined by the parameters: λ = 500nm, n = 1, NA = 1.49; three mask phases were used, φ_i = 0, $2\pi/3$, $4\pi/3$; two mask orientations were used, $\underline{\boldsymbol{p}}$ = [1,0; 0,1]; the spatial wavelength of the masks was 300nm; the noise parameter, w = 1 ; and the width of the desired OTF was half that of the original PSF. These parameters were chosen to optimise the resolution improvement in the final image.

The results are detailed below:

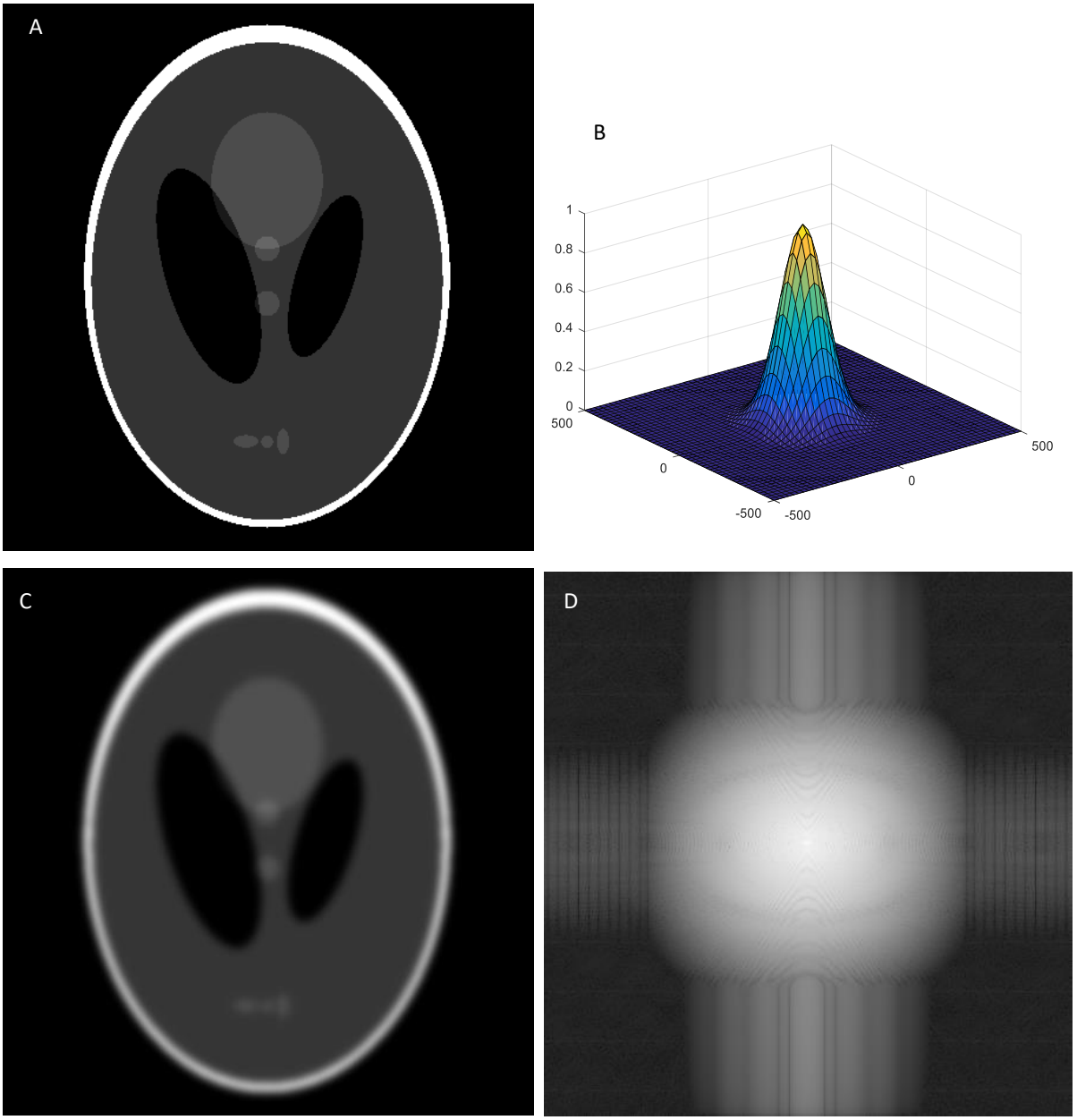

Figure 5.3: A – Ground truth image, 451×451 pixels modified Shepp-Logan phantom from MATLAB; B - Point spread function (PSF) used to blur the ground truth image, plotted in nm (51×51 pixels); C – the widefield image (451×451 pixels), created by convolving the ground truth image with the PSF; D – FFT of the widefield image (451×451 pixels).

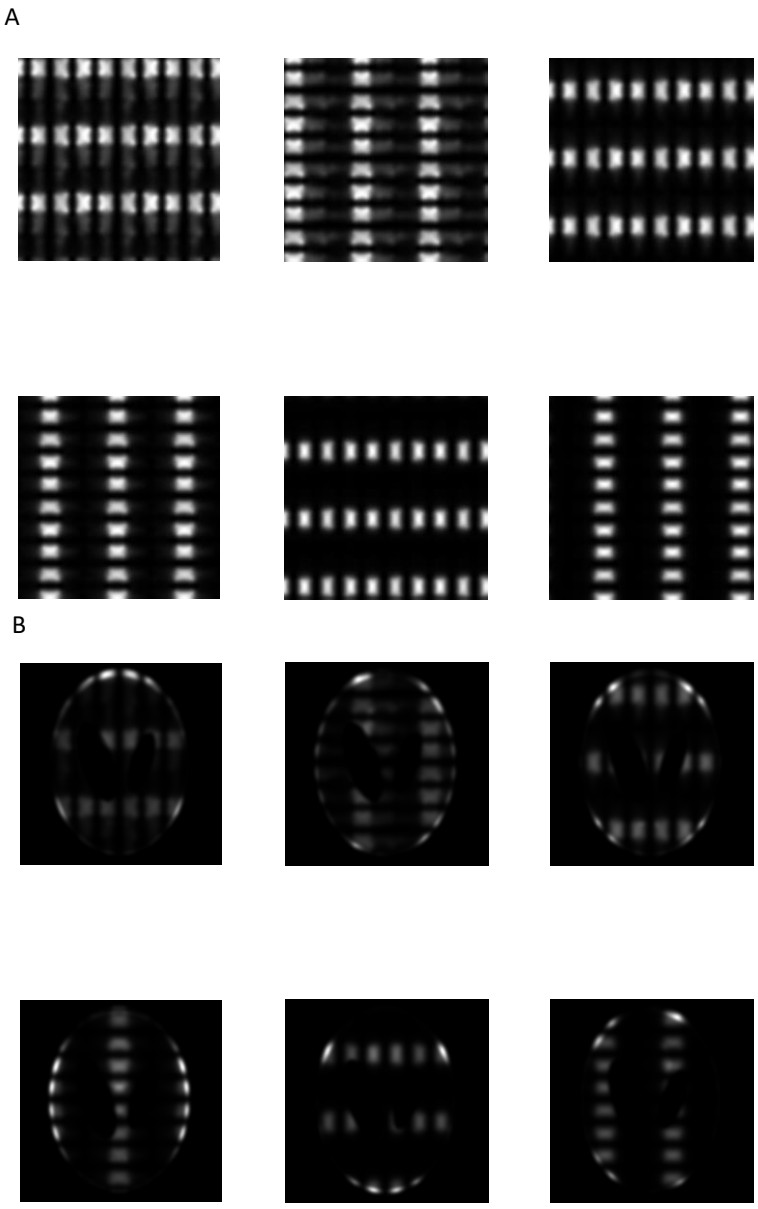

Figure 5.4: A - The six metamaterial masks used (451×451 pixels), created in simulation using the alternative metamaterial design, using the following parameters: three phases were used, φ_i = 0, 2π/3, 4π/3, corresponding to incident wavelengths of 712, 792 and 678nm respectively; two mask orientations were used, $\underline{\mathbf{p}}$ = [1,0; 0,1], corresponding to x- and y-polarised incident light respectively; the spatial wavelength of the masks is 300nm; B – the six acquired images (451×451 pixels), created by multiplying the masks and the ground truth image, and then convolving with the PSF.

A

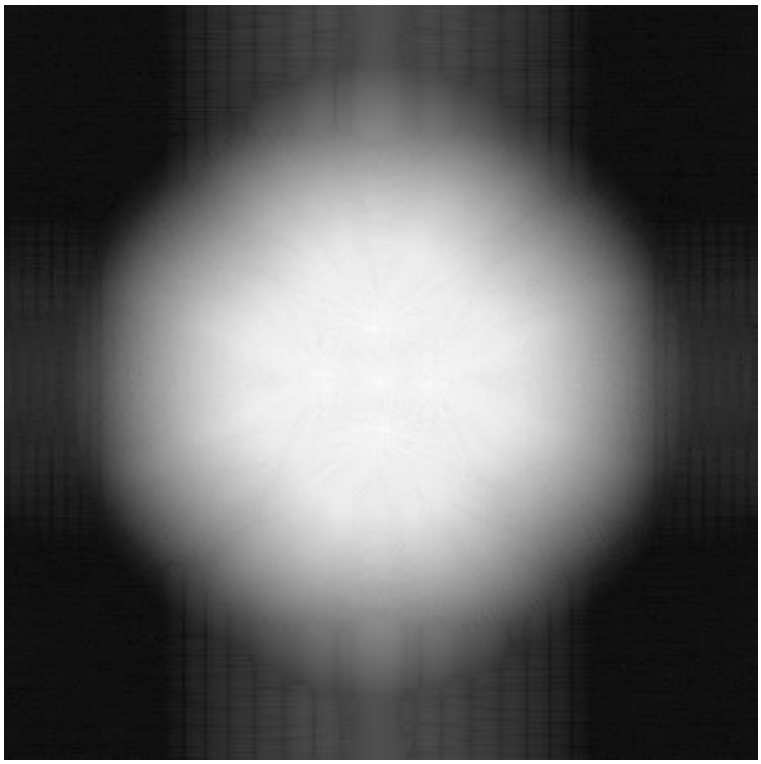

B

Figure 5.5: A – The reconstructed image in Fourier space (451×451 pixels); B – the final reconstructed image (451×451 pixels).

It can be seen that although the FFT of the reconstructed image covers a larger area of Fourier space than the FFT of the widefield image, meaning that there should be resolution improvement in the final reconstruction, the reconstructed image is poor. There are very strong artefacts in the reconstructed image, which obscure any potential resolution improvement. This is due to the use of standard SIM reconstruction using very abnormal SIM patterns, and thus the expanded SIM reconstruction methods developed in Chapter 3 were required to improve the image reconstruction quality. Another consideration is the FFT of the widefield image itself. As the phantom used is a constructed image, its Fourier components are atypical, as seen in the FFT of the widefield image. This may also have impacted the image reconstruction quality, as the Fourier components are critical to the reconstruction process.

Consequently, the standard SIM reconstruction algorithm was then also tested using an image of a sample of human platelets spread on a glass coverslip and stained for F-actin using phalloidin, provided by Dr Steve Thomas of the Institute of Cardiovascular Sciences, Institute of Biomedical Research, University of Birmingham, UK. The image size was 256×256 pixels, scaled to 451×451 pixels to match the metamaterial masks. The nm-to-pixel ratio was 20; the PSF was defined by the parameters: λ = 500nm, n = 1, NA = 1.49; three mask phases were used, φ_i = 0, $2\pi/3$, $4\pi/3$; two mask orientations were used, $\boldsymbol{p}$ = [1,0; 0,1]; the spatial wavelength of the masks was 300nm; the noise parameter, w = 1 ; and the width of the desired OTF was half that of the original PSF. These parameters were chosen to optimise the resolution improvement in the final image.

The results are detailed below:

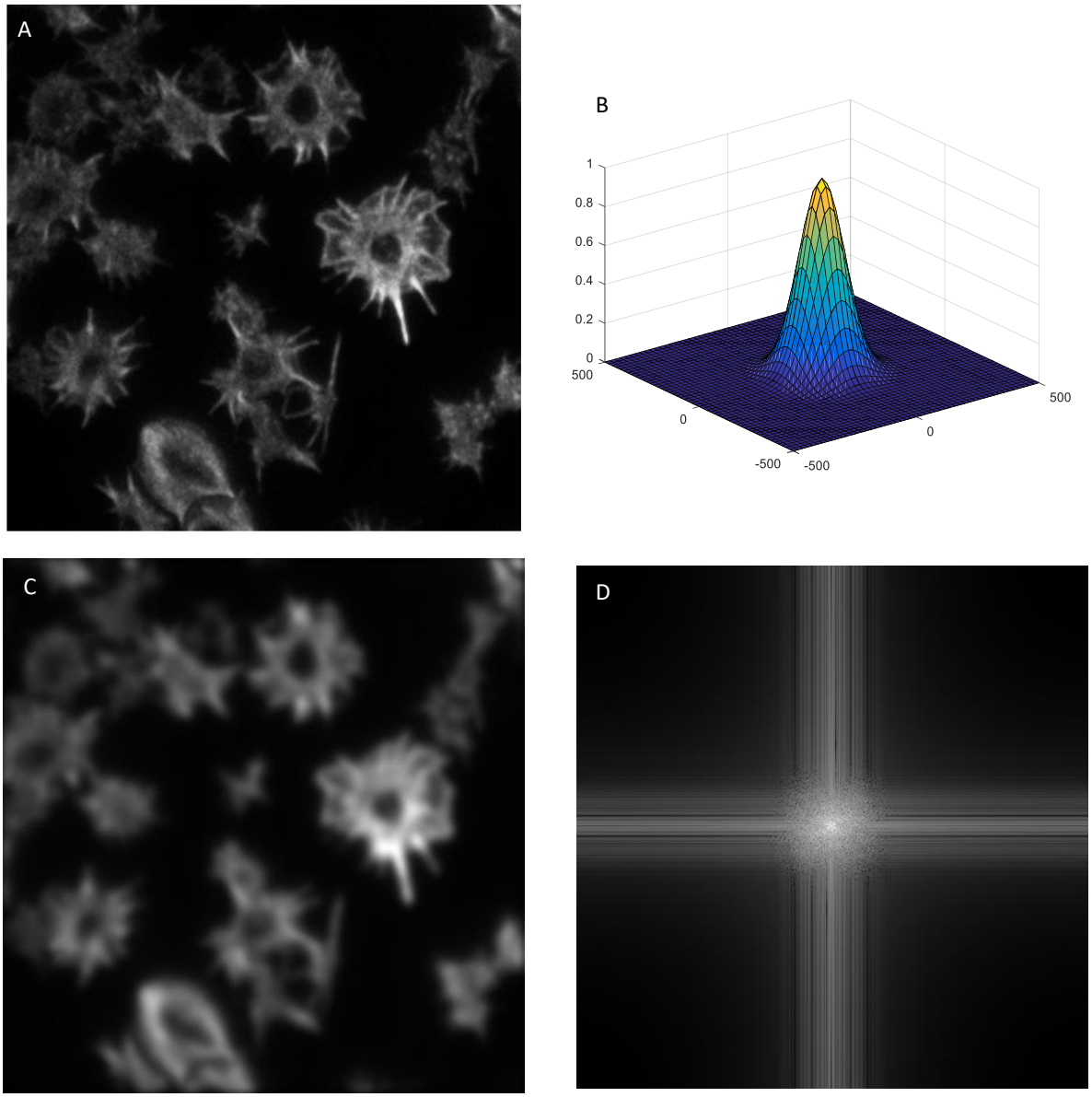

Figure 5.6: A – Ground truth image, 451×451 pixels scaled platelet image, courtesy of Dr Steve Thomas, University of Birmingham, UK; B - Point spread function (PSF) used to blur the ground truth image, plotted in nm (51×51 pixels); C – the widefield image (451×451 pixels), created by convolving the ground truth image with the PSF; D – FFT of the widefield image (451×451 pixels).

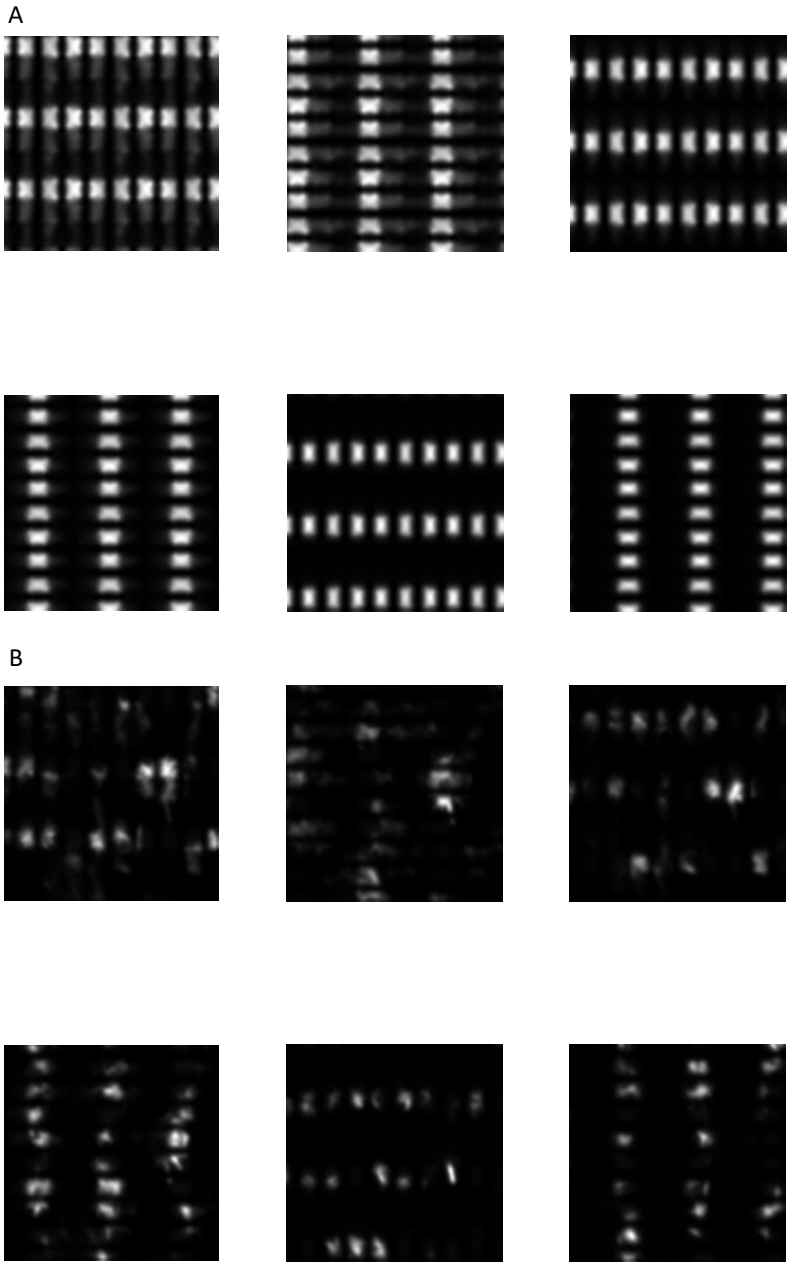

Figure 5.7: A - The six metamaterial masks used (451×451 pixels), created in simulation using the alternative metamaterial design, using the following parameters: three phases were used, φ_i = 0, 2π/3, 4π/3, corresponding to incident wavelengths of 712, 792 and 678nm respectively; two mask orientations were used, $\underline{\mathbf{p}}$ = [1,0; 0,1], corresponding to x- and y-polarised incident light respectively; the spatial wavelength of the masks is 300nm; B – the six acquired images (451×451 pixels), created by multiplying the masks and the ground truth image, and then convolving with the PSF.

A

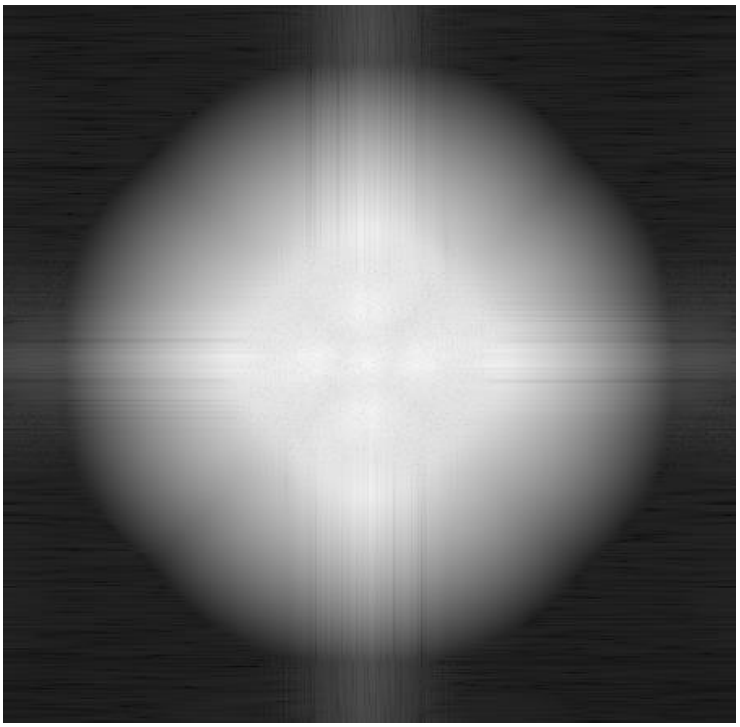

B

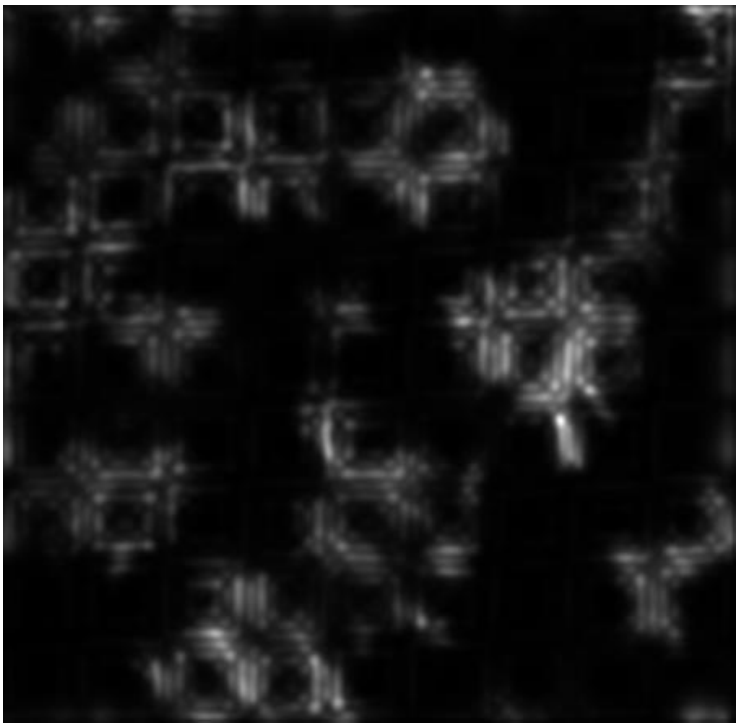

Figure 5.8: A – The reconstructed image in Fourier space (451×451 pixels); B – the final reconstructed image (451×451 pixels).

Again, it can be seen that the reconstructed image is poor and there are very strong artefacts in the reconstructed image, which obscure any potential resolution improvement. The sample image did not have abnormal Fourier components, unlike the Modified Shepp-Logan phantom used previously, thus it is unlikely that this has impacted the image reconstruction quality, meaning that the non-standard sinusoid masks are the cause. Thus the expanded SIM reconstruction methods developed in Chapter 3 could be utilised to improve the image reconstruction quality. Another consideration is the use of fewer than the ideal images, however this would not have produced the artefacts as in Fourier space there is good coverage. Instead this would have lessened any resolution improvement.

5.4.3 Discussion

The use of the standard SIM reconstruction algorithm has been demonstrated to be unsuccessful using the six masks produced by the alternative metamaterial design. There were significant artefacts that obscured any resolution improvement. As a result, the expanded SIM methods described in Chapter 3, involving mathematical expansions of the standard SIM reconstruction algorithm. Both a Fourier Series approach where a sum of sinusoids is used to describe the masks, and the use of a product of sinusoids were used to describe the masks produced by the original metamaterial design. However, these original patterns were not sufficiently different to a simple sinusoid to make these methods significantly better than the standard SIM reconstruction algorithm. Conversely, the patterns created by the alternative metamaterial design are very different to a simple sinusoid, so the expanded SIM methods should produce significantly better image reconstruction quality, in terms of lack of artefacts and in resolution improvement, compared to standard SIM.

5.5 Expanded SIM – Fourier Series SIM

5.5.1 Introduction

The standard SIM reconstruction algorithm proved unsuccessful with the metamaterial patterns. Therefore, in order to accommodate these atypical patterns, the adapted MATLAB algorithms were utilised. Ideally, the adapted algorithms needed to be able to encompass a more comprehensive mathematical description of the metamaterial masks, and accommodate for the fewer masks than the ideal nine, and still provide resolution enhancement.

The alternative metamaterial patterns are still predominantly sinusoidal, but with another sinusoidal component within the main sinusoid. The mathematical expansion first trialled was a Fourier Expansion, which describes the masks as a sum of sinusoids. By substituting a new expression for the masks into the standard SIM mathematics, the mathematics can be altered to better accommodate the atypical metamaterial masks, and theoretically provide a better final image reconstruction. This method was less successful than the Sinusoid Product-based algorithm, when reconstructing with the original metamaterial's structured illumination patterns, but could prove more successful with these patterns.

5.5.2 Simulating the patterns

The patterns were simulated as a sum of two sinusoids. The primary sinusoid that forms the main 'stripes' had a spatial wavelength of 300nm. The secondary sinusoid that forms the blocks within the main stripes had a spatial wavelength of 100nm, and was rotated to be perpendicular the primary sinusoid. Both of the sinusoids were formed on the basis to provide the two orientations, [1, 0] and [0, 1], and three phases, 0, 2π/3 and 4π/3, seen in the metamaterial masks. The simulated masks and actual masks are compared below.

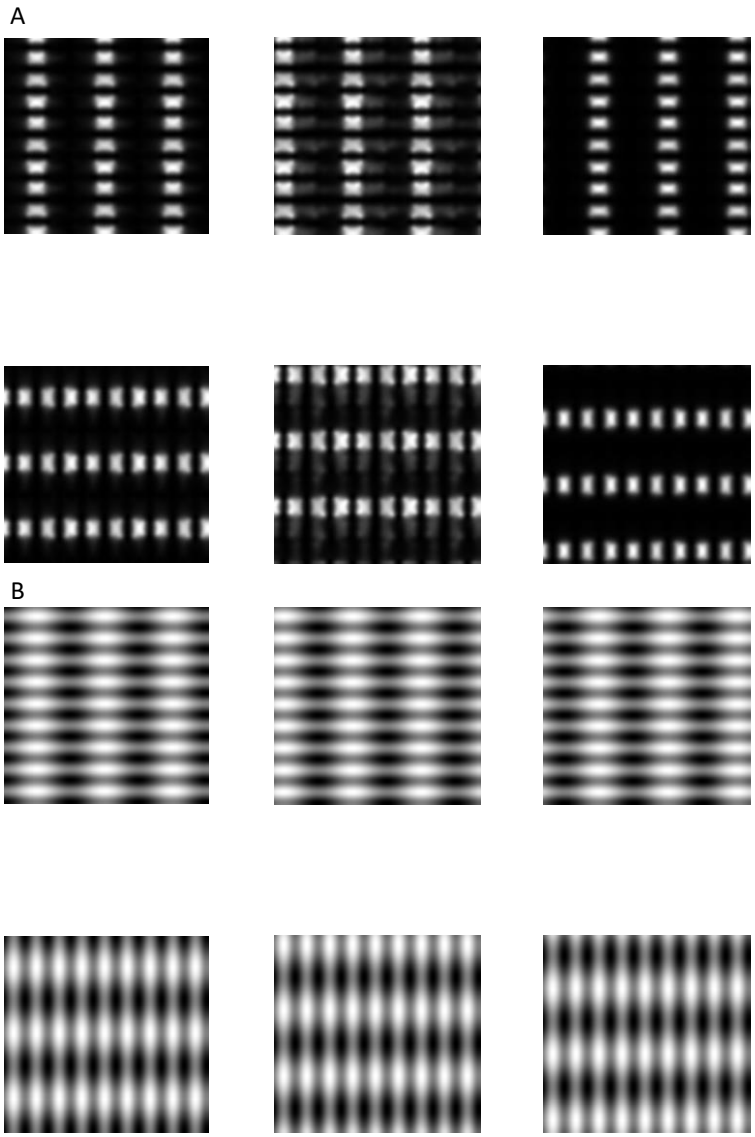

Figure 5.9: A - The six metamaterial masks created in simulation using the alternative metamaterial design; B – the six simulated approximations of the metamaterial masks created using a Fourier Series of two sinusoids in MATLAB.

The simulated masks represent how the image reconstruction algorithm models the masks when reconstructing, and the closer this is to the metamaterial masks, the better the image reconstruction quality.

It can be seen that the key ‘stripes’ and ‘blocks’ are achieved, as well as the phases and orientations of the patterns. Moreover, the ‘stripes’ and ‘blocks’ are matched in terms of positioning between the metamaterial and simulated masks. However, the simulated masks have wider, more continuous stripes and are smoother compared to the discrete ‘blocks’ of the metamaterial masks. This means that the simulation is not identical to the metamaterial masks, but they are more similar than a simple sinusoid and the metamaterial masks. This may impact the reconstruction quality, as was the case when using standard SIM image reconstruction, but as the masks are a closer estimate to the actual masks, the image reconstruction quality should be improved.

5.5.3 Results

The mathematical process and the different stages of this expanded Fourier Series SIM are described in Chapter 3. The image reconstruction has been performed with an example image, simulated microscope PSF, and the six metamaterial masks, utilising the algorithm in Appendix 5.

The example image was the inbuilt MATLAB 'Modified Shepp-Logan' head phantom, image size was 451×451 pixels. The nm-to-pixel ratio was 20; the PSF was defined by the parameters: λ = 500nm, n = 1, NA = 1.49; three mask phases were used, $\varphi_i = 0, 2\pi/3, 4\pi/3$; two mask orientations were used, $\underline{\boldsymbol{p}} = [1,0; 0,1]$; the spatial wavelengths of the masks were 300nm and 100nm; the noise parameter, $w = 1$; and the width of the desired OTF was half that of the original PSF. These parameters were chosen to optimise the resolution improvement in the final image.

The results are detailed below, see figures 5.3 & 5.4 for details of the ground truth image, PSF, and masks used:

A

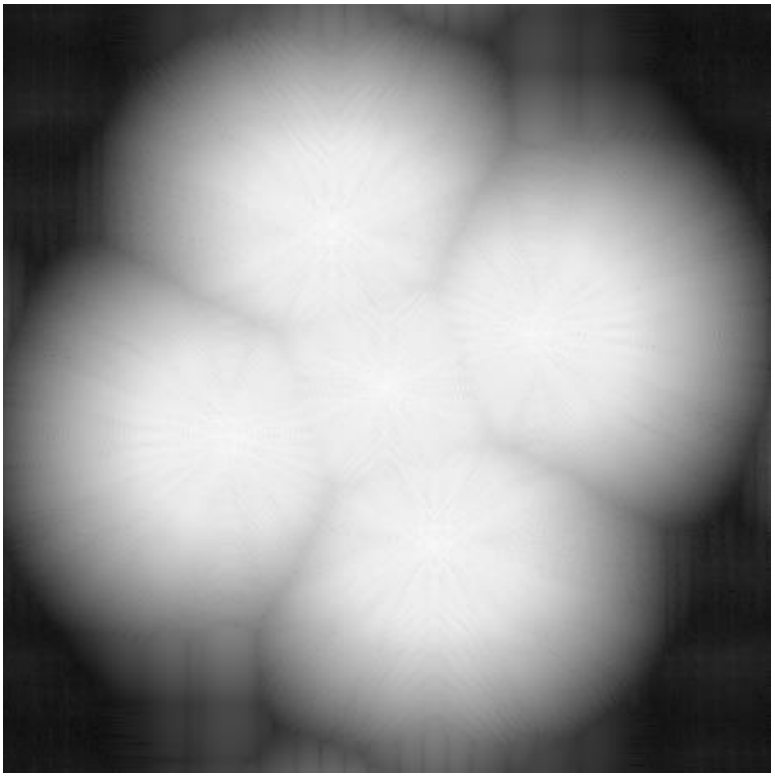

B

Figure 5.10: A – The reconstructed image in Fourier space (451×451 pixels); B – the final reconstructed image (451×451 pixels).

It can be seen that although the FFT of the reconstructed image covers a larger area of Fourier space than the FFT of the widefield image, meaning that there should be resolution improvement in the final reconstruction, the reconstructed image is poor. There are very strong artefacts in the reconstructed image, which obscure any potential resolution improvement. These artefacts are an improvement compared with the standard SIM reconstruction algorithm, see figure 5.5, but are still problematic. This is potentially due to the use of very abnormal SIM patterns even with an adapted image reconstruction algorithm, as the mathematical description of the patterns was not perfect. As discussed previously, another consideration is the FFT of the widefield image itself. As the phantom used is a constructed image, its Fourier components are atypical, as seen in the FFT of the widefield image. This may also have impacted the image reconstruction quality, as the Fourier components are critical to the reconstruction process.

Consequently, the Fourier Series expanded SIM reconstruction algorithm was then also tested using the image of a sample of human platelets used above. The image size was 256×256 pixels, scaled to 451×451 pixels to match the metamaterial masks. The nm-to-pixel ratio was 20; the PSF was defined by the parameters: λ = 500nm, n = 1, NA = 1.49; three mask phases were used, $\varphi_i = 0, 2\pi/3, 4\pi/3$; two mask orientations were used, $\underline{\boldsymbol{p}} = [1,0; 0,1]$; the spatial wavelengths of the masks were 300nm and 100nm; the noise parameter, $w = 1$; and the width of the desired OTF was half that of the original PSF. These parameters were chosen to optimise the resolution improvement in the final image.

The results are detailed below, see figures 5.6 & 5.7 for details of the ground truth image, PSF, and masks used:

A

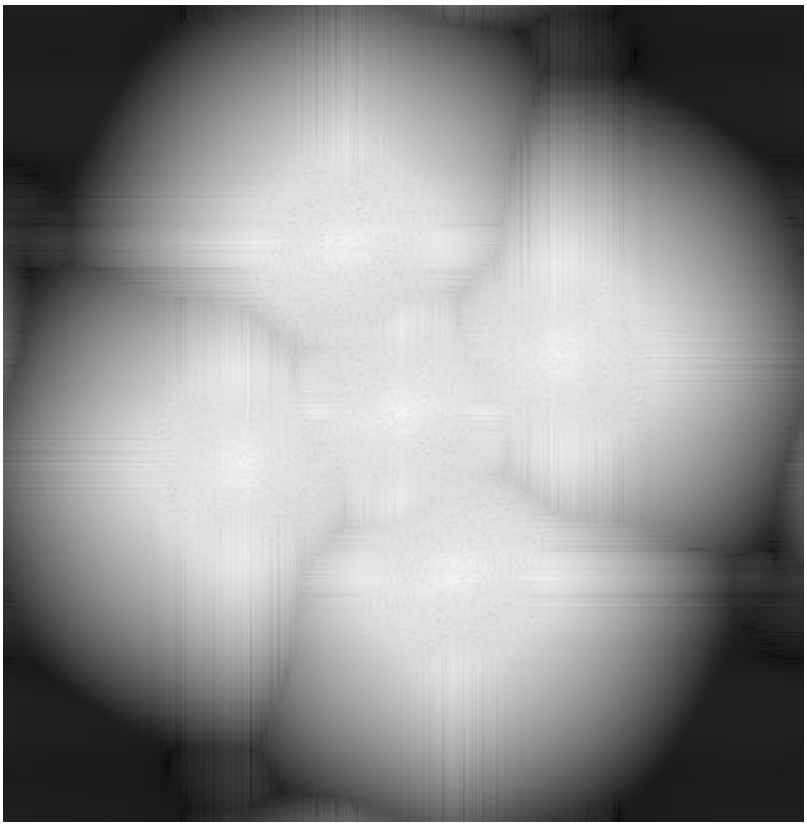

B

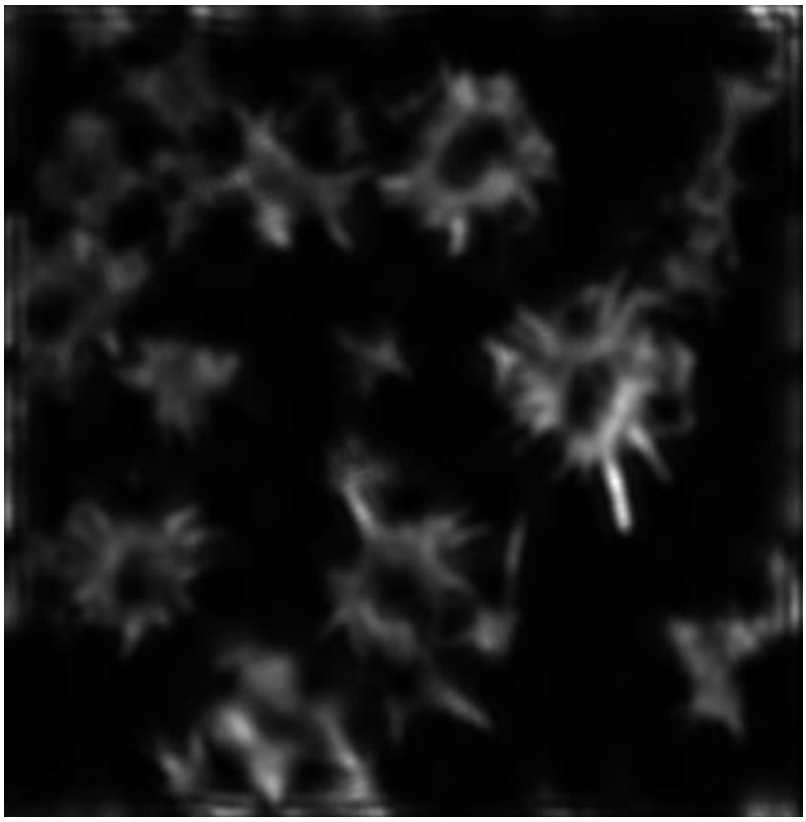

Figure 5.11: A – The reconstructed image in Fourier space (451×451 pixels); B – the final reconstructed image (451×451 pixels).

It can be seen the reconstruction quality is much improved compared to the reconstructed phantom image. This indicates that the phantom image's abnormal Fourier components did impact the reconstruction quality. There are artefacts at the edges of the reconstructed platelet image, but they are minimal, and are common in SIM reconstruction in general[34,37,39,40,113,123,124]. However, the image has reconstructed successfully with some resolution improvement.

5.5.4 Compare reconstruction quality to widefield and standard SIM

The original image, widefield image, standard SIM reconstructed image, and Fourier Series SIM reconstructed image are now presented together so that the reconstruction quality, in terms of resolution improvement and presence of artefacts, can be compared. See figure 5.12 below.

It can be seen that there is great improvement in reconstruction quality compared to the image reconstructed with standard SIM. Furthermore, there is resolution improvement compared with the widefield image. However, the Fourier Series reconstruction appears to have reconstructed the distinct edges of the stained actin more than other areas, thus expanding the dark centres of some the platelets compared to the ground truth image. This may be an issue with contrast in the image, and could be further post-processed to improve the image quality. If it is not related to contrast, then this aspect of the reconstruction needs to be taken into account with any other image reconstructions.

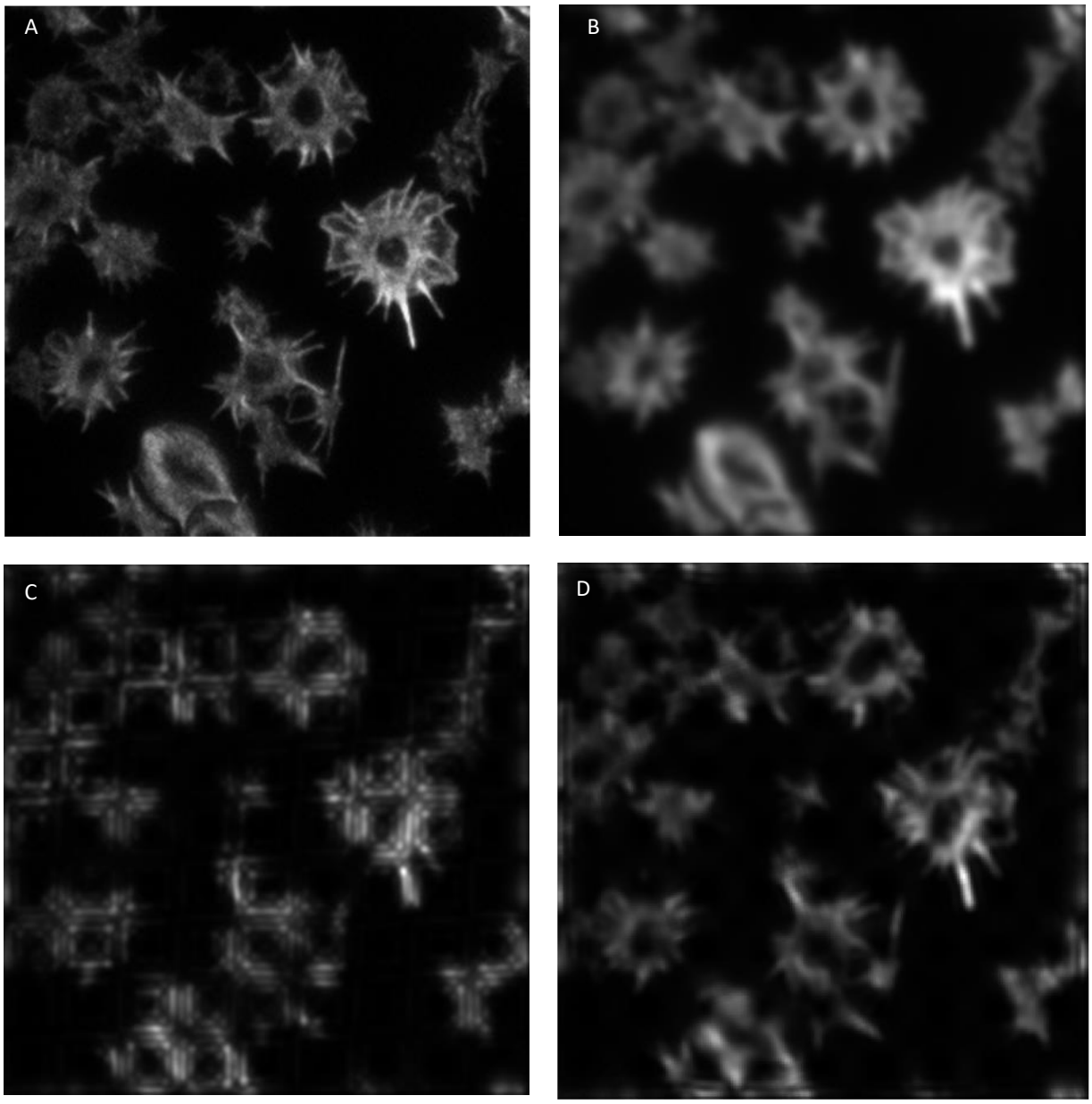

Figure 5.12: A – Ground truth image, 451×451 scaled platelet image, courtesy of Dr Steve Thomas, University of Birmingham, UK; B – the widefield image, created by convolving the ground truth image with the PSF; C – the image as reconstructed using the standard SIM reconstruction algorithm; D – the image as reconstructed using the Fourier Series SIM reconstruction algorithm.

5.5.5 Discussion

The image reconstruction with the Fourier Series SIM image reconstruction algorithm proved unsuccessful with a phantom sample image, but showed success with an image of platelets

stained for actin. This reconstruction showed minimal artefacts and resolution improvement. However, the reconstructed image did show 'selective' reconstruction in the areas with high actin staining, which could limit its practical use. Therefore, the other expanded SIM image reconstruction method was also used. The Fourier Series SIM reconstruction method was an improvement on standard SIM when used with the masks produced by the alternative metamaterial design, and could be further adapted for other atypical SIM masks.

5.6 Expanded SIM – Sinusoid Product-based SIM

5.6.1 Introduction

The standard SIM reconstruction algorithm proved unsuccessful with the metamaterial patterns. Therefore, in order to accommodate these atypical patterns, the adapted MATLAB algorithms were utilised. Ideally, the adapted algorithms needed to be able to encompass a more comprehensive mathematical description of the metamaterial masks, and accommodate for the fewer masks than the ideal nine, and still provide resolution enhancement.

The metamaterial patterns are still predominantly sinusoidal, but with another sinusoidal component within the main sinusoid. The mathematical expansion first trialled was a Fourier Expansion, but this method showed distinct artefacts, despite being able to create a reasonable approximation of the metamaterial masks. Consequently, a different mathematical expansion from the sinusoid was trialled, describing the masks based upon an expression which describes the masks as a product of sinusoids. This produces a chequerboard of peaks and troughs that can be rotated and scaled to produce an approximation to the metamaterial masks. By substituting a new expression for the masks into the standard SIM mathematics, the mathematics can be altered to better accommodate the atypical metamaterial masks, and theoretically provide a better final image reconstruction. The mathematics are described in Chapter 3.

5.6.2 Simulating the patterns

The patterns were simulated as a product of two sinusoids. The primary sinusoid that forms the main 'stripes' had a spatial wavelength of 300nm. The secondary sinusoid that forms the blocks within the main stripes had a spatial wavelength of 100nm, and together they form a chequerboard of peaks and troughs. This was rotated to form the two orientations achieved by the metamaterial patterns. Both of the sinusoids were formed on the basis to provide the two orientations, [1, 0] and [0, 1], and three phases, 0, $2\pi/3$ and $4\pi/3$, seen in the metamaterial masks. The simulated masks and actual masks are compared below.

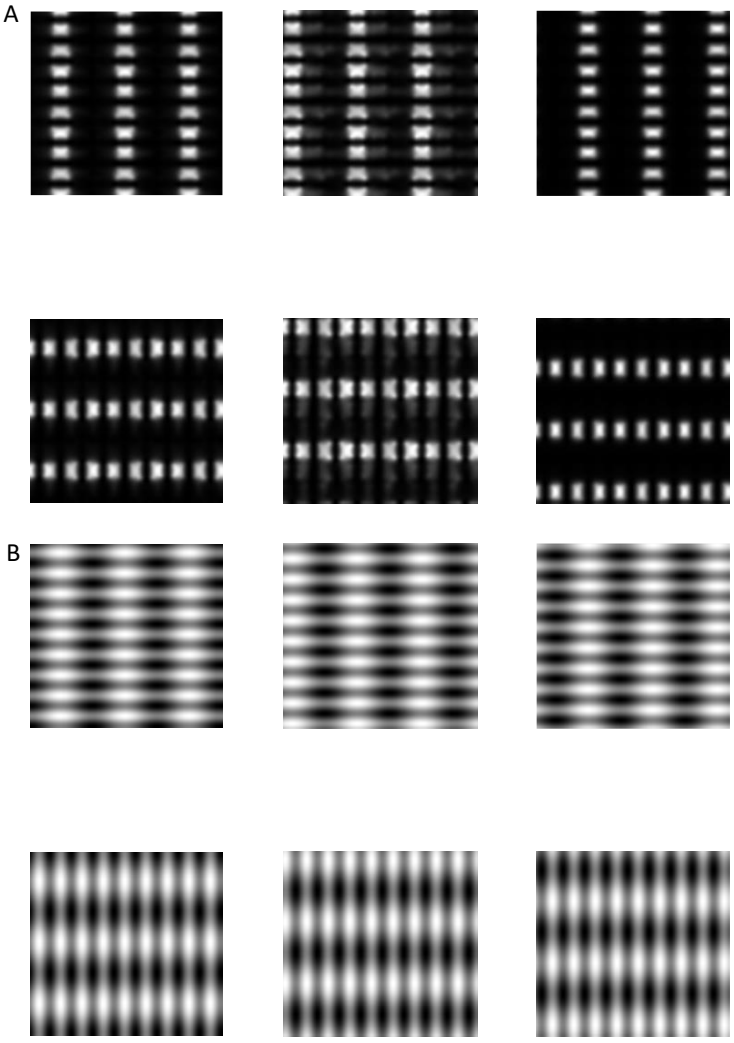

Figure 5.13: A - The six metamaterial masks created in simulation using the alternative metamaterial design; B – the six simulated approximations of the metamaterial masks created using a product of two sinusoids.

The simulated masks represent how the image reconstruction algorithm models the masks when reconstructing, and the closer this is to the metamaterial masks, the better the image reconstruction quality. As for the Fourier Series based approximation of the metamaterial masks, it can be seen that the key features of the metamaterial masks (the spatial wavelengths, phases, orientations, and the 'stripes' and 'blocks' of the patterns) are achieved; but as before the metamaterial patterns were more blocky and less smooth than the simulated approximations of the masks, and the metamaterial and simulated masks are not identical. This simulation of the masks is very similar to that seen for the Fourier Series approach, see figure 5.9, therefore similar results were expected for image reconstruction.

5.6.3 Results

The mathematical process and the different stages of this Sinusoid Product-based expanded SIM are described in Chapter 3. The image reconstruction has been performed with an example image, simulated microscope PSF, and the six metamaterial masks, utilising the algorithm in Appendix 7.

The example image was the inbuilt MATLAB 'Modified Shepp-Logan' head phantom, image size was 451×451 pixels. The nm-to-pixel ratio was 20; the PSF was defined by the parameters: λ = 500nm, n = 1, NA = 1.49; three mask phases were used, φ_i = 0, $2\pi/3$, $4\pi/3$; two mask orientations were used, $\underline{\boldsymbol{p}}$ = [1,0; 0,1]; the spatial wavelengths of the masks were 300nm and 100nm; the noise parameter, w = 1 ; and the width of the desired OTF was half that of the original PSF. These parameters were chosen to optimise the resolution improvement in the final image.

The results are detailed below, see figures 5.3 & 5.4 for details of the ground truth image, PSF, and masks used:

A

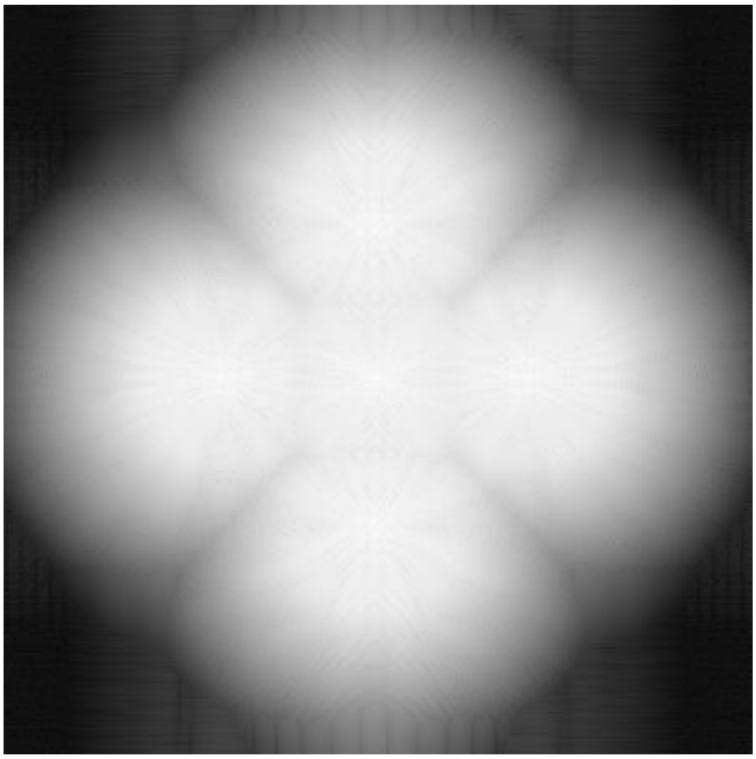

B

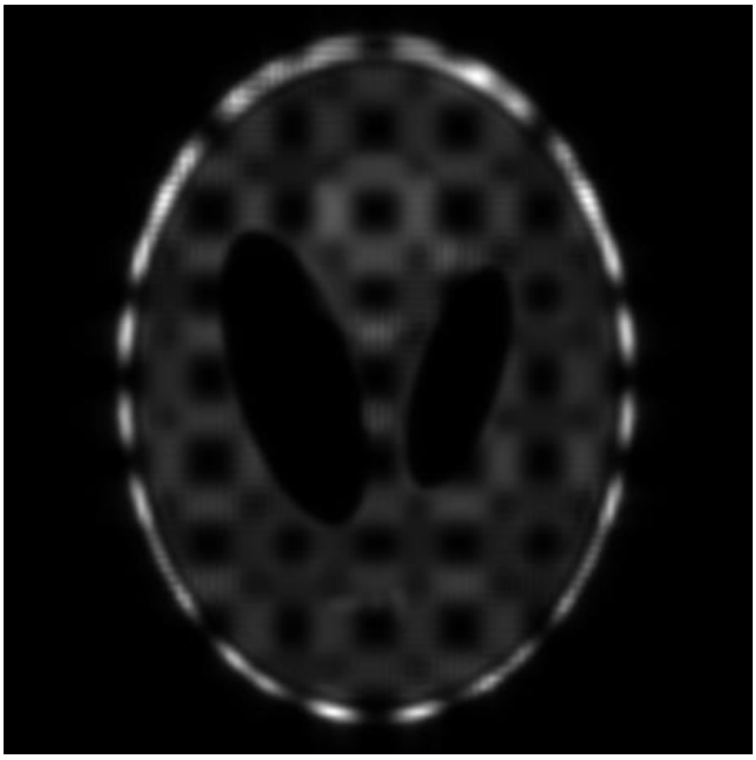

Figure 5.14: A – The reconstructed image in Fourier space (451×451 pixels); B – the final reconstructed image (451×451 pixels).

It can be seen as with the Fourier Series reconstruction of the phantom image, the image reconstruction is poor. Thus further indicating that this is due to the abnormal Fourier components of the phantom image. The FFT of the reconstructed image covers a larger area of Fourier space than the FFT of the widefield image, meaning that there should be resolution improvement in the final reconstruction, the reconstructed image is poor. There are very strong artefacts in the reconstructed image, which obscure any potential resolution improvement. These artefacts are an improvement compared with the standard SIM reconstruction algorithm, see figure 5.5, but are still problematic.

Consequently, the Sinusoid Product-based expanded SIM reconstruction algorithm was then also tested using the image of a sample of human platelets as above. The image size was 256×256 pixels, scaled to 451×451 pixels to match the metamaterial masks. The nm-to-pixel ratio was 20; the PSF was defined by the parameters: λ = 500nm, n = 1, NA = 1.49; three mask phases were used, $\varphi_i = 0, 2\pi/3, 4\pi/3$; two mask orientations were used, $\boldsymbol{p} = [1,0; 0,1]$; the spatial wavelengths of the masks were 300nm and 100nm; the noise parameter, $w = 1$; and the width of the desired OTF was half that of the original PSF. These parameters were chosen to optimise the resolution improvement in the final image.

The results are detailed below, see figures 5.6 & 5.7 for details of the ground truth image, PSF, and masks used:

A

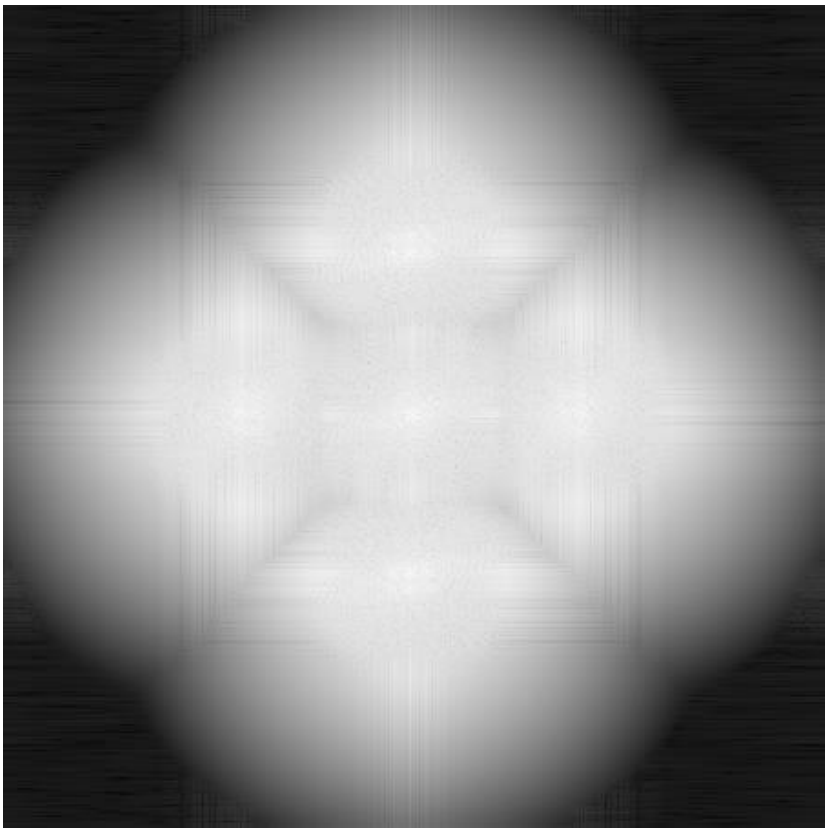

B

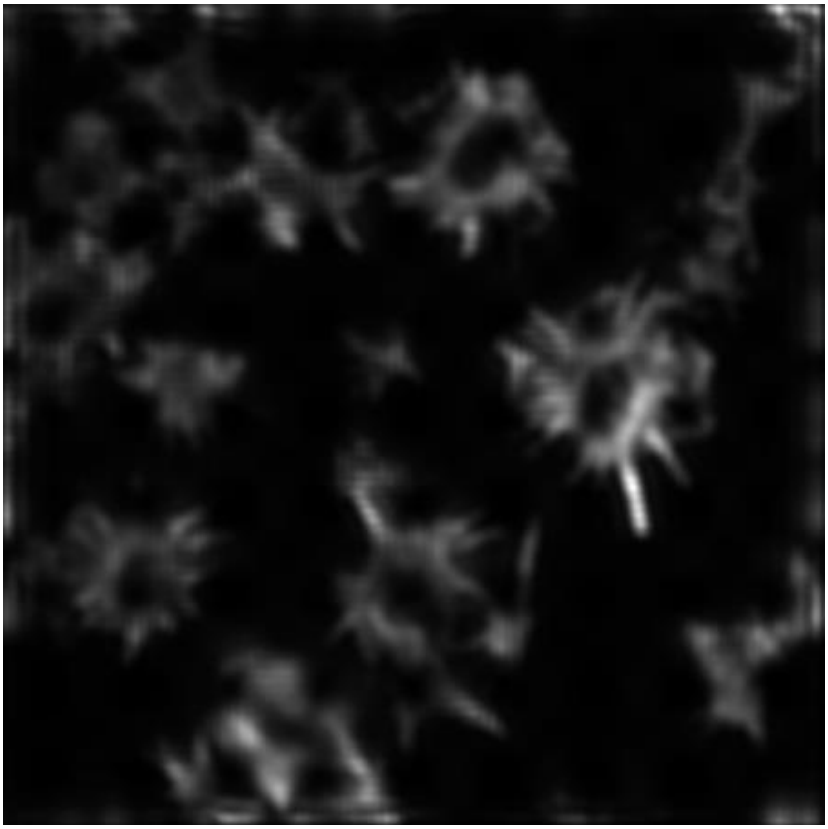

Figure 5.15: A – The reconstructed image in Fourier space (451×451 pixels); B – the final reconstructed image (451×451 pixels).

It can be seen that as with the Fourier Series SIM reconstruction of the platelet image, the image reconstruction is much better than for the phantom image. There are artefacts at the edges of the reconstructed platelet image, but they are minimal. However, the image has reconstructed successfully with some resolution improvement, and the coverage in Fourier space, by the typical 'flower' pattern of the FFT of the reconstructed image, is good and the 'flower' pattern is clear.

5.6.4 Compare reconstruction quality to widefield and standard SIM

The original image, widefield image, standard SIM reconstructed image, and Sinusoid Product-based SIM reconstructed image are now presented together so that the reconstruction quality, in terms of resolution improvement and presence of artefacts, can be compared. See figure 5.16 below.

It can be seen that there is improvement in reconstruction quality compared to the image reconstructed with standard SIM. Furthermore, there is resolution improvement compared with the widefield image. However, the Sinusoid Product-based reconstruction, as with the Fourier Series reconstruction, appears to have reconstructed the distinct edges of the stained actin more than other areas, thus expanding the dark centres of some the platelets compared to the ground truth image, and this aspect of the reconstruction needs to be taken into account with any other image reconstructions.

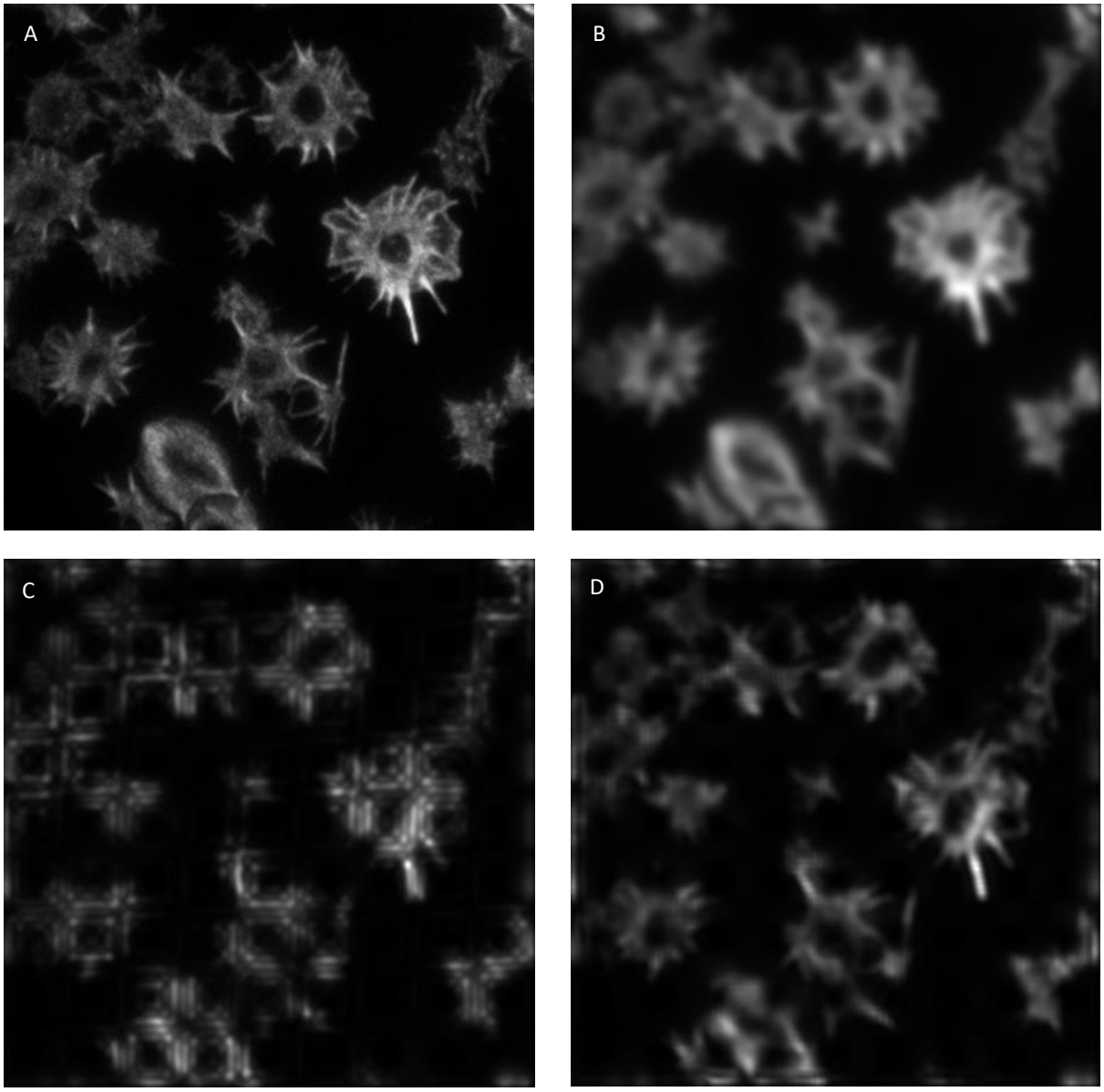

Figure 5.16: A – Ground truth image, 451×451 pixels scaled platelet image, courtesy of Dr Steve Thomas, University of Birmingham, UK; B – the widefield image, created by convolving the ground truth image with the PSF; C – the image as reconstructed using the standard SIM reconstruction algorithm; D – the image as reconstructed using the Sinusoid Product-based SIM reconstruction algorithm, all (451×451 pixels).

5.6.5 Compare reconstruction quality to Fourier Series SIM

The original image, widefield image, Fourier Series SIM reconstructed image, and Sinusoid Product-based SIM reconstructed image are now presented together so that the reconstruction quality, in terms of resolution improvement and presence of artefacts, can be compared. See figure 5.17 below.

It can be seen that the two expanded SIM reconstruction methods have reconstructed very similarly. Both show resolution improvement and similar artefacts at the edges of the reconstructed images. The two methods have the same modelling power, but the differences in that way that they have been formulated make the reconstruction processes different, which is in contrast to the results of Chapter 3 where for simulated masks the Sinusoid Product based SIM reconstruction was better than that for Fourier Series SIM. The image reconstruction for both is very successful when compared to standard SIM, however both are problematic in that the bright actin areas are more prominent and the dark centres of the cells are expanded compared to the ground truth image. This change between the ground truth and the reconstructed image could limit the practical applications of these image reconstruction methods, as the content of the image alters.

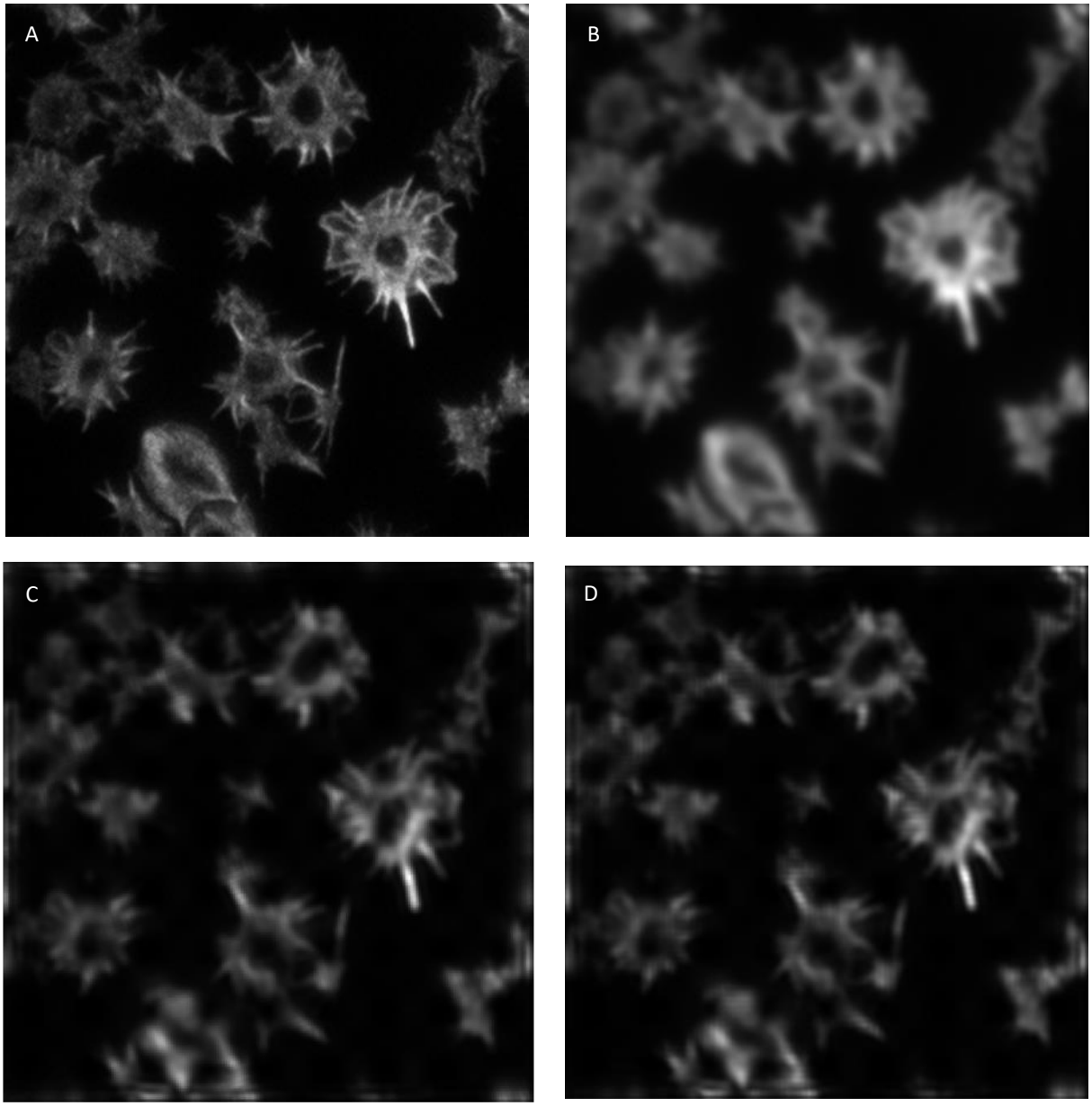

Figure 5.17: A – Ground truth image, 451×451 pixels scaled platelet image, courtesy of Dr Steve Thomas, University of Birmingham, UK; B – the widefield image, created by convolving the ground truth image with the PSF; C – the image as reconstructed using the Fourier Series SIM reconstruction algorithm; D – the image as reconstructed using the Sinusoid Product-based SIM reconstruction algorithm, all (451×451 pixels).

5.6.6 Discussion

The image reconstruction with the Sinusoid Product-based SIM image reconstruction algorithm proved unsuccessful with a phantom sample image, but showed great success with an image of platelets stained for actin. This reconstruction showed minimal artefacts and resolution improvement. However, the reconstructed image did show 'selective' reconstruction in the areas with high actin staining, which could limit its practical use. This was also the case for the Fourier Series SIM reconstruction method. The Sinusoid Product-based SIM reconstruction method was a great improvement on standard SIM when used with the masks produced by the alternative metamaterial design, and could be further adapted for other atypical SIM masks, either metamaterial produced or otherwise.

5.7 Conclusions

In conclusion, an alternative metamaterial design was developed in order to build upon the original 'H' shape based metamaterial design. This new design aimed to be simpler to fabricate whilst still producing the structured illumination required for the proposed TIRF-SIM type microscope. This design was indeed simpler and thus should be more easily fabricated, although this was not possible within the scope of this research. Furthermore, this alternative metamaterial design was capable in simulation of producing a form of structured illumination, with greater contrast between the peaks and troughs of the patterns compared to the original metamaterial design. It also had a shorter spatial frequency, 300nm compared to 600nm, than the original design, meaning that greater resolution improvement should be possible.

However, these patterns were even more different to the typical sinusoid used for standard SIM reconstruction than the original metamaterial design. Thus, standard SIM reconstruction was unsuccessful when using the masks produced by the alternative metamaterial design. Consequently, the two expanded SIM reconstruction methods were adapted to these masks and proved much more successful. Both the Fourier Series and the Sinusoid Product-based SIM reconstruction methods were able to reconstruct an image of platelets stained for actin successfully, with minimal artefacts and resolution improvement compared to the widefield image. Nonetheless there were issues with the reconstructions, as the actin stained areas were reconstructed differently to the dark areas within the cells. This could be potentially ameliorated with further post processing of the images or further adapting the reconstruction algorithms. The Fourier Series reconstruction and the Sinusoid Product-based reconstruction showed similar image reconstruction results.

Other methods such as Blind SIM, discussed in Chapter 1, could prove more successful, but Blind SIM suffers from the challenges of iterative methods, such as reaching false solutions, computational processing power required, and potentially long running time[120,124,127,128]. In contrast, the expanded SIM reconstruction algorithms are not iterative, and thus are quick to run and do not require large amounts of computer processing power. The expanded SIM image reconstruction algorithms could be improved by improving the mathematical models of the masks, for example introducing extra terms into the Fourier Series description of the masks in the Fourier Series SIM algorithm. Furthermore, the algorithms could be further adapted to allow masks that differ beyond the changes in phase and orientation; as seen in the masks produced by the original metamaterial, where not all of the masks deviated from being a single sinusoid, and this reduced the efficacy of the simulation. However, the

expanded SIM algorithms using a Fourier Series and a Sinusoid Product-based expansion have demonstrated great potential for a novel approach to SIM reconstruction.

Chapter 6: Conclusions & Evaluation

The key area of investigation of this research project was the application of metamaterials to super-resolution optical imaging. Specifically, an optical microscope was proposed to emulate a TIRF-SIM microscope, but using metamaterials to create a structured evanescent field.

6.1 Summary of research

This thesis has discussed the extant research that has motivated the research project, particularly in the fields of super-resolution optical microscopy and metamaterials. From this research, an optical microscope with the capabilities of a TIRF-SIM microscope was proposed and designed. Key to this design was the use of metamaterials to produce structured evanescent fields. These structured evanescent fields would allow for super-resolution imaging of the surfaces of samples, with the aim of applying the design to biomedical imaging. In order for this to be achieved, a metamaterial capable of producing sinusoidally structured illumination with multiple phases and orientations, resulting in at least nine sinusoidal masks, was required.

A metamaterial design comprised of a thin gold film mounted on glass, with unit cells of two 'H' shapes at ±45° to the normal cut out from the film, was developed. This metamaterial design was then simulated using CST MWS. These simulations demonstrated that the chosen metamaterial design was capable of producing sinusoidally structured illumination. In addition, by altering the polarisation of the incident light, it was possible to alter the phase of the structured illumination. Although, it was not possible in simulation to produce the desired changes to the orientation of the patterns, so only six patterns were produced by

the metamaterial design with a spatial wavelength of 600nm: three phases – 0, 2π/3, and 4π/3, and two orientations – [0, 1] and [1, 0]. However, the structured illumination patterns produced by the metamaterial deviated from being the desired simple sinusoid.

The next stage in this PhD was the development of a MATLAB algorithm for standard SIM image reconstruction, in order to be able to reconstruct the images produced by the proposed microscope. Then as a result of the atypical SIM masks produced in simulation, new approaches to SIM reconstruction were developed. These new approaches aimed to model the metamaterial patterns more closely than the sinusoid used in standard SIM, and thus improve the quality of image reconstruction by reducing artefacts and improving resolution enhancement in the final reconstructed image. Moreover, these new SIM image reconstruction methods aimed to provide resolution enhancement even with only six images, instead of the nine or more typically used in SIM. Two new image reconstruction approaches were created: Fourier Series SIM, which models the masks as a sum of sinusoids; and Sinusoid Product-based SIM, which models the masks as a product of sinusoids. The different SIM reconstruction methods were all mathematically robust, but proved unsuccessful when using the metamaterial masks; however clear resolution improvement was seen when using simulated approximations of the metamaterial masks.

In addition to the work on image reconstruction, fabrication of prototypes of the chosen metamaterial design was being carried out. This fabrication work was done in collaboration with Dr Alex Robinson, School of Chemical Engineering, University of Birmingham, UK, and Dr Mark Rosamond and Professor Edmund Linfield of the School of Electronic and Electrical Engineering, University of Leeds, UK. A fabrication protocol was developed utilising the key

techniques of electron-beam lithography and etching to produce the metamaterial. However, although the 50nm feature size was achieved and the unit cell design was able to be patterned over 100×100μm areas, the patterning was very rough and adhesion problems meant that fabrication of the metamaterial was poor, as seen when imaged using SEM. Then samples of the metamaterial were tested using FTIR spectroscopy and the results compared to simulations from CST MWS. The FTIR spectra produced were very different from the spectra produced using CST MWS simulations. Furthermore, when tested using a non-commercial optical setup similar to a brightfield microscope, there was negligible signal and high levels of noise. Consequently, the fabrication of the metamaterial was unsuccessful, both in terms of its visual appearance and in its functionality.

Consequently, a new metamaterial design was then developed in collaboration with Qilong Tan of the South China Normal University, Guangzhou, China, as an alternative to the original 'H' shape based metamaterial design. This design was much simpler than the original, consisting of a substrate of silicon dioxide, with gold cuboids of varying sizes arranged in unit cells, each unit cell containing nine of the gold cuboids, on top of it. In simulation, this design was able to produce six structured illumination patterns, which again was fewer than ideally desired, with a spatial wavelength of 300nm and three phases (0, $2\pi/3$, and $4\pi/3$) and two orientations ([0, 1] and [1, 0]). However, the structured illumination was not typically sinusoidal, deviating even more than for the masks produced by the original metamaterial design. These masks, produced by the alternative metamaterial design, were then used in the standard and the expanded SIM image reconstruction algorithms. The standard SIM reconstruction was unsuccessful when using these masks. Nevertheless, both the Fourier Series and the Sinusoid Product-based SIM reconstruction

methods were able to reconstruct successfully, with resolution improvement compared to the widefield image, but with artefacts.

6.2 Key findings

There were multiple findings from this research project that have been presented in this thesis. The first key finding was that the original 'H' shape based metamaterial design was unsuccessful, both in terms of fabrication and image reconstruction. The fabrication as imaged using SEM was flawed, and when tested using an optical setup and FTIR this was confirmed. Improving the fabrication methodology, by improving adhesion between the resist and the substrate or trying a different method such as focussed-ion beam lithography, could potentially improve this but was not possible within the scope of this PhD. Moreover, the masks produced by this metamaterial design in simulation using CST MWS were also unsuccessful, potentially due to their poor modulation depth.

However, the alternative metamaterial design developed later was more promising, even though its structured illumination masks were very different to those of a standard sinusoid, and those produced in simulation by the original metamaterial design. This design was able to produce six masks (three phases produced by changing the incident wavelength, and two orientations produced by changing the incident polarisation), which was fewer than the nine or more desired but with potential to produce more. In addition, the metamaterial unit cell of gold cuboids on a silicon dioxide substrate is a much simpler design, and thus would be potentially less challenging to fabricate. Fabrication of this metamaterial to allow for experimental testing would be desirable, but was not possible within the time frame of this PhD.

The most important findings of this PhD were the multiple approaches to SIM image reconstruction that were developed in MATLAB. Firstly, a standard SIM image reconstruction algorithm was implemented. This was able to show resolution enhancement with simulated atypical patterns, even using only six masks. Therefore, not only could such masks be used to reduce the number needed for SIM image reconstruction, potentially reducing imaging time and complexity, and reconstruction time; but the use of simulated patterns produced in MATLAB means that SIM could potentially be implemented in post processing using a single microscopy image and simulated masks, without using an actual SIM microscope. This would rely on the PSF of the microscope used being fully characterised, and such a methodology would need extensive validation.

Then novel SIM reconstruction methods were also developed. These methods used a new approach to SIM image reconstruction, by using different mathematical expressions (a sum of sinusoids and a product of sinusoids) to better model the metamaterial masks. These new methods were able to successfully reconstruct using the metamaterial masks from the alternative metamaterial design, when standard SIM was unsuccessful, meaning these new methods were required. With only six masks, distinct resolution improvement was seen although there were also image artefacts in the final reconstructed image. These novel methods could be further expanded to other atypical sets of SIM masks, or other mathematical expressions could also be implemented.

6.3 Future work

This thesis, as well as presenting novel results and techniques in the fields of optical microscopy and metamaterials, provides a foundation for future research. Directly building

upon this research, fabricating and testing the alternative metamaterial design would be the next step. Moreover, investigating if this metamaterial design has the capability to produce more than six masks, in order to be able to produce greater resolution enhancement and potentially reduce artefacts in the reconstructed image. Thus, if structured evanescent fields were produced, this metamaterial design could be implemented, as a metalens, in the original proposed super-resolution microscope design. Then its imaging capabilities could be evaluated, including determining any resolution improvement and suitability for biological samples, and then reconstructing super-resolution images. This image reconstruction could be done using the novel image reconstruction approaches discussed in Chapter 3. Another approach would be to try implementing Blind SIM image reconstruction, discussed in Chapter 1, using these metamaterial masks and comparing the results to those from the expanded SIM reconstruction methods.

Furthermore, the Fourier SIM and Sinusoid Product-based SIM image reconstruction methods need to be used on more images, and a wide variety of images, to determine their validity. They could also be further adapted so that they could be applied to different atypical sets of structured illumination masks. In addition, the Fourier Series SIM image reconstruction method could be further expanded to more terms, and tested using either the alternative metamaterial masks, or other sets of masks. Other mathematical expressions for the metamaterial, or other, masks could also be investigated. All with the aim of improving SIM image reconstruction by better modelling the masks to enable better quality SIM image reconstructions, and by potentially reducing the number of masks required for super-resolution imaging, reducing imaging and image reconstruction time.

Appendices

1) MATLAB code for reconstructing CST MWS data

This script was used for importing data exported from CST MWS as a .txt file, processing the data from being electric field data to intensity, and then displaying it both as 2D intensity plots and 1D line plots. This was done in MATLAB R2012a.

```
% Take E-field data from CST (as a txt file), look at the E-field at a
% certain z, look at all x & y points along this plane (2D dataset),
% reconstruct image here (treat end of volume as detector)

% I = (c.n.e0/2)|E|^2
% I = intensity, c = speed of light, n = refractive index, e0 = vacuum
% permittivity, |E| = electric field complex amplitude

clear all;
close all;

filename = 'filename.txt'; %remove titles (Non-numbers)
no_rows = ;% no of lines in text file
% in Notepad: Edit -> Go to -> choose line number > total number of lines

fid = fopen(filename,'r');

for i=1:no_rows
    file_data = str2num(fgetl(fid)); % read in info from file line by line
    x_coord(i) = file_data(1);
    y_coord(i) = file_data(2);
    z_coord(i) = file_data(3);
    Ex(i) = file_data(4);
    Ey(i) = file_data(5);
    Ez(i) = file_data(6);
    Ex_im(i) = file_data(7);
    Ey_im(i) = file_data(8);
    Ez_im(i) = file_data(9);
end

% Now have all coordinate and E-field data from file
% need to calculate amplitude of E at each point on z plane (detector)

z_chosen = ; % chosen z coordinate to extract data for
count = 0;
for i=1:no_rows
    if z_coord(i)==z_chosen
        count=count+1;
        Data_2D(count,1)= x_coord(i);
        Data_2D(count,2)= y_coord(i);
        Data_2D(count,3)= Ex(i);
        Data_2D(count,4)= Ey(i);
        Data_2D(count,5)= Ez(i);
        Data_2D(count,6)= Ex_im(i);
        Data_2D(count,7)= Ey_im(i);
        Data_2D(count,8)= Ez_im(i);
```

```
    end
end

E_detected = zeros(count,3);
for i=1:size(Data_2D,1)
    E_detected(i,1) = Data_2D(i,1); % x coordinate
    E_detected(i,2) = Data_2D(i,2); % y coordinate
    E_detected(i,3) =
((Data_2D(i,3)^2)+(Data_2D(i,6)^2)+(Data_2D(i,4)^2)+(Data_2D(i,7)^2)+
(Data_2D(i,5)^2)+(Data_2D(i,8)^2));
    % Ex^2 + Im(Ex)^2 + Ey^2 + Im(Ey)^2 + Ez^2 + Im(Ez)^2
end

c = 3e8; % speed of light
n = 1; % refractive index
e0 = 8.854e-12; % permittivity of free space/ electric constant
constant = c*n*e0/2;

Intensity(:,1) = E_detected(:,1); % x coordinate
Intensity(:,2) = E_detected(:,2); % y coordinate
Intensity(:,3) = constant*(E_detected(:,3)); % Intensity

% if need to rescale data
G = (Intensity(:,3)/max(Intensity(:,3)));
G2 = G - round(min(G),1);
Intensity_export = G2/max(G2);

% Now plot data as image...
figure;
xval = unique(Intensity(:,1));
yval = unique(Intensity(:,2));
X = reshape(Intensity(:,3),numel(xval),numel(yval));
RX = reshape(Intensity(:,1),numel(xval),numel(yval)); % x coord list
RY = reshape(Intensity(:,2),numel(xval),numel(yval)); % y coord list
imagesc(Intensity(:,1),Intensity(:,2),X')
axis equal
xlabel('x');
ylabel('y');
colorbar;

% Find spatial wavelength(s)by looking at 1D line plots
chosencoord = ;% chosen x or y coordinate
figure,plot(RX(:,1),X(:,chosencoord)); % line plot in x
xlabel('x');
ylabel('Intensity');
figure,plot(real(fftshift(fft(X(:,chosencoord))))); % Fourier Transform of
line plot in x

figure,plot(RX(:,1),X(chosencoord,:)); % line plot in y
xlabel('y');
ylabel('Intensity');
figure,plot(real(fftshift(fft(X(chosencoord,:))))); Fourier Transform of
line plot in y
```

2) MATLAB code for standard SIM image reconstruction using masks created in MATLAB

This script was used for performing the standard SIM image reconstruction on a user imported image, using masks created within the MATLAB algorithm. This was done in MATLAB R2012a.

```
close all; clear;
% Scale image by factor n
n= ;
f = double(imresize(imread('image.tif'),n));
% or f = phantom();
figure('Name','Base Image'), imshow(f,[]);
figure('Name','FFT Base Image'), imshow(log(abs(fftshift(fft2(f)))),[]);
% Set the scale inverse to the magnification
nmPerPx = ;
x_px = size(f,2);
y_px = size(f,1);

% Image size in nm
x_nm = x_px*nmPerPx;
y_nm = y_px*nmPerPx;
% Create image grid in nm
[Xnm,Ynm] = meshgrid(nmPerPx*(0:x_px-1), nmPerPx*(0:y_px-1));

% Create the PSF, in nm
wavelength = 500;
NA = 1.49;
[Xpsf,Ypsf] = meshgrid(-wavelength:nmPerPx:wavelength);
create_psf =
@(X,Y,wavelength,NA) exp(-(X.^2+Y.^2)/(2*(0.45*wavelength/(2*NA))^2));
psf = create_psf(Xpsf,Ypsf,wavelength,NA);
figure('Name','PSF'), surf(Xpsf,Ypsf,psf);
figure('Name','FFT PSF'), imshow(abs(fftshift(fft2(psf))),[]);

% Plot widefield image and its FFT
widefield = conv2(f,psf,'same');
figure('Name','Widefield Image'), imshow(widefield,[]);
figure('Name','FFT Widefield Image'),
imshow(log(abs(fftshift(fft2(widefield)))),[]);

%% Create the patterns
spatial_wavelength = ;
phi = [0, 2*pi()/3, 4*pi()/3];
% Pattern orientations
% Two Patterns
% p = [1,0; 0,1];
% Three patterns
p = [1,0; cos(pi()/3),sin(pi()/3); cos(2*pi()/3), sin(2*pi()/3)];
% Five patterns
%p = [1,0; cos(pi()/5),sin(pi()/5); cos(2*pi()/5), sin(2*pi()/5);
cos(3*pi()/5),sin(3*pi()/5); cos(4*pi()/5), sin(4*pi()/5)];
np = size(p,1);
nphi = length(phi);
spatial_freq = 2*pi()/spatial_wavelength;
masks = cell(np,nphi);
XY_vect = [reshape(Xnm,1,[]); reshape(Ynm,1,[])];
```

```
for ii=1:np
    for ij=1:nphi
        masks{ii,ij} = 1+cos(spatial_freq*p(ii,:)*XY_vect+phi(ij));
        masks{ii,ij} = reshape(masks{ii,ij}, [x_px,y_px]);
    end
end
figure('Name','Masks');
for ii=1:numel(masks)
    subplot(np,nphi,ii);
    imshow(masks{ii},[]);
end

%% Apply and display the patterns
g = cell(size(masks));
figure('Name','Acquired Images');
for ii=1:numel(masks)
    g{ii} = conv2(masks{ii}.*f,psf,'same');
    subplot(np,nphi,ii);
    imshow(g{ii},[]);
end

%% Compute and display the FT of the images
G = cell(size(masks));
figure('Name','FFT of acquired images');
for ii=1:numel(masks)
    G{ii} = fftshift(fft2(g{ii}));
    subplot(np,nphi,ii);
    imshow(log(abs(G{ii})),[]);
end

%% Invert the phases
C = cell(size(masks));
for ii=1:np
    C{ii,1} = G{ii,1} + G{ii,2} + G{ii,3};
    C{ii,2} = G{ii,1} + exp(1i*phi(2))*G{ii,2} + exp(1i*phi(3))*G{ii,3};
    C{ii,3} = G{ii,1} + exp(-1i*phi(2))*G{ii,2} + exp(-1i*phi(3))*G{ii,3};
end

figure('Name','Separated components');
for ii=1:numel(C)
    subplot(np,nphi,ii);
    imshow(log(abs(C{ii})),[]);
end

%% Shift the components
% Do this in real space
CS = cell(size(C));
otfk = cell(size(C));
otf = create_psf(Xnm-mean(Xnm(1,:)),Ynm-mean(Ynm(:,1)),wavelength,NA
for ii=1:np
    K = reshape(spatial_freq*p(ii,:)*XY_vect, [x_px,y_px]);
    CS{ii,1} = C{ii,1};
    CS{ii,2} = fftshift(fft2(exp(-1i*K).*ifft2(fftshift(C{ii,2}))));
    CS{ii,3} = fftshift(fft2(exp(1i*K).*ifft2(fftshift(C{ii,3}))));
    otfk{ii,1} = fftshift(fft2(otf));
    otfk{ii,2} = fftshift(fft2(exp(-1i*K).*otf));
    otfk{ii,3} = fftshift(fft2(exp(1i*K).*otf));
end
```

```
figure('Name','Shifted, separated components');
for ii=1:numel(CS)
    subplot(np,nphi,ii);
    imshow(log(abs(CS{ii})),[]);
end

figure('Name','Shifted OTFs');
for ii=1:numel(CS)
    subplot(np,nphi,ii);
    imshow((abs(otfk{ii})),[]);
end

%% Apply the Wiener Filter
num = 0;
denom = 0;
w = ; % noise factor
figure('Name','Components of Wiener Filter');
for ii=1:numel(CS)
    subplot(np,nphi,ii);
    imshow(log(abs(conj(otfk{ii}).*CS{ii})),[]);
    num = num + conj(otfk{ii}).*CS{ii};
    denom = denom + abs(otfk{ii}).^2 +w;
end

Sk = num./denom;
figure('Name','FFT Reconstructed image'), imshow(log(abs(Sk)),[]);

newotf = create_psf(Xpsf,Ypsf,wavelength/2,NA);
% Choose wavelength/$ for resolution improvement of factor of $
newotf_k = fftshift(fft2(newotf));
S = abs(fftshift(ifft2((Sk))));
figure('Name','Reconstructed image'), imshow(conv2(S,newotf,'same'),[]);
```

3) MATLAB code for standard SIM image reconstruction using imported masks

This script was used for performing the standard SIM image reconstruction on a user imported image, using masks imported by the user. This was done in MATLAB R2012a.

```
close all; clear;
% Scale image by factor n
no_rowsh = ; % no of rows in masks .txt files
image_size= ; % size of image used as sample
n=no_rowsh/image_size;

f = double(imresize(imread('image.tif'),n));
% or f = phantom();
figure('Name','Base Image'), imshow(f,[]);
figure('Name','FFT Base Image'), imshow(log(abs(fftshift(fft2(f)))),[]);
% Set the scale inverse to the magnification
nmPerPx =;
x_px = size(f,2);
y_px = size(f,1);

% Image size in nm
x_nm = x_px*nmPerPx;
y_nm = y_px*nmPerPx;
% Create image grid in nm
[Xnm,Ynm] = meshgrid(nmPerPx*(0:x_px-1), nmPerPx*(0:y_px-1));

% Create the PSF, in nm
wavelength = 500;
NA = 1.49;
[Xpsf,Ypsf] = meshgrid(-wavelength:nmPerPx:wavelength);
create_psf = @(X,Y,wavelength,NA) exp(-
(X.^2+Y.^2)/(2*(0.45*wavelength/(2*NA))^2));
psf = create_psf(Xpsf,Ypsf,wavelength,NA);
figure('Name','PSF'), surf(Xpsf,Ypsf,psf);
figure('Name','FFT PSF'), imshow(abs(fftshift(fft2(psf))),[]);

% Plot widefield image and its FFT
widefield = conv2(f,psf,'same');
figure('Name','Widefield Image'), imshow(widefield,[]);
figure('Name','FFT Widefield Image'),
imshow(log(abs(fftshift(fft2(widefield)))),[]);

%% Create the patterns
spatial_wavelength = ;
phi = [0, 2*pi()/3, 4*pi()/3];
% Two Patterns
p = [1,0; 0,1];
% Three patterns
%p = [1,0; cos(pi()/3),sin(pi()/3); cos(2*pi()/3), sin(2*pi()/3)];
% Five patterns
%p = [1,0; cos(pi()/5),sin(pi()/5); cos(2*pi()/5), sin(2*pi()/5);
cos(3*pi()/5),sin(3*pi()/5); cos(4*pi()/5), sin(4*pi()/5)];
np = size(p,1);
nphi = length(phi);
spatial_freq = 2*pi()/spatial_wavelength;
```

```
masks = cell(np,nphi);
XY_vect = [reshape(Xnm,1,[]); reshape(Ynm,1,[])];

%Create strings of filenames
file_no = ['678'; '712'; '792'];
file_no = cellstr(file_no);
XorY = ['-x';'-y'];
XorY = cellstr(XorY);
filestr1 = 'E-';
filestr2 = '.txt';

for k = 1:np
    for j=1:nphi
        filenames{k,j} = [filestr1 file_no{j} XorY{k} filestr2];
    end
end

for ii = 1:np
    for ij=1:nphi
        fid = fopen(filenames{ii,ij},'r');
        for ik=1:no_rowsh
            file_data = str2num(fgetl(fid));
            % read in info from file line by line
            imageh(ik,:) = file_data(:);
        end
        fclose(fid);

        masks{ii,ij} = flipud(imageh);
        %Images of illumination.*sample (m.*f)
    end
end
figure('Name','Masks');
for ii=1:numel(masks)
    subplot(np,nphi,ii);
    imshow(masks{ii},[]);
end

%% Apply and display the patterns
g = cell(size(masks));
figure('Name','Acquired Images');
for ii=1:numel(masks)
    g{ii} = conv2(masks{ii}.*f,psf,'same');
    subplot(np,nphi,ii);
    imshow(g{ii},[]);
end

%% Compute and display the FT of the images
G = cell(size(masks));
figure('Name','FFT of acquired images');
for ii=1:numel(masks)
    G{ii} = fftshift(fft2(g{ii}));
    subplot(np,nphi,ii);
    imshow(log(abs(G{ii})),[]);
end

%% Invert the phases
C = cell(size(masks));
for ii=1:np
```

```
    C{ii,1} = G{ii,1} + G{ii,2} + G{ii,3};
    C{ii,2} = G{ii,1} + exp(-1i*phi(2))*G{ii,2} + exp(-1i*phi(3))*G{ii,3};
    C{ii,3} = G{ii,1} + exp(1i*phi(2))*G{ii,2} + exp(1i*phi(3))*G{ii,3};
end

figure('Name','Separated components');
for ii=1:numel(C)
    subplot(np,nphi,ii);
    imshow(log(abs(C{ii})),[]);
end

%% Shift the components
% Do this in real space
CS = cell(size(C));
otfk = cell(size(C));
otf = create_psf(Xnm-mean(Xnm(1,:)),Ynm-mean(Ynm(:,1)),wavelength,NA);
for ii=1:np
    K = reshape(spatial_freq*p(ii,:)*XY_vect, [x_px,y_px]);
    CS{ii,1} = C{ii,1};
    CS{ii,2} = fftshift(fft2(exp(-1i*K).*ifft2(fftshift(C{ii,2}))));
    CS{ii,3} = fftshift(fft2(exp(1i*K).*ifft2(fftshift(C{ii,3}))));
    otfk{ii,1} = fftshift(fft2(otf));
    otfk{ii,2} = fftshift(fft2(exp(-1i*K).*otf));
    otfk{ii,3} = fftshift(fft2(exp(1i*K).*otf));
end

figure('Name','Shifted, separated components');
for ii=1:numel(CS)
    subplot(np,nphi,ii);
    imshow(log(abs(CS{ii})),[]);
end

figure('Name','Shifted OTFs');
for ii=1:numel(CS)
    subplot(np,nphi,ii);
    imshow((abs(otfk{ii})),[]);
end

%% Apply the Wiener Filter
num = 0;
denom = 0;
w = ; % noise factor
figure('Name','Components of Wiener Filter');
for ii=1:numel(CS)
    subplot(np,nphi,ii);
    imshow(log(abs(conj(otfk{ii}).*CS{ii})),[]);
    num = num + conj(otfk{ii}).*CS{ii};
    denom = denom + abs(otfk{ii}).^2 +w;
end

Sk = num./denom;
figure('Name','FFT Reconstructed image'), imshow(log(abs(Sk)),[]);

newotf = create_psf(Xpsf,Ypsf,wavelength/2,NA);
% Choose wavelength/$ for resolution improvement of factor of $
newotf_k = fftshift(fft2(newotf));
S = abs(fftshift(ifft2((Sk))));
figure('Name','Reconstructed image'), imshow(conv2(S,newotf,'same'),[]);
```

4) MATLAB code for Fourier Series SIM image reconstruction using masks created in MATLAB

This script was used for performing the Fourier Series SIM image reconstruction on a user imported image, using masks created within the MATLAB algorithm. This was done in MATLAB R2012a.

```
close all; clear;
% Scale image by factor n
no_rows = ; % no of rows in masks .txt files
image_size= ; % size of image used as sample
n=no_rowsh/image_size;

f = double(imresize(imread('image.tif'),n));
% or f = phantom();
figure('Name','Base Image'), imshow(f,[]);
figure('Name','FFT Base Image'), imshow(log(abs(fftshift(fft2(f)))),[]);
% Set the scale inverse to the magnification
nmPerPx = ;
x_px = size(f,2);
y_px = size(f,1);

% Image size in nm
x_nm = x_px*nmPerPx;
y_nm = y_px*nmPerPx;
% Create image grid in nm
[Xnm,Ynm] = meshgrid(nmPerPx*(0:x_px-1), nmPerPx*(0:y_px-1));

% Create the PSF, in nm
wavelength = 500;
NA = 1.49;
[Xpsf,Ypsf] = meshgrid(-wavelength:nmPerPx:wavelength);
create_psf = @(X,Y,wavelength,NA) exp(-
(X.^2+Y.^2)/(2*(0.45*wavelength/(2*NA))^2));
psf = create_psf(Xpsf,Ypsf,wavelength,NA);
figure('Name','PSF'), surf(Xpsf,Ypsf,psf);
figure('Name','FFT PSF'), imshow(abs(fftshift(fft2(psf))),[]);

% Plot widefield image and its FFT
widefield = conv2(f,psf,'same');
figure('Name','Widefield Image'), imshow(widefield,[]);
figure('Name','FFT Widefield Image'),
imshow(log(abs(fftshift(fft2(widefield)))),[]);

%% Create the patterns
N=2; % number of terms in Fourier Series
spatial_wavelength1 = ;% nm, period of 'stripes' in metamaterial pattern,
needs to scale with nmPerPx
spatial_wavelength2 = spatial_wavelength1/$;% nm, period of 'blobs' within
each 'stripe' in metamaterial pattern, choose $
spatial_freq1 = 2*pi()/spatial_wavelength1;
spatial_freq2 = 2*pi()/spatial_wavelength2;

phi = [0, 2*pi()/3, 4*pi()/3];
theta = zeros(size(phi));
```

```
a = spatial_freq1;
b = spatial_freq2;

R = [0 -1; 1 0]; % rotation matrix
Per{1,1} = a;
Per{2,1} = b*R;

% pattern orientations
% Two patterns
p = [1,0; 0,1];
% Three patterns
%p = [1,0; cos(pi()/3),sin(pi()/3); cos(2*pi()/3), sin(2*pi()/3)];
% Five patterns
%p = [1,0; cos(pi()/5),sin(pi()/5); cos(2*pi()/5), sin(2*pi()/5);
cos(3*pi()/5),sin(3*pi()/5); cos(4*pi()/5), sin(4*pi()/5)];
np = size(p,1);
nphi = length(phi);

Phases = cell(N,1); % all the phases used in the Fourier expansion
Phases{1,1} = phi;
Phases{2,1} = theta;

c = phi + 2*(N-1); % number of c's and thus CS's for each p

masks = cell(np,nphi);
XY_vect = [reshape(Xnm,1,[]); reshape(Ynm,1,[])];

for ii=1:np
    for ij=1:nphi
            Per_P{1} = (Per{1,1}*p(ii,:)');
            Per_P{2} = (Per{2,1}*p(ii,:)');
            masks{ii,ij} = 1 +
(cos((Per_P{1}(1)*Xnm+Per_P{1}(2)*Ynm)+Phases{1,1}(ij)))...
                + (cos((Per_P{2}(1)*Xnm+Per_P{2}(2)*Ynm)+Phases{2,1}(ij)));
    end
end


figure('Name','Masks');
for ii=1:numel(masks)
    subplot(np,nphi,ii);
    imshow(masks{ii},[]);
end

%% Apply and display the patterns
g = cell(size(masks));
figure('Name','Acquired Images');
for ii=1:numel(masks)
    g{ii} = conv2(masks{ii}.*f,psf,'same');
    subplot(np,nphi,ii);
    imshow(g{ii},[]);
end

%% Compute and display the FT of the images
G = cell(size(masks));
figure('Name','FFT of acquired images');
for ii=1:numel(masks)
```

```
    G{ii} = fftshift(fft2(g{ii}));
    subplot(np,nphi,ii);
    imshow(log(abs(G{ii})),[]);
end

%% Invert the phases
% Different in expanded SIM compared to standard SIM
C = cell(np,nphi+2);
for ii=1:np
    C{ii,1} = G{ii,1} + G{ii,2} + G{ii,3};
    C{ii,2} = exp(-1i*(phi(1)))*G{ii,1} + exp(-1i*(phi(2)))*G{ii,2}+ ...
        exp(-1i*(phi(3)))*G{ii,3};
    C{ii,3} = exp(1i*(phi(1)))*G{ii,1} + exp(1i*(phi(2)))*G{ii,2}+ ...
        exp(1i*(phi(3)))*G{ii,3};
    C{ii,4} = exp(-1i*(theta(1)))*G{ii,1} + exp(-1i*(theta(2)))*G{ii,2}+
... exp(-1i*(theta(3)))*G{ii,3};
    C{ii,5} = exp(1i*(theta(1)))*G{ii,1} + exp(1i*(theta(2)))*G{ii,2}+ ...
        exp(1i*(theta(3)))*G{ii,3};
end

figure('Name','Separated components');
for ii=1:numel(C)
    subplot(np,nphi+2,ii);
    imshow(log(abs(C{ii})),[]);
end

%% Shift the components
% Do this in real space
% Different in expanded SIM compared to standard SIM
CS = cell(size(masks));
otfk = cell(size(masks));
otf = create_psf(Xnm-mean(Xnm(1,:)),Ynm-mean(Ynm(:,1)),wavelength,NA);

for ii=1:np
    Per_P{1} = (Per{1,1}*p(ii,:)');
    Per_P{2} = (Per{2,1}*p(ii,:)');
    K1 = (Per_P{1}(1)*Xnm+Per_P{1}(2)*Ynm);
    K2 = (Per_P{2}(1)*Xnm+Per_P{2}(2)*Ynm);
    CS{ii,1} = C{ii,1};
    CS{ii,2} = fftshift(fft2(exp(-1i*(K1+K2)).*ifft2(fftshift(C{ii,2}))));
    CS{ii,3} = fftshift(fft2(exp(1i*(K1+K2)).*ifft2(fftshift(C{ii,3}))));
    otfk{ii,1} = fftshift(fft2(otf));
    otfk{ii,2} = fftshift(fft2(exp(-1i*(K1+K2)).*otf));
    otfk{ii,3} = fftshift(fft2(exp(1i*(K1+K2)).*otf));
end

figure('Name','Shifted, separated components');
for ii=1:numel(CS)
    subplot(np,nphi,ii);
    imshow(log(abs(CS{ii})),[]);
end

figure('Name','Shifted OTFs');
for ii=1:numel(CS)
    subplot(np,nphi,ii);
    imshow((abs(otfk{ii})),[]);
end
```

```
%% Apply the Wiener Filter
num = 0;
denom = 0;
w = ; % noise factor
figure('Name','Components of Wiener Filter');
for ii=1:numel(CS)
    subplot(np,nphi,ii);
    imshow(log(abs(conj(otfk{ii}).*CS{ii})),[]);
    % complex conjugate very important
    num = num + conj(otfk{ii}).*CS{ii};
    denom = denom + abs(otfk{ii}).^2 +w;
end

Sk = num./denom;
figure('Name','FFT Reconstructed image'), imshow(log(abs(Sk)),[]);

newotf = create_psf(Xpsf,Ypsf,wavelength/2,NA);
% Choose wavelength/$ for resolution improvement of factor of $
newotf_k = fftshift(fft2(newotf));
S = abs(fftshift(ifft2((Sk))));
figure('Name','Reconstructed image'), imshow(conv2(S,newotf,'same'),[]);
```

5) MATLAB code for Fourier Series SIM image reconstruction using imported masks

This script was used for performing the Fourier Series SIM image reconstruction on a user imported image, using masks imported by the user. This was done in MATLAB R2012a.

```
close all; clear;
% Scale image by factor n
no_rowsh = ; % no of rows in masks .txt files
image_size= ; % size of image used as sample
n=no_rowsh/image_size;

f = double(imresize(imread('image.tif'),n));
% or f = phantom();
figure('Name','Base Image'), imshow(f,[]);
figure('Name','FFT Base Image'), imshow(log(abs(fftshift(fft2(f)))),[]);
% Set the scale inverse to the magnification
nmPerPx = ;
x_px = size(f,2);
y_px = size(f,1);

% Image size in nm
x_nm = x_px*nmPerPx;
y_nm = y_px*nmPerPx;
% Create image grid in nm
[Xnm,Ynm] = meshgrid(nmPerPx*(0:x_px-1), nmPerPx*(0:y_px-1));

% Create the PSF, in nm
wavelength = 500;
NA = 1.49;
[Xpsf,Ypsf] = meshgrid(-wavelength:nmPerPx:wavelength);
create_psf = @(X,Y,wavelength,NA) exp(-
(X.^2+Y.^2)/(2*(0.45*wavelength/(2*NA))^2));
psf = create_psf(Xpsf,Ypsf,wavelength,NA);
figure('Name','PSF'), surf(Xpsf,Ypsf,psf);
figure('Name','FFT PSF'), imshow(abs(fftshift(fft2(psf))),[]);

% Plot widefield image and its FFT
widefield = conv2(f,psf,'same');
figure('Name','Widefield Image'), imshow(widefield,[]);
figure('Name','FFT Widefield Image'),
imshow(log(abs(fftshift(fft2(widefield)))),[]);

%% Create the patterns
N=2; % number of terms in Fourier Series
spatial_wavelength1 = ;% nm, period of 'stripes' in metamaterial pattern,
needs to scale with nmPerPx
spatial_wavelength2 = spatial_wavelength1/$;% nm, period of 'blobs' within
each 'stripe' in metamaterial pattern, choose $
spatial_freq1 = 2*pi()/spatial_wavelength1;
spatial_freq2 = 2*pi()/spatial_wavelength2;

phi = [0, 2*pi()/3, 4*pi()/3];
theta = zeros(size(phi));

a = spatial_freq1;
```

```
b = spatial_freq2;

R = [0 -1; 1 0]; % rotation matrix
Per{1,1} = a;
Per{2,1} = b*R;

% pattern orientations
% Two patterns
p = [1,0; 0,1];
% Three patterns
%p = [1,0; cos(pi()/3),sin(pi()/3); cos(2*pi()/3), sin(2*pi()/3)];
% Five patterns
%p = [1,0; cos(pi()/5),sin(pi()/5); cos(2*pi()/5), sin(2*pi()/5);
cos(3*pi()/5),sin(3*pi()/5); cos(4*pi()/5), sin(4*pi()/5)];
np = size(p,1);
nphi = length(phi);

Phases = cell(N,1); % all the phases used in the Fourier expansion
Phases{1,1} = phi;
Phases{2,1} = theta;

c = phi + 2*(N-1); % number of c's and thus CS's for each p

masks = cell(np,nphi);
XY_vect = [reshape(Xnm,1,[]); reshape(Ynm,1,[])];

%Create strings of filenames
file_no = ['678'; '712'; '792'];
file_no = cellstr(file_no);
XorY = ['-x';'-y'];
XorY = cellstr(XorY);
filestr1 = 'E_';
filestr2 = '.txt';

for k = 1:np
    for j=1:nphi
        filenames{k,j} = [filestr1 file_no{j} XorY{k} filestr2];
    end
end

for ii = 1:np
    for ij=1:nphi
        fid = fopen(filenames{ii,ij},'r');
        for ik=1:no_rowsh
            file_data = str2num(fgetl(fid));
            % read in info from file line by line
            imageh(ik,:) = file_data(:);
        end
        fclose(fid);

        masks{ii,ij} = flipud(imageh);
        %Images of illumination.*sample (m.*f)
    end
end

figure('Name','Masks');
for ii=1:numel(masks)
```

```
    subplot(np,nphi,ii);
    imshow(masks{ii},[]);
end

%% Apply and display the patterns
g = cell(size(masks));
figure('Name','Acquired Images');
for ii=1:numel(masks)
    g{ii} = conv2(masks{ii}.*f,psf,'same');
    subplot(np,nphi,ii);
    imshow(g{ii},[]);
end

%% Compute and display the FT of the images
G = cell(size(masks));
figure('Name','FFT of acquired images');
for ii=1:numel(masks)
    G{ii} = fftshift(fft2(g{ii}));
    subplot(np,nphi,ii);
    imshow(log(abs(G{ii})),[]);
end

%% Invert the phases
% Different in expanded SIM compared to standard SIM
C = cell(np,nphi+2);
for ii=1:np
    C{ii,1} = G{ii,1} + G{ii,2} + G{ii,3};
    C{ii,2} = exp(-1i*(phi(1)))*G{ii,1} + exp(-1i*(phi(2)))*G{ii,2}+ ...
        exp(-1i*(phi(3)))*G{ii,3};
    C{ii,3} = exp(1i*(phi(1)))*G{ii,1} + exp(1i*(phi(2)))*G{ii,2}+ ...
        exp(1i*(phi(3)))*G{ii,3};
    C{ii,4} = exp(-1i*(theta(1)))*G{ii,1} + exp(-1i*(theta(2)))*G{ii,2}+
... exp(-1i*(theta(3)))*G{ii,3};
    C{ii,5} = exp(1i*(theta(1)))*G{ii,1} + exp(1i*(theta(2)))*G{ii,2}+ ...
        exp(1i*(theta(3)))*G{ii,3};
end

figure('Name','Separated components');
for ii=1:numel(C)
    subplot(np,nphi+2,ii);
    imshow(log(abs(C{ii})),[]);
end

%% Shift the components
% Do this in real space
% Different in expanded SIM compared to standard SIM
CS = cell(size(masks));
otfk = cell(size(masks));
otf = create_psf(Xnm-mean(Xnm(1,:)),Ynm-mean(Ynm(:,1)),wavelength,NA);

for ii=1:np
    Per_P{1} = (Per{1,1}*p(ii,:)');
    Per_P{2} = (Per{2,1}*p(ii,:)');
    K1 = (Per_P{1}(1)*Xnm+Per_P{1}(2)*Ynm);
    K2 = (Per_P{2}(1)*Xnm+Per_P{2}(2)*Ynm);
    % Using 3 CS's see maths
    CS{ii,1} = C{ii,1};
    CS{ii,2} = fftshift(fft2(exp(-1i*(K1+K2)).*ifft2(fftshift(C{ii,2}))));
```

```
    CS{ii,3} = fftshift(fft2(exp(1i*(K1+K2)).*ifft2(fftshift(C{ii,3}))));
    otfk{ii,1} = fftshift(fft2(otf));
    otfk{ii,2} = fftshift(fft2(exp(-1i*(K1+K2)).*otf));
    otfk{ii,3} = fftshift(fft2(exp(1i*(K1+K2)).*otf));
end

figure('Name','Shifted, separated components');
for ii=1:numel(CS)
    subplot(np,nphi,ii);
    imshow(log(abs(CS{ii})),[]);
end

figure('Name','Shifted OTFs');
for ii=1:numel(CS)
    subplot(np,nphi,ii);
    imshow((abs(otfk{ii})),[]);
end

%% Apply the Wiener Filter
num = 0;
denom = 0;
w = ; % noise factor
figure('Name','Components of Wiener Filter');
for ii=1:numel(CS)
    subplot(np,nphi,ii);
    imshow(log(abs(conj(otfk{ii}).*CS{ii})),[]);
    % complex conjugate very important
    num = num + conj(otfk{ii}).*CS{ii};
    denom = denom + abs(otfk{ii}).^2 +w;
end

Sk = num./denom;
figure('Name','FFT Reconstructed image'), imshow(log(abs(Sk)),[]);

newotf = create_psf(Xpsf,Ypsf,wavelength/2,NA);
% Choose wavelength/$ for resolution improvement of factor of $
newotf_k = fftshift(fft2(newotf));
S = abs(fftshift(ifft2((Sk))));
figure('Name','Reconstructed image'), imshow(conv2(S,newotf,'same'),[]);
```

6) MATLAB code for Sinusoid Product-based SIM image reconstruction using masks created in MATLAB

This script was used for performing the Sinusoid Product-based SIM image reconstruction on a user imported image, using masks created within the MATLAB algorithm. This was done in MATLAB R2012a.

```
close all; clear;
% Scale image by factor n
no_rows = ; % no of rows in masks .txt files
image_size= ; % size of image used as sample
n=no_rowsh/image_size;

f = double(imresize(imread('image.tif'),n));
% or f = phantom();
figure('Name','Base Image'), imshow(f,[]);
figure('Name','FFT Base Image'), imshow(log(abs(fftshift(fft2(f)))),[]);
% Set the scale inverse to the magnification
nmPerPx = ;
x_px = size(f,2);
y_px = size(f,1);

% Image size in nm
x_nm = x_px*nmPerPx;
y_nm = y_px*nmPerPx;
% Create image grid in nm
[Xnm,Ynm] = meshgrid(nmPerPx*(0:x_px-1), nmPerPx*(0:y_px-1));

% Create the PSF, in nm
wavelength = 500;
NA = 1.49;
[Xpsf,Ypsf] = meshgrid(-wavelength:nmPerPx:wavelength);
create_psf = @(X,Y,wavelength,NA) exp(-
(X.^2+Y.^2)/(2*(0.45*wavelength/(2*NA))^2));
psf = create_psf(Xpsf,Ypsf,wavelength,NA);
figure('Name','PSF'), surf(Xpsf,Ypsf,psf);
figure('Name','FFT PSF'), imshow(abs(fftshift(fft2(psf))),[]);

% Plot widefield image and its FFT
widefield = conv2(f,psf,'same');
figure('Name','Widefield Image'), imshow(widefield,[]);
figure('Name','FFT Widefield Image'),
imshow(log(abs(fftshift(fft2(widefield)))),[]);

%% Create the patterns
spatial_wavelength1 = ;% nm, period of 'stripes' in metamaterial pattern,
needs to scale with nmPerPx
spatial_wavelength2 = spatial_wavelength1/$;% nm, period of 'blobs' within
each 'stripe' in metamaterial pattern, choose $
spatial_freq1 = 2*pi()/spatial_wavelength1;
spatial_freq2 = 2*pi()/spatial_wavelength2;

phi = [0, 2*pi()/3, 4*pi()/3];

a = spatial_freq1;
b = spatial_freq2;
```

```
period_x{1} = a;
period_x{2} = b;
period_y{1} = b;
period_y{2} = a;

% pattern orientations to create chequerboard of peaks
p1 = [1,1];
p2 = [1,-1];
p_orthog = dot(p1,p2); % check orthogonality, should be 0
% p_angles = [0, pi()/3, 2*pi()/3]; % three orientations
p_angles = [0, pi()/2]; % two orientations


np = length(p_angles);
nphi = length(phi);

p = [0.5*[a,b].*(p1-p2); 0.5*[b,a].*(p1+p2)]; % basic orientation [1,0]
 R = @(t) [cos(t),-sin(t);sin(t),cos(t)]; % rotation matrix


phi_x{1} = zeros(1,nphi); % x poln P
phi_x{2} = phi; % y poln P
phi_y{1} = phi; % x poln P
phi_y{2} = zeros(1,nphi); % y poln P

masks = cell(np,nphi);
XY_vect = [reshape(Xnm,1,[]); reshape(Ynm,1,[])];
for ii=1:np
    for ij=1:nphi
        masks{ii,ij} =
1+(cos((R(p_angles(ii))*([a,b].*p1)')'*XY_vect).*cos((R(p_angles(ii))*([a,b
].*p2)')'*XY_vect+phi(ij)));
        masks{ii,ij} = reshape(masks{ii,ij}, [x_px,y_px]);
    end
end

figure('Name','Masks');
for ii=1:numel(masks)
    subplot(np,nphi,ii);
    imshow(masks{ii},[]);
end

%% Apply and display the patterns
g = cell(size(masks));
figure('Name','Acquired Images');
for ii=1:numel(masks)
    g{ii} = conv2(masks{ii}.*f,psf,'same');
    subplot(np,nphi,ii);
    imshow(g{ii},[]);
end

%% Compute and display the FT of the images
G = cell(size(masks));
figure('Name','FFT of acquired images');
for ii=1:numel(masks)
    G{ii} = fftshift(fft2(g{ii}));
```

```
    subplot(np,nphi,ii);
    imshow(log(abs(G{ii})),[]);
end

%% Invert the phases
% Different in expanded SIM compared to standard SIM
C = cell(np,nphi+2);
for ii=1:np
    C{ii,1} = G{ii,1} + G{ii,2} + G{ii,3};
    C{ii,2} = exp(-1i*(phi_x{ii}(1)-phi_y{ii}(1)))*G{ii,1}+ ...
        exp(-1i*(phi_x{ii}(2)-phi_y{ii}(2)))*G{ii,2}+ ...
        exp(-1i*(phi_x{ii}(3)-phi_y{ii}(3)))*G{ii,3} ;
    C{ii,3} = exp(1i*(phi_x{ii}(1)-phi_y{ii}(1)))*G{ii,1}+ ...
        exp(1i*(phi_x{ii}(2)-phi_y{ii}(2)))*G{ii,2}+ ...
        exp(1i*(phi_x{ii}(3)-phi_y{ii}(3)))*G{ii,3} ;
    C{ii,4} = exp(-1i*(phi_x{ii}(1)+phi_y{ii}(1)))*G{ii,1}+ ...
        exp(-1i*(phi_x{ii}(2)+phi_y{ii}(2)))*G{ii,2}+ ...
        exp(-1i*(phi_x{ii}(3)+phi_y{ii}(3)))*G{ii,3} ;
    C{ii,5} = exp(1i*(phi_x{ii}(1)+phi_y{ii}(1)))*G{ii,1}+ ...
        exp(1i*(phi_x{ii}(2)+phi_y{ii}(2)))*G{ii,2}+ ...
        exp(1i*(phi_x{ii}(3)+phi_y{ii}(3)))*G{ii,3} ;
end

figure('Name','Separated components');
for ii=1:numel(C)
    subplot(np,nphi+2,ii);
    imshow(log(abs(C{ii})),[]);
end

%% Shift the components
% Do this in real space
% Different in expanded SIM compared to standard SIM
CS = cell(size(masks));
otfk = cell(size(masks));
otf = create_psf(Xnm-mean(Xnm(1,:)),Ynm-mean(Ynm(:,1)),wavelength,NA);
for ii=1:np
    K = reshape(p(ii,:)*XY_vect, [x_px,y_px]);
    % Using 3 CS's see maths
    CS{ii,1} = C{ii,1};
    CS{ii,2} = fftshift(fft2(exp(-1i*K).*ifft2(fftshift(C{ii,2}))));
    CS{ii,3} = fftshift(fft2(exp(1i*K).*ifft2(fftshift(C{ii,3}))));

    otfk{ii,1} = fftshift(fft2(otf));
    otfk{ii,2} = fftshift(fft2(exp(-1i*K).*otf));
    otfk{ii,3} = fftshift(fft2(exp(1i*K).*otf));
end

figure('Name','Shifted, separated components');
for ii=1:numel(CS)
    subplot(np,nphi,ii);
    imshow(log(abs(CS{ii})),[]);
end

figure('Name','Shifted OTFs');
for ii=1:numel(CS)
    subplot(np,nphi,ii);
    imshow((abs(otfk{ii})),[]);
end
```

```
%% Apply the Wiener Filter
num = 0;
denom = 0;
w = ; % noise factor
figure('Name','Components of Wiener Filter');
for ii=1:numel(CS)
    subplot(np,nphi,ii);
    imshow(log(abs(conj(otfk{ii}).*CS{ii})),[]);
    num = num + conj(otfk{ii}).*CS{ii};
    denom = denom + abs(otfk{ii}).^2 +w;
end
Sk = num./denom;
figure('Name','FFT Reconstructed image'), imshow(log(abs(Sk)),[]);

newotf = create_psf(Xpsf,Ypsf,wavelength/3,NA);
newotf_k = fftshift(fft2(newotf));
S = abs(fftshift(ifft2((Sk))));
figure('Name','Reconstructed image'), imshow(conv2(S,newotf,'same'),[]);
```

7) MATLAB code for Sinusoid Product-based SIM image reconstruction using imported masks

This script was used for performing the Sinusoid Product-based SIM image reconstruction on a user imported image, using masks imported by the user. This was done in MATLAB R2012a.

```
close all; clear;
% Scale image by factor n
no_rowsh = ; % no of rows in masks .txt files
image_size= ; % size of image used as sample
n=no_rowsh/image_size;

f = double(imresize(imread('image.tif'),n));
% or f = phantom();
figure('Name','Base Image'), imshow(f,[]);
figure('Name','FFT Base Image'), imshow(log(abs(fftshift(fft2(f)))),[]);
% Set the scale inverse to the magnification
nmPerPx = ;
x_px = size(f,2);
y_px = size(f,1);

% Image size in nm
x_nm = x_px*nmPerPx;
y_nm = y_px*nmPerPx;
% Create image grid in nm
[Xnm,Ynm] = meshgrid(nmPerPx*(0:x_px-1), nmPerPx*(0:y_px-1));

% Create the PSF, in nm
wavelength = 500;
NA = 1.49;
[Xpsf,Ypsf] = meshgrid(-wavelength:nmPerPx:wavelength);
create_psf = @(X,Y,wavelength,NA) exp(-
(X.^2+Y.^2)/(2*(0.45*wavelength/(2*NA))^2));
psf = create_psf(Xpsf,Ypsf,wavelength,NA);
figure('Name','PSF'), surf(Xpsf,Ypsf,psf);
figure('Name','FFT PSF'), imshow(abs(fftshift(fft2(psf))),[]);

% Plot widefield image and its FFT
widefield = conv2(f,psf,'same');
figure('Name','Widefield Image'), imshow(widefield,[]);
figure('Name','FFT Widefield Image'),
imshow(log(abs(fftshift(fft2(widefield)))),[]);

%% Create the patterns
spatial_wavelength1 = ;% nm, period of 'stripes' in metamaterial pattern,
needs to scale with nmPerPx
spatial_wavelength2 = spatial_wavelength1/$;% nm, period of 'blobs' within
each 'stripe' in metamaterial pattern, choose $
spatial_freq1 = 2*pi()/spatial_wavelength1;
spatial_freq2 = 2*pi()/spatial_wavelength2;

phi = [0, 2*pi()/3, 4*pi()/3];

a = spatial_freq1;
b = spatial_freq2;
```

```
period_x{1} = a;
period_x{2} = b;
period_y{1} = b;
period_y{2} = a;

% pattern orientations to create chequerboard of peaks
p1 = [1,1];
p2 = [1,-1];
p_orthog = dot(p1,p2); % check orthogonality, should be 0

% Pattern orientations
% Two patterns
p = [0.5*[a,b].*(p1-p2); 0.5*[b,a].*(p1+p2)];

np = size(p,1);
nphi = length(phi);

phi_x{1} = zeros(1,nphi); % x poln P
phi_x{2} = phi; % y poln P
phi_y{1} = phi; % x poln P
phi_y{2} = zeros(1,nphi); % y poln P

masks = cell(np,nphi);
XY_vect = [reshape(Xnm,1,[]); reshape(Ynm,1,[])];

%Create strings of filenames
file_no = ['678'; '712'; '792'];
file_no = cellstr(file_no);
XorY = ['-x';'-y'];
XorY = cellstr(XorY);
filestr1 = 'E-';
filestr2 = '.txt';

for k = 1:np
    for j=1:nphi
        filenames{k,j} = [filestr1 file_no{j} XorY{k} filestr2];
    end
end

for ii = 1:np
    for ij=1:nphi
        fid = fopen(filenames{ii,ij},'r');
        for ik=1:no_rowsh
            file_data = str2num(fgetl(fid));
            % read in info from file line by line
            imageh(ik,:) = file_data(:);
        end
        fclose(fid);

        masks{ii,ij} = flipud(imageh);
        %Images of illumination.*sample (m.*f)
    end
end

figure('Name','Masks');
for ii=1:numel(masks)
    subplot(np,nphi,ii);
```

```
    imshow(masks{ii},[]);
end

%% Apply and display the patterns
g = cell(size(masks));
figure('Name','Acquired Images');
for ii=1:numel(masks)
    g{ii} = conv2(masks{ii}.*f,psf,'same');
    subplot(np,nphi,ii);
    imshow(g{ii},[]);
end

%% Compute and display the FT of the images
G = cell(size(masks));
figure('Name','FFT of acquired images');
for ii=1:numel(masks)
    G{ii} = fftshift(fft2(g{ii}));
    subplot(np,nphi,ii);
    imshow(log(abs(G{ii})),[]);
end

%% Invert the phases
% Different in expanded SIM compared to standard SIM
C = cell(np,nphi+2);
for ii=1:np
    C{ii,1} = G{ii,1} + G{ii,2} + G{ii,3};
    C{ii,2} = exp(-1i*(phi_x{ii}(1)-phi_y{ii}(1)))*G{ii,1}+ ...
        exp(-1i*(phi_x{ii}(2)-phi_y{ii}(2)))*G{ii,2}+ ...
        exp(-1i*(phi_x{ii}(3)-phi_y{ii}(3)))*G{ii,3} ;
    C{ii,3} = exp(1i*(phi_x{ii}(1)-phi_y{ii}(1)))*G{ii,1}+ ...
        exp(1i*(phi_x{ii}(2)-phi_y{ii}(2)))*G{ii,2}+ ...
        exp(1i*(phi_x{ii}(3)-phi_y{ii}(3)))*G{ii,3} ;
    C{ii,4} = exp(-1i*(phi_x{ii}(1)+phi_y{ii}(1)))*G{ii,1}+ ...
        exp(-1i*(phi_x{ii}(2)+phi_y{ii}(2)))*G{ii,2}+ ...
        exp(-1i*(phi_x{ii}(3)+phi_y{ii}(3)))*G{ii,3} ;
    C{ii,5} = exp(1i*(phi_x{ii}(1)+phi_y{ii}(1)))*G{ii,1}+ ...
        exp(1i*(phi_x{ii}(2)+phi_y{ii}(2)))*G{ii,2}+ ...
        exp(1i*(phi_x{ii}(3)+phi_y{ii}(3)))*G{ii,3} ;
end

figure('Name','Separated components');
for ii=1:numel(C)
    subplot(np,nphi+2,ii);
    imshow(log(abs(C{ii})),[]);
end

%% Shift the components
% Do this in real space
% Different in expanded SIM compared to standard SIM
CS = cell(size(masks));
otfk = cell(size(masks));
otf = create_psf(Xnm-mean(Xnm(1,:)),Ynm-mean(Ynm(:,1)),wavelength,NA);
for ii=1:np
    K = reshape(p(ii,:)*XY_vect, [x_px,y_px]);
    % Using 3 CS's see maths
    CS{ii,1} = C{ii,1};
    CS{ii,2} = fftshift(fft2(exp(-1i*K).*ifft2(fftshift(C{ii,2}))));
    CS{ii,3} = fftshift(fft2(exp(1i*K).*ifft2(fftshift(C{ii,3}))));
```

```
    otfk{ii,1} = fftshift(fft2(otf));
    otfk{ii,2} = fftshift(fft2(exp(-1i*K).*otf));
    otfk{ii,3} = fftshift(fft2(exp(1i*K).*otf));
end

figure('Name','Shifted, separated components');
for ii=1:numel(CS)
    subplot(np,nphi,ii);
    imshow(log(abs(CS{ii})),[]);
end

figure('Name','Shifted OTFs');
for ii=1:numel(CS)
    subplot(np,nphi,ii);
    imshow((abs(otfk{ii})),[]);
end

%% Apply the Wiener Filter
num = 0;
denom = 0;
w = ; % noise factor
figure('Name','Components of Wiener Filter');
for ii=1:numel(CS)
    subplot(np,nphi,ii);
    imshow(log(abs(conj(otfk{ii}).*CS{ii})),[]);
    num = num + conj(otfk{ii}).*CS{ii};
    denom = denom + abs(otfk{ii}).^2 +w;
end

Sk = num./denom;
figure('Name','FFT Reconstructed image'), imshow(log(abs(Sk)),[]);

newotf = create_psf(Xpsf,Ypsf,wavelength/2,NA);
newotf_k = fftshift(fft2(newotf));
S = abs(fftshift(ifft2((Sk))));
figure('Name','Reconstructed image'), imshow(conv2(S,newotf,'same'),[]);
```

List of References

1 Chung, E., Kim, D., Cui, Y., Kim, Y.-H. & So, P. T. Two-dimensional standing wave total internal reflection fluorescence microscopy: superresolution imaging of single molecular and biological specimens. *Biophysical journal* **93**, 1747-1757 (2007).

2 Hamel, V. *et al.* Correlative multicolor 3D SIM and STORM microscopy. *Biomedical Optics Express* **5**, 3326-3336, doi:10.1364/BOE.5.003326 (2014).

3 Abramowitz, M. & Davidson, M. W. *Transmitted Light Illumination*, <http://www.olympusmicro.com/primer/techniques/fluorescence/anatomy/translightpaths.html> (2012).

4 Ravier, M. A., Tsuboi, T. & Rutter, G. A. Imaging a target of Ca 2+ signalling: dense core granule exocytosis viewed by total internal reflection fluorescence microscopy. *Methods* **46**, 233-238 (2008).

5 3DImaging&DisplayLab. *Structured illumination Microscopy*, <http://www.uv.es/imaging3/lineas/SIM.html> (2017).

6 Andor. *Super-Resolution Imaging - Structured Illumination Microscopy*, <http://www.andor.com/learning-academy/super-resolution-imaging-structured-illumination-microscopy-application-note> (2017).

7 Ashdown, G. W., Cope, A., Wiseman, P. W. & Owen, D. M. Molecular flow quantified beyond the diffraction limit by spatiotemporal image correlation of structured illumination microscopy data. *Biophysical journal* **107**, L21-L23 (2014).

8 Shalaev, V. M. Optical negative-index metamaterials. *Nature photonics* **1**, 41-48 (2007).

9 Shalaev, V. M. *et al.* Negative index of refraction in optical metamaterials. *Optics Letters* **30**, 3356-3358 (2005).

10 Kafesaki, M. *et al.* Left-handed metamaterials: detailed numerical studies of the transmission properties. *Journal of Optics A: Pure and Applied Optics* **7**, S12 (2005).

11 Smith, D. R., Pendry, J. B. & Wiltshire, M. C. K. Metamaterials and negative refractive index. *Science* **305**, 788-792 (2004).

12 Veselago, V. G. Waves in metamaterials: their role in modern physics. *Physics-Uspekhi* **54**, 1161 (2011).

13 Aydin, K. *et al.* Investigation of magnetic resonances for different split-ring resonator parameters and designs. *New journal of physics* **7**, 168 (2005).

14 Aydin, K., Bulu, I. & Ozbay, E. Subwavelength resolution with a negative-index metamaterial superlens. *Applied physics letters* **90**, 254102 (2007).

15 Aydin, K., Bulu, I. & Ozbay, E. Focusing of electromagnetic waves by a left-handed metamaterial flat lens. *Optics express* **13**, 8753-8759 (2005).

16 Aydin, K. & Ozbay, E. Left-handed metamaterial based superlens for subwavelength imaging of electromagnetic waves. *Applied Physics A* **87**, 137-141 (2007).

17 Chaturvedi, P. *et al.* A smooth optical superlens. *Applied Physics Letters* **96**, 043102 (2010).

18 Fang, N. & Zhang, X. Imaging properties of a metamaterial superlens. *Applied Physics Letters* **82**, 161-163 (2003).

19 Liu, Z. *et al.* Far-field optical superlens. *Nano Letters* **7**, 403-408 (2007).

20 Wang, W. *et al.* Far-field imaging device: planar hyperlens with magnification using multi-layer metamaterial. *Optics express* **16**, 21142-21148 (2008).

21 Iyer, A. K. & Eleftheriades, G. V. Mechanisms of subdiffraction free-space imaging using a transmission-line metamaterial superlens: An experimental verification. *Applied Physics Letters* **92**, 131105 (2008).

22 Chen, J., Radu, C. & Puri, A. Aberration-free negative-refractive-index lens. *Applied physics letters* **88**, 071119 (2006).

23 Jacob, Z., Alekseyev, L. V. & Narimanov, E. Optical hyperlens: far-field imaging beyond the diffraction limit. *Optics express* **14**, 8247-8256 (2006).
24 Liu, C., Yan, C., Chen, H., Liu, Y. & Gao, S. Evanescent field on the surface of a negative-index planar lens. *Applied physics letters* **88**, 231102 (2006).
25 Liu, Z., Lee, H., Xiong, Y., Sun, C. & Zhang, X. Far-field optical hyperlens magnifying sub-diffraction-limited objects. *Science* **315**, 1686-1686 (2007).
26 Lu, D. & Liu, Z. Hyperlenses and metalenses for far-field super-resolution imaging. *Nature communications* **3** (2012).
27 Zhang, X. & Liu, Z. Superlenses to overcome the diffraction limit. *Nature materials* **7**, 435-441 (2008).
28 Rao, X. S. & Ong, C. K. Subwavelength imaging by a left-handed material superlens. *Physical Review E* **68**, 067601 (2003).
29 McNicol, A. & Israels, S. J. Beyond hemostasis: the role of platelets in inflammation, malignancy and infection. *Cardiovascular & Haematological Disorders-Drug Targets (Formerly Current Drug Targets-Cardiovascular & Hematological Disorders)* **8**, 99-117 (2008).
30 Smyth, S. S. *et al.* Platelet functions beyond hemostasis. *Journal of Thrombosis and Haemostasis* **7**, 1759-1766 (2009).
31 von Hundelshausen, P. & Weber, C. Platelets as immune cells bridging inflammation and cardiovascular disease. *Circulation research* **100**, 27-40 (2007).
32 Shalaev, V. M. *Metamaterials, Part 2: Negative-Index, Nonlinear Optics and Super/Hyper-Lenses*, < https://nanohub.org/resources/4267> (2008).
33 Gustafsson, M. G. L. Surpassing the lateral resolution limit by a factor of two using structured illumination microscopy. *Journal of microscopy* **198**, 82-87 (2000).
34 Lukeš, T. *et al.* in *SPIE Proceedings.* 91293J.
35 Gustafsson, M. G. L. Nonlinear structured-illumination microscopy: wide-field fluorescence imaging with theoretically unlimited resolution. *Proceedings of the National Academy of Sciences of the United States of America* **102**, 13081-13086 (2005).
36 Gustafsson, M. G. L., Allen, J. R. & Davidson, M. W. *Superesolution Structured Illumination Microscopy*, <http://zeiss-campus.magnet.fsu.edu/articles/superresolution/supersim.html> (2017).
37 Heintzmann, R. Structured illumination methods. *Handbook of biological confocal microscopy*, 265-279 (2006).
38 Karadaglić, D. & Wilson, T. Image formation in structured illumination wide-field fluorescence microscopy. *Micron* **39**, 808-818 (2008).
39 Saxena, M., Eluru, G. & Gorthi, S. S. Structured illumination microscopy. *Advances in Optics and Photonics* **7**, 241-275 (2015).
40 Ströhl, F. & Kaminski, C. F. Frontiers in structured illumination microscopy. *Optica* **3**, 667-677 (2016).
41 Mattheyses, A. L., Simon, S. M. & Rappoport, J. Z. Imaging with total internal reflection fluorescence microscopy for the cell biologist. *Journal of cell science* **123**, 3621-3628 (2010).
42 KrotoImagingFacility. *Widefield Fluorescence Microscopy*, <https://www.sheffield.ac.uk/kroto/confocal/widefield> (2017).
43 Tkaczyk, T. S. *Field Guide to Microscopy*. (SPIE, 2010).
44 Shalaev, V. M. *Metamaterials, Part 1: Electrical and Magnetic Metamaterials*, <https://nanohub.org/resources/4263> (2008).
45 Liu, Y. & Zhang, X. Metamaterials: a new frontier of science and technology. *Chemical Society Reviews* **40**, 2494-2507 (2011).
46 Porter, J. Antony van Leeuwenhoek: tercentenary of his discovery of bacteria. *Bacteriological reviews* **40**, 260 (1976).

47 Zuylen, J. v. The microscopes of Antoni van Leeuwenhoek. *Journal of microscopy* **121**, 309-328 (1981).
48 Goldstein, J. *et al. Scanning Electron Microscopy and X-Ray Microanalysis: A Text for Biologists, Materials Scientists, and Geologists*. (Springer US, 2012).
49 Luts, J. *et al.* Nosologic imaging of the brain: segmentation and classification using MRI and MRSI. *NMR in Biomedicine* **22**, 374-390 (2009).
50 Preul, M. C. *et al.* Accurate, noninvasive diagnosis of human brain tumors by using proton magnetic resonance spectroscopy. *Nature medicine* **2**, 323-325 (1996).
51 Nelson, S. J. *et al.* In vivo molecular imaging for planning radiation therapy of gliomas: an application of 1H MRSI. *Journal of Magnetic Resonance Imaging* **16**, 464-476 (2002).
52 Bouchard, M. B. *et al.* Swept confocally-aligned planar excitation (SCAPE) microscopy for high-speed volumetric imaging of behaving organisms. *Nat Photon* **9**, 113-119, doi:10.1038/nphoton.2014.323

http://www.nature.com/nphoton/journal/v9/n2/abs/nphoton.2014.323.html#supplementary-information (2015).
53 Chen, B.-C. *et al.* Lattice light-sheet microscopy: imaging molecules to embryos at high spatiotemporal resolution. *Science* **346**, 1257998 (2014).
54 Kaufmann, A., Mickoleit, M., Weber, M. & Huisken, J. Multilayer mounting enables long-term imaging of zebrafish development in a light sheet microscope. *Development* **139**, 3242-3247 (2012).
55 Keller, P. J. *et al.* Fast, high-contrast imaging of animal development with scanned light sheet-based structured-illumination microscopy. *Nature methods* **7**, 637-642 (2010).
56 Mertz, J. & Kim, J. Scanning light-sheet microscopy in the whole mouse brain with HiLo background rejection. *BIOMEDO* **15**, 016027-016027-016027, doi:10.1117/1.3324890 (2010).
57 WHO. *Cardiovascular diseases (CVDs)*, <http://www.who.int/mediacentre/factsheets/fs317/en/> (2013).
58 Alwan, A. *Global status report on noncommunicable diseases 2010*. (World Health Organization, 2011).
59 Mathers, C. D. & Loncar, D. Projections of global mortality and burden of disease from 2002 to 2030. *PLoS medicine* **3**, e442 (2006).
60 Waterman, N. *Super-imaging with Metamaterials for Cardiovascular Disease: Year 2 Report* (University of Birmingham, unpublished work, 2016).
61 Sanz, J. & Fayad, Z. A. Imaging of atherosclerotic cardiovascular disease. *Nature* **451**, 953-957 (2008).
62 Moreno, N., Bougourd, S., Haseloff, J. & Feijó, J. A. in *Handbook of biological confocal Microscopy* 769-787 (Springer, 2006).
63 Pawley, J. & Masters, B. R. Handbook of biological confocal microscopy. *Optical Engineering* **35**, 2765-2766 (1996).
64 Cella Zanacchi, F. *et al.* Live-cell 3D super-resolution imaging in thick biological samples. *Nat Meth* **8**, 1047-1049, doi:http://www.nature.com/nmeth/journal/v8/n12/abs/nmeth.1744.html#supplementary-information (2011).
65 Chung, E., Kim, D. & So, P. T. Extended resolution wide-field optical imaging: objective-launched standing-wave total internal reflection fluorescence microscopy. *Optics letters* **31**, 945-947 (2006).
66 Erni, R., Rossell, M. D., Kisielowski, C. & Dahmen, U. Atomic-resolution imaging with a sub-50-pm electron probe. *Physical review letters* **102**, 096101 (2009).
67 Gartia, M. R., Hsiao, A., Sivaguru, M., Chen, Y. & Liu, G. L. Enhanced 3D fluorescence live cell imaging on nanoplasmonic substrate. *Nanotechnology* **22**, 365203 (2011).

68 Lu, D. & Liu, Z. Hyperlenses and metalenses for far-field super-resolution imaging. *Nature communications* **3**, 1205 (2012).
69 Patterson, G., Davidson, M., Manley, S. & Lippincott-Schwartz, J. Superresolution imaging using single-molecule localization. *Annual review of physical chemistry* **61**, 345 (2010).
70 Treves, S. & Zorzato, F. *TIRF: Evanescent waves for high resolution membrane fluorescence imaging*, <http://www.nikon.com/products/instruments/bioscience-applications/application-notes/pdf/nikon_note_11_LR.pdf> (2009).
71 Wiltshire, M., Hajnal, J., Pendry, J., Edwards, D. & Stevens, C. Metamaterial endoscope for magnetic field transfer: near field imaging with magnetic wires. *Optics express* **11**, 709-715 (2003).
72 Reichelt, R. in *Science of microscopy* 133-272 (Springer, 2007).
73 Reimer, L. *Transmission electron microscopy: physics of image formation and microanalysis*. Vol. 36 (Springer, 2013).
74 Williams, D. B. & Carter, C. B. in *Transmission electron microscopy* 3-17 (Springer, 1996).
75 Lichtman, J. W. & Conchello, J.-A. Fluorescence microscopy. *Nature methods* **2**, 910 (2005).
76 Ntziachristos, V. Going deeper than microscopy: the optical imaging frontier in biology. *Nature methods* **7**, 603-614 (2010).
77 Schmolze, D. B., Standley, C., Fogarty, K. E. & Fischer, A. H. Advances in microscopy techniques. *Archives of pathology & laboratory medicine* **135**, 255-263 (2011).
78 Schnell, U., Dijk, F., Sjollema, K. A. & Giepmans, B. N. Immunolabeling artifacts and the need for live-cell imaging. *Nature methods* **9**, 152-158 (2012).
79 Stephens, D. J. & Allan, V. J. Light microscopy techniques for live cell imaging. *Science* **300**, 82-86 (2003).
80 Gao, L. *et al.* Noninvasive imaging beyond the diffraction limit of 3D dynamics in thickly fluorescent specimens. *Cell* **151**, 1370-1385 (2012).
81 Alford, R. *et al.* Toxicity of organic fluorophores used in molecular imaging: literature review. *Molecular imaging* **8**, 7290.2009. 00031 (2009).
82 Halbhuber, K.-J. & König, K. Modern laser scanning microscopy in biology, biotechnology and medicine. *Annals of Anatomy - Anatomischer Anzeiger* **185**, 1-20, doi:http://dx.doi.org/10.1016/S0940-9602(03)80002-X (2003).
83 Stout, A. L. & Axelrod, D. Evanescent field excitation of fluorescence by epi-illumination microscopy. *Applied optics* **28**, 5237-5242 (1989).
84 Tan, P. S., Yuan, X. C., Yuan, G. H. & Wang, Q. High-resolution wide-field standing-wave surface plasmon resonance fluorescence microscopy with optical vortices. *Applied Physics Letters* **97**, 241109 (2010).
85 Semwogerere, D. & Weeks, E. R. Confocal microscopy. *Encyclopedia of Biomaterials and Biomedical Engineering*, 1-10 (2005).
86 Schropp, A. *et al.* Hard x-ray scanning microscopy with coherent radiation: Beyond the resolution of conventional x-ray microscopes. *Applied Physics Letters* **100**, 253112 (2012).
87 Johnson, N. P., Khokhar, A. Z., Chong, H. M., De La Rue, R. M. & McMeekin, S. Characterisation at infrared wavelengths of metamaterials formed by thin-film metallic split-ring resonator arrays on silicon. *Electronics Letters* **42**, 1117-1119 (2006).
88 Silfies, J. S., Schwartz, S. A., Davidson, M. W. & Nikon. *Stochastic Optical Reconstruction Microscopy (STORM)*, <http://www.microscopyu.com/articles/superresolution/stormintro.html> (
89 Allen, G. M. *Bats: biology, behavior, and folklore*. (Dover Publications, 2004).
90 Hecht, E. *Optics*. (Addison-Wesley, 2002).
91 EdmundOpticsInc. *Limitations on Resolution and Contrast: The Airy Disk*, <https://www.edmundoptics.com/resources/application-notes/imaging/limitations-on-resolution-and-contrast-the-airy-disk/> (2017).

92 H Sargent, E. Infrared quantum dots. *Advanced Materials* **17**, 515-522 (2005).
93 Webb, D. J. & Brown, C. M. Epi-fluorescence microscopy. *Cell Imaging Techniques: Methods and Protocols*, 29-59 (2013).
94 He, R.-Y. *et al.* Surface plasmon-enhanced two-photon fluorescence microscopy for live cell membrane imaging. *Optics express* **17**, 5987-5997 (2009).
95 König, K. Multiphoton microscopy in life sciences. *Journal of microscopy* **200**, 83-104 (2000).
96 Xu, C., Zipfel, W., Shear, J. B., Williams, R. M. & Webb, W. W. Multiphoton fluorescence excitation: new spectral windows for biological nonlinear microscopy. *Proceedings of the National Academy of Sciences* **93**, 10763-10768 (1996).
97 So, P. T., Dong, C. Y., Masters, B. R. & Berland, K. M. Two-photon excitation fluorescence microscopy. *Annual review of biomedical engineering* **2**, 399-429 (2000).
98 Young, L. J., Ströhl, F. & Kaminski, C. F. A guide to structured illumination TIRF microscopy at high speed with multiple colors. *Journal of visualized experiments: JoVE* (2016).
99 Jaykumar, A. B., Caceres, P. S., Sablaban, I., Tannous, B. A. & Ortiz, P. A. Real-time monitoring of NKCC2 endocytosis by total internal reflection fluorescence (TIRF) microscopy. *American Journal of Physiology - Renal Physiology* **310**, F183-F191, doi:10.1152/ajprenal.00104.2015 (2016).
100 Schermelleh, L., Heintzmann, R. & Leonhardt, H. A guide to super-resolution fluorescence microscopy. *The Journal of cell biology* **190**, 165-175 (2010).
101 Cox, G. & Sheppard, C. J. Practical limits of resolution in confocal and non-linear microscopy. *Microscopy research and technique* **63**, 18-22 (2004).
102 Masters, B. R., So, P. & Gratton, E. Multiphoton excitation fluorescence microscopy and spectroscopy of in vivo human skin. *Biophysical journal* **72**, 2405-2412 (1997).
103 Ahrens, M. B., Orger, M. B., Robson, D. N., Li, J. M. & Keller, P. J. Whole-brain functional imaging at cellular resolution using light-sheet microscopy. *Nature methods* **10**, 413-420 (2013).
104 Oshikane, Y. *et al.* Observation of nanostructure by scanning near-field optical microscope with small sphere probe. *Science and Technology of Advanced Materials* **8**, 181-185 (2007).
105 Betzig, E. & Trautman, J. Near-field optics- Microscopy, spectroscopy, and surface modification beyond the diffraction limit. *Science* **257**, 189-195 (1992).
106 Manzo, C., van Zanten, T. S. & Garcia-Parajo, M. F. Nanoscale fluorescence correlation spectroscopy on intact living cell membranes with NSOM probes. *Biophysical journal* **100**, L8-L10 (2011).
107 Wu, Y. *et al.* Spatially isotropic four-dimensional imaging with dual-view plane illumination microscopy. *Nat Biotech* **31**, 1032-1038, doi:10.1038/nbt.2713

http://www.nature.com/nbt/journal/v31/n11/abs/nbt.2713.html#supplementary-information (2013).
108 Gan, Y. Atomic and subnanometer resolution in ambient conditions by atomic force microscopy. *Surface Science Reports* **64**, 99-121 (2009).
109 Santos, S., Barcons, V., Christenson, H. K., Font, J. & Thomson, N. H. The intrinsic resolution limit in the atomic force microscope: implications for heights of nano-scale features. *PLoS One* **6**, e23821 (2011).
110 Rossberger, S. *et al.* Combination of structured illumination and single molecule localization microscopy in one setup. *Journal of Optics* **15**, 094003 (2013).
111 Watanabe, K. *et al.* Structured line illumination Raman microscopy. *Nature communications* **6** (2015).
112 Silván, U. *et al.* Contributions of the lower dimer to supramolecular actin patterning revealed by TIRF microscopy. *Journal of Structural Biology* **195**, 159-166, doi:http://dx.doi.org/10.1016/j.jsb.2016.05.008 (2016).

113 Chasles, F., Dubertret, B. & Boccara, A. C. Optimization and characterization of a structured illumination microscope. *Optics express* **15**, 16130-16140 (2007).
114 Dal Maschio, M. *et al.* Simultaneous two-photon imaging and photo-stimulation with structured light illumination. *Optics Express* **18**, 18720-18731 (2010).
115 Isobe, K. *et al.* Enhancement of lateral resolution and optical sectioning capability of two-photon fluorescence microscopy by combining temporal-focusing with structured illumination. *Biomedical optics express* **4**, 2396-2410 (2013).
116 Kner, P., Chhun, B. B., Griffis, E. R., Winoto, L. & Gustafsson, M. G. Super-resolution video microscopy of live cells by structured illumination. *Nature methods* **6**, 339-342 (2009).
117 Zeiss. *ELYRA: For Structured Illumination and Photoactivated Localization Microscopy of small structures*, <https://www.zeiss.com/microscopy/int/products/superresolution-microscopy.html> (2017).
118 Ponsetto, J. L. *et al.* Experimental Demonstration of Localized Plasmonic Structured Illumination Microscopy. *ACS nano* (2017).
119 Hirano, Y., Matsuda, A. & Hiraoka, Y. Recent advancements in structured-illumination microscopy toward live-cell imaging. *Microscopy* **64**, 237-249 (2015).
120 Labouesse, S. *et al.* Joint reconstruction strategy for structured illumination microscopy with unknown illuminations. *arXiv preprint arXiv:1607.01980* (2016).
121 Jost, A. & Heintzmann, R. Superresolution multidimensional imaging with structured illumination microscopy. *Annual Review of Materials Research* **43**, 261-282 (2013).
122 Zhao, M. *et al.* Cellular imaging of deep organ using two-photon Bessel light-sheet nonlinear structured illumination microscopy. *Biomedical optics express* **5**, 1296-1308 (2014).
123 Ayuk, R. *et al.* Structured illumination fluorescence microscopy with distorted excitations using a filtered blind-SIM algorithm. *Optics letters* **38**, 4723-4726 (2013).
124 Mudry, E. *et al.* Structured illumination microscopy using unknown speckle patterns. *Nature Photonics* **6**, 312-315 (2012).
125 Idier, J. *et al.* in *Mathematics in Imaging.* MM3C. 2 (Optical Society of America).
126 Mangeat, T. *et al.* in *Mathematics in Imaging.* MTh1C. 2 (Optical Society of America).
127 Nguyen, N., Milanfar, P. & Golub, G. A computationally efficient superresolution image reconstruction algorithm. *IEEE transactions on image processing* **10**, 573-583 (2001).
128 Calvetti, D. Preconditioned iterative methods for linear discrete ill-posed problems from a Bayesian inversion perspective. *Journal of Computational and Applied Mathematics* **198**, 378-395, doi:http://dx.doi.org/10.1016/j.cam.2005.10.038 (2007).
129 Kraus, F. *et al.* Quantitative 3D structured illumination microscopy of nuclear structures. *nature protocols* **12**, 1011-1028 (2017).
130 Miron, E., Innocent, C., Heyde, S. & Schermelleh, L. In Vivo and In Situ Replication Labeling Methods for Super-resolution Structured Illumination Microscopy of Chromosome Territories and Chromatin Domains. *Chromosome Architecture: Methods and Protocols*, 127-140 (2016).
131 Hong, S., Wilton, D. K., Stevens, B. & Richardson, D. S. Structured illumination microscopy for the investigation of synaptic structure and function. *Synapse Development: Methods and Protocols*, 155-167 (2017).
132 Komis, G. *et al.* Superresolution live imaging of plant cells using structured illumination microscopy. *Nature protocols* **10**, 1248 (2015).
133 Spira, F. *et al.* Patchwork organization of the yeast plasma membrane into numerous coexisting domains. *Nature cell biology* **14**, 640-648 (2012).
134 Huber, M. C. *et al.* Designer amphiphilic proteins as building blocks for the intracellular formation of organelle-like compartments. *Nature materials* **14**, 125-132 (2015).
135 Beach, J. R. *et al.* Nonmuscle myosin II isoforms coassemble in living cells. *Current Biology* **24**, 1160-1166 (2014).

136 Heintzmann, R. & Ficz, G. Breaking the resolution limit in light microscopy. *Briefings in Functional Genomics* **5**, 289-301 (2006).
137 Cai, W. & Shalaev, V. M. *Optical metamaterials*. Vol. 10 (Springer, 2010).
138 Pendry, J. B. *Negative Refraction & the Perfect Lens* <http://esc.u-strasbg.fr/docs/2010/lectures/StrasbourgTalk.pdf> (2010).
139 Ramakrishna, S. A. Physics of negative refractive index materials. *Reports on Progress in Physics* **68**, 449 (2005).
140 Veselago, V., Braginsky, L., Shklover, V. & Hafner, C. Negative refractive index materials. *Journal of Computational and Theoretical Nanoscience* **3**, 189-218 (2006).
141 Veselago, V. & Narimanov, E. The left hand of brightness: past, present and future of negative index materials. *Nature materials* **5**, 759-762 (2006).
142 Cai, W., Chettiar, U. K., Kildishev, A. V. & Shalaev, V. M. Optical cloaking with metamaterials. *Nature photonics* **1**, 224-227 (2007).
143 Chen, H., Chan, C. T. & Sheng, P. Transformation optics and metamaterials. *Nature materials* **9**, 387-396 (2010).
144 Chen, T., Li, S. & Sun, H. Metamaterials application in sensing. *Sensors* **12**, 2742-2765 (2012).
145 Huang, L. *et al.* Three-dimensional optical holography using a plasmonic metasurface. *Nature communications* **4** (2013).
146 Ishimaru, A., Jaruwatanadilok, S. & Kuga, Y. Generalized surface plasmon resonance sensors using metamaterials and negative index materials. *Progress In Electromagnetics Research* **51**, 139-152 (2005).
147 Page, J. Metamaterials: Neither solid nor liquid. *Nature materials* **10**, 565-566 (2011).
148 Poddubny, A., Iorsh, I., Belov, P. & Kivshar, Y. Hyperbolic metamaterials. *Nature Photonics* **7**, 948-957 (2013).
149 Torrent, D. & Sánchez-Dehesa, J. Acoustic metamaterials for new two-dimensional sonic devices. *New journal of physics* **9**, 323 (2007).
150 Solymar, L. & Shamonina, E. *Waves in metamaterials*. (Oxford University Press, 2009).
151 Sarychev, A. K. & Shalaev, V. M. *Electrodynamics of metamaterials*. (World Scientific, 2007).
152 Naik, G. V., Shalaev, V. M. & Boltasseva, A. Alternative plasmonic materials: beyond gold and silver. *Advanced Materials* **25**, 3264-3294 (2013).
153 Hardy, W. & Whitehead, L. Split-ring resonator for use in magnetic resonance from 200–2000 MHz. *Review of Scientific Instruments* **52**, 213-216 (1981).
154 Pendry, J. B., Holden, A. J., Robbins, D. & Stewart, W. Magnetism from conductors and enhanced nonlinear phenomena. *IEEE transactions on microwave theory and techniques* **47**, 2075-2084 (1999).
155 Cubukcu, E., Zhang, S., Park, Y.-S., Bartal, G. & Zhang, X. Split ring resonator sensors for infrared detection of single molecular monolayers. *Applied Physics Letters* **95**, 043113 (2009).
156 Marques, R., Martel, J., Mesa, F. & Medina, F. Left-handed-media simulation and transmission of EM waves in subwavelength split-ring-resonator-loaded metallic waveguides. *Physical review letters* **89**, 183901 (2002).
157 Martın, F., Bonache, J., Falcone, F. a., Sorolla, M. & Marqués, R. Split ring resonator-based left-handed coplanar waveguide. *Applied Physics Letters* **83**, 4652-4654 (2003).
158 Jackson, J. D. *Classical Electrodynamics*. 2nd edn, (Wiley, 1975).
159 Kock, W. E. Metal-lens antennas. *Proceedings of the IRE* **34**, 828-836 (1946).
160 Bose, J. C. On the rotation of plane of polarisation of electric waves by a twisted structure. *Proceedings of the Royal Society of London* **63**, 146-152 (1898).
161 Veselago, V. G. THE ELECTRODYNAMICS OF SUBSTANCES WITH SIMULTANEOUSLY NEGATIVE VALUES OF IMG align= ABSMIDDLE alt= ϵ eps/IMG AND μ. *Physics-Uspekhi* **10**, 509-514 (1968).
162 Pendry, J. B. Negative refraction makes a perfect lens. *Physical review letters* **85**, 3966 (2000).

163 Pendry, J. B., Schurig, D. & Smith, D. R. Controlling electromagnetic fields. *science* **312**, 1780-1782 (2006).
164 Valentine, J., Li, J., Zentgraf, T., Bartal, G. & Zhang, X. An optical cloak made of dielectrics. *Nature materials* **8**, 568-571 (2009).
165 Alù, A. & Engheta, N. Multifrequency optical invisibility cloak with layered plasmonic shells. *Physical review letters* **100**, 113901 (2008).
166 Ergin, T., Stenger, N., Brenner, P., Pendry, J. B. & Wegener, M. Three-dimensional invisibility cloak at optical wavelengths. *science* **328**, 337-339 (2010).
167 Ni, X., Wong, Z. J., Mrejen, M., Wang, Y. & Zhang, X. An ultrathin invisibility skin cloak for visible light. *science* **349**, 1310-1314 (2015).
168 Schurig, D. *et al.* Metamaterial electromagnetic cloak at microwave frequencies. *science* **314**, 977-980 (2006).
169 Zhang, J., Liu, L., Luo, Y., Zhang, S. & Mortensen, N. A. Homogeneous optical cloak constructed with uniform layered structures. *Optics express* **19**, 8625-8631 (2011).
170 Larouche, S., Tsai, Y.-J., Tyler, T., Jokerst, N. M. & Smith, D. R. Infrared metamaterial phase holograms. *Nature materials* **11**, 450-454 (2012).
171 Ni, X., Kildishev, A. V. & Shalaev, V. M. Metasurface holograms for visible light. *Nature communications* **4** (2013).
172 Zheng, G. *et al.* Metasurface holograms reaching 80% efficiency. *Nature nanotechnology* **10**, 308-312 (2015).
173 Dmitriev, A. *Nanoplasmonic sensors*. (Springer Science & Business Media, 2012).
174 Kravets, V. *et al.* Singular phase nano-optics in plasmonic metamaterials for label-free single-molecule detection. *Nature materials* **12**, 304-309 (2013).
175 Kabashin, A. *et al.* Plasmonic nanorod metamaterials for biosensing. *Nature materials* **8**, 867-871 (2009).
176 La Spada, L., Bilotti, F. & Vegni, L. in *Sensors, 2011 IEEE.* 627-630 (IEEE).
177 Melik, R., Unal, E., Perkgoz, N. K., Puttlitz, C. & Demir, H. V. Metamaterial-based wireless strain sensors. *Applied Physics Letters* **95**, 011106 (2009).
178 Li, J. & Chan, C. Double-negative acoustic metamaterial. *Physical Review E* **70**, 055602 (2004).
179 Zhang, S., Yin, L. & Fang, N. Focusing ultrasound with an acoustic metamaterial network. *Physical review letters* **102**, 194301 (2009).
180 Yang, Z., Dai, H., Chan, N., Ma, G. & Sheng, P. Acoustic metamaterial panels for sound attenuation in the 50–1000 Hz regime. *Applied Physics Letters* **96**, 041906 (2010).
181 Lezec, H. J., Dionne, J. A. & Atwater, H. A. Negative refraction at visible frequencies. *Science* **316**, 430-432 (2007).
182 Luo, C., Johnson, S. G., Joannopoulos, J. D. & Pendry, J. B. All-angle negative refraction without negative effective index. *PHYSICAL REVIEW-SERIES B-* **65**, 201104 (R)-201104 (R) (2002).
183 Parazzoli, C. G., Greegor, R. B., Li, K., Koltenbah, B. E. C. & Tanielian, M. Experimental verification and simulation of negative index of refraction using Snell's law. *Physical Review Letters* **90**, 107401 (2003).
184 Shelby, R. A., Smith, D. R. & Schultz, S. Experimental verification of a negative index of refraction. *Science* **292**, 77-79 (2001).
185 Valentine, J. *et al.* Three-dimensional optical metamaterial with a negative refractive index. *Nature* **455**, 376-379 (2008).
186 Veselago, V. G. Electrodynamics of materials with negative index of refraction. *Physics-Uspekhi* **46**, 764-768 (2003).
187 Pendry, J. B. & Smith, D. R. The quest for the superlens. *Scientific American* **295**, 60-67 (2006).

188 Zhang, S. *et al.* Negative refractive index in chiral metamaterials. *Physical review letters* **102**, 023901 (2009).
189 Boardman, A. Pioneers in metamaterials: John Pendry and Victor Veselago. *Journal of Optics* **13**, 020401 (2011).
190 Bliokh, K. Y. & Bliokh, Y. P. What are the left-handed media and what is interesting about them? *Physics-Uspekhi* **47**, 393 (2004).
191 Veselago, V. G. Formulating Fermat's principle for light traveling in negative refraction materials. *Physics-Uspekhi* **45**, 1097-1099 (2002).
192 Veselago, V. G. Energy, linear momentum and mass transfer by an electromagnetic wave in a negative-refraction medium. *Physics-Uspekhi* **52**, 649 (2009).
193 Soukoulis, C. M. & Wegener, M. Past achievements and future challenges in the development of three-dimensional photonic metamaterials. *Nature Photonics* **5**, 523-530 (2011).
194 Wuestner, S., Pusch, A., Tsakmakidis, K. L., Hamm, J. M. & Hess, O. Overcoming losses with gain in a negative refractive index metamaterial. *Physical review letters* **105**, 127401 (2010).
195 Boltasseva, A. & Atwater, H. A. Low-loss plasmonic metamaterials. *Science* **331**, 290-291 (2011).
196 Xiao, S. *et al.* Loss-free and active optical negative-index metamaterials. *Nature* **466**, 735-738 (2010).
197 Biener, J. *et al.* Nanoporous plasmonic metamaterials. *Advanced Materials* **20**, 1211-1217 (2008).
198 Johnson, T. W. *et al.* Highly reproducible near-field optical imaging with sub-20-nm resolution based on template-stripped gold pyramids. *ACS nano* **6**, 9168-9174 (2012).
199 Xiong, Y., Liu, Z. & Zhang, X. A simple design of flat hyperlens for lithography and imaging with half-pitch resolution down to 20 nm. *Applied Physics Letters* **94**, 203108 (2009).
200 Mandal, P. Plasmonic perfect absorber for refractive index sensing and SERS. *Plasmonics* **11**, 223-229 (2016).
201 Nagpal, P., Lindquist, N. C., Oh, S.-H. & Norris, D. J. Ultrasmooth patterned metals for plasmonics and metamaterials. *science* **325**, 594-597 (2009).
202 Ponsetto, J. L., Wei, F. & Liu, Z. Localized plasmon assisted structured illumination microscopy for wide-field high-speed dispersion-independent super resolution imaging. *Nanoscale* **6**, 5807-5812 (2014).
203 Wei, F. & Liu, Z. Plasmonic structured illumination microscopy. *Nano letters* **10**, 2531-2536 (2010).
204 Wei, F. *et al.* Wide field super-resolution surface imaging through plasmonic structured illumination microscopy. *Nano letters* **14**, 4634-4639 (2014).
205 Zhang, C., Min, C., Du, L. & Yuan, X.-C. Perfect optical vortex enhanced surface plasmon excitation for plasmonic structured illumination microscopy imaging. *Applied Physics Letters* **108**, 201601 (2016).
206 Barnes, W. L., Dereux, A. & Ebbesen, T. W. Surface plasmon subwavelength optics. *Nature* **424**, 824-830 (2003).
207 Balaa, K., Fort, E. & Instruments, N. Surface plasmon enhanced TIRF imaging. *Imaging & Microscopy* **11**, 55-56 (2009).
208 Cui, Z. in *Nanofabrication: Principles, Capabilities and Limits* 149-175 (Springer International Publishing, 2017).
209 CST. *CST - Computer Simulation Technology*, <https://www.cst.com/> (2014).
210 CST. *CST STUDIO SUITE 2014*, <https://www.cst.com/Content/Articles/article909/CST-STUDIO-SUITE-2014.pdf> (2014).
211 Chen, X. *et al.* Dual-polarity plasmonic metalens for visible light. *Nature communications* **3**, 1198 (2012).

212 Mohammadi, A., Sandoghdar, V. & Agio, M. Gold, copper, silver and aluminum nanoantennas to enhance spontaneous emission. *Journal of Computational and Theoretical Nanoscience* **6**, 2024-2030 (2009).
213 Deng, Z.-Y., Lin, C.-W., Kuo, Y.-T., Chen, K.-L. & Wu, C.-H. in *Nanotechnology (IEEE-NANO), 2016 IEEE 16th International Conference on.* 598-599 (IEEE).
214 Johnson, N. *et al.* A review of size and geometrical factors influencing resonant frequencies in metamaterials. *Opto-Electronics Review* **14**, 187-191 (2006).
215 Fan, W., Yan, B., Wang, Z. & Wu, L. Three-dimensional all-dielectric metamaterial solid immersion lens for subwavelength imaging at visible frequencies. *Science advances* **2**, e1600901 (2016).
216 Pala, N. & Karabiyik, M. in *Encyclopedia of Nanotechnology* (ed Bharat Bhushan) 718-740 (Springer Netherlands, 2012).
217 Choi, M. *et al.* A terahertz metamaterial with unnaturally high refractive index. *Nature* **470**, 369 (2011).
218 Křížek, P., Lukeš, T., Ovesný, M., Fliegel, K. & Hagen, G. M. SIMToolbox: a MATLAB toolbox for structured illumination fluorescence microscopy. *Bioinformatics* **32**, 318-320 (2015).
219 Křížek, P., Lukeš, T., Ovesný, M., Fliegel, K. & Hagen, G. M. *SIMToolbox: a MATLAB toolbox for structured illumination microscopy*, <http://mmtg.fel.cvut.cz/simtoolbox/> (2014).
220 Müller, M., Mönkemöller, V., Hennig, S., Hübner, W. & Huser, T. Open-source image reconstruction of super-resolution structured illumination microscopy data in ImageJ. *Nature communications* **7** (2016).
221 Müller, M., Mönkemöller, V., Hennig, S., Hübner, W. & Huser, T. *fairSIM, a free, open source ImageJ plugin for SR-SIM reconstructions*, <https://fairsim.github.io/> (2017).
222 MathWorks. *phantom*, <https://uk.mathworks.com/help/images/ref/phantom.html?s_tid=gn_loc_drop> (2017).
223 Jain, A. K. *Fundamentals of digital image processing*. (Prentice-Hall, Inc., 1989).
224 Weisstein, E. W. *Fourier Series.*, < http://mathworld.wolfram.com/FourierSeries.html> (2017).
225 MicroResistTechnology. *E-Beam/ Deep UV Lithography*, <http://microresist.de/en/product/negative-photoresists-1> (2017).